Annual Report
Jahresbericht

2012

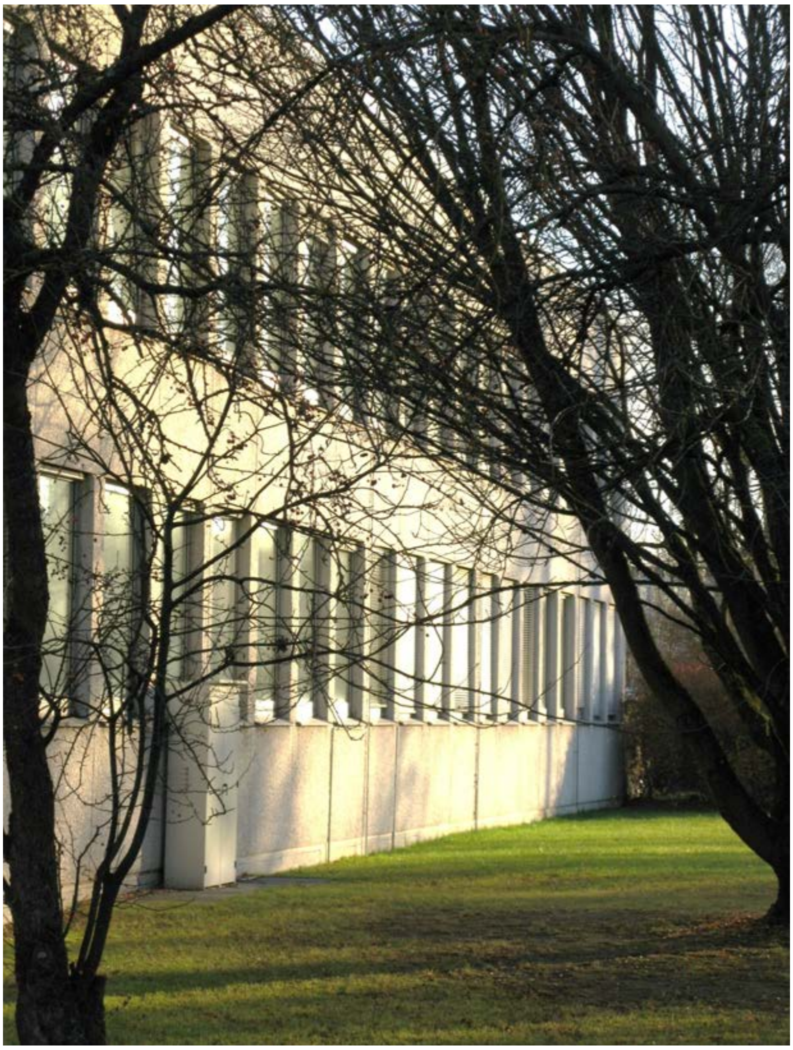

Walther–Meissner–Institut
für Tieftemperaturforschung
Bayerische Akademie der Wissenschaften

Contact:

Prof. Dr. Rudolf Gross
Walther–Meißner–Institut für Tieftemperaturforschung
Bayerische Akademie der Wissenschaften
and
Lehrstuhl für Technische Physik – E23
Technische Universität München

Address:

Walther–Meißner–Str. 8
D - 85748 Garching
GERMANY

Phone: +49 – (0)89 289 14201
Fax: +49 – (0)89 289 14206
e–mail: Rudolf.Gross@wmi.badw.de
WWW–address: http://www.wmi.badw.de

Secretary's Office and Administration:

Emel Dönertas
Phone: +49 – (0)89 289 14202
Fax: +49 – (0)89 289 14206
e–mail: Emel.Doenertas@wmi.badw.de
Sekretariat@wmi.badw.de

Ludwig Ossiander
Phone: +49 – (0)89 289 14205
Fax: +49 – (0)89 289 14206
e–mail: Ludwig.Ossiander@wmi.badw.de

Preface

Dear colleagues, friends, partners, and alumni of the Walther-Meißner-Institute for Low Temperature Research (WMI) of the Bavarian Academy for Sciences and Humanities (BAdW)!

On behalf of the members of WMI, I am pleased to present to you our ***Annual Report 2012***. The report intends to provide you an overview on our last year's activities ranging from fundamental studies in solid state physics, application oriented research, and materials science to technological developments in low temperature, thin film and nano-technology. Our research interests cover superconductivity and superfluidity, magnetism, strongly correlated electron systems, spin electronics and spin caloritronics, as well as quantum information processing and quantum coherence in solid state systems. The report is aiming to provide not only concise summaries of our ongoing research projects and their major results, but also information on our teaching activities as well as interesting data about publications, completed and ongoing Ph.D., diploma, master and bachelor theses, collaborations, funding, and recent developments in infrastructure and experimental facilities.

In 2012, we succeeded to further extend our efforts in research and teaching and to keep our internationally leading position in several areas of low temperature research. WMI was successful in extending long-term, coordinated research programs jointly put into effect in collaboration with partners from both Munich universities and other national and international research institutions. In particular, the proposal for the second funding period of the *Cluster of Excellence Nanosystems Initiative Munich (NIM)* has been positively evaluated in January 2012 and a second five-year funding period (11/2012 – 10/2017) has been granted by the the German Research Foundation (DFG) and the German Council of Science and Humanities (Wissenschaftsrat) on June 15, 2012. WMI is coordinating the Research Area on Quantum Nanophysics of NIM. We also successfully acquired a new EU Collaborative Project entitled *Quantum Propagating Microwaves in Strongly Coupled Environments – PROMISCE* funded by the FET-Open Initiative of the EU 7th Framework Program. This project studies the dynamics of microwave photons in quantum circuits, including their interaction with superconducting qubits, transmission lines and quantum metamaterials. It ultimately aims at merging the possibilities of all-optical quantum computing with superconducting circuits. Many other coordinated research programs, such as the *Collaborative Research Center 631* (*Solid State Quantum Information Processing*), the *Transregional Collaborative Research Center TRR 80* (*From Electronic Correlations to Functionality*), the EU network *Circuit and Cavity Quantum Electro-Dynamics (CC-QED)*, the *DFG Priority Program 1285* (*Semiconductor Spin Electronics*), the *DFG Priority Program 1485* (*High Temperature Superconductivity in the Iron-Pnictides*), and the *DFG Priority Program 1538* (*Spin Caloric Transport*) are successfully ongoing. In several of these programs, WMI is playing a leading role and providing the coordinator of the program.

Renovation and maintenance activities are necessary but usually annoying for the scientists since they are perturbing their research activities. Fortunately, after more than a year and spending more than 1 Mio. Euro, the construction activities required to update the fire safety systems of WMI to the present regulations could be finished in October 2012. We are grateful to the state government for the financial support and the department of planning and building inspection for the coordination of the activity. In 2012, we also could renovate several laboratories and could install new research equipment such as a new vector magnet for our research program on spin caloritronics. Two new dilution refrigerators for experiments on solid state quantum systems have been almost completed in 2012. We are particularly happy that we succeeded in keeping our high level of third-party funding in 2012 at about 40% of our full cost budget.

Throughout 2012, more than 70 people were working at WMI, including more than 20 Ph.D. students and a large number of bachelor, master and diploma students as well as international guests. In 2012, 5 Ph.D. theses, 18 diploma and master theses, and 10 bachelor theses were completed. Our successful research is reflected in a large number of excellent publications, new extramural funding, collaborations with industry, and many invited presentations at national and international conferences. WMI also has organized by itself or significantly contributed to the organization of several national and international workshops and conferences, in this way promoting its scientific visibility. This would not have been possible without the dedicated and hard work of all scientific and technical staff as well as doctorate, diploma, master and bachelor students. An important prerequisite of our successful research work is the continuous support of various funding agencies. In this context we gratefully acknowledge financial support from the BAdW, the DFG, the Bavarian Ministry for Science and Arts, the BMBF and the EU. A further key to our success in research is the recruitment of outstanding, scientifically independent group leaders with complementary research interests and technical expertise, a process which is supported and monitored by the scientific advisory board of WMI, and the excellent quality of our Ph.D., diploma and master students. We are particularly proud of the fact that Hans Huebl was awarded the ***Prize of the Karl Thiemig-Stiftung 2012*** of BAdW in recognition of his pioneering research on solid state quantum systems. In addition, Mathias Weiler received a ***Prize of the Dimitris N. Chorafas Foundation*** in recognition of his excellent Ph.D. thesis on “Magnon-Phonon Interactions in Ferromagnetic Thin Films”. He also received a DAAD postdoctoral scholarship for a two-year stay at NIST, Boulder. Despite the continuous expansion of WMI, we are much committed to support and promote young scientists in their career.

I hope that our Annual Report 2012 inspires your interest in WMI. I take this opportunity to thank all the colleagues, guests, students, post–docs and cooperating partners, who contributed to our research and teaching activities within the last year, and last but not least all our friends and sponsors for their interest, trust and continuous support.

Garching, December 2012

R. Gross
Rudolf Gross

Contents

Scientific Reports: **9**

Joint Research Project **9**

Basic Research **25**

The Walther–Meißner–Institute

General Information

The Walther–Meißner–Institute for Low Temperature Research (WMI) is operated by the Commission for Low Temperature Research of the Bavarian Academy of Sciences and Humanities (BAdW). The commission was founded in 1946 on Walther Meißner's initiative, who was president of BAdW from 1946 to 1950. The Commissions (Research Groups) of the Academy are set up in order to carry out long–term projects, which are too ambitious for the lifetime or capacity of any single researcher, or which require the collaboration of specialists in various disciplines. At present, the Bavarian Academy of Sciences and Humanities consists of 36 Commissions with more than 300 employees.

The Commission for Low Temperature Research of the BAdW started its research activities in 1946 in the Herrsching barracks. After the retirement of Walther Meißner in 1952, Heinz Maier-Leibnitz, who followed Walther Meißner on the Chair for Technical Physics of the Technische Universität München, became the new head of the Commission for Low Temperature Research. In 1967, the commission moved to the Garching research campus after the construction of the new "Zentralinstitut für Tieftemperaturforschung" (ZTTF) was completed (director: Prof. Heinz Maier-Leibnitz, technical director: Prof. Franz Xaver Eder). Until 1972, the theory group of the Institute Laue Langevin was hosted at the ZTTF. In 1980, Prof. Dr. Klaus Andres became the new director of the ZTTF again associated with the Chair for Technical Physics (E23) at the Technische Universität München, followed by Prof. Dr. Rudolf Gross in 2000. In 1982, the ZTTF was renamed into Walther-Meißner-Institute for Low Temperature Research (WMI) on the occasion of Walther Meißner's 100. birthday.

As already mentioned, it is a long tradition that WMI hosts the Chair for Technical Physics (E 23) of the Technische Universität München (TUM) with the director of the WMI being full professor at the Faculty of Physics of TUM. However, there are also close ties with the Ludwig-Maximilians-Universität (LMU). Between 2004 and 2010, WMI hosted a scanning probe division with the head of this division being professor at the Ludwig-Maximilians-Universität (LMU). In this way a tight collaboration has been established between WMI and research groups of both Munich universities, joining technological and human resources in the fields of experimental and theoretical solid-state and condensed matter physics, low temperature techniques, materials science as well as thin film and nanotechnology. Noteworthy, the WMI supplies liquid helium to more than 25 research groups at both Munich universities and provides the technological basis for low temperature research.

Research Activities

The research activities of the Walther–Meißner–Institute are focused on low temperature solid-state and condensed matter physics (see reports below). The research program is devoted to both **fundamental** and **applied research** and also addresses **materials science, thin film and nanotechnology** aspects. With respect to **basic research** the main focus of the WMI is on

- superconductivity and superfluidity,
- magnetism, spin transport, spin mechanics and spin caloritronics,
- quantum phenomena and quantum coherence in mesoscopic systems and nanostructures,
- circuit-quantum electrodynamics and circuit-nanomechanics,
- ordering and emergent phenomena in correlated electron systems,
- and the general properties of metallic systems at low and very low temperatures.

The WMI also conducts **applied research** in the fields of

- solid-state quantum information processing systems,
- superconducting and spintronic devices,
- oxide electronics,
- multi-functional and multiferroic materials,
- and the development of low and ultra low temperature systems and techniques.

With respect to **materials science, thin film and nanotechnology** the research program is focused on

- the synthesis of superconducting and magnetic materials,
- the single crystal growth of oxide materials,
- the thin film technology of complex oxide heterostructures including multi-functional and multiferroic material systems,
- and the fabrication of superconducting, magnetic, and hybrid nanostructures.

The WMI also develops and operates systems and techniques for low and ultra–low temperature experiments. A successful development have been dry mK-systems that can be operated without liquid helium by using a pulse-tube refrigerator for precooling. Meanwhile, these systems have been successfully commercialized by the company VeriCold Technologies GmbH at Ismaning, Germany, which was taken over by Oxford Instruments in 2007. As further typical examples we mention a nuclear demagnetization cryostat for temperature down to below 100 µK, or very flexible dilution refrigerator inserts for temperatures down to about 20 mK mK fitting into a 2 inch bore. These systems have been engineered and fabricated at the WMI. Within the last years, several dilution refrigerators have been provided to other research groups for various low temperature experiments. The WMI also operates a helium liquifier with an annual capacity of well above 150.000 liters and supplies both Munich universities with liquid helium. To optimize the transfer of liquid helium into transport containers the WMI has developed a pumping system for liquid helium that is commercialized in collaboration with a company.

To a large extent the research activities of WMI are integrated into national and international research projects such as Clusters of Excellence, Collaborative Research Centers, Research Units, or EU projects. The individual research groups of WMI offer a wide range of attractive research opportunities for diploma (graduate) students, PhD students and postdoctoral fellows.

Experimental Facilities and Resources

The WMI is equipped with state of the art facilities for the preparation and characterization of superconducting and magnetic materials as well as for various low and ultra–low temperature experiments. The main experimental and technological resources of WMI are listed in the following.

Materials Preparation and Fabrication of Nanostructures

- Laser Molecular Beam Epitaxy (L-MBE) system for oxide heterostructures (equipped with in–situ RHEED, Omicron AFM/STM system, atomic oxygen/nitrogen source, infrared-laser heating system, metallization)
- molecular beam epitaxy (MBE) system for metallic systems
- UHV magnetron sputtering systems for metals (e.g. Nb, Al, NiPd, ...)

- magnetron sputtering system for oxide heteroepitaxy (equipped with four sputtering guns and an oxygen ion gun)
- reactive ion etching (RIE) system, Plasmalab 80 Plus with ICP plasma source, Oxford Instruments Plasma Technology
- ion beam etching (IBE) system equipped with a LN_2 cooled sample holder
- polishing machine for substrate preparation
- ultrasonic bonding machine
- $50\,m^2$ class 1000 clean room facility
- optical lithography (Süss maskaligner MJB 3 and projection lithography)
- electron beam lithography (based on Philips XL 30 SFEG scanning electron microscope and Raith Elphy Plus lithography system including a laser stage)
- four-mirror image furnace for crystal growth

Characterization

- 2–circle x–ray diffractometer (Bruker D8 Advance, sample temperature up to 1 600°C)
- high resolution 4–circle x–ray diffractometer with Göbel mirror and Ge monochromator (Bruker D8 Discover)
- scanning electron microscope with EDX analysis
- UHV room temperature AFM/STM system
- 2048 u high resolution mass spectrometer (Fa. Pfeiffer, cross-beam ion source, SEM)
- Low Energy Electron Diffraction (SPECTA-LEED, Fa. Omicron)
- two Raman spectroscopy systems (1.5 to 300 K, in-situ sample preparation)
- SQUID magnetometer (Quantum Design, 1.5 to 700 K, up to 7 T)
- several high field magnet systems (up to 17 T Tesla) with variable temperature inserts
- 7 T split coil magnet systems with optical access and variable temperature insert
- experimental set–ups for the measurement of noise including low noise SQUID amplifiers and signal analyzers
- high-frequency network analyzers (up to 40 GHz) and various microwave components (sources, mixers, circulators, attenuators) for the determination of high frequency parameters
- high-frequency cryogenic probing station (up to 20 GHz, $T > 4\,K$)
- magnetooptical Kerr effect (MOKE) system
- ferromagnetic resonance (FMR) system

Low temperature systems and techniques

- 5 K-Scanning Tunneling Microscope (low temperature STM, Fa. Omicron)
- several $^3He/^4He$ dilution refrigerator inserts for temperatures down to 10 mK
- "dry" mK-cooler based on a dilution refrigerator with pulse-tube precooling
- "dry" dilution refrigerator with a base temperature of about 10 mK equipped with a 3D vector magnet (1/1/6 Tesla)
- ultra–low temperature facility for temperatures down to below 100 µK based on a nuclear demagnetization cryostat
- experimental set–ups for the measurement of specific heat, magnetization, thermal expansion as well as electrical and thermal transport properties as a function of temperature, magnetic field and pressure

Joint Research Projects

nim
nanosystems initiative munich

SFB 631

TRR 80

Schwerpunkt Halbleiter Spintronik

SPP 1285

SPP 1458

SPP 1538

QED
CIRCUIT AND CAVITY
QUANTUM ELECTRODYNAMICS

PROMISCE

The Collaborative Research Center 631

F. Deppe, R. Gross, H. Hübl, A. Marx[1]

The Collaborative Research Center 631 **(SFB 631) on Solid State Quantum Information Processing** was established in 2003 and extended for a second and a third four-year funding in 2007 and 2011, respectively. The third funding period will last until June, 2015.

Quantum information science is a fascinating and one of the most rapidly growing fields of science and technology, residing at the interface between physics, mathematics, computer and materials science, and engineering. It is concerned with both fundamental questions and technological developments, aiming at the realization of a useful quantum information hardware. Over the last decade, the physics of solid state quantum systems has developed into a key research field of Walther-Meißner-Institute (WMI). It does not only provide the foundations of quantum information systems and quantum technology, but also addresses key fundamental regarding quantum coherence, quantum dynamics and decoherence processes in solid state quantum systems. Furthermore, it requires extremely sensitive measurements at low and ultra-low temperatures and therefore perfectly fits to the research profile of WMI.

Solid state systems are considered a particularly promising platform for the successful implementation of quantum information systems. The Collaborative Research Center 631 studies the ***physical concepts, materials aspects, and technological foundations of solid state quantum information processing (SQIP)***. It deals with the coherent dynamics of solid state quantum systems and has the vision to engineer them so as to allow to process and communicate information on the basis of quantum mechanical principles. To realize this vision, SFB 631 aims at the clarification of the key physical questions as well as the materials aspects and technological problems that have to be solved for the successful implementation of SQIP. Particular goals are to design and implement solid state quantum bits (qubits) with long coherence times, to learn how to efficiently control, manipulate and read-out qubits, to couple them to complex systems as well as to develop theoretical tools for modeling the dynamics of driven, damped qubits in different experimental systems. The long-term goal is the development of small-scale solid state quantum systems that are capable of performing elementary processing and communication of quantum information. This involves the design, fabrication and investigation of solid state qubits, oscillators, cavities and transmission lines that can be combined to create hybrid quantum circuits.

To cover the broad spectrum of fundamental and application oriented questions related to solid state quantum information systems in a comprehensive way, SFB 631 joins research activities from quantum information theory, experimental and theoretical solid state physics, quantum optics, materials science, and nanotechnology. Today, within SFB 631 research groups from the Bavarian Academy of Sciences and Humanities (BAdW), the TU Munich (TUM), the Ludwig-Maximilians-University (LMU), the Max-Planck-Institute for Quantum Optics (MPQ), as well as Augsburg and Regensburg University are collaborating in 17 research projects. The main objective is to obtain a profound understanding of the physics, technology, and materials aspects of SQIP by making use of advanced experimental and theoretical methods in a coordinated interdisciplinary research effort. At present, SFB 631 joins more than 30 principal investigators and more than 60 Ph.D. and diploma students, as well

---

[1] This work is supported by the German Research Foundation through SFB 631.

as a large number of postdocs and guest scientists. WMI is one of the main actors, not only being involved in the three projects A3 (Gross, Hübl, Marx), A8 (Gross, Marx, Deppe) and C3 (Hübl), but also providing the coordination of the center from the beginning (spokesman: Rudolf Gross).

Within the project A3 on *Superconducting Quantum Circuits as Basic Elements for Quantum Information Processing* and project A8 on *Cavity Quantum Electrodynamics with Superconducting Devices*, the research program of WMI within SFB 631 is focusing on the fabrication and study of superconducting quantum information circuits. This includes the fabrication of superconducting flux qubits in which quantum mechanical superposition states of clockwise and counter-clockwise circulating persistent currents are used for the realization of solid state qubits. These qubits are coupled to superconducting microwave resonators. In this way fascinating quantum electrodynamic experiments with deliberately designed artificial solid state atoms become possible. Since such experiments are completely analogous to quantum optical experiments on natural atoms in optical resonators, this prospering new field is called circuit quantum electrodynamics (circuit QED). Here, particular goals are the strong and ultrastrong coupling of superconducting qubits to high-quality superconducting microwave resonators, the generation and detection of non-classical microwave states (e.g. Fock or squeezed states), the development of dispersive readout and quantum non-demolition measurements, and the entanglement of superconducting qubits via multiple resonators. Regarding these research goals the WMI team closely collaborates with the theory groups at LMU (von Delft), the University of Augsburg (Hänggi), the Universidad del País Vasco - Euskal Herriko Unibertsitatea at Bilbao (Solano), and the Instituto de Física Fundamental at Madrid (Garcia-Ripoll), as well as the experimental groups at the NTT Basic Research Laboratories (Semba) and the Nano Electronics Research Laboratories at NEC Corporation, Japan (Nakamura, Tsai, Yamamoto). The research work within SFB 631 is also closely linked to the activities within Research Area I of the Cluster of Excellence *Nanosystems Initiative Munich (NIM)* (see pp. 14–16).

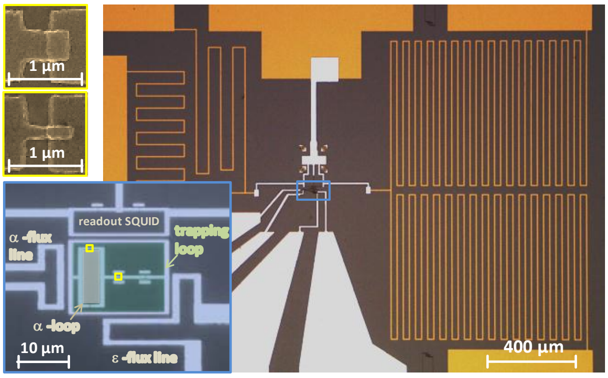

Figure 1: Optical micrograph of a chip containing a tunable-gap gradiometric flux qubit with the biasing lines and filter structures. The large inset shows the region marked with the blue rectangle: the gradiometric qubit with readout dc SQUID as well as the α- and ε-flux lines used for tuning the frustration of the α- and trapping loop. The two small insets show SEM images of a regular (top) and the α-junction (bottom). The position of these junction are marked with yellow rectangles in the large inset.

In 2012 we have demonstrated path entanglement of propagating quantum microwaves using superconducting circuits and quantum signal recovery techniques (see Ref. [1, 2] and report by F. Deppe *et al.*, pp. 30–31). We have optimized our gradiometric flux qubits employing an in-situ tunable tunnel coupling. We demonstrate a large tunability of the qubit gap both with an external coil and an on-chip bias line (see Ref. [3] and report by M. Schwarz *et al.*, pp. 75–77). We also have successfully performed measurements on a coupled flux qubit-resonator system [4] in the time domain and were able to observe the Rabi oscillations and to measure the T_1-time of our qubit (see report by A. Baust *et al.*, pp. 27–29). Moreover, we have successfully implemented and tested the superconducting quantum switch using two on-chip coplanar stripline resonators and a flux qubit. From spectroscopy data, we successfully extract the relevant system parameters and find conclusive evidence for tunable and switchable coupling between the two resonators (see report by E. Hoffmann *et al.*, pp. 49–51). Regarding superconducting quantum circuit technology, we have made progress in the fabrications of elements for low temperature microwave experiments. We have performed preliminary experiments on tunable resonator-resonator coupling and on a 90° hybrid ring, which is analogous to a semitransparent mirror for propagating microwaves and therefore is a basic building block for experiments on propagating quantum microwaves (see Ref. [5] and report by F. Wulschner *et al.*, pp. 77–79). We also have fabricated and characterized chains of up to three coupled transmission line resonators in a scalable layout. After introducing nonlinearities in the form of Josephson junctions and scaling to longer chains, these systems can serve as quantum simulators for Bose-Hubbard-type Hamiltonians in the future (see Ref. [6] and report by L. Zhong *et al.*, pp. 80–81).

References

[1] E. P. Menzel, R. Di Candia, F. Deppe, P. Eder, L. Zhong, M. Ihmig, M. Haeberlein, A. Baust, E. Hoffmann, D. Ballester, K. Inomata, T. Yamamoto, Y. Nakamura, E. Solano, A. Marx, and R. Gross, Phys. Rev. Lett. **109**, 250502 (2012).

[2] E. P. Menzel, F. Deppe, M. Mariantoni, M. A. Araque Caballero, A. Baust, T. Niemczyk, E. Hoffmann, A. Marx, E. Solano, and R. Gross, Phys. Rev. Lett. **105**, 100401 (2010).

[3] M. J. Schwarz, J. Goetz, Z. Jiang, T. Niemczyk, F. Deppe, A. Marx, and R. Gross. Gradiometric flux qubits with tunable gap. `arXiv:1210.3982` (2012).

[4] T. Niemczyk, F. Deppe, H. Huebl, E. P. Menzel, F. Hocke, M. J. Schwarz, J. J. Garcia-Ripoll, D. Zueco, T. Hümmer, E. Solano, A. Marx, and R. Gross, Nature Phys. **6**, 772–776 (2010).

[5] B. Peropadre, D. Zueco, F. Wulschner, F. Deppe, A. Marx, R. Gross, and J. García-Ripoll. Tunable coupling engineering between superconducting resonators: from sidebands to effective gauge fields. `arXiv:1207.3408` (2012).

[6] M. Leib, F. Deppe, A. Marx, R. Gross, and M. J. Hartmann, New Journal of Physics **14**, 075024 (2012).

The Cluster of Excellence “Nanosystems Initiative Munich – NIM”

F. Deppe, S.T.B. Gönnenwein, R. Gross, H. Hübl, A. Marx[1]

Systems with different appearance and function on the macroscopic scale often show striking analogies and even similarities regarding structure, dynamics and interaction on the nano-meter scale. In reverse, synthesis, manipulation and hybridization of nano-objects can drastically change or create new functionalities from the nano- to the macro-world and from inorganic matter to living cells. In order to fully exploit these cross-sectional and interdisciplinary opportunities and synergies the excellence cluster ***Nanosystems Initiative Munich (NIM)*** has been built on a unique strength in the Munich scientific area. NIM comprises internationally recognized expertises in all relevant research areas ranging from quantum nanophysics to the creation and study of nanosystems for biophysics and the life sciences. NIM’s overall scientific vision is to integrate nanometer sized building blocks as well as bio-molecular assemblies into entire functional systems.

NIM was launched in 2006 and joins research groups from LMU Munich, TU Munich, WMI, the University of Augsburg, the Munich University of Applied Science, the Max-Planck-Institutes for Biochemistry and Quantum Optics, and the Deutsches Museum. It merges their combined expertise on nanoscale systems into a coherent and focused nanoscience cluster. While many individual nanoscale building blocks and components have been devised in recent years using top-down and bottom-up strategies, little is known about their integration into entire functional systems. The overarching vision guiding the research in NIM is therefore to design, fabricate and achieve control of a broad range of artificial and multi-functional nanoscale systems, and to unlock their potential for possible applications in fields as diverse as future information technologies, the life sciences, or combinations of both. To this end, it is essential to gain a fundamental understanding of their properties and behavior, which range from being purely quantum mechanical to being governed mainly by stochastic effects.

The first six-year funding period of NIM ended in October 2012. The funding proposal for the second five-year funding period has been reviewed in January 2012. On June 15, 2012, the German Research Foundation (DFG) and the German Council of Science and Humanities (Wissenschaftsrat) announced that NIM will be funded for another five years. NIM’s future research activities are organized in five research areas (RAs) as illustrated in the figure: RA I – ***Quantum Nanophysics***, RA II – ***Hybrid Nanosystems***, RA III – ***Nanosystems for Energy Conversion***, RA IV – ***Biomolecular Nanosystems***, and RA V – ***Biomedical Nanotechnologies***. At WMI, several scientists (Deppe, Gönnenwein, Gross, Hübl, Marx) actively contributed to successfully implement the ambitious research program for the second funding period of NIM. The physics of quantum nanosystems is one of the main future research directions of NIM, in perfect agreement with the focus of several research activities at WMI. The major

---

[1] This work is supported by the German Excellence Initiative via the Nanosystems Initiative Munich (NIM).

contributions of WMI are to RA I: ***Quantum Nanophysics*** and RA II: ***Hybrid Nanosystems***. Research area I is coordinated by R. Gross of WMI.

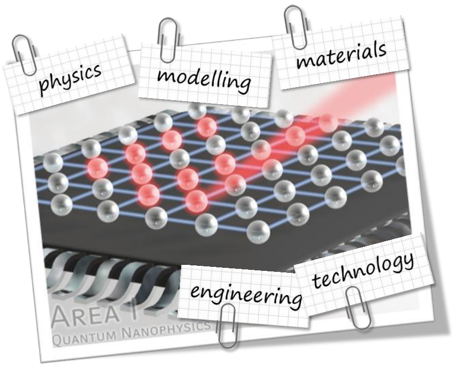

The scientific program of ***Research Area I*** is focused on quantum nanosystems. It aims at the modeling and understanding of such nanosystems on a quantum level. The modelling and understanding of nanosystems on a quantum level is a key prerequisite for their application in hybrid devices, energy conversion systems as well as in biomolecular and biomedical systems. The scientific program of research area I addresses this fundamental problem by systematically studying quantum systems based on solid state nanostructures and tailor-made meso-scale many body systems realized in optical lattices. In future, these research efforts particularly focus on (i) the design and fundamental mechanisms of nanoscale quantum matter, (ii) the development of hybrid quantum nanosystems, (iii) the study of nonequilibrium dynamics, and (iv) the foundations of quantum X-tronics (X = spin, charge, flux, plasmon, magnon, etc.). They aim to establish a thorough understanding of quantum nanosystems and to develop the techniques required for their realization, manipulation and control. To this end, a key objective of research area I is to provide the physical foundations and technological platform for novel quantum-based technologies and functionalities relevant for the other NIM research areas.

Examples of the planned WMI activities within NIM are the fabrication of linear arrays of interacting flux qubits as toy models for many-body quantum systems (see report by Zhong *et al.*, pp. 80–81) or the systematic study of the interaction between nanoscale solid state quantum systems and the modes of electromagnetic fields on a single quantum level (see report by Lotze *et al.*, pp. 61–62). In this field the research activities within NIM are closely linked to those of SFB 631 described already above (see pp. 11–13). The WMI research activities also aim at the study of pure spin currents in the quantum regime. It is planned to perform spin pumping experiments in ferromagnet/normal metal or antiferromagnet/normal metal structures in the limit of mK temperatures and single microwave photons. A number of successful experiments in this direction already have been performed (see Refs. [1–4] and report by Weiler *et al.*, pp. 68–70). Furthermore, the study of “Quantum Ferromagnetic Resonance”, which can be viewed as a coherent exchange of excitations between a harmonic oscillator and a ferromagnet, is an interesting field. Recently, the coherent exchange of photons and magnons could be observed for the first time in a coupled superconducting coplanar waveguide resonator/ferrimagnetic insulator hybrid system (see Ref. [5] and report by Lotze *et al.*, pp. 61–62).

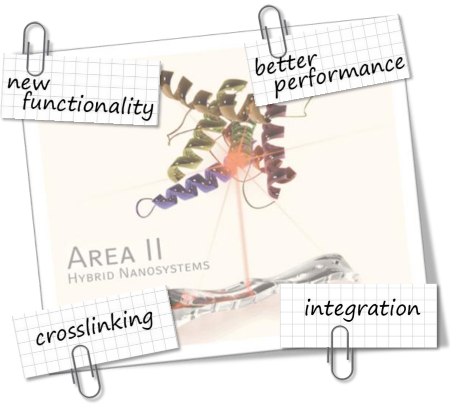

The ***Research Area II*** on Hybrid Nanosystems can be viewed as NIM’s main nanofoundry, where a great variety of solid state and nano-bio-systems are to be fabricated by advanced top-down and smart bottom-up approaches. A key goal is to exploit the potential and to realize functional nanosystems with optimized performance. To this end, nanosystems with various degrees of freedom such as optical, electrical or mechanical will cross-fertilize. It includes different quasiparticles and excitations ranging from photons over plasmons, magnons, and phonons to charge carriers, going along with a transfer of methods, materials and technologies. It utilizes the power of biological self-assembly to realize active devices or photons to control the mechanical and magnetic properties of nanoscale matter. RA II aims towards the realization of such hybrid nanosystems consisting of more than one constituent to meet the expectations given above. The representative examples all share the common ground of adding value by hybridization, combination and cross-linking between the projects as well as the four other areas of NIM. The aim is to integrate individual nanoscale building blocks and biomolecular assemblies into entire functional systems acting in complex environments, resulting in physical sensors and actuators to investigate and promote transport within various nanosystems.

Within RA II, WMI investigates the interaction of light with magnonic excitations using near-field and nano-optical effects (in collaboration with Grundler, TUM). Metallic nanostructures integrated into magnetic devices are used to locally enhance the light-induced electrical field due to plasmonic effects and to extend the wavevector spectrum by exploiting evanescent waves. Also, the coupling of magnonic and phononic modes is investigated in ferromagnetic/ferroelectric hybrid devices (in a cooperation with Krenner/Wixforth, University of Augsburg, and Weig, LMU). We already have shown that in such devices a surface acoustic wave (SAW) propagating in the ferroelectric induces local, radio-frequency, elastic strains in the adjacent ferromagnet [2]. This allows to elastically drive magnetization dynamics, and makes hypersound ferromagnetic resonance experiments with submicron spatial resolution possible.

A new research field started at WMI some years ago is nanomechanics. In a collaboration with E. Weig, LMU, and T. Kippenberg, EPFL Lausanne, we have successfully fabricated electro-mechanical nanosystems consisting of a superconducting nanobeam coupled to a high quality factor superconducting microwave resonator. These systems have been studied at mK temperatures and interesting features such as electro-mechanically induced transparency (EMIT) and absorption (EMIA) have been observed recently (see Refs. [6, 7] and report by Hocke *et al.*, pp. 45–48). Moreover, the coherent control of microwave signals using circuit nano-electromechanics could be demonstrated [7].

References

[1] M. Weiler, M. Althammer, F. D. Czeschka, H. Huebl, M. S. Wagner, M. Opel, I.-M. Imort, G. Reiss, A. Thomas, R. Gross, and S. T. B. Goennenwein, Phys. Rev. Lett. **108**, 106602 (2012).

[2] M. Weiler, H. Huebl, F. S. Goerg, F. D. Czeschka, R. Gross, and S. T. B. Goennenwein, Phys. Rev. Lett. **108**, 176601 (2012).

[3] F. D. Czeschka, L. Dreher, M. S. Brandt, M. Weiler, M. Althammer, I.-M. Imort, G. Reiss, A. Thomas, W. Schoch, W. Limmer, H. Huebl, R. Gross, and S. T. B. Goennenwein, Phys. Rev. Lett. **107**, 046601 (2011).

[4] M. Weiler, L. Dreher, C. Heeg, H. Huebl, R. Gross, M. S. Brandt, and S. T. B. Goennenwein, Phys. Rev. Lett. **106**, 117601 (2011).

[5] H. Huebl, C. Zollitsch, J. Lotze, F. Hocke, M. Greifenstein, A. Marx, R. Gross, and S. T. B. Goennenwein. High cooperativity in coupled microwave resonator ferrimagnetic insulator hybrids. `arXiv:1207.6039` (2012).

[6] F. Hocke, X. Zhou, A. Schliesser, T. J. Kippenberg, H. Huebl, and R. Gross. Electromechanically induced absorption in a circuit nano-electromechanical system. Accepted for publication in New J. Phys., `arXiv:1209.4470` (2012).

[7] X. Zhou, F. Hocke, A. Schliesser, A. Marx, H. Huebl, R. Gross, and T. J. Kippenberg. Control of microwave signals using circuit nano-electromechanics. Accepted for publication in Nature Physics, `arXiv:1206.6052v2` (2012).

The DFG Priority Program SPP 1285 “Semiconductor Spintronics”

M. Althammer, S. T. B. Goennenwein, R. Gross, M. Opel [1]

The use of electron and hole spins for future semiconductor devices is in the focus of current research. Key prerequisites for the development of novel device concepts for spin electronics and spin optoelectronics are the realization of an effective injection of spin-polarized charge carriers, as well as the thorough understanding of the transport, manipulation, and detection of the spin degree of freedom. To promote research in this field, the German Research Foundation (DFG) started the ***Priority Program SPP 1285*** entitled ***Semiconductor Spintronics*** in 2007. The general scientific objectives of this priority program are (i) the efficient injection of spin polarized electrons using para- and ferromagnetic semiconductors and ferromagnetic metal clusters, (ii) the transport of electron spins across interfaces and large distances, (iii) the direct manipulation of the orientation of electron spins, (iv) the study of spin-spin-interaction, (v) the development of concepts for spin electronics and spin-optoelectronics, and (vi) the study of basic principles of spin-quantum information processing in semiconductors.

The priority program SPP 1285 is presently funding 33 single projects all over Germany in basic and applied research. The Walther-Meißner-Institute (WMI) is participating in this program from the beginning in 2007 with the project *Spin Injection, Spin Transport and Controllable Ferromagnetism in Transition Metal-Doped ZnO*. The WMI funding proposal for the third two-year funding period (2011–2013) has been reviewed in early 2011 and been granted by the German Research Foundation. The key objectives of this project include (i) the fabrication of epitaxial ZnO thin films and heterostructures as well as [ZnO/ferromagnet]$_n$ digital alloys tailored to the needs of spin (opto)electronic devices, (ii) the study of the spin lifetime and spin coherence length in ZnO by optical pump & probe experiments, (iii) the optical study of electrical spin injection and spin transport in ferromagnet/ZnO heterostructures, and finally (iv) the investigation of all-electrical spin injection and spin transport in high quality epitaxial ZnO thin films.

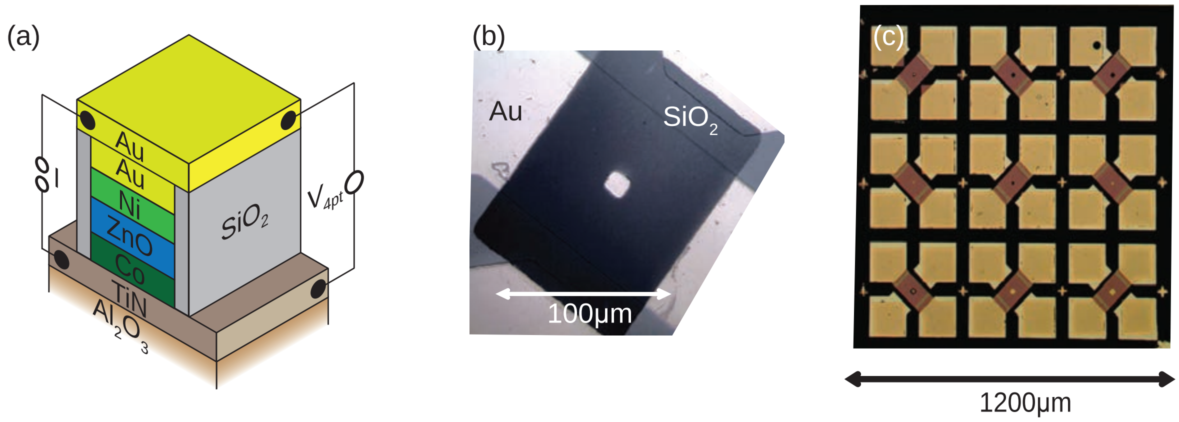

Figure 1: (a) Cross-sectional view and (b) optical micrograph in top view of a ZnO based spin-valve junction used for the study of all-electrical spin transport through ZnO. (c) Optical micrograph of the whole sample chip with 9 single junctions (taken from M. Althammer, Ph.D. thesis, TU Munich, 2012).

The wide bandgap semiconductor ZnO is interesting for spintronic applications because of its small spin-orbit coupling implying a large spin coherence length. Utilizing vertical spin valve

---

[1] This work is supported by the German Research Foundation via the Priority Program SPP 1285 (project number GR 1132/14).

devices (see Fig. 1) with ferromagnetic electrodes (TiN/Co/ZnO/Ni/Au), we succeeded in studying the spin-polarized transport across ZnO in all-electrical experiments (see Refs. [1, 2] and report by M. Opel *et al.*, pp. 65–67). The measured magnetoresistance was found to agree well with the prediction of a two spin channel model with spin-dependent interface resistance. Fitting the data yields spin diffusion lengths of 10.8 nm at 2 K, 10.7 nm at 10 K, and 6.2 nm at 200 K in ZnO, corresponding to spin lifetimes of 2.6 ns, 2.0 ns, and 31 ps at the respective temperatures. Our research activities are profiting from the close collaboration with various partners within SPP 1285.

References

[1] M. Althammer, E.-M. Karrer-Muller, S. T. B. Goennenwein, M. Opel, and R. Gross, Applied Physics Letters **101**, 082404 (2012).
[2] M. Opel, Journal of Physics D: Applied Physics **45**, 033001.

The DFG Priority Program SPP 1458 "Superconductivity in Iron-Based Compounds"

R. Hackl, B. Muschler, F. Kretzschmar, A. Baum, T. Böhm, R. Gross [1]
B. Büchner[2]*, C. Honercamp*[3]*, D. Johrendt*[4]

Iron-based superconductors (FeSC) [1, 2] exhibit transition temperatures T_c in the 50 K range, just a factor of two below those of the cuprates. They are studied intensively in the ***Priority Program SPP 1458*** entitled ***High-Temperature Superconductivity in Iron-Based Compounds***, which has been launched by the German Research Foundation in 2010. As demonstrated recently and shown in Fig. 1 (a) and (b) they can carry very high critical current densities in magnetic fields in excess of 40 T [3]. With respect to the basic understanding of Cooper pairing the various compound classes turn out to be model systems for studying unconventional mechanisms [Fig. 1 (c)]. Upon changing the relative size of the hole-like (blue) and electron-like (red) Fermi surfaces the strength of the interband coupling can be tuned while the intraband interaction should be constant to lowest order. Therefore, if the pairing symmetry changes with doping, interband pairing as, for instance, provided by spin fluctuations is more likely to drive Cooper pairing than other instabilities (see Ref. [4] and report by F. Kretzschmar *et al.*, pp. 53–57). While the hierarchy of pairing states becomes more transparent in the class of materials compared in Fig. 1 (c) there is no general convergence yet. For example, the pairing in LiFeAs is still controversial although the materials are very clean and well ordered [7, 8]. If the p-wave gap symmetry in LiFeAs could be further supported a new paradigm of Cooper pairing has to be considered in the Fe-based materials. Although the T_c record of 56 K has not been broken yet, new and interesting types of compounds are being discovered [9–11]. In fact, the variety of materials is much bigger than in the cuprates and poses challenges as to

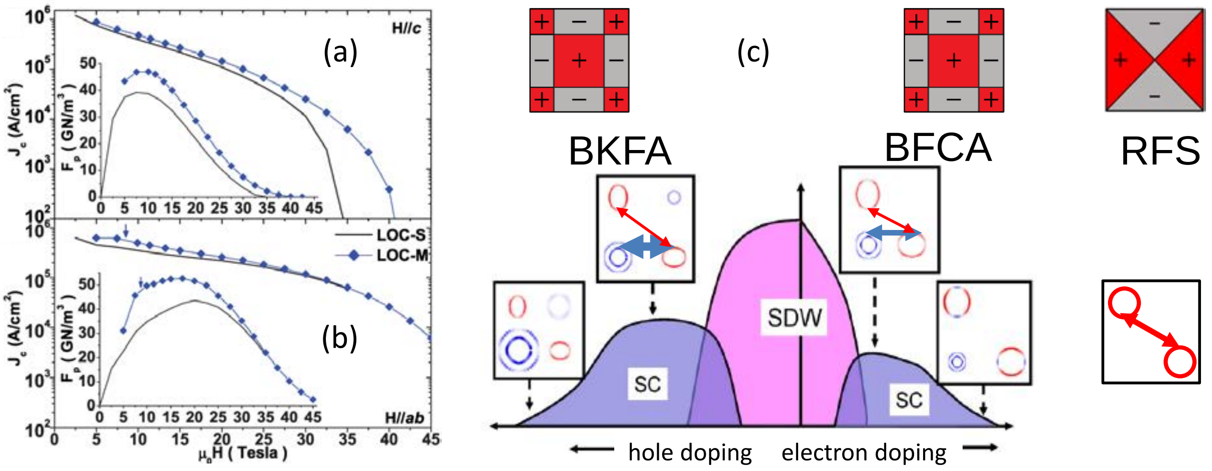

Figure 1: (a) and (b) Critical current and pinning force (insets) densities of $\mathrm{Ba(Fe_{1-x}Co_x)_2As_2}$ [3]. For the proper distribution of pinning centers the materials are still useful in fields above 40 T. (c) Schematic phase diagrams of $\mathrm{Ba_{1-x}K_xFe_2As_2}$ (BKFA), $\mathrm{Ba(Fe_{1-x}Co_x)_2As_2}$ (BFCA) [5], and $\mathrm{Rb_2Fe_4Se_5}$ (RFS). The predicted Fermi surfaces fit by and large the experiments. The pairing interactions expected for a spin fluctuation scenario are indicated by arrows. The better the nesting of the bands the stronger the interaction. The pairing symmetries expected from the interband coupling are shown in the top part [6]. For RFS the gap has a lower symmetry than the lattice. In contrast to the cuprates, the nodes are not on the Fermi surface and the gap looks isotropic.

---

[1] This work is supported by the German Research Foundation (DFG) via the Priority Program SPP 1458.
[2] Leibniz Institute for Soild State and Materials Research (IFW), 01069 Dresden, Germany
[3] Institute for Theoretical Solid State Physics, RWTH Aachen, 52074 Aachen, Germany
[4] Department of Chemistry, LMU München, 81377 München, Germany

finding the systematics. The new materials along with the application related developments and the large number of open fundamental questions show that research into the iron-based compounds is a vibrant field even if the hype slowly tails off.

These objectives are in the main focus of the Priority Program SPP 1458. The Walther-Meißner-Institute hosts one of the coordinators (Rudi Hackl) and participates with the project *"Light scattering studies of iron pnictides"*. Pinning down the origin of Cooper pairing and of the magnetic and structural phase transitions remains among the important open problems in the FeSC. In addition, any progress here is a step towards a deeper understanding of unconventional superconductivity in general and in the record-holding cuprates in particular. Given the continuous improvement of the materials and experimental techniques exciting new insight can be expected during the second funding period supposed to start in 2013.

References

[1] Y. Kamihara, T. Watanabe, M. Hirano, and H. Hosono, J. Am. Chem. Soc. **130**, 3296 (2008).
[2] M. Rotter, M. Tegel, and D. Johrendt, Phys. Rev. Lett. **101**, 107006 (2008).
[3] C. Tarantini, S. Lee, F. Kametani, J. Jiang, J. D. Weiss, J. Jaroszynski, C. M. Folkman, E. E. Hellstrom, C. B. Eom, and D. C. Larbalestier, Phys. Rev. B **86**, 214504 (2012).
[4] F. Kretzschmar, B. Muschler, T. Böhm, A. Baum, R. Hackl, H.-H. Wen, V. Tsurkan, J. Deisenhofer, and A. Loidl. Evidence of competing s- and d-wave pairing channels in iron-based superconductors. `arXiv:1208.5006` (2012).
[5] P. J. Hirschfeld, M. M. Korshunov, and I. I. Mazin, Rep. Prog. Phys. **74**, 125508 (2011).
[6] W.-C. Lee, S.-C. Zhang, and C. Wu, Phys. Rev. Lett. **102**, 217002 (2009).
[7] T. Hänke, S. Sykora, R. Schlegel, D. Baumann, L. Harnagea, S. Wurmehl, M. Daghofer, B. Büchner, J. van den Brink, and C. Hess, Phys. Rev. Lett. **108**, 127001 (2012).
[8] T. Hanaguri, K. Kitagawa, K. Matsubayashi, Y. Mazaki, Y. Uwatoko, and H. Takagi, Phys. Rev. B **85**, 214505 (2012).
[9] J. Guo, S. Jin, G. Wang, S. Wang, K. Zhu, T. Zhou, M. He, and X. Chen, Phys. Rev. B **82**, 180520 (2010).
[10] C. Löhnert, T. Stürzer, M. Tegel, R. Frankovsky, G. Friederichs, and D. Johrendt, Angew. Chem. Int. Ed. **50**, 9195 (2011).
[11] V. Tsurkan, J. Deisenhofer, A. Günther, H.-A. Krug von Nidda, S. Widmann, and A. Loidl, Phys. Rev. B **84**, 144520 (2011).

The DFG Priority Program SPP 1538 "Spin Caloric Transport"

M. Althammer, S. Geprägs, S. T. B. Goennenwein, R. Gross, H. Huebl, J. Lotze, S. Meyer, M. Opel, M. Schreier, M. Weiler [1]

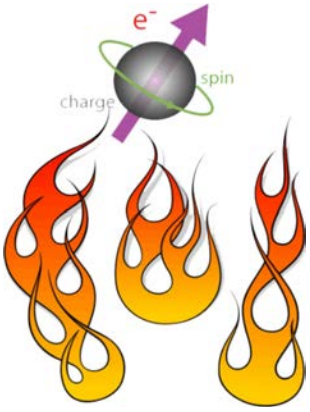

The spin degree of freedom impacts the electronic charge transport in ferromagnetic metals, as evident from magneto-resistive phenomena such as anisotropic magneto-resistance or giant magneto-resistance. In an analogous fashion, the spin degree of freedom also influences the thermal transport in ferromagnets. The corresponding, so-called *spin caloritronic* effects are vividly investigated at present – since it became clear only recently that spin caloritronic phenomena are much more than spin-dependent replica of the well-established, thermo-galvanic effects. In other words, recent theoretical and experimental studies demonstrate that the long-known thermoelectric phenomena such as the Seebeck or Peltier effect must re-considered, taking into account the spin degree of freedom. One prototype example is the spin Seebeck effect, i.e., the occurrence of an electric field in ferromagnet/normal metal hybrid structures exposed to a thermal gradient. In contrast to the long-known "charge" Seebeck effect, the *spin* Seebeck effect not only occurs in electrically conductive magnetic materials, but also in electrically insulating magnets (so-called magnetic insulators). Spin caloritronic effects thus are qualitatively new phenomena, which need to be studied and discussed in their own right [1]. This avenue is expected to reveal novel, spin-related properties in the solid state, and suggest that spin entropy can be created, manipulated and transported by non-equilibrium charge and heat currents in magnetic systems.

To stimulate research activities on spin caloric phenomena, the German Research Foundation (DFG) has launched the Priority Program SPP 1538 entitled ***Spin Caloric Transport (SpinCaT)*** in 2011. The aim of SPP 1538 is to develop the new research field of spin-related caloric effects. The research program is focused on four priority areas: (i) spin caloric effects and spin mediated heat transport in planar geometry, (ii) thermal spin-based conductivities across interfaces in nanopatterned magnetic devices, (iii) spin currents induced by large temperature gradients, and (iv) materials for spin caloric applications. The Walther-Meißner-Institute (WMI) participates in this program with the project ***Spin-dependent Thermo-galvanic Effects***. The first three-year funding period started in mid 2011. One focus of our corresponding research activities is on spatially resolved spin caloritronic experiments. As detailed in [2] and the report by M. Weiler *et al.* on pp. 68–70, we use a focussed laser beam to generate a local thermal gradient in magnetic thin films as well as hybrid heterostructures, and investigate the resulting spin caloritronic response. In particular, we could show that the spin Seebeck effect in yttrium iron garnet/platinum (YIG/Pt) hybrids enables the generation of local, bipolar, magnetically controllable spin currents. Spin caloritronic phenomena thus can be exploited for the realization of simple and versatile pure spin current sources. We plan to pursue these activities, aiming to quantify the spin current generation efficiency in various heterostructures as well as the relevant time constants.

We also could show that the resonant coupling of phonons and magnons can be exploited to generate spin currents at room temperature [3]. Surface acoustic wave pulses with a frequency of 1.55 GHz and duration of 300 ns provide coherent elastic waves in a ferromagnetic thin film/normal metal (Co/Pt) bilayer. We use the inverse spin Hall voltage in the Pt as a measure

---

[1] This work is supported by the German Research Foundation via the Priority Program SPP 1538 (project number GO 944/4-1).

for the spin current and record its evolution as a function of time and external magnetic field magnitude and orientation. Our experiments show that a spin current is generated in the exclusive presence of a resonant elastic excitation. This establishes acoustic spin pumping as a resonant analogue to the spin Seebeck effect.

A puzzling discovery was the observation of an anisotropic magnetoresistance in Pt/YIG bilayers [4]. In spite of YIG being a very good electrical insulator, the resistance of the Pt layer reflects its magnetization direction. The effect persists even when a Cu layer is inserted between Pt and YIG, excluding the contribution of induced equilibrium magnetization at the interface. Instead, we show that the effect originates from concerted actions of the direct and inverse spin Hall effects and therefore call it "spin Hall magnetoresistance" (SMR).

References

[1] S. T. Goennenwein, and G. E. Bauer, Nature Nanotechnology **7**, 145–147 (2012).

[2] M. Weiler, M. Althammer, F. D. Czeschka, H. Huebl, M. S. Wagner, M. Opel, I.-M. Imort, G. Reiss, A. Thomas, R. Gross, and S. T. B. Goennenwein, Phys. Rev. Lett. **108**, 106602 (2012).

[3] M. Weiler, H. Huebl, F. S. Goerg, F. D. Czeschka, R. Gross, and S. T. B. Goennenwein, Phys. Rev. Lett. **108**, 176601 (2012).

[4] H. Nakayama, M. Althammer, Y.-T. Chen, K. Uchida, Y. Kajiwara, D. Kikuchi, T. Ohtani, S. Geprägs, M. Opel, S. Takahashi, R. Gross, G. E. W. Bauer, S. T. B. Goennenwein, and E. Saitoh, ArXiv e-prints (2012). `arXiv:1211.0098 [cond-mat.mtrl-sci]`.

The EU Marie Curie Initial Training Network "Circuit and Cavity Quantum Electrodynamics (CCQED)"

F. Deppe, R. Gross, A. Marx [1]

The european network ***Circuit and Cavity Quantum Electro-Dynamics (CCQED)*** has been granted 3.5 Million Euros by the European Union through a Marie Curie Action within the Seventh Framework Program Initial Training Network ITN-People-2010. The aim of CCQED is to bridge two communities in physics, in the academic and private sectors, to share, pursue and diffuse within Europe the benefits of collaborations in the science of elementary quanta. CCCQED provides a Europe-wide bridge between two very active disciplines in physics. One is quantum electrodynamics of atoms or ions strongly interacting with light in resonators, the other the emerging field of solid-state superconducting circuit quantum electrodynamics. The interdisciplinary training of a new generation of young researchers strengths the European expertise in those fields, and allows for a new discipline to emerge that combines single atom control methods with superconductor micro-chip fabrication. The use of high-quality resonators, whether superconducting transmission lines or highly-reflecting mirrors, coupled to a controlled number of particles opens novel avenues to explore quantum dynamics via hitherto inaccessible physical mechanisms.

CCQED involves 10 research centres and 3 companies, representing the cutting edge of research in the quantum electrodynamics of fundamental systems in Europe. The network trains 12 early stage researchers (Ph.D. students) and 2 experienced researchers (postdocs). They focus on establishing bonds between solid-state and quantum optics physics, strengthening the communication between theory and experiment, and establishing links between fundamental and applied research. Prominent scientists and industry leaders contribute to the schools and workshops. Special attention is given to the development of complementary skills, such as communication, presentation, project planning, and management. The WMI contributes with its expertise on the design, fabrication, and measurement of superconducting quantum circuits. In particular, the focus lies on the exploration of quantum correlations in the important microwave frequency domain.

In February 2012, *CCQED* has organized the *Winter School on Circuit and Cavity Quantum Electrodynamics"* at Les Houches, France. The school aimed at Ph.D. students and Postdocs working in the field of circuit and cavity QED. Besides a general introductory course on the principles of the field, there were lectures on the experimental realizations in different physical systems such as atoms in optical cavities, superconducting circuits, quantum dots in photonic crystal cavities and many more. The participants learnt about the possibilities and the difficulties that each of the systems is offering. Theory sessions complemented the experimental lectures to give a deeper insight in current theoretical approaches. In September 2012, *CCQED* has organized the *Summer School on FPGA and High Performance Computing Technologies* at Garching, Germany. The school included lectures, lab sessions and excursions to CCQED network partners such as Walther-Meißner-Institute. The lectures were based on High Perfomance Computing, and topics like real-time math or developing dynamic system models were discussed. The school covered LabView, LV Real Time and LV FPGA training. Separated tracks for beginners and experienced users were provided.

---

[1] This work is supported by the EU projects CCQED.

The EU small or medium-scale focused research project "Quantum Propagating Microwaves in Strongly Coupled Environments (PROMISCE)"

F. Deppe, R. Gross, A. Marx [2]

The EU Collaborative Project entitled ***Quantum Propagating Microwaves in Strongly Coupled Environments – PROMISCE*** is funded by the FET-Open Initiative of the EU 7^{th} Framework Program since early 2012. It studies the dynamics of microwave photons in quantum circuits, including their interaction with superconducting qubits, transmission lines and quantum metamaterials. The aim of ***PROMISCE*** is to provide the foundations for a novel research field: propagating quantum microwave technologies in strongly and ultrastrongly coupled environments. It emerged from the challenging and controversial idea that microwave photons can interact strongly among each other and with their environment, even in the absence of confining cavities. ***PROMISCE*** combines two major innovative and interdisciplinary components. The first one, propagating quantum microwave photonics, focuses on the generation, control, and detection of quantum microwave beams and photons using superconducting quantum circuits. The second one aims at the exploration of interactions between propagating quantum microwaves and their potential for quantum information processing. The ultimate goal of PROMISCE is to merge the possibilities of all-optical quantum computing with superconducting circuits. The result should be quantum networks that perform useful tasks such as scalable quantum gates or quantum simulation of condensed matter and field quantum theory problems.

The research efforts at WMI employ superconducting quantum circuits to explore novel paths in engineering strong and ultrastrong controlled interactions between propagating microwave photons and their environment as well as among photons themselves. The WMI is an early player on these fields and therefore contributes with pronounced experimental expertise.

---

[2] This work is supported by the EU project PROMISCE.

Basic Research

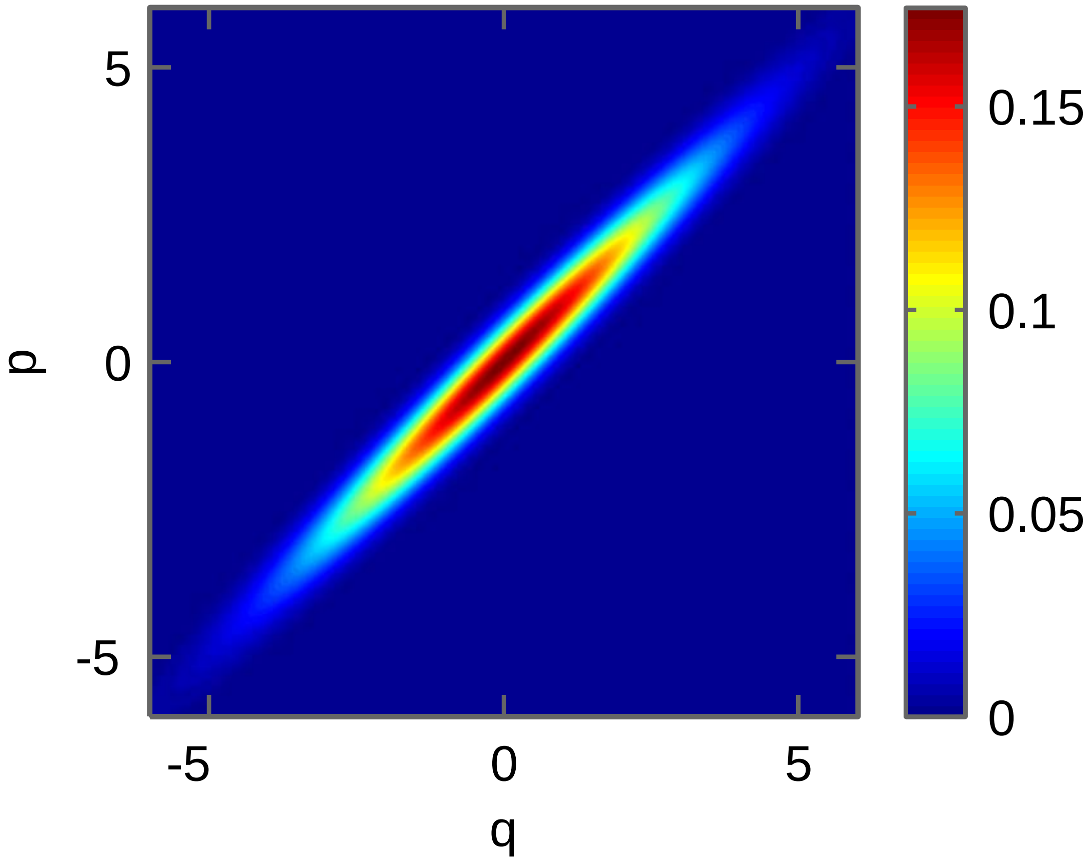

Wigner function reconstruction of a squeezed microwave state.

Time-domain Measurements on a Strongly Coupled Qubit-resonator System

A. Baust, T. Losinger, M. Haeberlein, E. Hoffmann, E. M. Menzel, H. Huebl, F. Deppe, A. Marx, R. Gross [1]

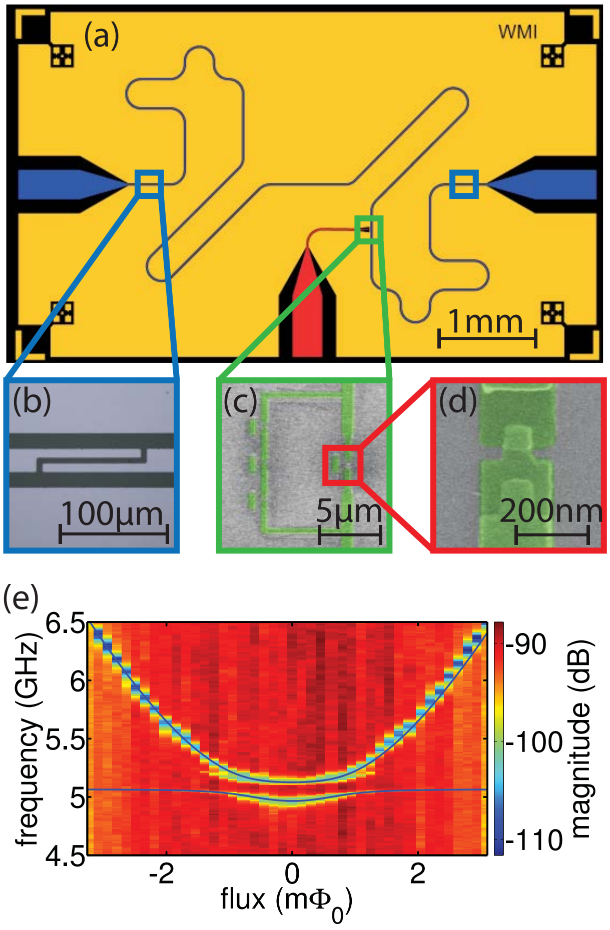

Figure 1: **(a)** False-color image of the sample. The meandering structure in blue is the resonator with in- and output terminals at the sides of the chip. The red structure is the antenna. **(b)** Gap capacitor defining the resonator (blue boxes in (a)). **(c)** Scanning Electron Microscope micrograph of the flux qubit. **(d)** Close-up of one of the Josephson junctions. **(e)** Two-tone spectroscopy data. An excitation tone is applied to the qubit via the antenna. When the qubit is excited, a drop in resonator transmission is observed. Repeating this protocol for different excitation frequencies and flux values makes the qubit hyperbola visible. Around 5 GHz, an anticrossing with a resonator mode is observed. Blue line: Fit to theory.

Superconducting quantum bits (qubits) coupled to coplanar waveguide resonators have not only proven to be essential building blocks of quantum information architectures [1], but are also capable of giving deep insight into the physics of light-matter interaction. In analogy to cavity QED, where natural atoms interact with the laser field confined in an optical cavity, superconducting qubits acting as 'artificial atoms' interact with the modes of a one-dimensional superconducting microwave transmission line resonator. As the mode volumes of these transmission line resonators are small compared to those of optical cavities and the dipole moments of the artificial atoms are large compared to those of their natural counterparts, the regime of strong and even ultrastrong light-matter interaction is easily achieved in circuit QED [2, 3].

In our experiments, we study a superconducting flux qubit coupled galvanically to the center conductor of a superconducting (Nb) coplanar waveguide resonator. The sample used in the course of our experiment is shown in Fig. 1. For the measurements, the sample is mounted on the sample stage of a dilution refrigerator and cooled to the base temperature of about 35 mK. In the first step, we characterize the coupled qubit-resonator system by means of continuous-wave spectroscopy, i.e. we measure the transmission through our sample depending on the probe signal frequency and the magnetic flux penetrating the qubit loop. The qubit is read out dispersively using one resonator mode. We derive the qubit state from the magnitude and phase of the transmitted signal. In Fig. 1(e) we show two-tone spectroscopy [4] from which we determine the qubit gap to 5.02 GHz. The coupling strength between the qubit and the

---

[1] We gratefully acknowledge financial support by the German Research Foundation through SFB 631, the German Excellence Initiative through NIM, and the EU projects CCQED and PROMISCE.

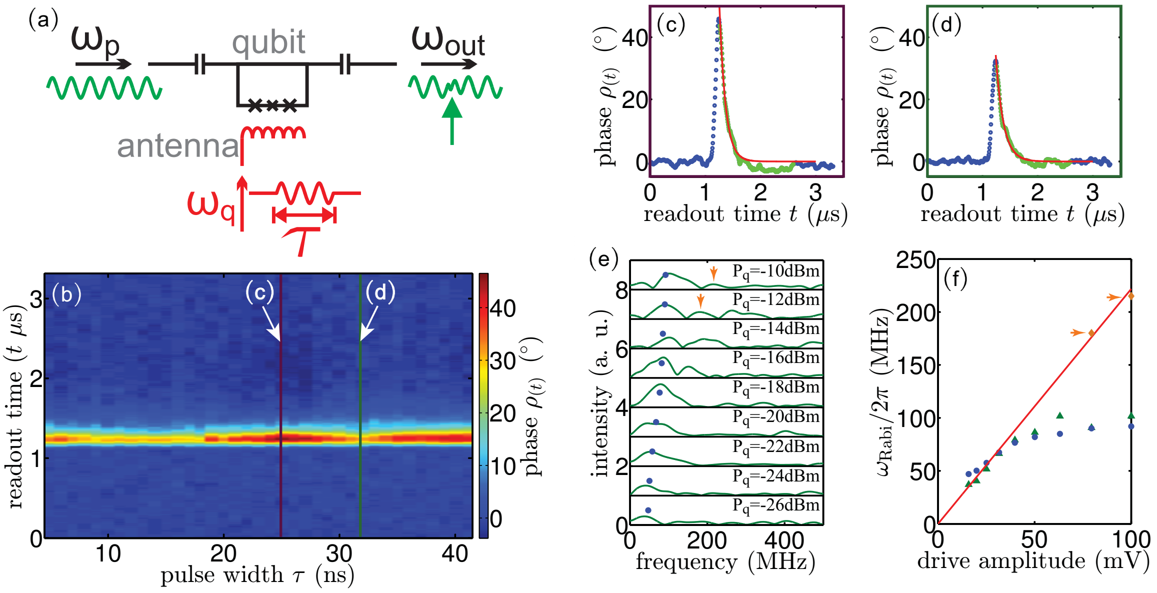

Figure 2: (a) Measurement protocol. Deviations in magnitude and phase (green arrow) in the transmitted probe tone signal are detected when the qubit state is changed by means of an excitation pulse applied to the qubit via the antenna. **(b)** Phase deviation of the transmitted probe signal as a function of pulse width and readout time. **(c,d)** Averaged time traces recorded for value of the pulse width where the probability to find the qubit in the excited state is maximum (minimum). From the exponential decay, the T_1-time can be extracted. **(e)** Fourier transform of the phase-time-dependence as described in the text. Blue dots: Extracted frequency from a sinusoidal fit to the phase-time-dependence, corresponding well with the frequencies extracted from the Fourier spectra. **(f)** Green triangles: Maxima from the Fourier spectra. Brown diamonds: Second-most prominent peaks in the Fourier spectra. Blue dots: Frequencies extracted from sinusoidal fits. Good agreement with the expected direct proportionality is observed.

resonator readout mode is given by $g/2\pi = 76.8\,\text{MHz}$, corresponding to approximately 1% of the resonator mode frequency. For a detailed description of the spectroscopy measurements and also of the measurement setup, we refer to [5].

Next, we perform time-domain experiments. For these measurements, the qubit was set to the degeneracy point where the magnetic flux detuning equals zero, cf. Fig. 1(e). The (simplified) measurement protocol used for the time-domain characterization of the qubit is depicted in Fig. 2(a). We probe the qubit-resonator-system with a continuous-wave signal (the *probe signal*) at the resonance frequency ω_p of the coupled system comprised of the qubit and the third resonator mode. At the qubit degeneracy point and with the qubit in the ground state, this frequency was determined to 7.106 GHz. Via the antenna (cf. Fig. 1(a)) we have applied microwave pulses to the qubit at its excitation frequency $\omega_\text{q} = 5.02\,\text{GHz}$. The external drive induces coherent population oscillations between the qubit ground and excited state (Rabi oscillation). In analogy to the data shown in Fig. 1(e), a change in transmission magnitude and phase is expected depending on the qubit state.

Typical results of a measurement performed in this way are shown in Fig 2(b). The phase of the transmitted signal is measured over 3.2 μs for values of the pulse lengths ranging between 5 ns and 40 ns. For all values, 10^7 time traces are recorded and averaged using an FPGA-enhanced A/D converter. The qubit excitation pulse is triggered 1 μs after the phase measurement is started. It can be seen that for certain values of the pulse length (25 ns and 39 ns) the change in phase is maximum. At these values, the probability to prepare the qubit in the excited state is maximum whereas applying a pulse with length of 32 ns implies a minimum probability of exciting the qubit. The inverse of the time between two subsequent maxima is called the Rabi frequency. In Fig. 2(c-d), we show the time traces for those values of the pulse length with maximum and minimum qubit excitation probability. From the exponential decay found in these time traces, we extract the coherence time of the qubit and find $T_1 \approx 125\,\mathrm{ns}$. In addition, we have repeated the measurement described in Fig. 2(b) for different pulse amplitudes. According to theory, we expect a direct proportionality between the Rabi frequency and the qubit excitation pulse amplitude. We extract the Rabi frequencies from the phase-time-dependence [cf. Fig. 2(b)] for $t = 1.2\,\mu\mathrm{s}$ where the phase deviation is maximum in two different ways. In Fig. 2(e) we show Fourier transforms of the phase-time-dependence (green lines) where we identify the highest peak as the Rabi frequency. Additionally, we extract the frequency from sinusoidal fits of the phase-time-dependence (blue dots). In Fig. 2(f), we plot the extracted frequencies against the pulse amplitude and find good agreement with a direct proportionality. However, for a Rabi frequency of about 90 MHz, corresponding to the coupling strength g, we find significant deviation from the linear behavior. It was shown in [6], though for higher frequencies, that deviations from the expected linear behavior can occur at characteristic system frequencies.

In conclusion, we have successfully performed measurements on a coupled qubit-resonator system in the time domain and were able to find the Rabi frequency and the T_1-time of our qubit. The aim of future measurements will be to further improve data quality, measure dephasing times and use the measurement techniques applied here to perform time-domain experiments with more complex systems like gradiometric qubits (see report by M. Schwarz *et al.*, 75–77) or quantum switches (see report by E. Hoffmann *et al.*, pp. 49–51).

We acknowledge programming support by M. Ihmig and would like to thank our cryogenic experts C. Probst, K. Uhlig and K. Neumaier for technical support.

References

[1] M. Mariantoni, H. Wang, T. Yamamoto, M. Neeley, R. C. Bialczak, Y. Chen, M. Lenander, E. Lucero, A. D. O'Connell, D. Sank, M. Weides, J. Wenner, Y. Yin, J. Zhao, A. N. Korotkov, A. N. Cleland, and J. M. Martinis, Science **334**, 61 (2011).

[2] A. Wallraff, D. I. Schuster, A. Blais, L. Frunzio, R.-S. Huang, J. Majer, S. Kumar, S. M. Girvin, and R. J. Schoelkopf, Nature **431**, 162 (2004).

[3] T. Niemczyk, F. Deppe, H. Huebl, E. P. Menzel, F. Hocke, M. J. Schwarz, J. J. Garcia-Ripoll, D. Zueco, T. Hummer, E. Solano, A. Marx, and R. Gross, Nat. Phys. **6**, 772 (2010).

[4] T. Niemczyk. *From strong to ultrastrong coupling in circuit QED architectures*. Ph.D. thesis, Technische Universität München (2011).

[5] T. Losinger. *Time-domain control of light-matter interaction with superconducting circuits*. Diplomarbeit, Technische Universität München (2012).

[6] I. Chiorescu, P. Bertet, K. Semba, Y. Nakamura, C. J. P. M. Harmans, and J. E. Mooij, Nature **431**, 159 (2004).

Path Entanglement of Continuous-Variable Quantum Microwaves

F. Deppe, E. P. Menzel, P. Eder, L. Zhong, M. Haeberlein, A. Baust, E. Hoffmann, A. Marx, R. Gross [1]
M. Ihmig,[2] *R. Di Candia,*[3] *D. Ballester,*[4] *E. Solano,*[5] *K. Inomata,*[6] *T. Yamamoto,*[7] *Y. Nakamura*[8]

Entanglement is one of the most fascinating phenomena in the world of quantum mechanics. It describes the counterintuitive situation, where a composite system is in a well-defined state, while the knowledge of the states of the subsystems can remain minimal. In more physical terms, entanglement is the generalization of quantum superpositions to multiple Hilbert spaces. Under the important condition that the subsystems are spatially separated, such quantum correlations constitute an essential resource in quantum information and communication protocols. Therefore, they were an important subject in the studies on fundamental light-matter interaction in quantum optics and atomic physics. While the latter mostly focused on optical frequencies, the field of superconducting quantum circuits has brought fundamental quantum physics to the microwave domain. Here, quantum two-level circuits (qubits) and linear electromagnetic resonator circuits act as artificial atoms and standing-wave quantized light, respectively. Based on the good ratio between coherence rate and achievable interaction strength, entanglement of a superconducting qubit with other qubits [1] and with resonators was observed. While this is useful for quantum information processing applications, quantum microwave communication requires the investigation of propagating fields.

Based on this insight, we demonstrate path entanglement of propagating quantum microwaves [2]. We focus on the continuous-variable regime and, most importantly, take particular care that the entangling and the detection process are based on different experimental techniques. The concept of our experiment is sketched in Fig. 1(a). A squeezed state [2, 3] and the vacuum, both at a frequency of 5.637 GHz, are combined by means of a microwave beam splitter, which serves as entangling device. While the vacuum is emitted from a $50\,\Omega$ load, the squeezed state is produced by a flux-driven Josephson parametric amplifier (JPA). The JPA [4] consists of a superconducting quarter wavelength transmission line resonator, whose inner conductor is at one end connected to ground via a direct current superconducting quantum interference device (dc SQUID) [2]. The degree of squeezing depends on the power of the pump signal of frequency $2 \times 5.637\,\mathrm{GHz}$ applied to the dc SQUID. Since the exact pump power is experimentally not well accessible, we express it in terms of the non-degenerate JPA signal gain. The latter can be straightforwardly measured and increases with increasing pump power.

The entanglement is then extracted from auto and cross-correlation measurements between the output ports [see Fig. 1(b)] . This measurement is complicated by the fact that no efficient single microwave photon counters are available. Instead, we use linear amplifiers, which add approximately 12 noise photons to the signal. We make use of two quantum signal recovery techniques to remove this noise. With the dual-path method [5, 6] we reconstruct the squeezed state at the *input* of the beam splitter and with the reference state method [2, 7] we independently quantify the entanglement in the beam splitter *output*. Conceptually, this

---

[1] We gratefully acknowledge financial support by the German Research Foundation through SFB 631, the German Excellence Initiative through NIM, and the EU projects CCQED and PROMISCE.

[2] Lehrstuhl für Integrierte Systeme, Technische Universität München, Germany
[3] Universidad del País Vasco UPV/EHU, Spain
[4] University College London, United Kingdom
[5] Universidad del País Vasco UPV/EHU and IKERBASQUE Basque Foundation for Science, Spain
[6] RIKEN Advanced Science Institute, Japan
[7] RIKEN Advanced Science Institute and NEC Smart Energy Research Laboratories, Japan
[8] RIKEN Advanced Science Institute and The University of Tokyo, Japan

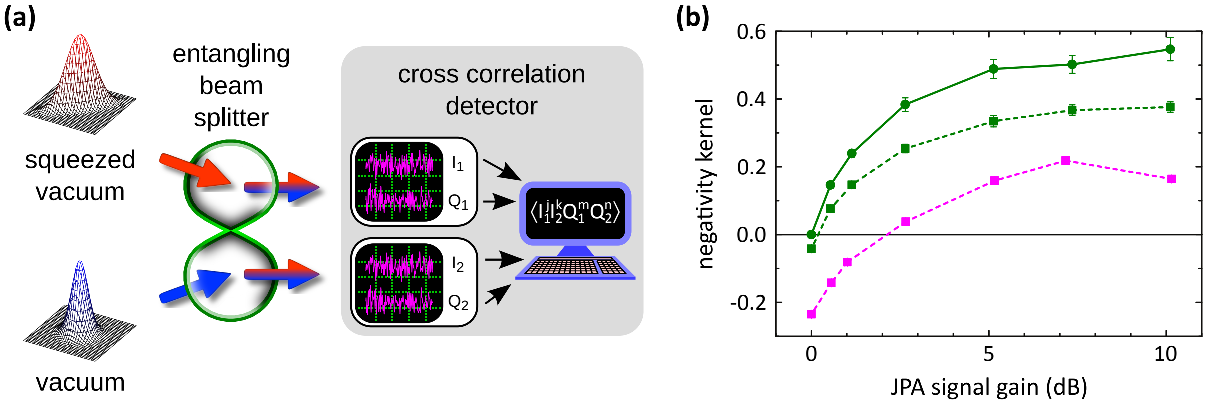

Figure 1: Path entanglement of continuous-variable quantum microwaves. **(a)** Conceptual sketch of the experiment. The oscilloscope symbols represent the noisy amplification and downconversion of the path entangled state (blue-and-red arrows) signals. After extracting the in-phase components $I_{1,2}$ and the quadrature components $Q_{1,2}$, the averaged correlations $\langle I_1^j I_2^k Q_1^m Q_2^n \rangle$ are computed in real time for $j{+}k{+}m{+}n \leq 4$ and $j,k,m,n \in \mathbb{N}_0$. **(b)** Negativity kernel computed as a function of the JPA signal gain from the averaged correlations $\langle I_1^j I_2^k Q_1^m Q_2^n \rangle$. The actual negativity is the maximum of the negativity kernel and zero. The squeezed state can be either squeezed vacuum (green) or squeezed thermal fluctuations (magenta). Circles: analysis of the output state. Squares: analysis based on a reconstruction of the squeezed input states. Error bars represent statistical error.

difference is best understood by observing that the dual-path method relies on the knowledge of the beam splitter functionality and the vacuum being present in the second input port, while the reference state method treats the beam splitter as a black box device. By checking that the third and fourth order cumulants vanish, we verify that all signals involved in our measurements are Gaussian. Hence, we can quantify the entanglement using the negativity. The maximum negativity we observe is 0.55 ± 0.04, corresponding to that of a state squeezed by (3.2 ± 0.2) dB below the two-mode vacuum.

In summary, we use superconducting circuits and quantum signal recovery techniques to demonstrate path entanglement of a continuous-variable state in the microwave domain. Our results pave the way towards exciting physics and application in the microwave regime, such as quantum microwave communication, quantum teleportation or even quantum radar.

We acknowledge discussions with C. Eichler and important support from C. Probst, K. Neumaier, and K. Uhlig in the design and operation of the cryogenic equipment.

References

[1] M. A. Sillanpää, J. I. Park, and R. W. Simmonds, Nature **449**, 438 (2007).
[2] E. P. Menzel, R. Di Candia, F. Deppe, P. Eder, L. Zhong, M. Ihmig, M. Haeberlein, A. Baust, E. Hoffmann, D. Ballester, K. Inomata, T. Yamamoto, Y. Nakamura, E. Solano, A. Marx, and R. Gross, Phys. Rev. Lett. **109**, 250502 (2012).
[3] E. P. Menzel, F. Deppe, A. Baust, P. Eder, A. Marx, R. Gross, E. Solano, K. Inomata, T. Yamamoto, and Y. Nakamura. Squeezing the Vacuum with a Flux-Driven Josephson Parametric Amplifier.
[4] A. Baust, E. P. Menzel, T. Niemczyk, E. Hoffmann, M. Häberlein, F. Deppe, A. Marx, R. Gross, K. Inomata, T. Yamamoto, and Y. Nakamura. Characterization of a Flux-Driven Josephson Parametric Amplifier.
[5] E. P. Menzel, F. Deppe, M. Mariantoni, M. Á. Araque Caballero, A. Baust, T. Niemczyk, E. Hoffmann, A. Marx, E. Solano, and R. Gross, Phys. Rev. Lett. **105**, 100401 (2010).
[6] E. P. Menzel, F. Deppe, M. Mariantoni, A. Baust, M. Á. Araque Caballero, E. Hoffmann, T. Niemczyk, C. Probst, K. Neumaier, K. Uhlig, A. Marx, E. Solano, and R. Gross. Dual-Path State Reconstruction Scheme for Propagating Quantum Microwaves and Detector Noise Tomography.
[7] C. Eichler, D. Bozyigit, C. Lang, L. Steffen, J. Fink, and A. Wallraff, Phys. Rev. Lett. **106**, 220503 (2011).

Gap Suppression in Superconductors: Analytic Ginzburg-Landau Results

D. Einzel [1]

Introduction

This contribution is devoted to the study of superconductors, which form two kinds of interfaces with the vacuum: (i) a superconducting half-space and (ii) a superconducting slab of thickness d. If an external field $\mathbf{B}_0$ is applied on the vacuum side of and parallel to these interfaces, it will generally decay away from the surface inside the superconductor, which is nothing but the *screening side* of the Meißner-Ochsenfeld effect [1]. The early phenomenological theories of superconductivity by F. and H. London [2] and V. L. Ginzburg and L. D. Landau (GL) [3] are based on the description of the superconducting Cooper-pair condensate by a macroscopic (quasi-boson) pair field $\Psi(\mathbf{r})$, which may at the same time be viewed as the superconducting *order parameter*. The London's approach to the description of magnetic field screening (connected with the London's magnetic field penetration depth $\lambda_{\rm L}(T)$) is to assume that the order parameter $\Psi(\mathbf{r}) = \Psi_0$ remains unaffected by the presence of $\mathbf{B}_0$ and stays at its equilibrium value $\Psi_0 = \sqrt{n^{\rm s}/2}$, with $n^{\rm s}$ the superfluid density. On the contrary, the GL approach allows for a spatial dependence of the normalized order parameter $f(\mathbf{r}) = \Psi(\mathbf{r})/\Psi_0$ (connected with the GL coherence length $\xi_{\rm GL}(T)$), induced by the external field. A comprehensive numerical treatment of the problem applied to superconducting full cylinders was provided by Doll and Graf [4]. Our aim is a rigorous *analytic* calculation of the *linear response* of the order parameter $f(\mathbf{r})$ to externally applied magnetic fields in the Ginzburg-Landau temperature regime. Linear order parameter response implies that $f(\mathbf{r})$ does not deviate significantly from 1. As a consequence, the magnetic induction decay profile inside the superconductor is known analytically for various sample geometries (London's solution) and can be inserted into the linearized second-order differential equation for the order parameter $f(\mathbf{r})$, where it enters in the form of an *inhomogeneity*. Its solution provides us with the information on the spatial dependence of the superconducting order parameter in the presence of external magnetic fields for various material parameters, (such as transition temperature $T_{\rm c}$, GL parameter $\kappa = \lambda_{\rm L}/\xi_{\rm GL}$, slab thickness d) and for various experimental parameters (such as the external field B_0 and the temperature T). The analytic form of these results has, at least to my knowledge, not been provided in the literature before.

The nonlinear Ginzburg-Landau equations for superconducting slabs

In what follows, we restrict our considerations to superconductors confined in a slab of thickness d, i.e. the vector $\mathbf{r} = \{x, y, z\}$ is restricted by the conditions $-d/2 \le x \le d/2$, $-\infty \le y, z \le \infty$. The case of large slab thickness $d \to \infty$ is topologically equivalent to a superconducting half-space with $0 \le x < \infty$. In such a case, the first GL differential equation for the normalized order parameter $f(x)$ is of the simple form:

$$0 = \xi_{\rm GL}^2 \frac{d^2 f(x)}{dx^2} + f(x)[1 - b^2(x)] - f^3(x) \qquad (1)$$

$$\xi_{\rm GL}(T) = \frac{\hbar v_{\rm F}}{\sqrt{6}\Delta(T)} \; ; \; b(x) = \frac{1}{\sqrt{2}} \frac{A_y(x)}{\lambda_{\rm L}(T) B_{\rm c}(T)} \; ; \; B_{\rm c}(T) = \frac{1}{\sqrt{2}} \frac{\Phi_0}{2\pi \xi_{\rm GL}(T) \lambda_{\rm L}(T)}$$

---

[1] Dedicated to Robert Doll on the occasion of his 90th birthday on January 16, 2013.

Here $\Phi_0 = hc/2e$ represents the fluxoid quantum, from which the thermodynamic critical field $B_c(T)$ may be constructed and $\Delta(T)$ is the energy gap of the superconductor in the GL regime. $A_y(x)$ is the relevant component of the vector potential, from which the magnetic induction $B_z(x) = dA_y/dx$ may be derived. For the slab geometry in the absence of any fluxoid quanta inside the superconductor, the supercurrent density $\mathbf{j}_e^{\mathrm{s}} = j_{ey}^{\mathrm{s}}\hat{\mathbf{y}}$ assumes the form of a nonlinear generalization of London's relation

$$j_{ey}^{\mathrm{s}} = -\frac{n^{\mathrm{s}}e^2}{mc} f^2(x) A_y(x)$$

and one obtains the second GL equation in the form of a *nonlinear screening* differential equation:

$$\frac{\partial^2 A_y(x)}{\partial x^2} = \frac{f^2(x)}{\lambda_{\mathrm{L}}^2} A_y(x) \ ; \ \frac{1}{\lambda_{\mathrm{L}}^2} = \frac{4\pi n^{\mathrm{s}} e^2}{mc^2} = \frac{\omega_{\mathrm{P}}^2}{c^2} \tag{2}$$

with λ_{L} the London's magnetic penetration depth and ω_{P} the *condensate plasma frequency*. The coupled GL equations (1) and (2) have to be supplemented by boundary conditions for both the order parameter $f(x)$ and the vector potential $B_z(x) = dA_y(x)/dx = A_y'(x)$:

$$f'(w) = 0 \ ; \quad A_y'(w) = B_0 \ ; \ w = \begin{cases} 0 & \mathrm{half-space} \\ \pm\frac{d}{2} & \mathrm{slab} \end{cases} \tag{3}$$

Analytic solutions of the linearized Ginzburg-Landau equations

In order to proceed with an analytic solution of the coupled GL equations, we perform the *linearization ansatz* $f(x) = 1 - \delta f(x)$ and immediately obtain

$$\delta f''(x) - \frac{\delta f(x)}{\xi^2} = -\frac{b^2(x)}{2\xi^2} \ ; \ \xi = \frac{\xi_{\mathrm{GL}}(T)}{\sqrt{2}} \tag{4}$$

$$A_y''(x) - \frac{A_y(x)}{\lambda_{\mathrm{L}}^2} = 0 \tag{5}$$

Here the function $b(x)$, which enters the linearized first GL equation (4) as an *inhomogeneity*, can be expressed by the solution of the linearized second GL equation (5) as follows:

$$A_y(x) = \lambda_{\mathrm{L}} B_0 a(x) \ ; \ b(x) = b_0 a(x) \ ; \ a(x) = \begin{cases} -\mathrm{e}^{-\frac{x}{\lambda_{\mathrm{L}}}} & \mathrm{half-space} \\ \frac{\sinh\frac{x}{\lambda_{\mathrm{L}}}}{\cosh\frac{d}{2\lambda_{\mathrm{L}}}} & \mathrm{slab} \end{cases} \tag{6}$$

with the amplitude $b_0 = B_0/\sqrt{2}B_c(T)$. Note that Eq. (6) can be referred to as the *London's solution* of the screening equation, which can be found in standard textbooks on superconductivity. The solution of the *homogeneous* differential equation (4) is of the form

$$\delta f_h''(x) - \frac{\delta f_h(x)}{\xi^2} = 0 \ ; \ \delta f_h(x) = c\phi(x) \ ; \ \phi(x) = \begin{cases} \mathrm{e}^{-\frac{x}{\xi}} & \mathrm{half-space} \\ \cosh\frac{x}{\xi} & \mathrm{slab} \end{cases}$$

with the *Wronskian* $W(x) = -2/\xi$. A particular solution of the *inhomogeneous* differential equation (4) can generally be written in the form [5]

$$\delta f_p(x) = \frac{b_0^2}{4\xi} \sum_{s=\pm 1} s\mathrm{e}^{-\frac{sx}{\xi}} \int dx \mathrm{e}^{\frac{sx}{\xi}} a^2(x) = \frac{b_0^2}{2} \cdot \begin{cases} \alpha \mathrm{e}^{-\frac{2x}{\lambda_{\mathrm{L}}}} & \mathrm{half-space} \\ \frac{\alpha\cosh\frac{2x}{\lambda_{\mathrm{L}}} - 1}{2\cosh^2\frac{d}{2\lambda_{\mathrm{L}}}} & \mathrm{slab} \end{cases}$$

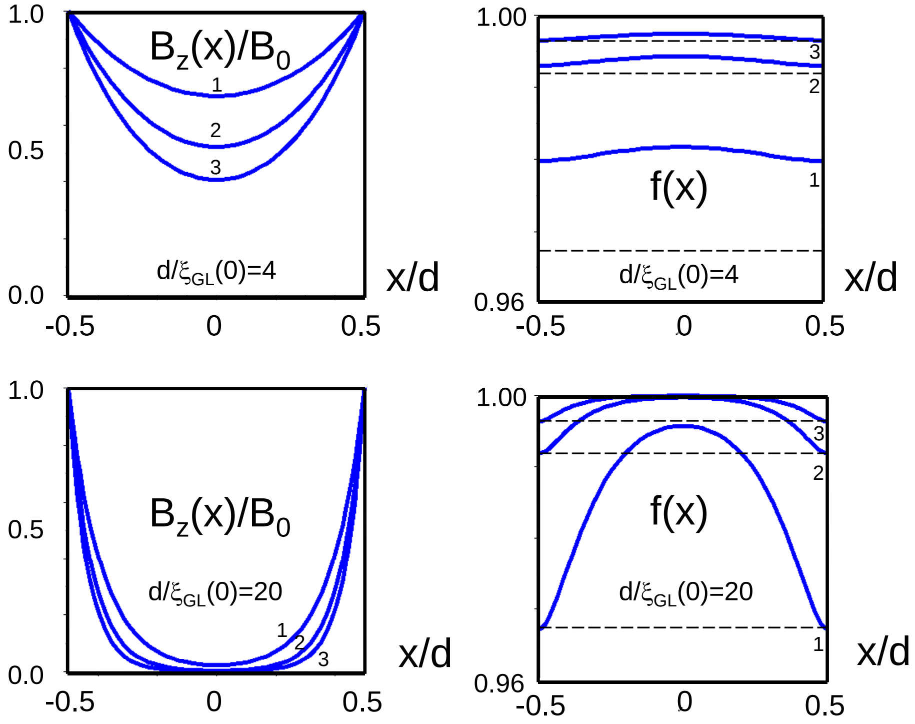

Figure 1: Spatial dependence of the normalized magnetic induction $B_z(x)/B_0$ and the normalized order parameter $f(x) = \Psi(x)/\Psi_0$ inside a superconducting slab of thickness d for $\kappa = 0.5$, $B_0/B_c(0) = 0.035$ and $\zeta_0 = d/\xi_{\rm GL}(0) = 4$, $\zeta_0 = 20$ at the reduced temperatures $T/T_c = 0.95$ (curves 1), $T/T_c = 0.9$ (curves 2) and $T/T_c = 0.85$ (curves 3). The dashed lines in the $f(x)$-plots represent the values for $\lim_{d\to\infty} f(\frac{d}{2})$.

where $\alpha = \xi^{-2}/(\xi^{-2} + 4\lambda_{\rm L}^{-2}) = \kappa^2/(2+\kappa^2)$. Finally, the general solution $\delta f(x)$ of (4) is the linear combination $\delta f(x) = c\phi(x) + \delta f_p(x)$ The unknown integration constant c can be fixed by the boundary condition (3), yielding $c = -\delta f'_p(w)/\phi'(w)$, where $w = 0$ (half-space) and $w = \pm d/2$ (slab). Our final result for the normalized order parameter $f(x) = 1 - \delta f(x)$ can be written in the surprisingly simple form

$$\delta f(x) = \delta f_p(x) - \underbrace{\frac{\delta f'_p(w)}{\phi'(w)}}_{=c} \phi(x) \quad ; \quad w = \begin{cases} 0 & \text{half} - \text{space} \\ \pm\frac{d}{2} & \text{slab} \end{cases} \tag{7}$$

Discussion and conclusions

Equations (7) forms the central result of this paper, which will be analyzed in what follows. In Fig. 1 we have plotted the normalized magnetic induction $B_z(x)/B_0$ together with the normalized order parameter $f(x) = \Psi(x)/\Psi(0)$ in a superconducting slab of thickness d vs. x/d. The parameters used in these plots are $\kappa = 0.5$, $B_0/B_c(0) = 0.035$, and two values for $\zeta_0 \equiv d/\xi_{\rm GL}(0) = 4$ and $\zeta_0 = 20$. The results are shown for three different temperatures $T/T_c = 0.95$ (curves 1), $T/T_c = 0.9$ (curves 2) and $T/T_c = 0.85$ (curves 3). The major difference between the pairs of plots for $B_z(x)/B_0$ and $f(x)$ lies in the choice of the ratio ζ_0. For small values of ζ_0, the magnetic field can penetrate into the slab and the order parameter profile varies from almost constant to bell-shaped (*field penetration regime*). For large values of ζ_0, on the other hand, the field can penetrate only near the superconductor/vacuum interface and we are in the *field screening regime*, in which the order parameter becomes flat and equal to 1 near the symmetry center and is only suppressed near the boundaries. It is clearly seen from the dashed lines (representing the limiting values $\lim_{d\to\infty} f(\frac{d}{2})$) in the curves for $f(x)$

in Fig. 1, that the order parameter profile $f(x)$ for the case $\zeta_0 = 20$ can be well characterized by the half-space limit of (7). The limit of small ζ_0 has actually been treated in the bachelor thesis [6], starting from the *nonlinear* GL equations and using truncated Taylor representations for the order parameter and the vector potential. An analytic treatment of the linearized GL equations for superconducting cylinders should be straightforward, and will be published in a separate paper [7]. A numerical treatment of the nonlinear GL equations for superconducting cylinders is presently dealt with by Robert Doll. By comparison of these results with the analytical results obtained in the linear regime, one will hopefully understand the importance of nonlinear effects in the GL description of gap suppression.

References

[1] W. Meißner, and R. Ochsenfeld, Naturwissenschaften **21**, 787 (1933).
[2] F. London, and H. London, Proc. R. Soc. Lond. A **149**, 71 (1935).
[3] V. L. Ginzburg, and L. D. Landau, Zh. Eksp. Teor. Fiz. **20**, 1064 (1950).
[4] R. Doll, and P. Graf, Z. Phys. **197**, 172 (1966).
[5] D. Einzel. Lecture Notes: Mathematical methods in physics II. Unpublished (2012).
[6] J. Woste. *Analytic Ginzburg–Landau description of superconducting slabs and cylinders*. Bachelor thesis, Technische Universität München (2012).
[7] D. Einzel, and R. Doll. To be published (2013).

Response and Collective Modes in Two-band Superconductors

D. Einzel and N. Bittner

We present a systematic study of the response properties of two–band (multi–gap) superconductors with conventional and unconventional spin-singlet pairing correlations. Particular emphasis is on the existence, the dispersion and the general role of a new massive order parameter collective mode, the so-called Leggett mode, which arises as a consequence of interband pairing correlations. The subtle interplay between the gauge mode or Nambu-Goldstone Boson and the Leggett mode is studied in view of both the validity of the charge conservation law and the participation in the Higgs mechanism. The occurrence of the Leggett-mode is analyzed with respect to its experimental observability in all physically relevant spin-independent collisionless response functions like the Lindhard density response, the dielectric function, the supercurrent response (condensate dynamic conductivity) and the electronic Raman response. Possible applications of this theory include systems like various cuprates, $\mathrm{MgB_2}$, pnictides and non-centrosymmetric superconductors. A detailed and comprehensive discussion of the results can be found in the Diploma Thesis of Nikolaj Bittner [1]

BCS–Leggett theory for two–band superconductors

The BCS Hamiltonian [2] can be generalized to apply to the case of two bands $i = 1,2$ as follows:

$$\hat{H}_{\mathrm{BCS}} \;=\; \sum_{\mathbf{k}\sigma i}\xi_{\mathbf{k}\sigma i}\hat{n}_{\mathbf{k}\sigma i} + \sum_{\mathbf{k}i}\left\{\Delta_{\mathbf{k}i}\hat{g}^{\dagger}_{\mathbf{k}i} + \Delta^{*}_{\mathbf{k}i}\hat{g}_{\mathbf{k}i}\right\} \tag{1}$$

In Eq. (1) $\xi_{\mathbf{k}\sigma i} = \epsilon_{\mathbf{k}\sigma i} - \mu_i$ is the band energy measured from the chemical potential μ_i in the i–th band. $\hat{n}_{\mathbf{k}i} = \hat{c}^{\dagger}_{\mathbf{k}i}\hat{c}_{\mathbf{k}i}$ denotes the occupation number operator, $\hat{g}_{\mathbf{k}i} = \hat{c}_{-\mathbf{k}\downarrow i}\hat{c}_{\mathbf{k}\uparrow i}$ represents the Gor'kov spin singlet pairing operator and $\Delta_{\mathbf{k}i}$ is the gap function on the i-th band:

$$\Delta_{\mathbf{k}i} = \sum_{\mathbf{p}j}\Gamma^{(ij)}_{\mathbf{kp}}g_{\mathbf{p}j} \tag{2}$$

where $g_{\mathbf{p}j} = \langle\hat{g}_{\mathbf{p}j}\rangle$ is the statistical average of $\hat{g}$. In (2) $\Gamma^{ij}_{\mathbf{kp}}$ represents the BCS pairing interaction in the weak coupling limit, readily generalized to include intraband ($\Gamma^{ii}_{\mathbf{kp}}, i = 1,2$) and interband ($\Gamma^{12}_{\mathbf{kp}}$, $\Gamma^{21}_{\mathbf{kp}}$) contributions. The self–consistency equation (2) can be solved using the weak coupling ansatz

$$\Gamma^{(ij)}_{\mathbf{kp}} \;=\; \begin{cases} -\Gamma_{ij}\hat{f}_{\mathbf{k}i}\hat{f}_{\mathbf{p}j} & ; \quad |\xi_{\mathbf{k}i}|, |\xi_{\mathbf{p}j}| < \epsilon_0,\ i = 1,2 \\ 0 & ; \quad \text{otherwise} \end{cases}$$

Here the quantities $\hat{f}_{\mathbf{k}i}$ are normalized gap anisotropy functions, which are defined by $\hat{f}_{\mathbf{k}i} = f_{\mathbf{k}i}/\sqrt{\langle f^2\rangle_{\mathrm{FS}i}}$. From this one may derive the following result for the common transition temperature for the two bands:

$$T_{\mathrm{c}} = \frac{2e^{\gamma}}{\pi k_{\mathrm{B}}}\epsilon_0 \exp\left(-\frac{1}{2}\frac{\lambda_{11}+\lambda_{22}-\sqrt{(\lambda_{11}-\lambda_{22})^2+4\lambda_{12}^2}}{\lambda_{11}\lambda_{22}-\lambda_{12}^2}\right) \tag{3}$$

where we have introduced the dimensionless coupling constants $\lambda_{ij} = N(0)\Gamma_{ij}$. A careful analysis of Eq. (3) shows that it is the larger of the two coupling constants λ_{11} and λ_{22} that determines the transition temperature $T_c(\lambda_{12} = 0)$ in the absence of the coupling $\lambda_{12} \to 0$. For a finite coupling $\lambda_{12} > 0$ the common transition temperature $T_c(\lambda_{12})$ for both bands is always seen to *exceed* the largest of the transition temperatures $T_c(\lambda_{12} = 0)$.

Collective modes in two–band superconductors

The dynamical properties of a superconductor can conveniently be described by the linearized (Nambu–) matrix kinetic equation, which assumes the following form in ω–$\mathbf{q}$–space [3]:

$$\hbar\omega\delta\underline{n}_{\mathbf{k}i} + \delta\underline{n}_{\mathbf{k}i}\underline{\xi}^0_{\mathbf{k}i-} - \underline{\xi}^0_{\mathbf{k}+}\delta\underline{n}_{\mathbf{k}i} = \delta\underline{\xi}_{\mathbf{k}i}\underline{n}^0_{\mathbf{k}i-} - \underline{n}^0_{\mathbf{k}+}\delta\underline{\xi}_{\mathbf{k}i} + i\hbar\delta\underline{I}_{\mathbf{k}i} \tag{4}$$

Here ω is the frequency of the external perturbation and $\mathbf{k}_\pm = \mathbf{k} \pm \frac{\mathbf{q}}{2}$ with $\mathbf{q}$ the wave number of the external perturbation. In (4) we have defined the following non–equilibrium two–band Nambu matrices

$$\delta\underline{n}_{\mathbf{k}i} = \begin{pmatrix} \delta n_{\mathbf{k}i} & \delta g_{\mathbf{k}i} \\ \delta g^*_{\mathbf{k}i} & -\delta n_{-\mathbf{k}i} \end{pmatrix} \; ; \; \delta\underline{\xi}_{\mathbf{k}i} = \begin{pmatrix} \delta\xi_{\mathbf{k}i} & \delta\Delta_{\mathbf{k}i} \\ \delta\Delta^*_{\mathbf{k}i} & -\delta\xi_{-\mathbf{k}i} \end{pmatrix} \tag{5}$$

In Eq. (5) the diagonal and off–diagonal energy shifts are given by

$$\delta\xi_{\mathbf{k}i} = U^{\mathrm{ext}}_{\mathbf{k}i} + \sum_{\mathbf{p}\sigma}(f^s_{\mathbf{kp}} + V_{\mathbf{q}})\delta n_{\mathbf{p}i} \; ; \; \delta\Delta_{\mathbf{k}i} = \sum_{\mathbf{p}j}\Gamma^{(ij)}_{\mathbf{kp}}\delta g_{\mathbf{p}j} \tag{6}$$

where $f^s_{\mathbf{kp}}$ represents the spin–symmetric contribution to the short–range Fermi liquid interaction and $V_{\mathbf{q}} = 4\pi e^2/\mathbf{q}^2$ is the Fourier transform of the long range Coulomb interaction. The equation for $\delta\Delta_{\mathbf{k}i}$ results from a straightforward variation of the equilibrium gap equation (2). The quantity $U^{\mathrm{ext}}_{\mathbf{k}i}$ represents a certain collection of external perturbation potentials

$$U^{\mathrm{ext}}_{\mathbf{k}i} = e\Phi - \frac{e}{c}\mathbf{v}_{\mathbf{k}i}\cdot\mathbf{A} + \frac{e^2}{c^2}A^I_\alpha \cdot M^{-1}_{\alpha\beta i}(\mathbf{k})\cdot A^S_\beta = e\Phi + \mathbf{v}_{\mathbf{k}i}\cdot\delta\boldsymbol{\xi}_1 + \gamma_{\mathbf{k}i}\delta\xi_\gamma$$

Here Φ and $\mathbf{A}$ denote, as usual, the electromagnetic scalar and vector potential. Furthermore we have defined $\delta\boldsymbol{\xi}_1 = -(e/c)\mathbf{A}$, $\delta\xi_\gamma = r_0|\mathbf{A}^I||\mathbf{A}^S|$ and $r_0 = e^2/mc^2$ denotes the Thompson radius. The quantity $\gamma_{\mathbf{k}i} = m\hat{\mathbf{e}}^I\cdot\mathbf{M}^{-1}_i(\mathbf{k})\cdot\hat{\mathbf{e}}^S$ denotes the Raman vertex in an approximate representation in terms of the inverse effective mass tensor $\mathbf{M}^{-1}_i(\mathbf{k})$. The solutions of the nonequilibrium gap equation (6) can be classified according to $\delta\Delta^{(s)}_{\mathbf{k}i} = \frac{1}{2}\left[\delta\Delta_{\mathbf{k}i}(\mathbf{q},\omega) + s\delta\Delta^*_{\mathbf{k}i}(-\mathbf{q},-\omega)\right]$ such that the real part $\delta\Delta^{(+)}_{\mathbf{k}i}$ represents the amplitude and the imaginary part $\delta\Delta^{(-)}_{\mathbf{k}i}$ represents the phase fluctuations of the order parameter. It turns out that the contributions of $\delta\Delta^{(+)}_{\mathbf{k}i}$ to the response consists in a 2Δ–mode, which lies in the pair–breaking continuum and has a tiny coupling to physical observables. The contribution of $\delta\Delta^{(-)}_{\mathbf{k}i}$, on the other hand, will be discussed now. Let us first define the condensate response or Tsuneto function $\lambda_{\mathbf{k}i}$ [4]:

$$\lambda_{\mathbf{k}i} = \frac{4\Delta^2_{\mathbf{k}i}\left[\theta_{\mathbf{k}i}(\omega^2 - \eta^2_{\mathbf{k}i}) + \Phi_{\mathbf{k}i}\eta^2_{\mathbf{k}i}\right]}{\omega^2(4E^2_{\mathbf{k}i} - \omega^2) - \eta^2_{\mathbf{k}i}(4\xi^2_{\mathbf{k}i} - \omega^2)} \tag{7}$$

where $\theta_{\mathbf{k}i} = (1/2E_{\mathbf{k}i})\tanh(E_{\mathbf{k}i}/2k_BT)$, $\Phi_{\mathbf{k}i} = -\partial n_{\mathbf{k}i}/\partial\xi_{\mathbf{k}i}$, $E_{\mathbf{k}i} = [\xi^2_{\mathbf{k}i} + \Delta^2_{\mathbf{k}i}]^{\frac{1}{2}}$ and $\eta_{\mathbf{k}i} = \mathbf{q}\cdot\mathbf{v}_{\mathbf{k}i}$. A few further definitions are required

$$D_{\mathbf{q}i} = \omega^2 - \omega^2_{\mathbf{q}i} \; ; \; \omega^2_{\mathbf{q}i} = \frac{\langle\eta^2\lambda\rangle_i}{\langle\lambda\rangle_i} \; ; \; C_i = \langle(\omega + \eta)\lambda\delta\xi\rangle_i \; ; \; \langle A\rangle_i = \sum_{\mathbf{k}i} A_{\mathbf{k}i}$$

and we may summarize our result for $\delta\Delta^{(-)}_{\mathbf{k}i}$ as follows:

$$\delta\Delta^{(-)}_{\mathbf{k}i} = \frac{2\Delta_{\mathbf{k}i}}{\langle\lambda\rangle_i D_{\mathbf{q}i}} \frac{D_{\mathbf{q}1}D_{\mathbf{q}2}C_i - \omega^2_{\mathrm{L}i} D_{\mathbf{q}i}\sum_j C_j}{D_{\mathbf{q}1}D_{\mathbf{q}2} - \sum_j \omega^2_{\mathrm{L}j} D_{\mathbf{q}j}} \; ; \; \omega^2_{\mathrm{L}j} = \frac{4\lambda_{12}}{\det\boldsymbol{\lambda}}\frac{\Delta_1\Delta_2\langle\lambda\rangle_j}{\langle\lambda\rangle_1\langle\lambda\rangle_2} \; ; \; \omega^2_{\mathrm{L}} = \sum_j \omega^2_{\mathrm{L}j} \tag{8}$$

The quantity $\omega_{\mathbf{q}i}$ represents the band–selected frequency of the so–called Anderson–Bogoliubov or gauge mode. In order to understand the physical meaning of the new frequency ω_{L}, one may factorize the denominator of $\delta\Delta^{(-)}_i$ as follows:

$$\begin{aligned}
D_{\mathbf{q}1}D_{\mathbf{q}2} - \sum_j \omega^2_{\mathrm{L}j} D_{\mathbf{q}j} &= \left[\omega^2 - \omega^2_{\mathbf{q}}\right]\left[\omega^2 - \omega^2_{\mathrm{L}}(\mathbf{q})\right] \qquad (9)\\
\omega^2_{\mathbf{q}} &= \frac{\omega^2_{\mathbf{q}1}\langle\lambda\rangle_1}{\langle\lambda\rangle_1 + \langle\lambda\rangle_2} + \frac{\omega^2_{\mathbf{q}2}\langle\lambda\rangle_2}{\langle\lambda\rangle_1 + \langle\lambda\rangle_2} \quad \text{gauge mode}\\
\omega^2_{\mathrm{L}}(\mathbf{q}) &= \omega^2_{\mathrm{L}} + \frac{\omega^2_{\mathbf{q}1}\langle\lambda\rangle_2}{\langle\lambda\rangle_1 + \langle\lambda\rangle_2} + \frac{\omega^2_{\mathbf{q}2}\langle\lambda\rangle_1}{\langle\lambda\rangle_1 + \langle\lambda\rangle_2} \quad \text{Leggett mode}
\end{aligned}$$

We are now in a position to state that the two zeroes of the denominator of $\delta\Delta^{(-)}_{\mathbf{k}i}$ correspond to precisely two collective excitations of the two–band superconductor, namely (i) the gauge mode, and (ii) the so–called Leggett mode, which was first derived in ref. [5]. Since there can only be one gauge mode in a superconductor, the gauge mode of the two–band superconductor is seen to emerge as a superposition of the band–selected gauge mode frequencies $\omega_{\mathbf{q}1}$ and $\omega_{\mathbf{q}2}$. The Leggett mode is clearly seen to originate from the interband pairing interaction $\propto \lambda_{12}$. The response of the nonequilibrium density $\delta n_{\mathbf{k}i}$ in phase space to the external potentials $U^{\mathrm{ext}}_{\mathbf{k}i}$ can be cast into a form reminiscent of the continuity equation:

$$\omega\delta n_{\mathbf{k}i} - \eta_{\mathbf{k}i}\left[\delta n_{\mathbf{k}i} + \Phi_{\mathbf{k}i}\delta\xi_{\mathbf{k}i}\right] = \lambda_{\mathbf{k}i}\left[(\omega^2 - \eta^2_{\mathbf{k}i})\frac{\delta\Delta^{(-)}_{\mathbf{k}i}}{2\Delta_{\mathbf{k}i}} - (\omega + \eta_{\mathbf{k}i})\delta\xi_{\mathbf{k}i}\right]$$

Upon summation over $\mathbf{k}$ and the band index i we indeed recover a conservation law for the particle number

$$\omega\delta n - \mathbf{q}\cdot\mathbf{j} \;=\; N_{\mathrm{F}}\sum_i\left\{-C_i + \langle\lambda\rangle_i D_{\mathbf{q}i}\frac{\delta\Delta^{(-)}_{\mathbf{k}i}}{2\Delta_{\mathbf{k}i}}\right\} = N_{\mathrm{F}}\left\{-\sum_i C_i + \sum_i C_i\right\} = 0$$

It is seen in particular, that *both* collective modes of the order parameter, namely the gauge mode (or the Nambu–Goldstone boson) and the Leggett mode have to be accounted for in order to satisfy the charge conservation law. In the absence of the Leggett mode, it is the gauge mode alone, that does this job, allowing for the traditional interpretation that there is an equivalence between the existence of a conservation law for the particle density and the gauge invariance of the theory. It should be noted that although the Leggett mode represents a massive collective mode of the order parameter, it must not be confused with analogies to the *Higgs mass*. This is because the Higgs mass corresponds to *amplitude fluctuations* of the order parameter, whereas the Leggett mode occurs in the *phase fluctuation* channel of the order parameter dynamics.

Response properties of two–band superconductors

The response properties of two–band superconductors can in general be divided into the *electromagnetic response* (i.e. the Lindhard response, the dielectric function and the dynamic conductivity) and the *electronic Raman response* (i.e. the pair–breaking effect of inelastic light scattering from the superconductor). For lack of space we can not give a detailed account of the calculations here and therefore limit ourselves to describing one representative result, namely the one for the condensate dielectric function $\epsilon_c(\mathbf{q}, \omega)$ for two–band superconductors, which reads in the long wavelength limit:

$$\epsilon_c(\mathbf{q}, \omega) = 1 - \frac{\omega_{pc}^2}{\omega^2 - \omega_{\mathbf{q}}^2} \cdot \frac{\omega^2 - \omega_L^2 - c_L^2 \mathbf{q}^2}{\omega^2 - \omega_L^2 - c_{L0}^2 \mathbf{q}^2} \tag{10}$$

Here $\omega_{pc}^2 = V_{\mathbf{q}} \sum_i \langle \eta^2 \lambda \rangle_i = c^2/\lambda_L^2$ is condensate plasma frequency, as related to the magnetic penetration depth λ_L. With the aid of Eq. (10) one can easily demonstrate the Higgs mechanism of two–band superconductors: the gauge mode $\omega_{\mathbf{q}}$ gets shifted to the plasma frequency ω_{pc} of the condensate. In addition there is a contribution from the Leggett mode, which is unaffected by the long–range Coulomb interaction and which vanishes in the long wavelength limit $\mathbf{q} \to 0$ as can be seen from the different dispersion velocities c_L, c_{L0}. A careful study reveals, however, that the Leggett mode enters both the Lindhard response function and the dynamic conductivity with an almost vanishing residue and can therefore not be expected to be observable. The situation is different in the case of the electronic Raman response, where the Leggett mode appears as a large additional term in the scattering intensity, which vanishes in the limit $\lambda_{12} \to 0$. An application of the theory to realistic two–band superconductors, such as MgB_2, pnictides, non–centrosymmetric superconductors and probably others waits for a realization.

References

[1] N. Bittner. *Response und kollektive Anregungen in Zweiband–Supraleitern*. Diploma thesis, Technische Universität München (2012).

[2] J. Bardeen, L. N. Cooper, and J. R. Schrieffer, Phys. Rev. **106**, 162 (1957).

[3] O. Betbeder-Matibet, and P. Nozieres, Ann. Phys. **51**, 392 (1969).

[4] T. Tsuneto, Phys. Rev. **118**, 1029 (1960).

[5] A. J. Leggett, Prog. Theor. Phys. **36**, 901 (1966).

Charge Density Wave Formation in Multi-band Systems

H.-M. Eiter, M. Lavagnini, R. Hackl [1], *L. Degiorgi*[2]
E. A. Nowadnick, A. F. Kemper, T. P. Devereaux, J.-H. Chu, J. G. Analytis, I. R. Fisher[3,4]

Superconductivity and density waves, periodic modulations of the electron or magnetization density, are among the most abundant low-temperature ordered phases in condensed matter. In many cases such as the copper-oxygen or iron-based compounds the two types of order are in close proximity, and their interrelation is considered relevant for understanding superconductivity at high transition temperature T_c. Beyond this interrelation the density wave systems themselves withhold answers to tantalizing questions: Why, as opposed to superconductors, T_c may be well above room temperature? Why does charge density wave (CDW) order win over superconductivity? What determines the ordering direction of a CDW system? Yet, the first two questions are by far too complicated, and we discuss only the last one in this report. We show how an enhanced electron-lattice interaction can contribute to or even determine the selection of the ordering vector and summarize results of a joint experimental and theoretical study of the model CDW system $ErTe_3$ [1].

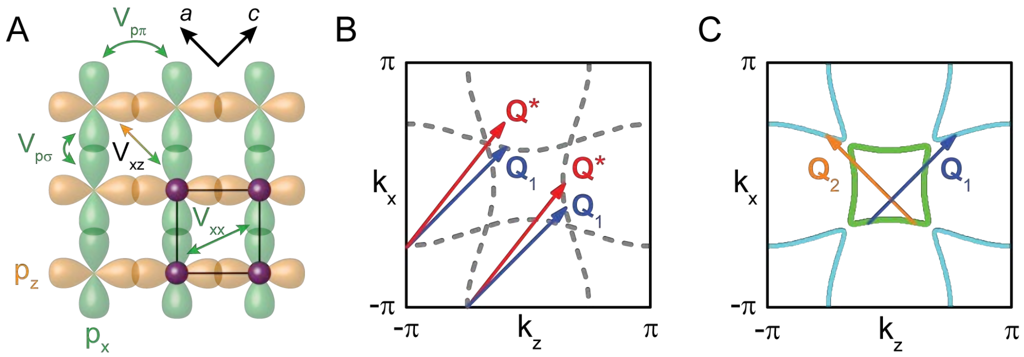

Figure 1: Real and reciprocal space structure of rare earth tri-tellurides. (*A*) Orbital character of the Te $5p$ orbitals in the Te plane. The various hopping matrix elements are indicated. (*B*) Fermi surface as derived from the p_x and p_z orbitals alone ($V_{xz} = 0$). There are two energetically possible orientations for CDW ordering, $\mathbf{Q}_1$ and $\mathbf{Q}^*$. (C) Theoretical Fermi surface for $V_{xz} \neq 0$ best reproducing the experimental findings [2]. Also shown are the two experimentally observed orthogonal ordering vectors $\mathbf{Q}_1$ and $\mathbf{Q}_2$.

$ErTe_3$ undergoes a first CDW transition at $T_{\mathrm{CDW1}} = 265\,\mathrm{K}$, followed by a second one at $T_{\mathrm{CDW2}} = 155\,\mathrm{K}$. The ordering vectors $\mathbf{Q}_1$ and $\mathbf{Q}_2$ are parallel to but incommensurate with the reciprocal lattice vectors $c^* \parallel c$ and $a^* \parallel a$, respectively [3]. The electronic properties can be modeled by considering a single Te plane. Fig. 1 A shows the orbital structure and the dominant hopping terms $V_{p\sigma}$ and $V_{p\pi}$ along and perpendicular to the overlapping p_x or p_z orbitals, leading to slightly warped Fermi surface planes (Fig. 1 B). For this Fermi surface, nesting predicts the ordering vector $\mathbf{Q}^*$ [4], while in experiment $\mathbf{Q}_1$ is observed [2, 3]. If additional hopping terms V_{xz} between p_x and p_z orbitals are included the degeneracy at the intersection points of the bands is lifted (Fig. 1 C) improving the agreement of the model with ARPES measurements [2]. However, the nesting conditions are hardly changed and $\mathbf{Q}^*$ remains the favorable ordering vector. With Raman scattering experiments we identified a novel mechanism, driven by band hybridization, that contributes to the selection of the ordering vector and finally explains the selection of $\mathbf{Q}_1$ over $\mathbf{Q}^*$.

---

[1] This work was supported by the German Research Foundation via HA 2071/5-1 and the Collaborative Research Centre/Transregio TRR 80.

[2] Laboratorium für Festkörperphysik, ETH-Zürich, Switzerland

[3] Stanford Institute for Materials and Energy Sciences, SLAC National Accelerator Laboratory, USA

[4] Geballe Laboratory for Advanced Materials & Dept. of Applied Physics, Stanford University, USA

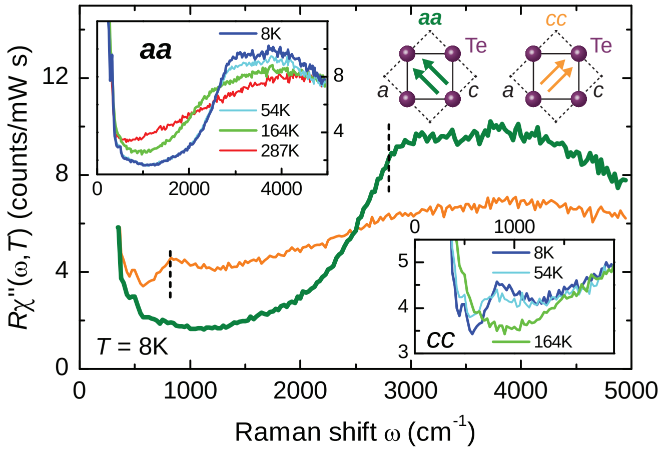

Figure 2: CDW energy gap of $ErTe_3$. The insets show the temperature dependencies of the electronic Raman response in *aa* and *cc* polarization. At 8 K the electronic gaps with edges at 800 and 2800 cm^{-1} (dashed lines) are fully developed and observable separately with orthogonal polarization settings.

Fig. 2 depicts the electronic Raman response $R\chi''_{i,s}(\omega, T)$ of $ErTe_3$ versus energy shift ω with i and s indicating the polarizations of incoming and scattered photons. Measurements were performed with two different settings referred to as *aa* and *cc*. In *aa* (*cc*) configuration both incoming and scattered photons are polarized along the *a* (*c*) axis of the crystal (Fig. 2). The insets show the temperature dependencies of the *aa* and *cc* spectra. At high temperature, the Raman response rises almost linearly between 1000 and 4000 cm^{-1}. Upon lowering the temperature spectral weight is transferred from low to high energies as a consequence of the CDW energy gap. The main panel of the figure shows *aa* and *cc* spectra at 8 K. The orthogonal CDW gaps are detected independently. The gap edges are marked by dashed lines.

The Raman selection rules can be derived directly from the band structure and the momentum dependencies of the CDW gaps [5]. The light scattering intensity is determined by the Raman vertices given by the band curvature. For degenerate bands the vertices are almost featureless [1]. Upon including hybridization, the band degeneracy is lifted (Fig. 1 C). The resulting strong curvatures enhance the Raman vertices and, concomitantly, the light scattering amplitude precisely at the Fermi surface points connected by the experimentally observed CDW ordering wavevectors. For the analogy between electron-photon and electron-phonon scattering [6], the electron-phonon coupling vertex is also strongly anisotropic in *k*-space and highlights the regions close to the lifted band degeneracies, hence along the observed ordering direction.

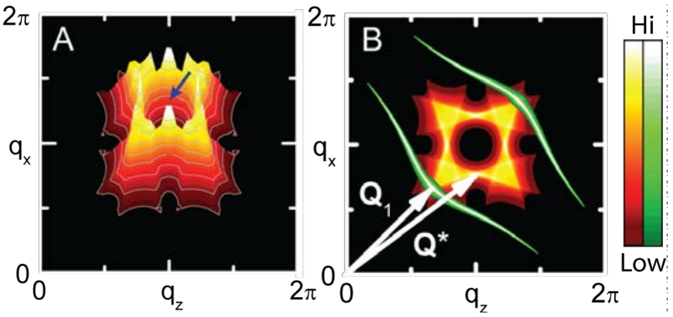

Figure 3: (*A*) 3D plot of the real part of the Lindhard susceptibility. There is little structure around the rim, but ordering along $\mathbf{Q}^*$ (blue arrow) is slightly favored. (*B*) 2D superposition of the real parts of the Lindhard susceptibility (yellow-red) and the projected susceptibility (green). It is this focusing effect which selects the experimentally observed ordering wave vector $\mathbf{Q}_1$ over $\mathbf{Q}^*$.

More quantitatively, the conventional Lindhard susceptibility needs to be supplemented. It has maxima of comparable height in momentum space but slightly favors $\mathbf{Q}^*$ (blue arrow in Fig. 3 A) over $\mathbf{Q}_1$. In the case of multi-band systems with lifted band degeneracies the strongly momentum dependent electron-phonon vertex has to be included in the electronic susceptibility, highlighting particular parts of the Brillouin zone. The superposition of both contributions finally selects the experimentally observed ordering vector $\mathbf{Q}_1$ (Fig. 3 B) below T_{CDW1}. Upon further cooling the second CDW appears and aligns along $\mathbf{Q}_2$ (Fig. 2 C) since the Fermi surface in the orthogonal direction is already fully gapped by the first transition [2, 3]. In addition to the well known Lindhard theory we identify, on a microscopic basis, the focusing effect near lifted band degeneracies to be a more generic paradigm for multiband materials. It seems particularly interesting to explore this scenario more generally in materials such as the iron-based superconductors, where density-wave order and superconductivity are interrelated on a microscopic scale.

References

[1] H.-M. Eiter, M. Lavagnini, R. Hackl, E. A. Nowadnick, A. F. Kemper, T. P. Devereaux, J.-H. Chu, J. G. Analytis, I. R. Fisher, and L. Degiorgi. Charge density wave formation near band degeneracies: a new paradigm towards broken symmetry ground states. Accepted for publication in PNAS, `arXiv:1208.5701` (2012).

[2] R. G. Moore, V. Brouet, R. He, D. H. Lu, N. Ru, J.-H. Chu, I. R. Fisher, and Z.-X. Shen, Phys. Rev. B **81**, 073102 (2010).

[3] N. Ru, C. L. Condron, G. Y. Margulis, K. Y. Shin, J. Laverock, S. B. Dugdale, M. F. Toney, and I. R. Fisher, Phys. Rev. B **77**, 035114 (2008).

[4] M. D. Johannes, and I. I. Mazin, Phys. Rev. B **77**, 165135 (2008).

[5] A. Ványolos, and A. Virosztek, Phys. Rev. B **72**, 115119 (2005).

[6] T. P. Devereaux, Phys. Rev. B **45**, 12965 (1992).

Absence of Spin Splitting in the Electron-doped High Temperature Superconductor $Nd_{2-x}Ce_xCuO_4$

T. Helm, M. V. Kartsovnik, N. Bittner, W. Biberacher, A. Erb, and R. Gross [1]
E. Kampert, C. Putzke, F. Wolf-Fabris, and J. Wosnitza [2]

With its simple crystal structure as compared to other cuprate superconductors, $Nd_{2-x}Ce_xCuO_4$ (NCCO) was predicted to have a simple single-band Fermi surface (FS) [1]. The recent discovery of magnetic quantum oscillations (MQO) in this system revealed a more complex FS, consisting of electron- and hole-like parts [2, 3]. A superlattice potential, responsible for this FS-reconstruction, is found to be present over a wide electron-doping region, ranging from optimum, $x = 0.145$, up to strong overdoping at $x = 0.17$ where superconductivity is close to vanish.

MQO are a powerful tool for extracting information about the electronic system in the normal state such as the size of the FS, the effective cyclotron mass of the charge carriers, the scattering time, etc.. The MQO originate from the oscillating density of states when the Landau levels shift across the Fermi energy on varying the applied magnetic field **B**. Due to the spin-degeneracy each level is split into two, as soon as **B** is switched on. This Zeeman splitting gives rise to an additional damping term $R_S = \cos(\pi g \mu / 2\cos\theta)$ for the amplitude of MQO in layered compounds, $A \propto R_S \cdot \cos\left[2\pi(F_0/B\cos\theta) + \gamma\right]$, depending on the field-orientation. Here, g is the gyromagnetic ratio and $\mu/\cos\theta = (m_c/\cos\theta)\cdot(1/m_e)$ the effective cyclotron mass in units of the free-electron mass depending on the field orientation) [4]. Destructive interference between oscillations from the two spin channels leads to a vanishing amplitude at certain, so-called *'spin-zero'* angles followed by a π-shift in the oscillation phase. Therefore, by varying the polar angle θ with respect to the conducting layers one can gain information about the spin-orbit coupling and many-body-interactions which lead to a renormalization of the product $g\mu$ [4].

To investigate the angle dependence of the Shubnikov-de Haas oscillations for almost optimally doped single-crystals of NCCO, we have carried out measurements with a rotating sample stage at the high field facility (HLD) of the Helmholtz-Forschungszentrum Dresden-Rossendorf. We designed and built this probe in collaboration with the HLD for four-probe-magnetoresistance measurements in pulsed magnetic fields up to 70 T at liquid helium temperatures. It fits into a cryostat with an inner diameter of $d \leq 9.5$ mm. A special rigid design (see inset of Fig. 1) was chosen to withstand the expected strong magnetic torque of our samples caused by a huge non-saturating contribution from Nd^{3+}-ions ($S = 9/2$): Two cone-headed pushing-rods press against the rotation platform. The sample is fixed on a triangular prism so that, after having the platform

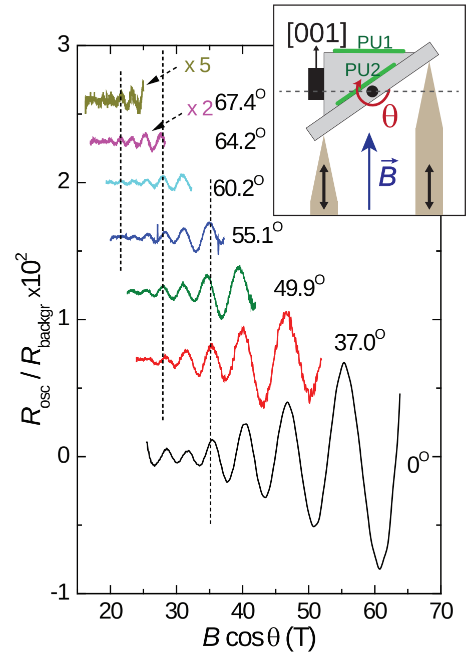

Figure 1: SdH oscillations at different polar angles θ plotted vs. the out-of-plane field component $B\cos\theta$ for a $x = 0.15$ sample. Inset: Sketch of the rotation setup using two cone-headed pushing-rods (brown) and two pick-up coils (green) to set and determine θ.

---

[1] This work was supported by the German Research Foundation via grant GR 1132/15, as well as by EuroMagNET II under the EC contract 228043.

[2] Hochfeld-Magnetlabor Dresden, Helmholtz-Zentrum Dresden Rossendorf, Deutschland

set to an angle of ≈ 35°, the initial polar orientation is $\theta = 0°$, that is, $B||[001]$. Two small pickup coils (green bars in the inset) were used to precisely determine angle *in situ*.

In Fig. 1 we present SdH oscillations at different polar angles plotted versus the out-of-plane field component $B\cos\theta$. We were able to trace the evolution of the oscillations over 4 decades of their amplitude, in a broad angular range up to 71°. The vertical dashed lines connect maxima at constant out-of-plane field component for different angles and highlight the absence of a phase inversion. The inset in Fig. 2 shows the oscillation frequency plotted versus the *in situ* determined angle θ. It increases proportional to $1/\cos\theta$ (black curve), as it is expected for a layered metal. The main panel of Fig. 2 shows the θ-dependent oscillation amplitude obtained from a fast Fourier transformation (FFT) in a fixed field window of 40 to 60 T. Using the Lifshitz-Kosevich formalism, the θ-dependence can be fitted. The temperature- and Dingle-damping factors are included in the fit, as well as a correction for the effect of magnetic breakdown known to be present at strong fields for NCCO [3]. For comparison we show what would be expected for $g = 2.0$ (green curve), that is, the non-renormalized free-electron value and for $g = 1.0$, showing a *spin-zero* close to 70°. Only if we neglect the spin-splitting by choosing $g = 0$ (red curve), the fit coincides nicely with our experimental results.

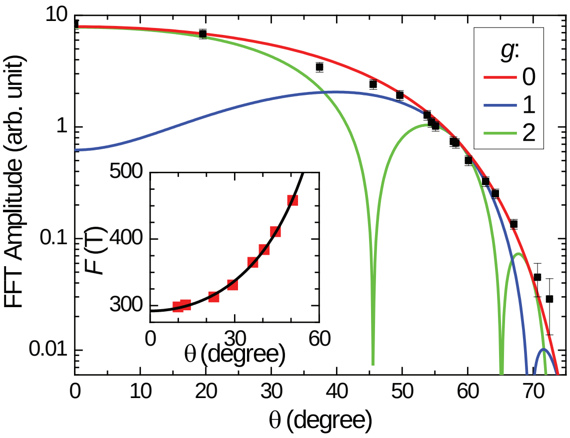

Figure 2: SdH oscillation amplitude obtained from FFT for a field window of $40 \leq B \leq 60\,\mathrm{T}$ for different polar angles θ. Also shown is a Lifshitz-Kosevich fit for $g = 2.0$ (green), $g = 1.0$ (blue) and $g = 0$ (red, absence of the spin-zero effect). Inset: SdH oscillation frequency vs. the angle θ. The black curve is a fit to $F = 292\,\mathrm{T}/\cos\theta$.

How can this observation be understood? For the hole-doped cuprate $YBa_2Cu_3O_{6+x}$ spin-zeros were found [5, 6], indicating that the quasiparticles behave as a nearly free spins. Thus, for NCCO we simply could have missed the sharp *spin-zero* dips. However, since in our case there is no discernible phase inversion such a scenario is ruled out. Our observation could rather be a hint to the nature of the ground state of NCCO, associated with the FS reconstruction. It has been shown by Ramazashvilli [7] that spin-splitting effects can be canceled due to the anisotropic spin-orbit character of the Zeeman coupling in an easy-axis antiferromagnet. This effect depends on the orientation of the magnetic field with respect to the staggered magnetization rather than to the crystal axes. Therefore, our results provide strong evidence in favor of an antiferromagnetic low-temperature ground state for optimally doped NCCO, at least at a high magnetic field.

References

[1] O. Andersen, A. Liechtenstein, O. Jepsen, and F. Paulsen, J. Phys. Chem. Solids **56**, 1573 (1995).

[2] T. Helm, M. V. Kartsovnik, I. Sheikin, M. Bartkowiak, F. Wolff-Fabris, N. Bittner, W. Biberacher, M. Lambacher, A. Erb, J. Wosnitza, and R. Gross, Phys. Rev. Lett. **105**, 247002 (2010).

[3] M. V. Kartsovnik, T. Helm, C. Putzke, F. Wolff-Fabris, I. Sheikin, S. Lepault, C. Proust, D. Vignolles, N. Bittner, W. Biberacher, A. Erb, J. Wosnitza, and R. Gross, New J. Phys. **13**, 015001 (2011).

[4] D. Shoenberg. *Magnetic oscillations in metals* (Cambridge University Press, 1984).

[5] B. J. Ramshaw, B. Vignolle, J. Day, R. Liang, W. N. Hardy, C. Proust, and D. A. Bonn, Nat. Phys. **7**, 234 (2011).

[6] S. E. Sebastian, N. Harrison, M. M. Altarawneh, F. F. Balakirev, C. H. Mielke, R. Liang, D. A. Bonn, W. N. Hardy, and G. G. Lonzarich. `arXiv:1103.4178` (2011).

[7] R. Ramazashvili, Phys. Rev. Lett. **105**, 216404 (2010).

Electromechanically Induced Absorption in a Circuit Nanoelectromechanical System

F. Hocke, H. Huebl, R. Gross [1]
X. Zhou, A. Schliesser, T. J. Kippenberg [2,3,4]

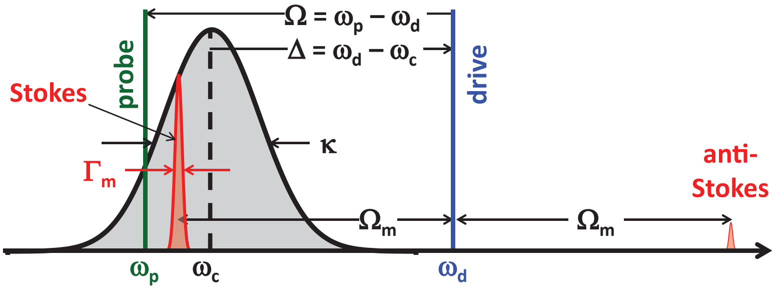

Figure 1: Schematic diagram explaining the various frequencies: driving tone frequency ω_d (blue line), probe tone frequency ω_p (green line), cavity resonant frequency ω_c (black line), drive tone detuning $\Delta = \omega_\mathrm{d} - \omega_\mathrm{c}$, probe tone detuning $\Omega = \omega_\mathrm{p} - \omega_\mathrm{d}$. Varying Δ shifts the drive tone with respect to the cavity resonance (grey-shaded area). Since the Stokes line (red shaded area) is fixed to the drive tone at $\omega_\mathrm{d} - \Omega_\mathrm{m}$, the variation of Δ also shifts the Stokes line with respect to the cavity resonance. Varying Ω at constant Δ shifts the probe tone with respect to the cavity resonance and the Stokes line.

The combination of cavities for electromagnetic radiation with engineered mechanical resonators to form cavity electromechanical systems allows for quantum control over mechanical motion or, conversely, mechanical control over electromagnetic fields. Depending on the frequency of the electromagnetic field, this class of hybrid systems forms the new fields of cavity opto- or cavity electromechanics [1–4]. Cavity opto- and electromechanical systems allow us to study a wealth of interesting physical phenomena and to design novel devices that can probe extremely tiny forces [5], enable the mechanical detection and imaging of a single electron spin, or allow us to control the quantum state of mechanical oscillators. Additionally, the mechanical oscillator in this hybrid system is affected by the radiation pressure force induced by the electromagnetic field of an optical or microwave cavity which leads to a parametric electromechanical coupling allowing for both, heating and cooling of the mechanical mode.

An important ingredient for these experiments is the application of two-tone spectroscopy. Here, the system is driven by a strong drive tone at angular frequency ω_d, which is red- or blue-detuned from the cavity resonant angular frequency ω_c by about the mechanical resonant angular frequency Ω_m, while a weak probe tone at angular frequency ω_p probes the modified cavity resonance (cf. Fig. 1). Two-tone spectroscopy has been successfully used for the study of opto-/electromechanically induced transparency (OMIT/EMIT) or absorption (OMIA/EMIA) [6–8]. Here, the electromagnetic response of the system to a weak probe field is controlled by the drive field, driving the lower or upper motional sideband, respectively. The resulting destructive or constructive interference of different excitation pathways of the intracavity field results in a narrow window of enhanced or reduced transparency when the two-photon resonance condition is met. Both EMIT and EMIA are key requirements for protocols to manipulate and control electromagnetical signals [7–10].

In the following, we consider only the case of blue-detuning ($\Delta \simeq +\Omega_\mathrm{m}$) [6]. In this case a strong drive tone at ω_d close to the upper motional sideband of the cavity is applied to the

---

[1] The authors acknowledge financial support from the German Excellence Initiative via the "Nanosystems Initiative Munich'" (NIM).

[2] École Polytechnique Fédérale de Lausanne (EPFL), CH-1015 Lausanne, Switzerland

[3] Max-Planck-Institut für Quantenoptik, D-85748 Garching, Germany

[4] T.J.K acknowledges support by the ERC grant SIMP and X.Z. by the NCCR of Quantum Engineering. Samples were grown and fabricated at the Center of MicroNanotechnology (CMi) at EPFL.

system, while a second, much weaker tone probes the modified cavity resonance at frequency $\omega_\mathrm{p} = \omega_\mathrm{d} + \Omega$. The simultaneous presence of the drive and the probe tone result in a radiation pressure force oscillating at $\Omega = \omega_\mathrm{p} - \omega_\mathrm{d}$. If this difference frequency is close to the mechanical resonance frequency, $\Omega \simeq -\Omega_\mathrm{m}$, a coherent oscillation of the mechanical system is induced. As a consequence of this oscillation, Stokes and anti-Stokes fields build up at $\omega_\mathrm{d} \pm \Omega_\mathrm{m}$ around the strong driving field. Additionally, the microwave resonator acts as a narrow-band filter for these fields. If the system is in the resolved-sideband regime, $\Omega_\mathrm{m} > \kappa$, the anti-Stokes line at $\omega_\mathrm{d} + \Omega_\mathrm{m} > \omega_\mathrm{c}$ is strongly suppressed because it is off-resonant with the cavity, whereas the Stokes line at $\omega_\mathrm{d} - \Omega_\mathrm{m} \simeq \omega_\mathrm{c}$ is enhanced. Moreover, since the Stokes scattered field is degenerate with the probe field sent to the cavity, it allows for constructive interference of the two fields enhancing the build-up of the intra-cavity probe field. This can be viewed as a self-interference between two different excitation pathways. The resulting increased feeding ("absorption") of probe photons into the cavity manifests itself as a reduced cavity transmission (Fig. 1b). At even higher drive field power, the system switches from EMIA to parametric amplification, resulting in electromagnetic signal amplification, and eventually phonon-lasing. In the picture of parametric amplification, the electromechanical system can be viewed as a parametric amplifier strongly pumped at ω_d and amplifying the weak input signal at ω_p. This amplification is detected as an enhanced cavity transmission.

The circuit nano-electromechanical device studied in our experiments is a hybrid system, consisting of a high quality superconducting coplanar waveguide (CPW) microwave resonator capacitively coupled to a nanomechanical beam, realizing a parametric coupling of the microwave resonator to the vibrational mode of a nanomechanical beam. The superconducting CPW resonator is operated in a dilution refrigerator at a temperature of $T_\mathrm{cryo} \approx 200\,\mathrm{mK}$, has an eigenfrequency of $\omega_\mathrm{c}/2\pi = 6.07\,\mathrm{GHz}$, and is fabricated of a 200 nm thick Nb film deposited on a silicon substrate (cf. Fig. 2 a). The CPW resonator has a coupling rate of $\kappa_\mathrm{ex} = 2\pi \times 339\,\mathrm{kHz}$ to the feedline and a cavity linewidth (total loss rate) of $\kappa = 2\pi \times 759\,\mathrm{kHz}$ close to the critical coupling $\eta_\mathrm{c} = 1/2$.

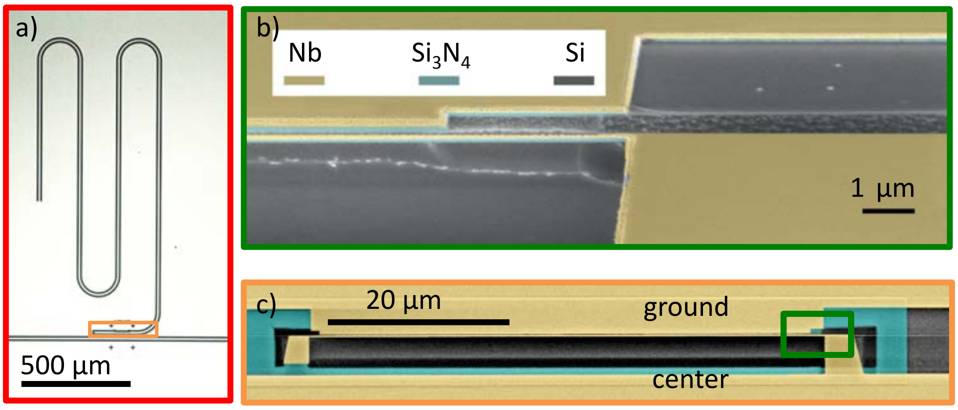

Figure 2: Superconducting circuit nano-electromechanical system. a) Falsed-colored scanning electron microscopy (SEM) of a quarter-wavelength coplanar waveguide (CPW) resonator, coupled to a CPW feedline. The 6 μm gaps are patterned by etching through the Nb layer (yellow) down to the Si (green). b) False-colored SEM yellow: Nb, green: Si, violet: Si3N4) of a 60 μm × 140 nm × 200 nm long mechanical beam integrated in the microwave cavity. c) A zoomed-in view, showing the mechanical beam released from the Si substrate.

Figure 2 b) and c) show the Nb/$\mathrm{Si_3N_4}$ nanomechanical resonator (NR) clamped on both ends. The Nb/$\mathrm{Si_3N_4}$ bilayer is RIE etched out of a 130 nm thick Nb film sputtered on top of a 70 nm thick layer of highly strained (tensile) $\mathrm{Si_3N_4}$ layer and has a high aspect ratio with a length of 60 μm and a width of 140 nm [11]. This results in a high mechanical eigenfrequency of $\Omega_\mathrm{m}/2\pi = 1.45\,\mathrm{MHz}$ and a narrow linewidth of $\Gamma_\mathrm{m}/2\pi = 11\,\mathrm{Hz}$, corresponding to a quality factor of $Q_\mathrm{m} = 1.32 \times 10^5$ at 200 mK. The nanobeam is placed 200 nm from the ground plane

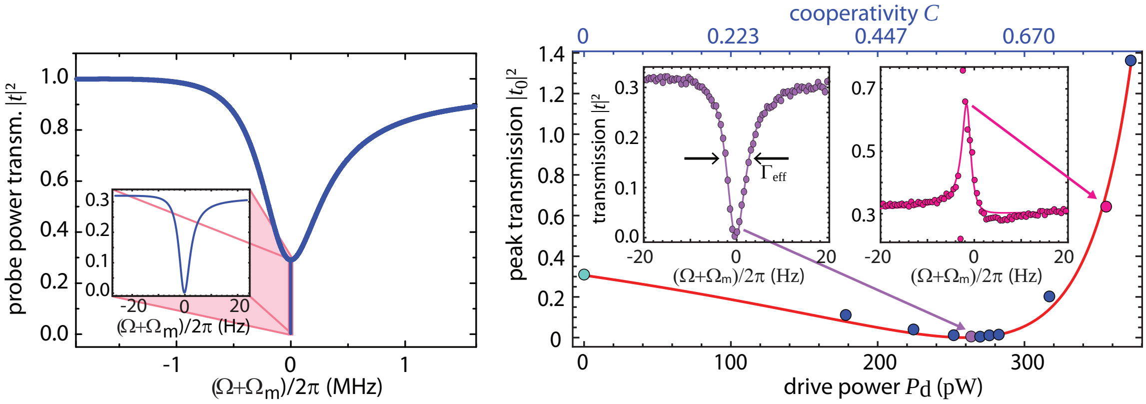

Figure 3: a) Schematic of a typical probe power transmission spectrum of a superconducting CPW microwave resonator with an optimally detuned driving tone applied at $\Delta = \Omega_m$. The inset shows the very sharp absorption feature close to $\Omega + \Omega_m = 0$ on an enlarge scale. b) Shows the measured peak probe power transmission $|t_0|^2$ at optimum drive tone detuning $\Delta = \Omega_m$ as a function of the drive power P_d. The solid red line is a fit of the data to the theory. In the left (right) inset of panel b), the probe power transmission $|t|^2$ is plotted versus the probe tone detuning $\Omega + \Omega_m$ for a constant drive power of 264 pW, (356 pW) showing the typical EMIA dip (peak) at $\Omega = -\Omega_m$. From this type of spectra, the peak transmission $|t_0|^2$ is obtained for $\Omega = -\Omega_m$ using a particular drive power.

and couples capacitively beeing at a voltage antinode of the CPW microwave resonator. The finite coupling capacitance C_g gives rise to the electromechanical coupling $g_0 = Gx_{zp}$ between the mechanical displacement and the microwave mode inside the CPW resonator (Fig. 1a) with $G = 2\pi \times 36.3\,\text{kHz/nm}$ or a a normalized vacuum coupling of $g_0 = Gx_{zp} = 2\pi \times 1.26\,\text{Hz}$ corroborated by frequency noise calibration [11].

In the following, we discuss the behavior of the EMIA dip at optimum detuning for varying drive power. In Fig. 3 b), the peak probe power transmission $|t_0|^2$ at optimum detuning is plotted versus the drive power. It is given by the minimum of the narrow absorption dip shown in the inset of Fig. 3 b), which is determined by fitting the data by a damped harmonic oscillator spectrum. The peak probe power transmission decreases with increasing drive power from about 0.3 for the bare cavity minimum ($P_d = 0$) to a minimum value of $|t_0|^2 = 0.0046$ for a drive power of $P_d = 270\,\text{pW}$.

This corresponds to an additional absorption of 18.3 dB with respect to the bare microwave cavity background and 23.4 dB with respect to unity transmission. Increasing the drive power further, $|t_0|^2$ increases again and exceeds the initial value of the bare cavity, $|t_0|^2\,(P_d = 0) \simeq 0.3$, at higher drive powers. In other words, the transmission reduction (“absorption”) turns into a transmission enhancement (“emission”). At drive powers above 380 pW, $|t_0|^2 > 1$, i.e. it even exceeds the undisturbed transmission of the feedline. At this power level we are entering the regime of parametric amplification. Finally, when the drive power is increased even further, the beam starts to perform self-oscillations at $P_d \simeq 390\,\text{pW}$. Here, the electromechanical linewidth narrowing induced by the driving field cancels the internal losses of the mechanical system, leading to a regime of zero damping (i.e. parametric instability) and resulting in self-oscillations of the system.

In summary, we have presented an analysis of electromechanically induced absorption by performing two-tone spectroscopy on a circuit nano-electromechanical system showing quantitative agreement between experiment and theory. Our results clearly demonstrate that the studied electromechanical system can be applied to filter out extreme narrow frequency bands ($\sim$ Hz) of the much wider frequency band ($\sim$ MHz) defined by the linewidth of the microwave cavity. The amount of absorption as well as the filtering frequency is tunable around the cavity resonance over about 1 MHz by adjusting the power and frequency of the drive field.

References

[1] F. Marquardt, and S. M. Girvin, Physics **2**, 40 (2009).
[2] M. Aspelmeyer, S. Gröblacher, K. Hammerer, and N. Kiesel, J. Opt. Soc. Am. B **27**, A189 (2010).
[3] C. A. Regal, and K. W. Lehnert, J. Phys.: Conf. Ser. **264**, 012025 (2011).
[4] M. Aspelmeyer, P. Meystre, and K. Schwab, Physics Today **65**, 29 (2012).
[5] J. Chaste, A. Eichler, J. Moser, G. Ceballos, R. Rurali, and A. Bachtold, Nat. Nanotech. **7**, 301 (2012).
[6] F. Hocke, X. Zhou, A. Schliesser, T. J. Kippenberg, H. Huebl, and R. Gross. Electromechanically induced absorption in a circuit nano-electromechanical system. Accepted for publication in New J. Phys., `arXiv:1209.4470` (2012).
[7] S. Weis, R. Rivière, S. Deléglise, E. Gavartin, O. Arcizet, A. Schliesser, and T. J. Kippenberg, Science **330**, 1520 (2010).
[8] A. H. Safavi-Naeini, T. P. M. Alegre, J. Chan, M. Eichenfield, M. Winger, Q. Lin, J. T. Hill, D. E. Chang, and O. Painter, Nature **472**, 69 (2011).
[9] J. D. Teufel, D. Li, M. S. Allman, K. Cicak, A. J. Sirois, J. D. Whittaker, and R. W. Simmonds, Nature **471**, 204 (2011).
[10] F. Massel, T. T. Heikkilaä, J.-M. Pirkkalainen, S. U. Cho, H. Saloniemi, P. J. Hakonen, and M. A. Sillanpää, Nature **480**, 351 (2011).
[11] X. Zhou, F. Hocke, A. Schliesser, A. Marx, H. Huebl, R. Gross, and T. J. Kippenberg. Control of microwave signals using circuit nano-electromechanics. Accepted for publication in Nature Physics, `arXiv:1206.6052v2` (2012).

Tunable Coupling Between Two Resonators Controlled by a Flux Qubit - The Quantum Switch

E. Hoffmann, F. Deppe, M. Haeberlein, A. Baust, M. Schwarz, E. P. Menzel, A. Marx, R. Gross [1]
D. Zueco,[2] *J.-J. García-Ripoll,*[3] *E. Solano*[4]

In the field of quantum information processing, superconducting circuits have become a well-established platform [1, 2]. In particular, systems consisting of a few qubits coupled to a harmonic oscillator have been intensively studied [3–5]. In order to scale these systems up to many constituents, controllable interactions are highly desirable. To this end, for example, the coupling between two superconducting charge qubits via a bus resonator was investigated [4]. Here, we report on experimental progress on the complementary situation: one flux qubit mediating a tunable coupling between two superconducting transmission line resonators. In future, we envision this so-called *quantum switch* [6] to allow for the controlled transfer of excitations between a fast bus resonator, to which additional qubits can be coupled, and a long-lived storage resonator serving as a quantum memory.

Figure 1(a) shows a sketch of the layout of our device. A three Josephson junction flux qubit is coupled to the antinodes of the current ground modes of two $\lambda/2$-resonators with equal eigenfrequencies $\omega_\mathrm{r}/2\pi = 4.896\,\mathrm{GHz}$. The qubit transition frequency $\omega_\mathrm{Q} = \sqrt{[\varepsilon/\hbar]^2 + \Delta^2}$ can be tuned by an external flux Φ_x threading the qubit loop. Here, $\varepsilon \equiv 2I_\mathrm{p}(\Phi_\mathrm{x} - \Phi_0/2)$ denotes the energy bias, I_p the persistent current, and Δ the minimum transition frequency of the qubit; $\hbar$ and Φ_0 are Planck's constant and the flux quantum, respectively. In the dispersive regime, where the detuning $\delta \equiv |\omega_\mathrm{Q} - \omega_\mathrm{r}|$ between qubit and resonators is much larger than their coupling rate g, the Hamiltonian can be written as [6]

$$\hat{H}_\mathrm{eff} = \hbar(g_\mathrm{geo} + g_\mathrm{dyn})\left(\hat{a}^\dagger\hat{b} + \hat{a}\hat{b}^\dagger\right) .$$

This equation has the structure of a beam splitter Hamiltonian, where $\hat{a}$ and $\hat{b}$ ($\hat{a}^\dagger$ and $\hat{b}^\dagger$) are the photon annihilation (creation) operators of resonator A and B, respectively. The total coupling constant is the sum of the two contributions g_geo and g_dyn, as sketched in Fig. 1(a). While the geometric coupling $g_\mathrm{geo} = 8.5\,\mathrm{MHz}$ is defined by the geometry of the chip-layout, the dynamic coupling $g_\mathrm{dyn} = (g^2 \sin^2\theta/\delta)\sigma_\mathrm{z}$ depends on the qubit state (σ_z) and the applied flux Φ_x. Here, the mixing angle θ is defined as $\tan\theta \equiv \Delta/\varepsilon$ and g is the coupling constant between the qubit and one resonator. Balancing the geometric and dynamic coupling rates leads to the *switch setting condition*, where $g_\mathrm{geo} = |g_\mathrm{dyn}|$. In this situation, the two resonators are completely decoupled when the qubit is in the ground state, but exhibit a finite coupling rate otherwise.

The two resonators are fabricated from niobium on a thermally oxidized silicon substrate, using a coplanar stripline design. The qubit, which is shown in Fig. 1(b), is made using aluminum shadow evaporation [7]. The sample is mounted into a dilution refrigerator and cooled to a temperature of 50 mK. We extract the parameters of the qubit from the two-tone spectroscopy measurement shown in Fig. 1(c). From a numerical fit, we find $I_\mathrm{p} = 540\,\mathrm{nA}$, $\Delta = 4.3\,\mathrm{GHz}$ and $g = 87\,\mathrm{MHz}$.

---

[1] We gratefully acknowledge financial support by the German Research Foundation through SFB 631, the German Excellence Initiative through NIM, and the EU projects CCQED and PROMISCE.

[2] CSIC-Universidad de Zaragoza, Spain. D.Z. acknowledges financial support by ARAID

[3] IFF-CSIC, Madrid, Spain

[4] Universidad del País Vasco UPV/EHU and Ikerbasque, Spain. E.S. acknowledges financial support from PROMISCE, SOLID, the Basque Foundation for Science, Basque Government IT472-10, and Spanish MICINN FIS2009-12773-C02-01.

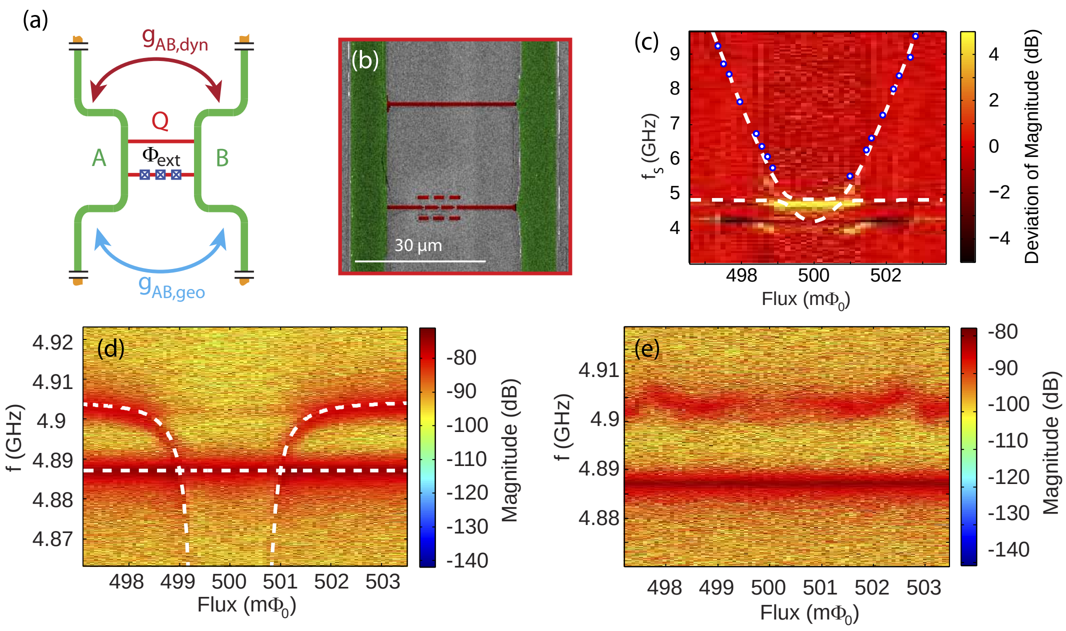

Figure 1: (a) Sketch of the coupling channels between the two resonators. The qubit (red) is placed between the two resonators (green). (b) False-color scanning electron micrograph of the qubit (red) fabricated between the two resonators (green lines) (c) Two-tone spectroscopy. White dashed lines: numerical fit. Colored dots: selected dip positions on the qubit hyperbola. (d) Flux dependence of the resonator transmission when the qubit is in the ground state. The white line shows the theoretical prediction based on the fit results from (c). Flux dependence of the resonator transmission when the qubit is saturated by a microwave drive tone to a mixed state.

Next we investigate the quantum switch properties by recording the flux-dependent transmission through one of the resonators. The result is shown in Fig. 1(d). We observe two modes: a flux-independent one at 4.887 GHz (lower mode) and a flux dependent one crossing this lower mode. The observation of crossings instead of anticrossings already indicates that this is the switch setting condition, where $g_{\text{geo}} + g_{\text{dyn}} = 0$. This conclusion is supported by the fact that at the crossing points, the transmission through the resonator rises by approximately a factor of two (data not shown). Finally, we confirm the switch operation by exciting the qubit to a saturated mixed state. In this case, as shown in Fig. 1(e), the crossings disappear because the magnitude and sign of the dynamical coupling depend on the qubit state. As a consequence, the two resonators are coupled in the whole flux range.

In summary, we built a superconducting quantum switch [6] consisting of two coplanar stripline resonators and a flux qubit. Spectroscopy experiments provide all relevant system parameters and clear evidence for tunable and switchable coupling between the two resonators.

We acknowledge fruitful discussions with H. Huebl, F. Wulschner, J. Goetz, L. Zhong, P. Eder, G. Romero, M. Mariantoni, C. Probst, K. Neumaier, and K. Uhlig.

References

[1] J. Clarke, and F. K. Wilhelm, Nature **453**, 1031 (2008).
[2] R. J. Schoelkopf, and S. M. Girvin, Nature **451**, 664 (2008).
[3] A. Wallraff, D. Schuster, A. Blais, L. Frunzio, R.-S. Huang, J. Majer, S. Kumar, S. Girvin, and R. Schoelkopf, Nature **431**, 162 (2004).
[4] M. A. Sillanpää, J. I. Park, and R. W. Simmonds, Nature **449**, 438 (2007).
[5] T. Niemczyk, F. Deppe, H. Huebl, E. P. Menzel, F. Hocke, M. J. Schwarz, J. J. Garcia-Ripoll, D. Zueco, T. Hummer, E. Solano, A. Marx, and R. Gross, Nat. Phys. **6**, 772 (2010).
[6] M. Mariantoni, F. Deppe, A. Marx, R. Gross, F. K. Wilhelm, and E. Solano, Phys. Rev. B **78**, 104508 (2008).
[7] T. Niemczyk, F. Deppe, M. Mariantoni, E. P. Menzel, E. Hoffmann, G. Wild, L. Eggenstein, A. Marx, and R. Gross, Supercond. Sci. Technol. **22**, 034009 (2009).

Magnetic-Field-Induced Dimensional Crossover in an Organic Metal

M. V. Kartsovnik, W. Biberacher [1]
P. D. Grigoriev [2]

Dimensional crossovers and their influence on transport properties and electronic states are a long standing and still controversial issue in the field of highly anisotropic correlated conductors, such as organic metals, high-T_c superconducting cuprates as well as pnictides, cobaltates, heterostructure superlattices, and intercalated compounds. Despite numerous predictions of a breakdown of the coherent interlayer charge transport due to impurity scattering, temperature or magnetic field, no convincing experimental evidence for this feature has been found so far. Moreover, it was shown that the interlayer coherence does persist at scattering rates [1] and temperatures [2] corresponding to energy scales much higher than the interlayer electron transfer energy $t_\perp$. On the other hand, it was recently suggested [3] that a magnetic field **B** applied perpendicular to conducting layers might considerably change the electron dynamics in a strongly anisotropic metal when the cyclotron frequency $\omega_c = eB/m_c$ (where e is the elementary charge and m_c the electron cyclotron mass) exceeds the interlayer hopping frequency $\tau^{-1} \sim t_\perp/\hbar$. Here, we present experimental data on the interlayer magnetoresistance $R_{zz}(B)$ of the layered organic metal α-(BEDT-TTF)$_2$KHg(SCN)$_4$ [4]. Our results confirm the theoretical predictions and provide clear evidence for a field-induced crossover into a new, so-called "weakly coherent" regime of the interlayer transport, significantly differing from the conventional three-dimensional (3D) coherent regime.

The experiment was performed on a single crystal of α-(BEDT-TTF)$_2$KHg(SCN)$_4$ at $T = 1.6\,\mathrm{K}$ at an applied pressure of 6 kbar and magnetic field up to 28 T applied perpendicular to the conducting molecular layers. The pressure was applied in order to avoid complications related to the charge-density-wave state characteristic of this compound at ambient pressure [5]. Fig. 1 shows the interlayer resistance as a function of $\sqrt{B}$. The dashed line represents the raw data with strong Shubnikov-de Haas (SdH) oscillations developing at $B > 12\,\mathrm{T}$. The black curve is the monotonic magnetoresistance background R^{b}_{zz}, obtained after filtering out the SdH oscillations. One can see that, in contrast to a conventional saturating behavior (the interlayer current is parallel to the field direction!), R^{b}_{zz} continuously grows with field. We interpret this growth in terms of the weakly coherent regime implying a B-dependent scattering rate, $1/\tau \propto \sqrt{B}$. The theory [3] predicts an approximately square-root dependence of the interlayer resistance in this case:

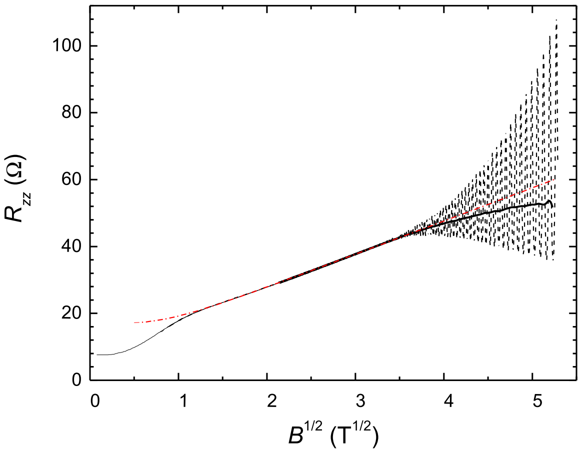

Figure 1: Interlayer resistance of α-(BEDT-TTF)$_2$KHg(SCN)$_4$: raw data (dashed line) and its nonoscillating component (solid line) plotted against $\sqrt{B}$. The red dashed-dotted line is a fit to the data by Eq. (1).

$$R^{\mathrm{b}}_{zz} \propto \frac{1}{\sigma^{\mathrm{b}}_{zz}(B)} \approx \frac{1}{\sigma_0}\left[(\alpha\omega_c\tau)^2 + 1\right]^{1/4}, \tag{1}$$

---

[1] The work was supported, in part, by EuroMagNET II under the EU contract 228043. The measurements in magnetic fields up to 28 T were carried out at the Laboratoire National des Champs Magnétiques Intenses, Grenoble, France.

[2] L. D. Landau Institute for Theoretical Physics, Rus. Acad. Sci., 142432 Chernogolovka, MD, Russia

where σ_0 and σ^{b}_{zz} are the zero-field and semiclassical field-dependent conductivities, respectively, and $\alpha \approx 2$ is a nonuniversal constant. The data in Fig. 1 shows a linear dependence on $\sqrt{B}$ in an extended field range, $1.5\,\mathrm{T} \lesssim B \lesssim 16\,\mathrm{T}$, in perfect agreement with Eq. (1) (cf. red line in Fig. 1), yielding an estimate for the zero-field scattering time of $\tau \approx 4.3\,\mathrm{ps}$.

The low-field data shows a deviation from the theoretical prediction because the strong-field criterion, $\omega_c\tau > 1$, is not fulfilled for this crystal at $B < 1.5\,\mathrm{T}$. Furthermore, the low-field interlayer magnetoconductivity is additionally contributed by a channel associated with a planar Fermi surface [4]. At fields above 16 T, the amplitude of the SdH oscillations becomes of the same order as the background component $R^{\mathrm{b}}_{zz}(B)$. This gives rise to sizable quantum corrections to the non-oscillating conductivity [6], leading to a deviation of the monotonic magnetoresistance from the semiclassical form given by Eq. (1). All in all, the observed behavior of $R^{\mathrm{b}}_{zz}(B)$ appears to be fully consistent with the predicted field-induced crossover of the interlayer charge transport to the weakly coherent regime.

Intuitively, the B-dependence of the scattering rate should also be reflected in the behavior of quantum SdH oscillations. Due to finite scattering, quantized Landau levels (LLs) acquire a finite width $\Gamma(B) = \hbar/2\tau(B)$, which determines the field dependence of the oscillation amplitude through the Dingle factor R_{D}. For a traditional Lorentzian broadening R_{D} is similar to the usual 3D form, $R_{\mathrm{D}} \approx \exp(-2\pi\Gamma/\hbar\omega_c)$. It can be determined from the so-called Dingle plot of the oscillation amplitude linearized in the coordinates shown in Fig. 2(a). However, our data strongly deviates from the linear shape at $B > 14\,\mathrm{T}$. Even worse is the linear fit to the $1/\sqrt{B}$ dependence [see Fig. 2(b)] naively expected for $\Gamma \propto \sqrt{B}$ in the weakly coherent regime. On the other hand, the high-field data is perfectly linear in the $1/B^2$ scale, as shown in Fig. 2(c). As explained in Ref. [4], this behavior is a signature of Gaussian-shaped LLs with a constant width Γ determined by long-range crystal imperfections such as mosaicity or internal strains. This regime sets in when the LL spacing becomes larger than both Γ and $t_\perp$, i.e. it is associated with an effective reduction of dimensionality.

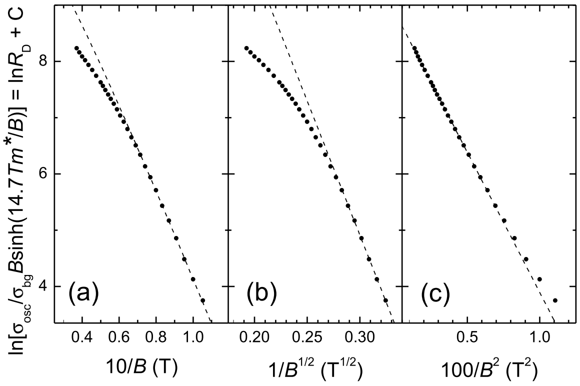

Figure 2: Dingle plots for the field-dependent amplitude of the SdH oscillations, assuming a Lorentzian shape of LLs with a constant width (a) and with $\Gamma \propto \sqrt{B}$ (b) and a Gaussian shape of LLs with $\Gamma = \mathrm{const}$. Dashed lines are fits of the corresponding models to the data at $B < 12\,\mathrm{T}$ (a), (b) and at $B > 12\,\mathrm{T}$ (c), see text.

In summary, our data on the magnetoresistance of a strongly anisotropic layered organic metal α-(BEDT-TTF)$_2$KHg(SCN)$_4$ reveal a novel magnetic field driven dimensional crossover from the conventional 3D coherent to a quasi-two-dimensional weakly coherent charge transport regime.

References

[1] M. V. Kartsovnik, D. Andres, S. V. Simonov, W. Biberacher, I. Sheikin, N. D. Kushch, and H. Mueller, Phys. Rev. Lett **96**, 166601 (2006).

[2] J. Singleton, P. A. Goddard, A. Ardavan, A. I. Coldea, S. J. Blundell, R. D. McDonald, S. Tozer, and J. A. Schlueter, Phys. Rev. Lett. **99**, 027004 (2007).

[3] P. D. Grigoriev, Phys. Rev. B **83**, 245129 (2011).

[4] P. D. Grigoriev, M. V. Kartsovnik, and W. Biberacher, Phys. Rev. B **86**, 165125 (2012).

[5] M. V. Kartsovnik. *The Physics of Organic Superconductors and Conductors*, chap. 8, Layered organic conductors in strong magnetic fields, 185 (Springer Verlag Berlin Heidelberg, 2008).

[6] T. Champel, and V. P. Mineev, Phys. Rev. B **66**, 195111 (2002).

Fermiology and Pairing in Iron-based Superconductors

F. Kretzschmar, B. Muschler, T. Böhm, R. Hackl [1]
Hai-Hu Wen,[2] *V. Tsurkan,*[3,4] *J. Deisenhofer, A. Loidl*[5]

In conventional superconductors the strong coupling theory of Eliashberg made connection to real materials [1] thus augmenting the idealized BCS model. McMillan and Rowell showed how Eliashberg's coupling function $\alpha^2F(\omega)$ can be derived from the tunneling spectra [2]. In materials as diverse as Pb or Nb_3Sn the comparison with the phonon density of states $F(\omega)$, as measured with neutron scattering, demonstrates how the lattice provides a potential for Cooper pairing, $V_{\mathbf{k},\mathbf{k}'}$, which depends only weakly on momentum $\mathbf{k}$. Consequently, the energy gap in the electronic excitation spectrum $\Delta_\mathbf{k}$ is essentially isotropic what, in turn, is a condition for prominent structures to be observable in tunneling and other spectroscopies at $\hbar\omega_\mathbf{q} + \Delta$ with $\hbar\omega_\mathbf{q}$ denoting the maxima in $F(\omega)$. In unconventional systems such as the cuprates, some heavy fermion compounds or the iron-based superconductors, experimental information on the interaction processes is more complicated to obtain. This is because the gaps $\Delta_\mathbf{k}$ are strongly anisotropic hampering the derivation of the pairing potential. Therefore, evidence for the type of pairing is usually indirect [3–7] and can hardly be quantified even if the theoretical framework is elaborate. The iron-based superconductors [8, 9] open up new vistas. Since the hole- and electron-like Fermi surfaces can be tuned by carrier doping or atomic substitution [see Fig. 1], they are a laboratory for studying the pairing interaction in anisotropic multiband systems.

Most of the pairing interaction in the Fe-based systems is believed to originate from unconventional channels because the electron-phonon coupling is considered insufficient for transition temperature T_c in the 50 K range [10]. Orbital [11] and spin [12] fluctuations are possible candidates for unconventional pairing mechanisms. Spin-fluctuation mediated pairing as opposed to orbital fluctuations is repulsive and thus requires a sign change of the superconducting order parameter between the participating Fermi surfaces. As a result of the complex Fermi surface topology of iron-based superconductors, there are several possible pairing channels. The most prominent scenarios are (i) interband pairing between the hole band encircling the Γ point in the center of the Brillouin zone (BZ) and the electron bands around the X points on the principal axes of the (1 Fe) BZ mediated by orbital fluctuations [11]. This coupling mechanism entails isotropic gaps with the same phase on all bands (s_{++}). (ii) interband pairing between the hole band and electron bands mediated by spin fluctuations [12]. Here, the gaps are also isotropic but have a phase difference of π on the respective bands. The resulting state has $s_\pm$ symmetry as shown Fig. 1(d) still maintaining the full fourfold lattice symmetry. (iii) spin-mediated interband pairing between the electron bands alone. Now, due to the repulsive character of the interaction, the superconducting state has $d_{x^2-y^2}$ symmetry which breaks the C_4 rotational symmetry as shown in Fig. 1(f). Lee and coworkers raised the question as to the proper pairing symmetry if the pairing potentials V_s and V_d [see Fig.1(c)] are approximately frustrated [13] as indicated in Fig. 1(e).

---

[1] This work is supported by the German Research Foundation via the Priority Program SPP 1458 and the Collaborative Research Centre/Transregio TRR 80.

[2] National Laboratory of Solid State Microstructures and Department of Physics, Nanjing University, Nanjing 210093, China. Hai-Hu Wen acknowledges financial support by the NSF of China and the Ministry of Science and Technology of China (973 projects: 2011CBA00102 and 2012CB821403).

[3] Experimental Physics 5, Center for Electronic Correlations and Magnetism, Institute of Physics, University of Augsburg, 86159 Augsburg, Germany

[4] Institute of Applied Physics, Academy of Sciences of Moldova, MD-2028, Chisinau, Republic of Moldova.

[5] Experimental Physics 5, Center for Electronic Correlations and Magnetism, Institute of Physics, University of Augsburg, 86159 Augsburg, Germany.

In the iron-based superconductors, the conditions for spin-fluctuation mediated pairing can be changed by the variation of nesting conditions between the Fermi surfaces [Fig. 1(c)-(e)]. For instance, according to band structure calculations and photoemission experiments the nesting conditions between the hole and electron surfaces are optimal in $Ba_{0.6}K_{0.4}Fe_2As_2$ and, in a spin-fluctuation scenario, favor an $s_\pm$ state. In $Rb_{0.8}Fe_{1.6}Se_2$ there is no or a marginal hole band, and the coupling is supposed to come from the interaction between the electron bands leading to a $d_{x^2-y^2}$ state. $Ba(Fe_{0.939}Co_{0.061})_2As_2$ is between the two extremes and, as mentioned above, the s and the d channel may be frustrated [13].

The competition between $s_\pm$ and $d_{x^2-y^2}$ symmetry can be scrutinized with Electronic Raman Scattering (ERS). ERS is sensitive to both the quasi-particles and the condensate. If a Cooper pair in the condensate is broken by a photon the two electrons are being separated energetically but not in space. The separation by 2Δ quenches the interaction in the dominant pairing channel at the origin of superconductivity. Now the anisotropic contributions to $V_{\mathbf{k},\mathbf{k}'}$ become effective and lead to a δ-like bound state at $\hbar\Omega_b$ below the gap edge similar to the formation of an exciton in a semiconductor [19] as shown schematically in Fig. 3(a). Hence, if narrow excitonic Bardasis-Schrieffer modes are observed one can conclude that $V_{\mathbf{k},\mathbf{k}'}$ is anisotropic. Once again in analogy to semiconductors, the difference $E_b = 2\Delta - \hbar\Omega_b$ encodes the coupling strength in the subdominant channel. In the weak-coupling limit one finds $E_b/2\Delta \simeq (V_d/V_s)^2$ with V_s the dominant channel [20]. The appearance and the properties of these modes in Fe-based superconductors with isotropic and anisotropic gaps is predicted by theory [18], and the symmetry of the modes is that of the subdominant contributions to $V_{\mathbf{k},\mathbf{k}'}$.

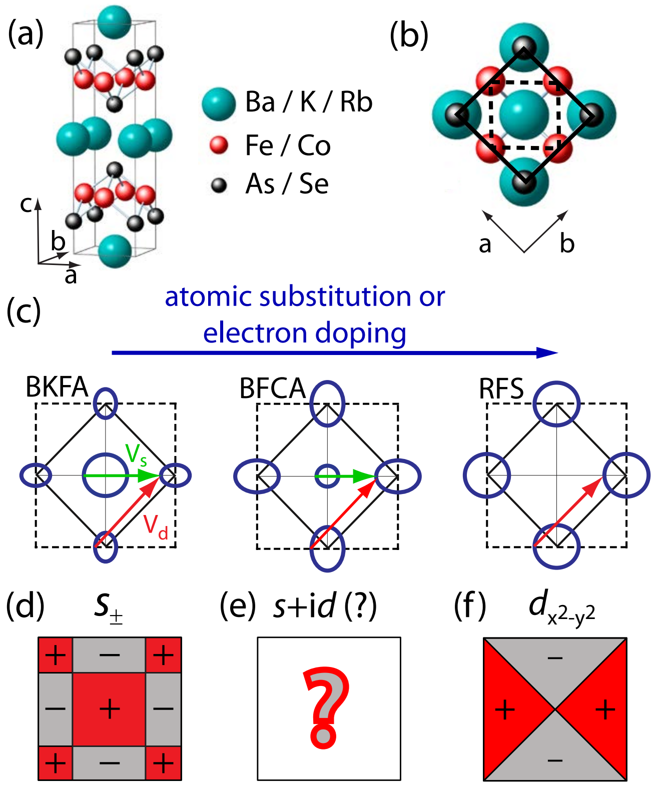

Figure 1: Crystal and reciprocal lattices of iron-based superconductors. (a) FeAs/Se layers (small spheres) and (earth) alkali metals (big spheres). (b) 1 Fe (dashes) and 2 Fe unit cell (full line). (c) First Brillouin zones (BZ, dashes for the 1 Fe cell) with schematic Fermi surfaces of $Ba_{0.6}K_{0.4}Fe_2As_2$ [14], $Ba(Fe_{0.939}Co_{0.061})_2As_2$ [15] and $Rb_{0.8}Fe_{1.6}Se_2$ [16, 17]. Also indicated are the two dominant interaction potentials V_s and V_d. (d) For $V_s > V_d$ the pairing state is predicted to have $s_\pm$ symmetry for which the phase of the gap on the hole and electron bands differs by π [12]. (e) Substitution or carrier doping change the FSs and can drive the system to a state where $s_\pm$ and $d_{x^2-y^2}$ pairing interactions are nearly frustrated [13]. (f) Here, $V_d > V_s$ and $d_{x^2-y^2}$ symmetry is favored [13, 18].

In Fig. 2 we show our ERS results on $Ba_{0.6}K_{0.4}Fe_2As_2$. For the symmetry assignment we use the 1 Fe unit cell since all bands at the Fermi surface derive from Fe orbitals. We observe superconductivity-induced features in all symmetries. Below a symmetry independent threshold of approximately $25\,\mathrm{cm}^{-1}$ the response is very small and nearly energy independent. Although the intensity is not exactly zero it is safe to conclude that there is a full gap on all bands having a magnitude of at least $0.9\,k_BT_c$. The excess intensity in the range $130 < \Omega < 300\,\mathrm{cm}^{-1}$ originates from either pair-breaking [Fig. 2(a) and (b)] or from the predicted collective modes [Fig. 2(c)]. The spectral features in A_{1g} and B_{2g} symmetry [Fig. 2(a) and (b)] are broad and asymmetric and originate from the breaking of Cooper pairs, whereas the peaks in B_{1g} symmetry [Fig. 2(c)] are rather sharp and symmetric as expected for the Bardasis-Schrieffer collective modes. It is not only the line shape of these modes but also the reduced intensity above the modes which supports the interpretation: Although one would expect intensity above the modes for the finite gap on the electron bands there is almost no pair-breaking feature since the spectral weight is transferred into the collective modes. The important secondary structures of the spectra between the minimal and the maximal gaps are better resolved in the difference spectra in panel (d) of Fig. 2. In this way, the contributions from phonons are by and large subtracted out. Only the Fe vibration at 215 cm^{-1} in the B_{2g} spectrum (B_{1g} phonon in the crystallographic cell) has an anomalous intensity for its proximity to the gap edge and is truncated. Both the A_{1g} and B_{2g} spectra have edge-like onsets above approximately 150 cm^{-1} before reaching the maxima and decaying slowly. In addition, in either case there are shoulders in the range of 80 cm^{-1} which originate from anisotropies on individual bands and from gaps having different magnitudes on individual bands.

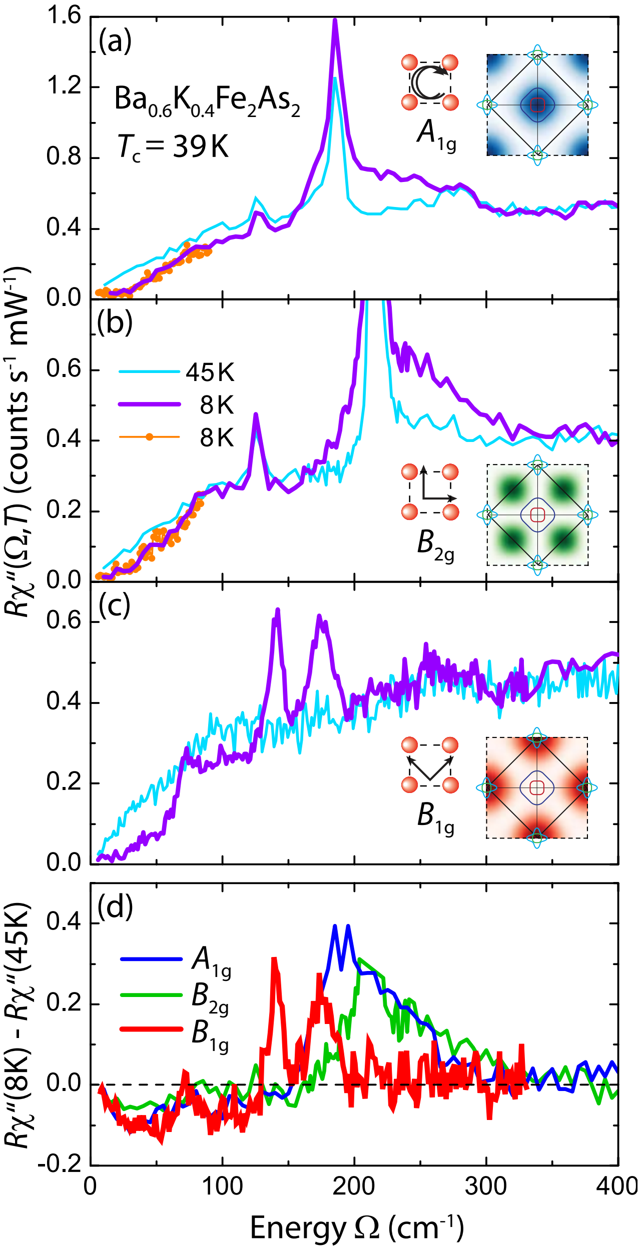

Figure 2: Normal and superconducting Raman spectra of Ba$_{0.6}$K$_{0.4}$Fe$_2$As$_2$ at temperatures as indicated. The spectra plotted with full lines in panel (a) and (b) are measured with a resolution of 6.5 cm^{-1} whereas the spectra in panel (c) and the spectra displayed with orange points are measured with a resolution of 4.7 cm^{-1}. The insets show the correspondence between light polarizations and sensitivities in momentum space for the 1 Fe unit cell. (a)-(c) Spectra in A_{1g}, B_{2g}, and B_{1g} symmetries. (d) Difference between superconducting and normal-state spectra. In B_{2g} symmetry (green), the phonon at 215 cm^{-1} is truncated.

The comparison of the spectra in A_{1g} and B_{2g} symmetry and the positions of the B_{1g} collective excitations allow us to derive a consistent scenario for the variation of the gaps on the individual bands as shown in Fig. 3(b). All excitons appear in B_{1g} symmetry and indicate that the subdominant channel originates from the interaction between the electron bands and has $d_{x^2-y^2}$ symmetry. Consequently, the dominant channel driving superconductivity has $s_\pm$ symmetry and results from the interaction between the electron and hole bands. The energies E_b [see Fig. 2(d)] indicate that $V_d \simeq 0.5V_s$. A detailed analysis of the data and a derivation of the gap distribution in Ba$_{0.6}$K$_{0.4}$Fe$_2$As$_2$ along with the results in Ba(Fe$_{1-x}$Co$_x$)$_2$As$_2$ [21, 22] and Rb$_{0.8}$Fe$_{1.6}$Se$_2$ [23] reveals a continuous change of the pairing hierarchy. Rb$_{0.8}$Fe$_{1.6}$Se$_2$ is an end point at which the hole bands are negligibly small or absent. The missing A_{1g} and B_{2g} gap features [23, 24] are compatible with this Fermiology.

In a spin fluctuation scenario, V_s vanishes, and V_d is the only surviving interaction. The resulting ground state is expected to be node-less d-wave since the gap nodes are off the Fermi surface as shown schematically in Fig. 1(f). The clean gap observed in the B_{1g} spectra of $Rb_{0.8}Fe_{1.6}Se_2$ is compatible with this scenario but inconclusive since a clean gap can also result from intraband electron-phonon coupling, for instance. Only with the results in the other compounds having a higher hole concentration and with the hierarchy of pairing states, as pinned down via the Bardasis Schrieffer modes, one can conclude that the Fermi surface plays a major role in determining the pairing interaction.

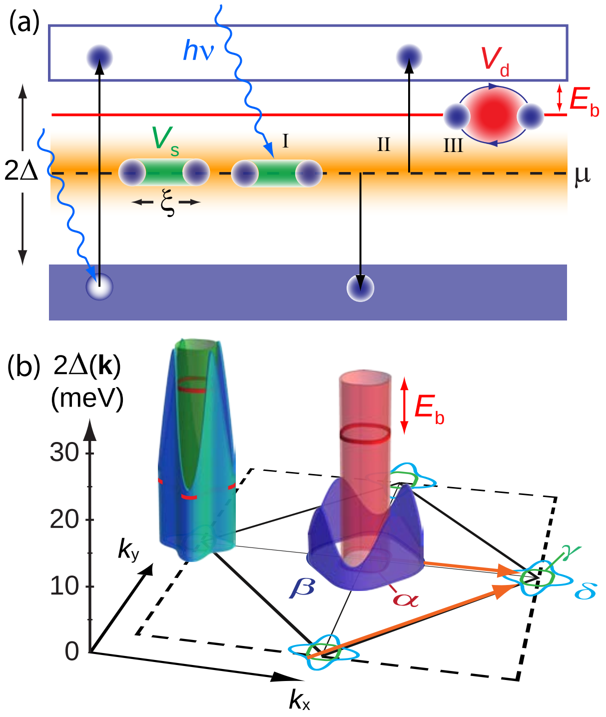

Figure 3: Energy gaps and excitons in superconductors. (a) Mechanism for Bardasis-Schrieffer excitonic modes. (b) Most probable scenario for the anisotropy of the energy gap in $Ba_{0.6}K_{0.4}Fe_2As_2$ as derived from Fig. 2. The energy of the bound state E_b (red line) is largest on the α band.

In conclusion, the synopsis of the light scattering results in a series of Fe-based compounds reveals a systematic dependence of the superconducting properties on the Fermi surface topology. In particular, one obtains an idea of how the pairing potential $V_{\mathbf{k},\mathbf{k}'}$ depends on momentum and on the Fermiology. This makes the case for spin fluctuation mediated Cooper pairing. Beyond that the result show more generally how light scattering may provide access to the pairing interaction in anisotropic superconductors thus supplementing the Eliashberg approach.

References

[1] G. M. Eliashberg, Sov. Phys. JETP **11**, 696 (1960).
[2] W. L. McMillan, and J. M. Rowell, Phys. Rev. Lett. **14**, 108 (1965).
[3] T. Dahm, V. Hinkov, S. V. Borisenko, A. A. Kordyuk, V. B. Zabolotnyy, J. Fink, B. Buchner, D. J. Scalapino, W. Hanke, and B. Keimer, Nat. Phys. **5**, 217 (2009).
[4] A. D. Christianson, E. A. Goremychkin, R. Osborn, S. Rosenkranz, M. D. Lumsden, C. D. Malliakas, I. S. Todorov, H. Claus, D. Y. Chung, M. G. Kanatzidis, R. I. Bewley, and T. Guidi, Nature **456**, 930 (2008).
[5] S. Caprara, C. Di Castro, B. Muschler, W. Prestel, R. Hackl, M. Lambacher, A. Erb, S. Komiya, Y. Ando, and M. Grilli, Phys. Rev. B **84**, 054508 (2011).
[6] J. T. Park, G. Friemel, Y. Li, J.-H. Kim, V. Tsurkan, J. Deisenhofer, H.-A. Krug von Nidda, A. Loidl, A. Ivanov, B. Keimer, and D. S. Inosov, Phys. Rev. Lett. **107**, 177005 (2011).
[7] W. Li, H. Ding, P. Deng, K. Chang, C. Song, K. He, L. Wang, X. Ma, J.-P. Hu, X. Chen, and Q.-K. Xue, Nat. Phys. **8**, 126 (2012).
[8] Y. Kamihara, T. Watanabe, M. Hirano, and H. Hosono, J. Am. Chem. Soc. **130**, 3296 (2008).
[9] M. Rotter, M. Tegel, and D. Johrendt, Phys. Rev. Lett. **101**, 107006 (2008).
[10] L. Boeri, O. V. Dolgov, and A. A. Golubov, Phys. Rev. Lett. **101**, 026403 (2008).
[11] H. Kontani, and S. Onari, Phys. Rev. Lett. **104**, 157001 (2010).
[12] I. I. Mazin, D. J. Singh, M. D. Johannes, and M. H. Du, Phys. Rev. Lett. **101**, 057003 (2008).
[13] W.-C. Lee, S.-C. Zhang, and C. Wu, Phys. Rev. Lett. **102**, 217002 (2009).
[14] H. Ding, P. Richard, K. Nakayama, K. Sugawara, T. Arakane, Y. Sekiba, A. Takayama, S. Souma, T. Sato, T. Takahashi, Z. Wang, X. Dai, Z. Fang, G. F. Chen, J. L. Luo, and N. L. Wang, EPL **83**, 47001 (2008).
[15] K. Terashima, Y. Sekiba, J. H. Bowen, K. Nakayama, T. Kawahara, T. Sato, P. Richard, Y.-M. Xu, L. J. Li, G. H. Cao, Z.-A. Xu, H. Ding, and T. Takahashi, Proceed. Nat. Acad. Sci. **106**, 7330 (2009).

[16] Y. Zhang, L. X. Yang, M. Xu, Z. R. Ye, F. Chen, C. He, H. C. Xu, J. Jiang, B. P. Xie, J. J. Ying, X. F. Wang, X. H. Chen, J. P. Hu, M. Matsunami, S. Kimura, and D. L. Feng, Nat. Mater. **10**, 273 (2011).

[17] T. Qian, X.-P. Wang, W.-C. Jin, P. Zhang, P. Richard, G. Xu, X. Dai, Z. Fang, J.-G. Guo, X.-L. Chen, and H. Ding, Phys. Rev. Lett. **106**, 187001 (2011).

[18] D. J. Scalapino, and T. P. Devereaux, Phys. Rev. B **80**, 140512 (2009).

[19] A. Bardasis, and J. R. Schrieffer, Phys. Rev. **121**, 1050 (1961).

[20] H. Monien, and A. Zawadowski, Phys. Rev. B **41**, 8798 (1990).

[21] B. Muschler, W. Prestel, R. Hackl, T. P. Devereaux, J. G. Analytis, J.-H. Chu, and I. R. Fisher, Phys. Rev. B **80**, 180510 (2009).

[22] L. Chauvière, Y. Gallais, M. Cazayous, M. A. Méasson, A. Sacuto, D. Colson, and A. Forget, Phys. Rev. B **82**, 180521 (2010).

[23] T. Böhm. *Raman-Streuung an unkonventionellen Supraleitern*. Diplomarbeit, Technische Universität München (2012).

[24] F. Kretzschmar, B. Muschler, T. Böhm, A. Baum, R. Hackl, H.-H. Wen, V. Tsurkan, J. Deisenhofer, and A. Loidl. Evidence of competing s- and d-wave pairing channels in iron-based superconductors. `arXiv:1208.5006` (2012).

Graphite Oxide Structure and Acidity

A. Lerf
P. Feicht, J. Breu [1]
T. Szabó, I. Dékány [2]

Graphite oxide (GO) has been prepared in 1860 by Brodie [1]. Despite a lot of experimental work GO has received great attention only recently as a precursor of functionalized graphene layers (excellently reviewed by Ruoff *et al.* [2, 3]). Considering the wide range of potential applications (as an electrode in lithium cells, e.g. [5], as supercapacitors, as nanocomposites [6] and as a catalyst, e.g. [7]) precise knowledge of the structure of GO is essential. In 1998 Lerf *et al.* [4] proposed a new structural model based on solid-state nuclear magnetic resonance experiments, assuming the existence of epoxy groups (as proposed by Hofmann *et al.* [8]) instead of ether functions, hydroxyl groups and unchanged aromatic regions (one possible distribution of these functional groups on the graphite carbon grid is shown in Fig. 1). The carbon layers are therefore slightly bent and warped in regions containing sp^3 orbitals, but flat in the region bonded with sp^2 orbitals. Modifications of this general model take into considerations also isolated and conjugated double bonds. This model is now well confirmed by molecular simulation [9] and chemical modification of the oxygen functions [3].

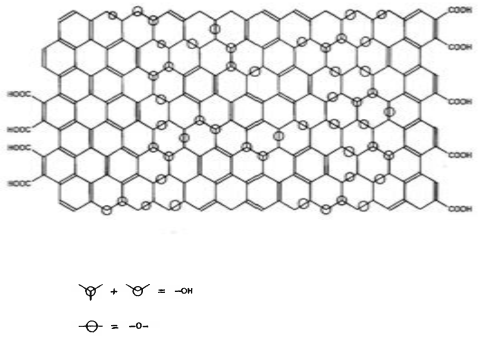

Figure 1: The structural model of graphite oxide as proposed by Lerf et al. [4].

In this structural model the tendency to form stable, negatively charged colloidal suspensions and the high cation exchange capacity cannot be explained easily. If one follows the argumentation of Hofmann, Boehm and coworkers [10–12] the degree of deprotonation depends on the base which is used for titration: 1 acidic group per 8 C atoms should result by applying NaOH as the base and 1 acidic group per ~ 5 C atoms in the case of sodium ethanolate ($NaOC_2H_5$). The resulting acidity is so large that the negative charge resulting from full deprotonation of the OH functions is in the order of that of low charged montmorillonites [12].

However, the carboxyl groups at the periphery of the graphene sheets which are considered to be present in all published structural models are not enough to explain the high acidity [13]. These authors discussed additional carboxyl groups located at the border of internal wholes in partially broken graphene sheets. Even this is not enough. Although these CO_2^--groups have been detected in most recent ^{13}C MAS-NMR spectra, their concentration is very low ($< 5\%$).

Clauss *et al.* brought into discussion the presence of more acidic groups like enols or phenols with pK_a values of $8 - 10$ [12]. However, enols are very unstable and transform easily into ketons or aldehyds. For this functional unit a new signal at about 90 – 100 ppm should appear in the ^{13}C NMR spectra. Most recent ^{13}C NMR spectra with higher resolution show a signal at 102 ppm but also an additional one at 190 ppm, both of very low intensity [14]. A combination of signals 110 ppm/190 ppm could be indicative for keto-enol tautomerism as observed in acetylacetone or dimedone. It cannot be ruled out that such sort of arrangements exist at the external border of the graphene sheets. To explain the high acidity of GO these groups should be spread over the whole graphene sheets. However, this would be accompanied with a partial destruction of the carbon grid [12].

---

[1] Institut für Anorganische Chemie I, Universität Bayreuth, Universitätsstraße 31, Bayreuth, Germany.
[2] Department of Physical Chemistry and Materials Sciences, University of Szeged, Szeged, Hungary.

Phenols (characterized by ^{13}C chemical shifts at $\sim$ 150 ppm and 110 ppm) cannot be detected in as-prepared GO, but can indeed be formed to a considerable extent under special experimental conditions (heat treatment in vacuum, reaction with iodide) [4]. As in the case of the keto-enol system the formation of phenols on the graphene sheets is unambiguously connected with a breaking of C-C bonds. According to our own experiments we have no evidence that just base treatment at room temperature produces the quantity of these peculiar OH functions required to explain the high acidity of GO (see WMI Annual Report 2009), and, if so, we would expect an irreversible increase of the acidity which has never been observed [15].

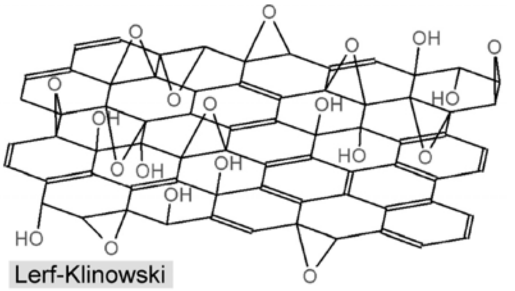

Figure 2: The modified structural model of graphite oxide. Figure taken from [16].

On the other hand isolated tertiary alcohols (OH functions on sp^3 carbons directly connected to three other sp^3 carbons) show pK$_a$ values (these are the negative decadic logarithm of the acidity constants) larger than 18 far out of the region of interest. To solve the puzzle one should have in mind first that the OH functions in GO are not isolated: There can be other OH functions on the next nearest carbons. In addition the OH functions can be located near to aromatic rings, isolated double bonds or the epoxide functions. Secondly, one can rethink the distribution and possible correlations of the functional groups with respect to the possibility of enhancing the acidity by cooperative interactions. An extreme modification of our previous structural model shows a grid of carbon hexagons carrying one epoxide function, one isolated double bond and two OH functions in a completely regular distribution [17]. A more random distribution of the functional groups is shown in Fig. 2.

In these new arrangements one can recognize coupled functionalities, for example allylic alcohols or vicinal diols with the OH in cis positions. This is not in conflict with the ^{13}C NMR data: so it is not possible in solid state NMR to distinguish aromatic from isolated C=C double bonds; in addition the chemical shift of the allylic OH (1-en-3-ol) is also around 60 ppm as for epoxides; the chemical shifts of the alcohol functions with 70 ppm is found more frequently for carbons in adjacent vicinal diols than for carbons carrying OH groups in molecular tertiary alcohols.

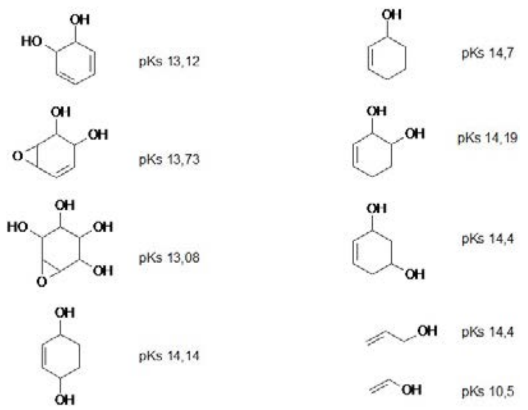

Figure 3: Typical model compounds for functional group arrangements and the theoretical pK$_a$ values calculated via science finder.

To find out whether these combinations of functional groups lead to a decrease in the pK$_a$ values we calculated them for various arrangements of functional groups in possible organic model compounds via science finder. A selection of model compounds with the theoretical pK$_a$ values is shown in Fig. 3. Whenever these theoretical values can be compared with experimentally determined pK$_a$ values the agreement is fairly good, showing the high quality of the calculation procedure reached in the meantime. The most functionalized cyclohexane model compounds carrying varying numbers of double bonds, epoxide and adjacent OH groups (see Fig. 3) do not give pK$_a$ values smaller than 13, and even highly hydroxylated carbohydrates show pK$_a$ $>$ 12. These values are significantly lower than pK$_a$ values of tertiary alcohols like tertiary butanol. This is the right tendency towards higher acidities, but these values are still too high. To explain the titration curves one would expect pK_a values between 7 and 10. Thus, additional cooperative effects must exist, to explain the titration curves of GO. Such cooperative effects have been observed for a low molecular aliphatic poly-alcohol dissolved in an aprotic solvent like dimethylsulfoxide. Under these conditions the alcohol shows a strong increase in acidity due to the stabilization of the alcoholate function (R-C-O^-) by an intramolecular hydrogen bond network [18]. It is possible that such a hydrogen bond network in the confined space of GO produces a similar effect. Support of this idea is the higher acidity of water in the interlayer space of clay minerals or the high acidity of surface silanol groups on SiO_2 nanoparticles [19] if compared with the very low acidity of silicic acid.

References

[1] B. Brodie, Ann. Chim. Phys. **59**, 466 (1860).
[2] S. Park, and R. S. Ruoff, Nature Nanotechn. **4**, 217 (2009).
[3] D. D. Dreyer, S. Park, C. W. Bielawski, and R. S. Ruoff, Chem. Soc. Rev. **39**, 228 (2010).
[4] A. Lerf, H. He, M. Forster, and J. Klinowski, J. Phys. Chem. **102**, 4477 (1998).
[5] T. Cassagneau, and J. H. Fendler, Adv. Mater. **10**, 877–881 (1998).
[6] T. Kuilla, S. Bhadra, D. Yao, N. H. Kim, S. Bose, and J. H. Lee, Prog. Polym. Sci. **35**, 1350 (2010).
[7] J. Pyun, Angew. Chem. **123**, 46 (2011).
[8] U. Hofmann, A. Frenzel, and E. Csalan, Lieb. Ann. Chem. **510**, 1 (1934).
[9] J. Paci, T. Belytschko, and G. E. Schatz, J. Phys. Chem. C **111**, 18099 (2007).
[10] U. Hofmann, and R. Holst, Ber. Dtsch. Chem. Ges. **72**, 754 (1939).
[11] W. Scholz, and H. P. Boehm, Z. Anorg. Allg. Chem. **369**, 327 (1969).
[12] A. Clauss, R. Plass, H. P. Boehm, and U. Hofmann, Z. Anorg. Allg. Chem. **291**, 205 (1957).
[13] U. Hofmann, and E. Koenig, Z. Anorg. Allg. Chem. **234**, 311 (1937).
[14] W. Gao, L. B. Alemany, L. Ci, and P. M. Ajayan, Nature Chem. **1**, 403 (2009).
[15] T. Szabó, E. Tombácz, E. Illés, and I. Dékány, Carbon **44**, 537 (1996).
[16] T. Szabó, O. Berkesi, P. Forgó, K. Josepovits, Y. Sanakis, D. Petridis, and I. Dékány, Chem. Mater. **18**, 2740 (2006).
[17] A. Buchsteiner, A. Lerf, and J. Pieper, J. Phys. Chem. B **110**, 22328 (2006).
[18] A. Shokri, A. Abedin, and S. K. A. Fattah and, J. Amer. Chem. Soc. **134**, 10646 (2012).
[19] M. Borkovec, Langmuir **13**, 2608 (1997).

High Cooperativity in a Coupled Microwave Resonator - Ferrimagnetic Insulator System

J. Lotze, C. W. Zollitsch, F. Hocke, M. Greifenstein, A. Marx, R. Gross, S. T. B. Goennenwein, H. Huebl [1]

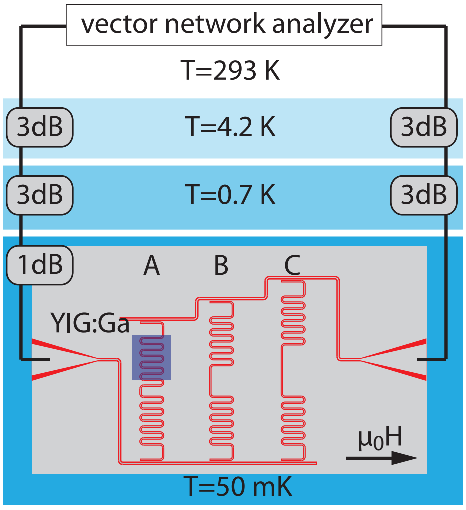

Figure 1: Schematic of the experimental setup. The YIG:Ga is cemented onto the microwave resonator A. Microwave transmission is measured as a function of the applied magnetic field at millikelvin temperatures.

Hybrid quantum systems are in the focus of quantum physics research, because they are envisaged to provide a solution for quantum information processing and storage. The ingredients of these hybrid systems include: (i) qubits, used for information processing, (ii) a bus system, used for information processing and for mediating the information between several subsystems of the hybrid, and (iii) a quantum memory. Using this strategy allows one to combine the best of all worlds, e.g. superconducting qubits for fast information processing, microwave resonators as efficient quantum bus and atom clouds or spin ensembles well known for their long coherence times as memory units. Important for the realization is the strong interaction between all the constituents of the hybrid system, making the coupling rates larger than the loss rates of the subsystems. Recently, the coupling of electron spins to superconducting microwave resonators has been studied [1, 2]. Although the coupling of a single electron spin to a coplanar microwave resonator is typically only in the order of 10 Hz, the use of a spin ensemble allows to achieve the strong coupling condition, due to the enhanced collective coupling strength $g_{\text{eff}} = g\sqrt{N}$. Here, N is the number of spins and g is the coupling of a single spin to the resonator mode. In strong coupling regime, g_{eff} exceeds both the loss rate of the resonator κ and that of the spin system γ, allowing for coherent information transfer with negligible loss of information. For practical systems, coupling rates of 10 MHz have to be achieved, and therefore about 10^{12} spins are required to reach the strong coupling regime. Complementary to using paramagnetic, uncoupled spin systems, the use of systems of exchange-coupled spin systems like ferromagnets has been proposed [3]. The most notable advantage of exchange coupled systems is their much higher spin density, making either an even stronger coupling possible, or allowing a significant reduction of the system size at the same coupling strength.

We have investigated the coupling between a superconducting niobium coplanar waveguide resonator and the Ga-doped ferrimagnet Yttrium Iron Garnet (YIG:Ga) [4]. Several superconducting coplanar waveguide resonator structures were patterned on a silicon substrate using optical lithography and reactive ion etching. A $2 \times 0.5 \times 0.7\,\text{mm}^3$ piece of YIG:Ga was cemented onto the resonator A with the highest resonance frequency of 5.90 GHz (cf. Fig. 1). From the sample overlap with the resonator magnetic field, the number of spins interacting with the microwave magnetic field can be estimated to 4.5×10^{16}. The resonator was then put into a dilution cryostat. The microwave transmission $|S21|^2$ was measured with a vector network analyzer at 50 mK as a function of frequency and a static magnetic field applied in the plane of the chip.

---

[1] This work is supported by the German Research Foundation via the Collaborative Research Centre 631 and the German Excellence Initiative via the Nannosystems Initiative Munich (NIM).

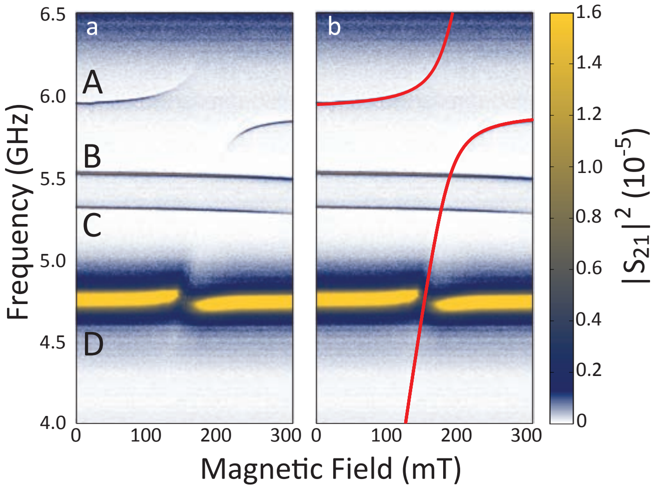

Figure 2: (a) Transmission spectrum of the YIG:Ga-microwave resonator system measured at $T = 50\,\mathrm{mK}$ as a function of the magnetic field. Resonator A shows a large avoided crossing with the spin resonance line at $B = 170\,\mathrm{mT}$. (b) Fit to the coupled harmonic oscillator model.

The transmission spectrum [see Fig. 2(a)] at $B = 0\,\mathrm{T}$ shows four transmission peaks. Three of them (A,B,C) belong to the superconducting resonators with frequencies of $f_A = 5.90\,\mathrm{GHz}$, $f_B = 5.53\,\mathrm{GHz}$, and $f_C = 5.30\,\mathrm{GHz}$. The fourth transmission peak (D) is due to a parasitic mode of the sample box. Resonators B and C show only a weak magnetic field dependence, since they do not interact with the spins in the YIG:Ga sample. Conversely, the resonator A and the box mode D couple to the spins. This interaction can be understood in terms of a model of two coupled harmonic oscillators. The first one, the microwave resonator, oscillates at a constant frequency ω_r, while the oscillation frequency of the spin system ω_FMR can be tuned with the applied magnetic field. At the degeneracy point, an avoided crossing is observed. Using a two-level model, we obtain the dispersion of the resonance frequencies as $\omega_{1,2} = \omega_r - \frac{\Delta}{2} \pm \frac{1}{2}\sqrt{\Delta^2 + 4g_\mathrm{eff}^2}$, where $\Delta = \omega_\mathrm{r} - \omega_\mathrm{FMR} = g_S \mu_\mathrm{B}(B - B_\mathrm{FMR})/\hbar$ is the field dependent detuning. Fitting this model to the resonance positions [see Fig. 2(b)] yields an effective coupling constant of $g_\mathrm{eff}/2\pi = 450\,\mathrm{MHz}$, which is compatible with our estimation of a single spin coupling of $g = 5\,\mathrm{Hz}$ and a number of spins of $N = 4 \times 10^{16}$ to within a factor of two. To verify that the strong coupling limit is reached, this has to be compared to the loss rates κ and γ. While the loss rate of the resonator can be easily extracted by fitting a Lorentzian to the resonator transmission line when the magnetic field is set to a value outside the avoided crossing, extracting the spin relaxation rate requires us to analyze the evolution of the observed resonator linewidth in the magnetic field range of the avoided crossing. This evolution of the linewidth with respect to the magnetic field can be understood in terms of the input-output formalism [5], yielding a resonator relaxation rate of $\kappa/(2\pi) = 3\,\mathrm{MHz}$ and a spin relaxation rate of $\gamma/(2\pi) = 50\,\mathrm{MHz}$. The cooperativity of the system is therefore obtained to $C = 1350 \gg 1$, what is well in the strong coupling regime.

In conclusion, we have demonstrated that an exchange-coupled spin system can be used to coherently store quantum information. Additionally, our work suggests that the amount of material needed to achieve strong coupling can be further reduced. This opens up the possibility of placing more than a single magnetic system onto the microwave resonator. Studying the exchange of magnetic excitation between multiple spin systems via a microwave resonator bus should therefore be feasible.

References

[1] D. I. Schuster, A. P. Sears, E. Ginossar, L. DiCarlo, L. Frunzio, J. J. L. Morton, H. Wu, G. A. D. Briggs, B. B. Buckley, D. D. Awschalom, and R. J. Schoelkopf, Phys. Rev. Lett. **105**, 140501 (2010).

[2] Y. Kubo, F. R. Ong, P. Bertet, D. Vion, V. Jacques, D. Zheng, A. Dréau, J.-F. Roch, A. Auffeves, F. Jelezko, J. Wrachtrup, M. F. Barthe, P. Bergonzo, and D. Esteve, Phys. Rev. Lett. **105**, 140502 (2010).

[3] O. O. Soykal, and M. E. Flatté, Phys. Rev. Lett. **104**, 077202 (2010).

[4] H. Huebl, C. Zollitsch, J. Lotze, F. Hocke, M. Greifenstein, A. Marx, R. Gross, and S. T. B. Goennenwein. High cooperativity in coupled microwave resonator ferrimagnetic insulator hybrids. `arXiv:1207.6039` (2012).

[5] D. F. Walls, and G. J. Milburn. *Quantum Optics* (Springer, Berlin, 1994), 1st edn.

Is there an Induced Pt Magnetic Polarization in Pt/$Y_3Fe_5O_{12}$ Bilayers?

S. Meyer, S. Geprägs, S. Altmannshofer, M. Opel, R. Gross, and S.T.B. Goennenwein [1]
F. Wilhelm, A. Rogalev [2]

A fascinating manifestation of spin physics in the solid state are pure spin currents. Their generation or detection is often based on the conversion from or to charge currents, taking advantage of the spin Hall or the inverse spin Hall effect, respectively [1]. To this end, normal metal/ferromagnetic metal (NM/FMM) or normal metal/ferromagnetic insulator (NM/FMI) heterostructures are applied where the NM layer is commonly considered as 'non-magnetic' in the sense that its spin polarization is negligibly small. However, in NM/FMM heterostructures, the presence of an induced spin polarization in the NM layer in proximity to the interface has been reported by X-ray magnetic circular dichroism (XMCD) experiments [2, 3]. For the case of NM/FMI structures in contrast, no such study of an induced spin polarization in the NM layer has been published to date.

Here, we present a comprehensive study taking advantage of the element-specific XMCD technique using bilayer thin films of polycrystalline Pt as NM and epitaxial $Y_3Fe_5O_{12}$ (yttrium iron garnet, YIG) as FMI [4]. A series of Pt/YIG samples was fabricated by laser-MBE and subsequent electron-beam evaporation in ultra-high vacuum on single crystalline $Y_3Al_5O_{12}$ substrates. We investigated three samples with similar thickness of the YIG thin film (≈ 62 nm) and different thicknesses (3 nm, 7 nm, 10 nm) of the Pt layer. For comparison, we fabricated a polycrystalline Pt (10 nm)/Fe(10 nm) reference sample solely by electron-beam evaporation in ultra-high vacuum. The XMCD measurements were performed at the European Synchrotron Radiation Facility (ESRF) at the beam line ID12 using the total fluorescence yield (TFY) detection mode. X-ray absorption near edge spectra (XANES) were recorded at the Pt L_3 edge (11 564 eV) with right and left circularly polar-

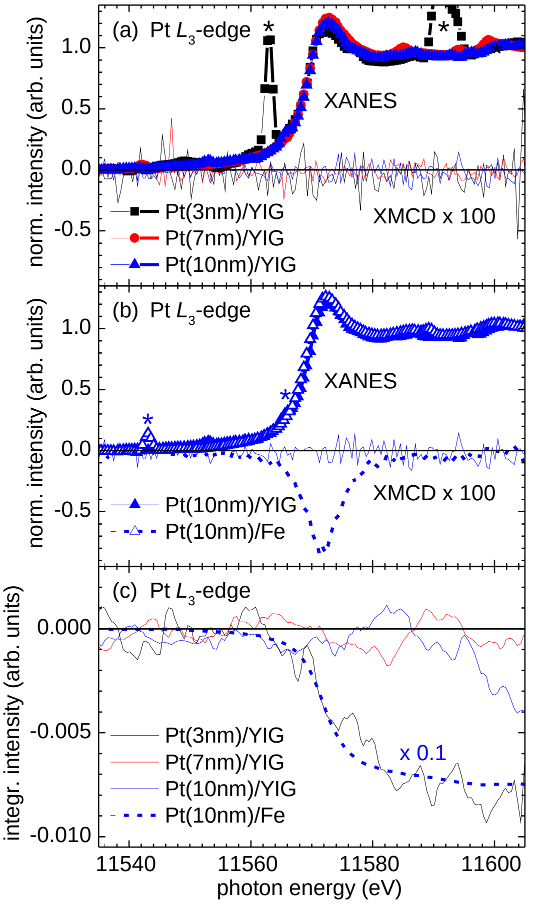

Figure 1: (a) Normalized Pt L_3 edge XANES (symbols) and XMCD (lines) spectra from Pt/YIG bilayers with different Pt thicknesses: 3 nm (black), 7 nm (red), and 10 nm (blue). Diffraction peaks are marked by asterisks. (b) Corresponding XANES and XMCD signal from a Pt(10 nm)/Fe bilayer (open symbols and dashed line). The normalized XANES (full symbols) and XMCD spectrum (solid line) from the Pt(10 nm)/YIG bilayer is shown for comparison. For better illustration, all XMCD spectra are multiplied by a factor of 100. (c) Corresponding integrated XMCD intensity. Before the integration, a small background slope was subtracted from the spectra. The integrated intensity of the Pt(10 nm)/Fe bilayer was multiplied by a factor of 0.1 (dashed line).

---

[1] This work was supported by the German Research Foundation via Priority Program SPP 1538 (project GO 944/4-1), and the German Excellence Initiative via the Nanosystems Initiative Munich (NIM).

[2] European Synchrotron Research Facility (ESRF), Grenoble, France. This work was supported by the European Synchrotron Research Facility (ESRF) via HE-3784.

ized light as well as positive and negative magnetic fields of ±60 mT. Several spectra were measured to improve the signal-to-noise ratio and then normalized to an edge jump of unity. The normalized and averaged spectra were used to calculate the XMCD signal as the direct difference between consecutive XANES recorded either with right and left circularly polarized light or while applying positive and negative magnetic fields.

The normalized XANES (symbols) for three Pt/YIG bilayers with different thicknesses of the Pt layer are displayed in Fig. 1(a). Some spurious peaks are caused by elastic diffraction from the substrate and marked by asterisks. Apparently, the XMCD spectra do not show indications for a finite XMCD signal at the Pt L_3 edge, not even in the sample with the thinnest Pt layer having the largest interface-to-volume ratio. To cross-check our experimental approach and to confirm earlier XMCD results from Pt/Ni multilayers [2, 5], XANES and XMCD spectra were also recorded from the Pt(10 nm)/Fe(10 nm) reference sample. Figure 1(b) reveals almost no difference between the XANES from Pt/Fe and from Pt/YIG. However, in contrast to the Pt/YIG bilayer, a clear XMCD signal is detected in the Pt/Fe bilayer. This result unambiguously demonstrates the presence of induced magnetic moments in the Pt layer deposited on Fe, which is in agreement with earlier XMCD results.

To extract the total magnetic moment μ of Pt via the standard magneto-optical sum rules, we integrate the XMCD intensity [Fig. 1(c)]. We obtain an average of $\mu = (0.0325 \pm 0.0004)\mu_B$ per Pt atom in the Pt/Fe bilayer [4], which is comparable to earlier experiments [3]. In Pt(10 nm)/YIG and Pt(7 nm)/YIG, however, the integrated Pt XMCD signal shows no indication for induced magnetic moments within the experimental detection limit. In contrast, the integrated XMCD intensity of the Pt(3 nm)/YIG sample reveals a tiny possible XMCD signal [Fig. 1(c)], which is about ten times smaller than the integrated XMCD signal from the Pt(10 nm)/Fe bilayer. We estimate an upper limit for the induced total magnetic moment of $\mu \leq (0.003 \pm 0.001)\mu_B$ per Pt atom in the Pt(3 nm)/YIG sample averaged over the layer thickness.

In summary, taking advantage of the element-specific XMCD technique, we have investigated the possible occurrence of induced magnetic moments in Pt films deposited onto the ferromagnetic insulator $Y_3Fe_5O_{12}$(YIG). Our data do no show evidence of an induced Pt magnetic polarization in Pt/YIG (NM/FMI) bilayers with a Pt thickness of 10 nm and 7 nm, whereas it is present in Pt(10 nm)/Fe (NM/FMM). A small but finite integrated XMCD signal appears in the Pt(3 nm)/YIG sample. Our data thus demonstrate that if a finite moment is induced in the Pt at all, it is at least 30 times smaller than in the corresponding Pt(10 nm)/Fe reference sample [4]. This tiny moment cannot be responsible for the reported magnetoresistance of Pt thin films on YIG [6].

References

[1] E. Saitoh, M. Ueda, H. Miyajima, and G. Tatara, Appl. Phys. Lett. **88**, 182509 (2006).

[2] F. Wilhelm, P. Poulopoulos, G. Ceballos, H. Wende, K. Baberschke, P. Srivastava, D. Benea, H. Ebert, M. Angelakeris, N. K. Flevaris, D. Niarchos, A. Rogalev, and N. B. Brookes, Phys. Rev. Lett. **85**, 413 (2000).

[3] F. Wilhelm, P. Poulopoulos, H. Wende, A. Scherz, K. Baberschke, M. Angelakeris, N. K. Flevaris, and A. Rogalev, Phys. Rev. Lett. **87**, 207202 (2001).

[4] S. Geprägs, S. Meyer, S. Altmannshofer, M. Opel, F. Wilhelm, A. Rogalev, R. Gross, and S. T. B. Gönnenwein. Investigation of induced Pt magnetic polarization in Pt/$Y_3Fe_5O_{12}$ bilayers. Accepted for publication in Appl. Phys. Lett., `arXiv:1211.0916` (2012).

[5] P. Poulopoulos, F. Wilhelm, H. Wende, G. Ceballos, K. Baberschke, D. Benea, H. Ebert, M. Angelakeris, N. K. Flevaris, A. Rogalev, and N. B. Brookes, J. Appl. Phys. **89**, 3874 (2001).

[6] S. Y. Huang, X. Fan, D. Qu, Y. P. Chen, W. G. Wang, J. Wu, T. Y. Chen, J. Q. Xiao, and C. L. Chien, Phys. Rev. Lett. **109**, 107204 (2012).

Spin Transport in Zinc Oxide

M. Althammer, E.-M. Karrer-Müller, S. T. B. Goennenwein, M. Opel, and R. Gross [1]

The successful injection, transport, manipulation, and detection of spin-polarized currents in semiconductors is a prerequisite for semiconductor spintronics. In this context, the spin dephasing time $T_2^\star$ of mobile charge carriers – and the associated length scale for coherent spin transport – are fundamental parameters. The wide bandgap II-VI semiconductor zinc oxide has a small spin-orbit coupling [1] implying a large spin coherence length. This makes ZnO interesting for (opto)electronics or spin-based quantum information processing. Using time-resolved Faraday rotation (TRFR), electron spin coherence up to room temperature in ZnO thin films was first observed in 2005 with a spin dephasing time of $T_2^\star \simeq 2\,\mathrm{ns}$ at 10 K [2]. As reported last year, our epitaxial ZnO thin films display $T_2^\star \simeq 14\,\mathrm{ns}$ in similar optical experiments [3]. Studies of electrical spin injection into ZnO, however, are rare and mainly focus on technical aspects rather than fundamental spin-dependent properties. Here, we investigate the transport and the dephasing of spin-polarized charge carriers in ZnO utilizing all-electrical, vertical spin valve devices with ferromagnetic (FM) electrodes (TiN/Co/ZnO/Ni/Au) [4].

The thin film multilayer heterostructures were fabricated on (0001)-oriented, single crystalline Al_2O_3 substrates via laser-MBE in combination with electron-beam physical vapor deposition (EBPVD) in an ultra-high vacuum cluster system. Laser-MBE was carried out by pulsed laser deposition (PLD) from stoichiometric polycrystalline targets in Ar atmosphere, EBPVD was performed in high vacuum. The multilayer stack consists of (i) a 12 nm thin TiN film as a non-ferromagnetic, metallic bottom electrode; (ii) a 11 nm thin Co film as the first ferromagnetic electrode; (iii) a semiconducting ZnO film with its thickness t_{ZnO} systematically varied in the range from 15 nm to 100 nm in a series of samples; (iv) a 11 nm thin Ni film as the second ferromagnetic electrode; and finally (v) a 24 nm thin Au film as a capping layer and top electrode [4].

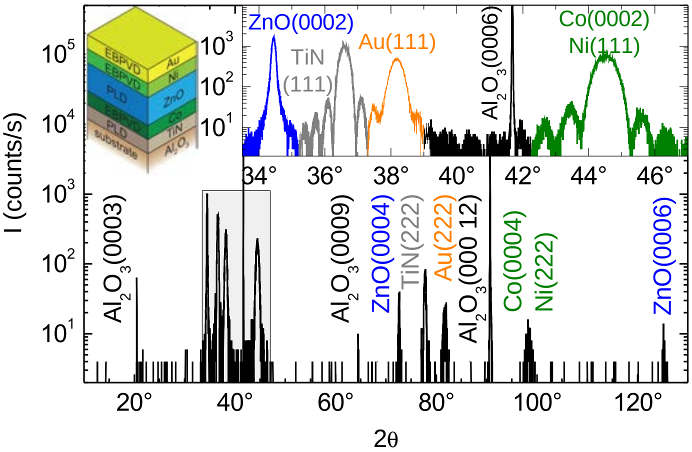

Figure 1: High-resolution X-ray diffraction diagram from a TiN/Co/ZnO(80 nm)/Ni/Au multilayer stack, deposited by pulsed laser deposition (PLD) or electron beam physical vapor deposition (EBPVD). The ω-2θ-scan does not show any secondary phases. The shaded area around the Al_2O_3(0006) reflection is displayed in the inset on an enlarged scale. Satellites due to Laue oscillations are clearly resolved for TiN(111) and Co(0002).

The structural quality of the multilayer stack was investigated by high-resolution X-ray diffraction. The out-of-plane ω-2θ-scan does not reveal any secondary phases. All reflections can be assigned to the respective materials of the spin valve multilayer structure (see Fig. 1). The cubic materials TiN, Ni, and Au grow (111)-oriented, the hexagonal Co and ZnO layers (0001)-oriented. For the TiN, Co, and Au layers, the ω-2θ-scan shows satellites due to Laue oscillations (inset of Fig. 1) demonstrating coherent growth with small interface roughness and indicating a high structural quality. From a detailed analysis [4], we find that each layer is aligned with respect to the oxygen sublattice of the (0001)-oriented Al_2O_3 substrate. Our results prove that the respective in-plane orientations of the single layers are preserved with excellent quality when grown on top of each other.

---

[1] This work was supported by the DFG via the Priority Program SPP 1285 (project GR 1132/14).

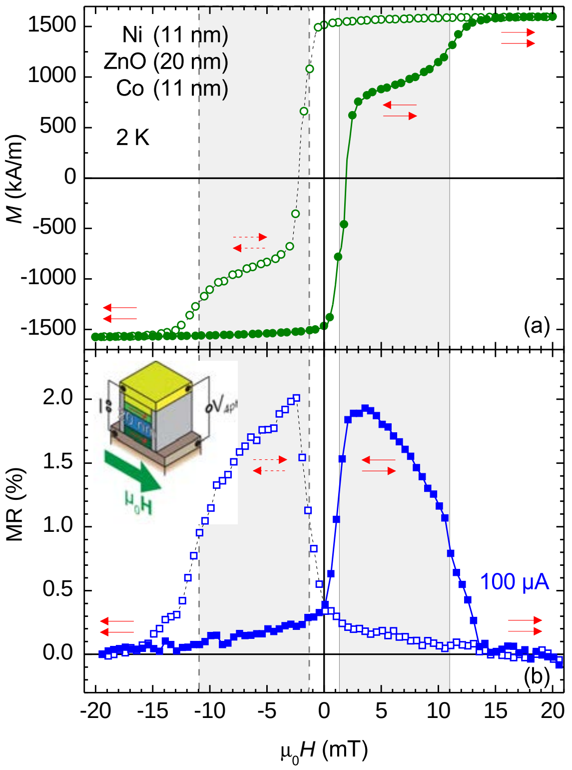

Figure 2: (a) Magnetization M of the multilayer stack normalized to the total volume of both ferromagnetic layers, (b) magnetoresistance MR for the patterned spin valve device (left inset) with an area of 400 μm^2. The data were taken for a ZnO thickness of 20 nm at 2 K as a function of the in-plane magnetic field H for up (closed symbols) and down sweep (open symbols). The MR effect is correlated to the coercive fields of Co and Ni (vertical lines); its maximum of 1.93% appears in the regime where the magnetization directions of Co and Ni (red arrows) are aligned antiparallel (grey shaded areas).

The magnetic properties were studied via superconducting quantum interference device (SQUID) magnetometry. At all investigated temperatures, the magnetization M shows a ferromagnetic hysteresis for low fields. The shape of $M(H)$ represents a superposition of two distinct hysteresis curves with different coercive fields H_c [see Fig. 2(a)]. We assign the larger H_c to the Ni film and the lower H_c to the Co layer. From these coercivities, the magnetization directions of Ni and Co (red horizontal arrows in Fig. 2) are expected to be aligned parallel for $|H| \gg H_c^{Ni}, H_c^{Co}$ and antiparallel (shaded regions in Fig. 2) for $H_c^{Co} < H < H_c^{Ni}$ for the field up-sweep direction or $-H_c^{Co} > H > -H_c^{Ni}$ for the down-sweep direction, respectively. This independent switching of the magnetization directions is a key requirement for the successful realization of a spin valve device.

Using optical lithography, Ar ion beam milling, and lift-off processes, the multilayer stack was patterned into vertical mesa structures with junction areas of 400 μm^2. Their resistance R was investigated by magnetotransport in standard four-point geometry across the spin valve junction [inset of Fig. 2(b)]. When sweeping the magnetic field, $R(H)$ shows a hysteresis between the field up-sweep and down-sweep directions with two resistive states [Fig. 2(b)], very well corresponding to the $M(H)$ hysteresis discussed above. For magnetic fields with an antiparallel magnetization configuration of the Ni and Co electrodes (shaded regions in Fig. 2), R is significantly higher than for the parallel configurations. This shows that our vertical mesa structures act as spin valve devices [4]. Evaluating $R(H)$ from different samples with different thicknesses $t_{ZnO} = 15 \ldots 80$ nm of the semiconducting ZnO layer, we find that its maximum value MR^{max} sensitively depends on t_{ZnO}. At 2 K, MR^{max} = 8.4% for 15 nm, by far exceeding previously published values [5], and decreases to 0.06% for 80 nm [Fig. 3(a)]. The same behavior is observed at higher temperatures of 50 K, 100 K, and 200 K with the overall values becoming significantly smaller [Fig. 3(b-d)].

Following the Valet-Fert approach [6], we fit MR^{max} to a two-spin channel model with spin-dependent conductivities to extract the spin diffusion length $l_{sf}^{ZnO}(T)$ for ZnO [4]. The fit curves clearly reproduce the measured MR^{max}, reflecting a fair agreement between model and experiment [red lines in Fig. 3(a-d)]. From these fits, we extract $l_{sf}^{ZnO}(T)$ and obtain a value of (10.8 ± 1.0) nm for 2 K [Fig. 3(f)]. For increasing temperature, $l_{sf}^{ZnO}(T)$ stays first nearly constant with a value of (10.7 ± 0.2) nm at 10 K. On further increasing temperature, it decreases to (6.2 ± 0.2) nm at 200 K. The spin relaxation rate $1/\tau_{sf}^{ZnO}$ [4] decreases from (32.0 ± 1.7)/ns at 200 K to (0.490 ± 0.011)/ns at 10 K and further to (0.3900 ± 0.0021)/ns at 2 K [Fig. 3(g)]. Evidently, this behavior obtained from our all-electrical detection scheme agrees well with the temperature dependence of $1/T_2^\star$ derived from optical TRFR experiments [2] in an intermediate temperature range of $10\,\mathrm{K} \leq T \leq 150\,\mathrm{K}$ [Fig. 3(g)]. For lower temperatures, however, $1/T_2^\star$ increases again while $1/\tau_{\mathrm{sf}}^{\mathrm{ZnO}}$ becomes constant below 10 K.

Two different spin relaxation mechanisms are considered important in ZnO: (i) the Dzyaloshinsky-Moriya (DM) mechanism due to an anisotropic exchange between localized electronic states and (ii) the D'yakonov-Perel' (DP) mechanism due to the reflection asymmetry of the crystal lattice along the *c*-axis [7]. At high temperatures ($T > 50\,\mathrm{K}$), the DP process becomes dominant [7]. A fit reproduces our data very well for $T \gtrsim 30\,\mathrm{K}$ [blue line in Fig. 3(g)]. For $T < 50\,\mathrm{K}$, however, the DM mechanism is predicted to become dominant, resulting in a nearly T-independent spin relaxation rate [7]. This behavior was not reported from optical TRFR experiments in ZnO thin films [2], but is indeed observed in our ZnO-based spin valves [4] for temperatures down to 2 K [dashed line in Fig. 3(g)].

In summary, we all-electrically inject and detect a spin-polarized current in ZnO and for the first time demonstrate the transport of spin-polarized charge carrier across several nanometers in ZnO. We determine the spin diffusion length $l_{\mathrm{sf}}^{\mathrm{ZnO}}$ and the spin lifetime $\tau_{\mathrm{sf}}^{\mathrm{ZnO}}$ and obtain large values of $l_{\mathrm{sf}}^{\mathrm{ZnO}} = 10.8\,\mathrm{nm}$ and $\tau_{\mathrm{sf}}^{\mathrm{ZnO}} = 2.6\,\mathrm{ns}$ at 2 K. The evolution of the measured spin relaxation rates with temperature is consistent with the D'yakonov-Perel' mechanism for $T \gtrsim 30\,\mathrm{K}$.

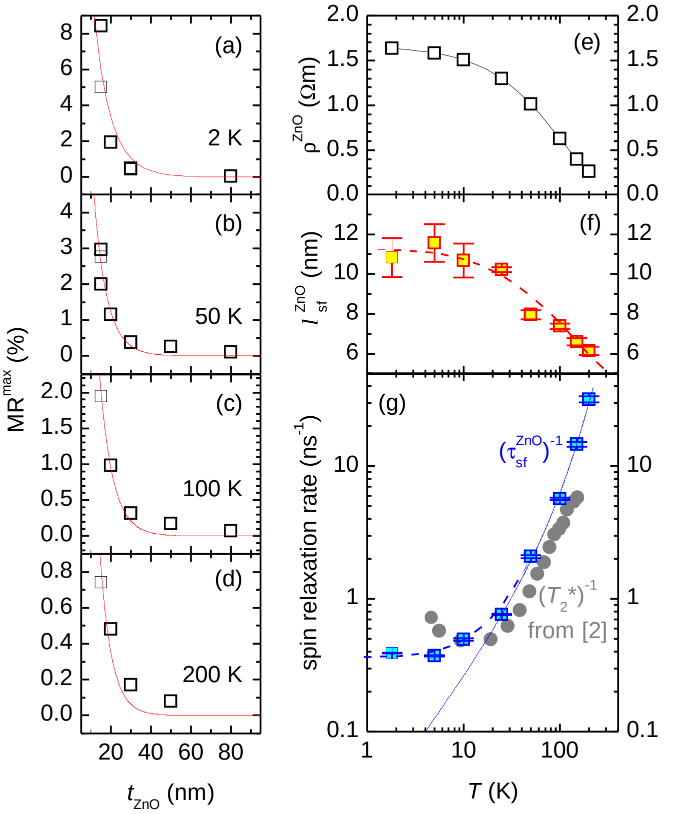

Figure 3: (a–d) Maximum MR as a function of the ZnO thickness t_{ZnO} at 2 K (a), 50 K (b), 100 K (c), and 200 K (d). The symbols represent the experimental data, the red lines are fits with the two spin channel model [6]. (e) Temperature dependence of the resistivity ρ_{ZnO}, experimentally determined from a TiN/ZnO/Au reference sample. (f) Spin diffusion length $l_{\mathrm{sf}}^{\mathrm{ZnO}}$, obtained from the fits in (a–d). The dashed line is a guide to the eye. (g) Inverse spin lifetime $\tau_{\mathrm{sf}}^{\mathrm{ZnO}}$ (blue squares), obtained from $l_{\mathrm{sf}}^{\mathrm{ZnO}}$ [4]. The solid line corresponds to the D'yakonov-Perel' mechanism [7], the dashed line is a guide to the eye. The panel also shows $T_2^\star$ data (grey circles), determined optically by Ghosh *et al.* [2].

References

[1] J. Y. Fu, and M. W. Wu, J. Appl. Phys. **104**, 093712 (2008).

[2] S. Ghosh, V. Sih, W. H. Lau, D. D. Awschalom, S. Bae, S. Wang, S. Vaidya, and G. Chapline, Appl. Phys. Lett. **86**, 232507 (2005).

[3] M. Althammer, D.Venkateshvaran, R. Gross, S. T. B. Goennenwein, M. Opel, C. Schwark, V. Klinke, and B. Beschoten. Spin injection and spin transport in the wide bandgap semiconductor zinc oxide. In **WMI Annual Report**, 64 (Walther-Meißner-Institut, Garching, 2011).

[4] M. Althammer, E.-M. Karrer-Müller, S. T. B. Goennenwein, M. Opel, and R. Gross, Appl. Phys. Lett. **101**, 082404 (2012).

[5] G. Ji, Z. Zhang, Y. Chen, S. Yan, Y. Liu, and L. Mei, Acta Metallurgica Sinica (English Letters) **22**, 153 (2009).

[6] A. Fert, and H. Jaffrès, Phys. Rev. B **64**, 184420 (2001).

[7] N. J. Harmon, W. O. Putikka, and R. Joynt, Phys. Rev. B **79**, 115204 (2009).

Spin and Charge Currents in Magneto-thermal Landscapes

M. Weiler, M. Schreier, M. Althammer, S. Meyer, H. Huebl, M. Opel, S. Geprägs, R. Gross, S. T. B. Goennenwein [1]
I.-M. Imort, G. Reiss, A. Thomas [2]

In conductive materials, Ohm's law relates the electric field to electrical charge motion. In a similar fashion, a temperature gradient ∇T drives a charge redistribution, and thus induces thermoelectric phenomena such as the Seebeck [1] and Nernst [2] effects. Since the electrons carrying the charge also transport spin, thermo-electric effects become spin orientation-dependent in materials with finite spin polarization. In other words, ferromagnetic conductors exhibit characteristic magneto-thermoelectric effects, e.g., the anomalous Nernst effect (ANE). In the latter, an electric field

$$\mathbf{E}_{\mathrm{ANE}} = -N\mu_0 \boldsymbol{M} \times \boldsymbol{\nabla} T\,, \tag{1}$$

with a characteristic dependence on the ferromagnetic conductor's magnetization $\boldsymbol{M}$ is induced by the temperature gradient $\boldsymbol{\nabla} T$, with the (anomalous) Nernst coefficient N. Even more intriguingly, it was recently discovered that thermal gradients in magnetic media also induce pure spin currents, i.e., a flow of spin angular momentum only. The corresponding phenomenon is called spin Seebeck effect (SSE) [3, 4], and expressed as

$$\mathbf{E}_{\mathrm{ISHE}} = -S_{\mathrm{SSE}} \boldsymbol{\sigma} \times \boldsymbol{\nabla} T\,, \tag{2}$$

with the spin Seebeck coefficient S_{SSE} and the spin orientation $\boldsymbol{\sigma}$. In the literature, both charge and spin based magneto-thermoelectric effects have been investigated using spatially homogeneous temperature gradients, such that only the integral properties were probed.

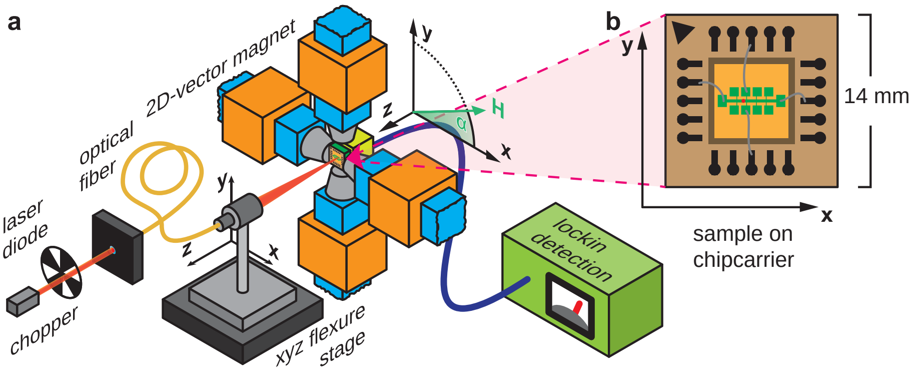

Figure 1: **a** Schematic illustration of the experimental setup. A scannable laser beam is focused on the sample surface to provide the thermal landscape. An external magnetic field can be applied within the sample plane via a 2D-vector magnet. **b** Closeup of sample with Hall bar (green, not to scale) mounted and wired on a chip carrier.

In the following, we present a quantitative, spatially resolved experimental study of the spin Seebeck and the anomalous Nernst effect, arising in magnetic media exposed to a magneto-thermal landscape [5]. We use a scannable laser beam to generate local thermal gradients in metallic Heusler compound (Co_2FeAl) or electrically insulating yttrium iron garnet ($Y_3Fe_5O_{12}$, or YIG for short) ferromagnetic thin films, and measure the resulting local charge or spin currents (see Fig. 1). The key idea behind the experiments is that since the sample at least partially absorbs the laser light, its intensity and thus the energy deposited decrease as a function of depth. Hence, the energy absorption profile of the laser beam into the film thickness gives rise to a thermal gradient $\boldsymbol{\nabla} T(x,y)$ perpendicular to the sample plane, laterally confined to a region around

---

[1] We gratefully acknowledge financial support from the German Research Foundation via the Priority Program SPP 1538 (SpinCAT, project GO 944/4).

[2] Fakultät für Physik, Universität Bielefeld, Germany.

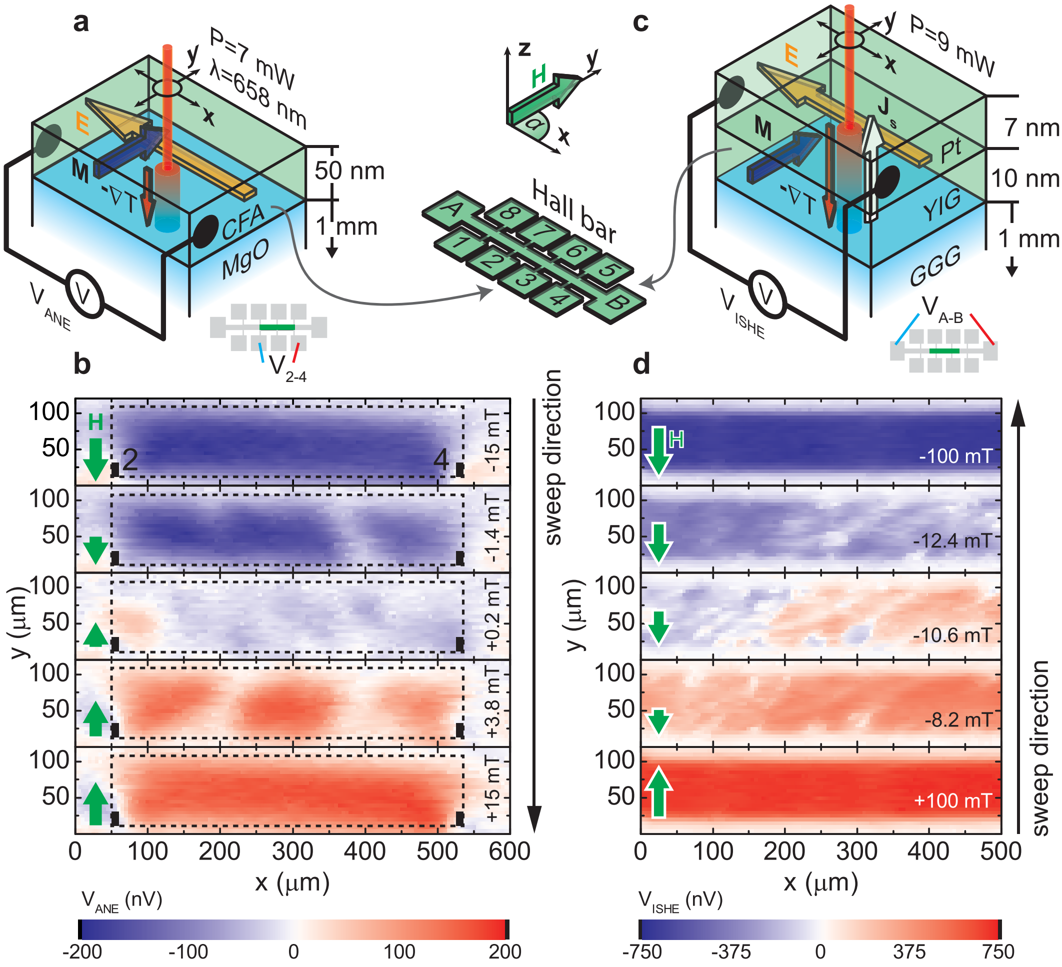

Figure 2: **a** The scannable laser beam generates a local temperature gradient ∇T normal to the ferromagnetic thin film plane. The dc voltage V_{ANE} which arises due to the anomalous Nernst effect depends on the local magnetization $\boldsymbol{M}$ at the position (x, y) of the laser beam. **b** V_{ANE} determined between contacts 2 and 4 of a 50 nm thick Co_2FeAl (CFA) Hall bar as a function of the laser-spot position (x, y) and the external magnetic field magnitude $\mu_0 H$ ($\alpha = 90°$). The small full rectangles indicate the location of the used electric contacts and the dashed rectangle depicts the region on the main Hall bar enclosed by said contacts. **c** Schematic illustration of the GGG/YIG/Pt sample. The spin Seebeck effect yields a pure, local spin current $\boldsymbol{J}_{\text{s}}$ along $\boldsymbol{\nabla} T$ in YIG. $\boldsymbol{J}_{\text{s}}$ depends on the local magnetization $\boldsymbol{M}(x, y)$ and is detected using the inverse spin Hall effect in Pt, which gives rise to a dc voltage V_{ISHE}. **d** V_{ISHE} determined between contacts A and B as a function of the laser-spot position (x, y) and the external magnetic field magnitude $\mu_0 H$ applied along $\boldsymbol{y}$ in a 10 nm YIG / 7 nm Pt hybrid sample.

the position (x, y) of the laser spot [6]. In the local ANE experiments, we detect the voltage in the Co_2FeAl thin film plane as a function of the laser spot position and external magnetic field magnitude and orientation. The local spin current generated by the SSE effect is detected in a similar fashion, after converting the spin current to a charge current via the inverse spin Hall effect [7, 8] in the Pt layer deposited on top of the YIG. Note that YIG is a ferromagnetic insulator, such that no anomalous Nernst effect is expected in the YIG/Pt samples, since there are no mobile, spin-polarized charge carriers. However, the spin Seebeck effect persists [4], since spin currents can flow also in the absence of charge carrier mobility due to angular momentum transport by magnons.

Figure 2 shows the dc voltage V_{ANE} as a function of position (x, y) of the laser spot, recorded in a 50 nm thick ferromagnetic Co_2FeAl film deposited on a MgO substrate at the University of Bielefeld, and subsequently patterned into a Hall bar mesa structure (Fig. 2a). For each value of the in-plane magnetic field $\mu_0 H$ applied at an angle $\alpha = 90°$ to the $\boldsymbol{x}$ axis, we scanned the laser beam over the central Hall bar area and recorded $V_{\text{ANE}}(x, y)$. At $\mu_0 H = -15\,\text{mT}$

($\boldsymbol{H} \parallel -\boldsymbol{y}$, cf. the solid green arrow to the left), we observe a voltage $V_{\mathrm{ANE}} \approx -150\,\mathrm{nV}$ in the Hall bar region independent of the laser spot position (x, y). At $\mu_0 H = -15\,\mathrm{mT}$, the film is in magnetic saturation with $\boldsymbol{M} \parallel \boldsymbol{H}$. Hence, no magnetic microstructure is present and $V_{\mathrm{ANE}}(x, y)$ does not depend on x or y. As the magnetic field magnitude is decreased, magnetic domain formation is evident from the V_{ANE} maps. Upon increasing the external magnetic field to $\mu_0 H = 3.8\,\mathrm{mT}$, magnetic domains exhibiting $V_{\mathrm{ANE}} > 0$ become visible. In magnetic saturation at $\mu_0 H = 15\,\mathrm{mT}$, $V_{\mathrm{ANE}} \approx 150\,\mathrm{nV}$ in the entire Hall bar region. The sign reversal of V_{ANE} with the reversal of the direction of $\boldsymbol{H}$ (and thus $\boldsymbol{M}$) is a clear indication that the observed V_{ANE} indeed is caused by a term $\nabla T \times \boldsymbol{M}$, i.e., by the anomalous Nernst effect.

We now turn to the generation and detection of local spin currents via the longitudinal spin Seebeck effect in a ferromagnetic insulator exposed to magnetothermal landscapes. We employ a $\mathrm{Gd_3Ga_5O_{12}}\,(0.5\,\mathrm{mm})/\mathrm{Y_3Fe_5O_{12}}\,(10\,\mathrm{nm})/\mathrm{Pt}\,(7\,\mathrm{nm})$ hybrid sample fabricated at the WMI (Fig. 2c) and then also patterned into a Hall bar. Upon application of a temperature gradient along the hybrid normal, the longitudinal SSE [9] effect yields a pure spin current $\boldsymbol{J}_{\mathrm{s}}$ in the YIG film parallel to $\boldsymbol{\nabla} T$ which can be detected by exploiting the inverse spin Hall effect in the Pt layer. Note that YIG is an electrical insulator, such that it does not show an anomalous Nernst effect. In Fig. 2d, we present a spatially resolved measurement of the spin Seebeck effect voltage V_{ISHE} as a function of H. Since V_{ISHE} is a measure of the spin current with spin orientation $\boldsymbol{\sigma}$, Fig. 2d represents a map of the local spin (magnetization) orientation in the ferromagnetic insulator YIG, detected by local electric fields in the Pt layer deposited on top. At $\mu_0 H = \pm 100\,\mathrm{mT}$ (bottom and top panel), the YIG thin film is in a single domain state with $\boldsymbol{M} \parallel \boldsymbol{H}$. As $\boldsymbol{H}$ is applied along $\boldsymbol{y}$, we can observe $\boldsymbol{E}_{\mathrm{ISHE}} \propto \boldsymbol{M} \times \nabla T$ along $\boldsymbol{x}$ by probing V_{ISHE} (cf. Eq. (2)). Magnetic texture is observed during the magnetic field sweep in the images recorded with $\mu_0 H = 8.2\,\mathrm{mT}$ to $\mu_0 H = -12.4\,\mathrm{mT}$ (middle panels). The YIG magnetic domain pattern is more complex than the one observed in $\mathrm{Co_2FeAl}$, since the in-plane magnetic anisotropy of our YIG thin films is small, such that magnetic domain formation is not energy costly.

In conclusion, our findings demonstrate that spatially confined thermal gradients allow for the generation of local, bipolar and magnetically controllable electric fields or spin currents that can be used to, e.g., electrically image the magnetic microstructure in ferromagnetic metals and insulators. For more details regarding both the experiment as well as the analysis, we refer the publications Refs. [5], [10], [11].

References

[1] T. Seebeck, Abh. K. Akad. Wiss. Berlin 265 (1823).

[2] W. Nernst, Ann. Phys. **267**, 760 (1887).

[3] K. Uchida, S. Takahashi, K. Harii, J. Ieda, W. Koshibae, K. Ando, S. Maekawa, and E. Saitoh, Nature **455**, 778 (2008).

[4] K. Uchida, J. Xiao, H. Adachi, J. Ohe, S. Takahashi, J. Ieda, T. Ota, Y. Kajiwara, H. Umezawa, H. Kawai, G. E. W. Bauer, S. Maekawa, and E. Saitoh, Nat. Mater. **9**, 894 (2010).

[5] M. Weiler, M. Althammer, F. D. Czeschka, H. Huebl, M. S. Wagner, M. Opel, I.-M. Imort, G. Reiss, A. Thomas, R. Gross, and S. T. B. Goennenwein, Phys. Rev. Lett. **108**, 106602 (2012).

[6] M. Reichling, and H. Grönbeck, J. Appl. Phys. **75**, 1914 (1994).

[7] J. E. Hirsch, Phys. Rev. Lett. **83**, 1834 (1999).

[8] E. Saitoh, M. Ueda, H. Miyajima, and G. Tatara, Appl. Phys. Lett. **88**, 182509 (2006).

[9] K. Uchida, H. Adachi, T. Ota, H. Nakayama, S. Maekawa, and E. Saitoh, Appl. Phys. Lett. **97**, 172505 (2010).

[10] M. Weiler. *Magnon-phonon interactions in ferromagnetic thin films*. Ph.D. thesis, Technische Universität München (2012).

[11] R. Myers, and J. Heremans, Physics **5**, 29 (2012).

Application–Oriented Research

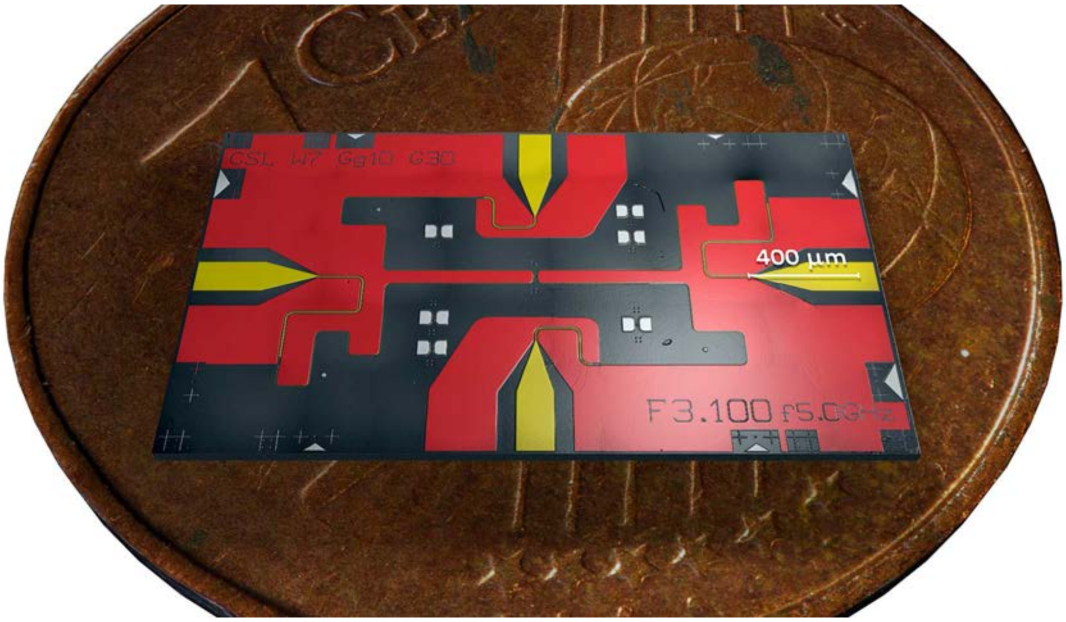

The Quantum Switch:
a tunable coupling between two superconducting microwave resonators is realized by a flux qubit

Fast Microwave Beam Splitters from Superconducting Resonators

M. Haeberlein, E. Hoffmann, P. Assum, F. Deppe, A. Marx and R. Gross [1]
D. Zueco,[2] *T. Weiß,*[3] *B. Peropadre,*[4] *J.J. García-Ripoll,*[5] *E. Solano*[6]

Recent advances in quantum electrodynamics with superconducting circuits (circuit QED) allow to implement and study basic quantum simulations [1]. In order to outrival classical simulations, digital quantum simulations require a large number of nonlinear elements and sophisticated error-correction schemes. Therefore, in the short term it is more promising to investigate so-called analog quantum simulations. Here, a specific quantum system is hard-wired in a nonlinear superconducting circuitry. The input and output channels of the model system are easily accessible, allowing to trace the quantum evolution. Many of these superconducting circuitries rely on beam splitters. These can e.g. create superposition states which are building blocks of interferometers [2].

In our work, we design, fabricate and characterize microwave beam splitters consisting of two frequency-degenerate coupled superconducting transmission line resonators. In this way we are able to test the validity of theoretical model considerations [3] which have been recently developed for the description of such beam splitters. To achieve a very high coupling strength, we use a distributed coupling where the coupling region extends over a large fraction of the total resonator length. Due to the very large coupling strength, our devices work on timescales which can become comparable to the inverse of the eigenfrequencies $\omega/2\pi$ of the two resonators. In this case the interaction Hamiltonian $\mathcal{H}_\mathrm{i}$ of the two resonators with uncoupled resonant frequency ω_0 can no longer be described by the simple beam splitter type interaction Hamiltonian $\mathcal{H}_\mathrm{BS} = \hbar g_\mathrm{BS}\left(a^\dagger b + a b^\dagger\right)$. For high coupling strength it rather has to be expressed as [3]

$$\mathcal{H}_\mathrm{i} = \hbar g_\mathrm{BS}\left(a^\dagger b + a b^\dagger\right) + \hbar g_\mathrm{TMS}\left(a^\dagger b^\dagger + a b\right) . \tag{1}$$

Here, $a^\dagger$ and $b^\dagger$ (a and b) are the bosonic creation (annihilation) operators of the two resonators, g_BS is the beam splitter coupling rate and g_TMS is the two-mode-squeezer (TMS) coupling rate. The interaction results in two coupled harmonic oscillators with renormalized resonant frequency $\widetilde{\omega}$, which is split – in general asymmetrically with respect to the uncoupled resonant frequency ω_0 – into two normal modes of frequencies $\omega_\pm$ [3]. Our model predicts that the two coupling rates between the two resonators are related to the inductive (capacitive) coupling rate g_i (g_c) via $g_\mathrm{BS} = g_\mathrm{i} + g_\mathrm{c}$ and $g_\mathrm{TMS} = g_\mathrm{i} - g_\mathrm{c}$ [3]. In our sample design, we can tune the relative strength of the inductive and capacitive coupling rate by simply shifting the center position of the coupling region. In this way, we can suppress the TMS term [4] to achieve at the same time a pure beam splitter type interaction and a large coupling strength.

We fabricate our samples on 250 µm thick silicon wafers which are covered with 50 nm SiO_2. These wafers are sputtered coated with 100 nm niobium on both sides. One side is patterned using optical lithography and reactive ion etching, the other serves as ground plane. We end up with the microstrip waveguide structure shown in Fig. 1(a-c). Both resonators have

---

[1] We gratefully acknowledge financial support by the German Research Foundation through the Collaborative Research Center 631, the German Excellence Initiative through the Nanosystems Initiative Munich (NIM), and the EU projects CCQED and PROMISCE.

[2] Instituto de Ciencia de Materiales de Aragón y Departamento de Física de la Materia Condensada CSIC - Universidad de Zaragoza C, Pedro Cerbuna 12, 50009 Zaragoza and Fundación ARAID, Paseo María Agustín 36, 50004 Zaragoza, Spain.

[3] Institut Néel, CNRS, F-38042 Grenoble cedex 9, France.

[4] Instituto de Física Fundamental, CSIC, Serrano 113-B, 28006 Madrid, Spain.

[5] Instituto de Física Fundamental, CSIC, Serrano 113-B, 28006 Madrid, Spain.

[6] Departamento de Química Física, Universidad del País Vasco UPV/EHU, Apartado 644, 48080 Bilbao and IKERBASQUE, Basque Foundation for Science, Alameda Urquijo 36, 48011 Bilbao, Spain.

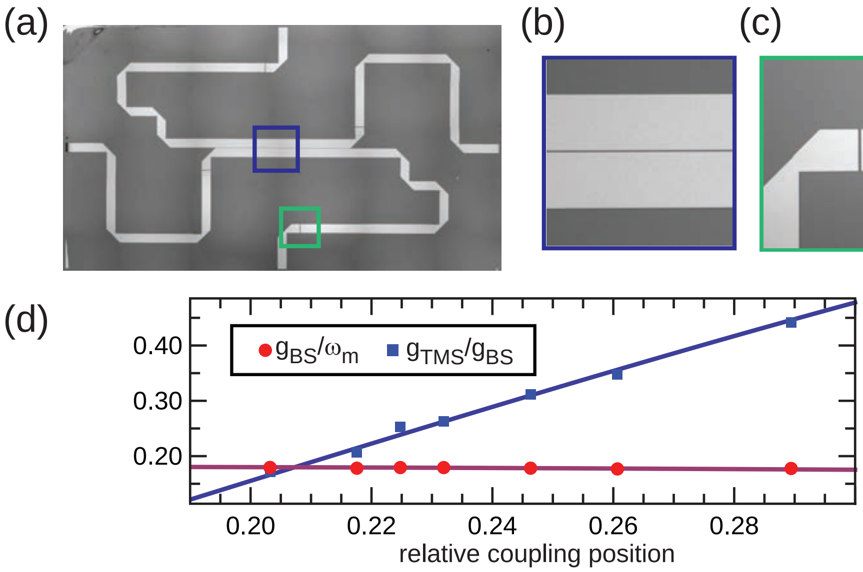

Figure 1: (a) Microstrip circuit layout of the coupled resonators. The microstrip is patterned by standard optical lithography and reactive ion etching into a niobium thin film. (b) Optical micrograph showing the 2 µm wide gap between the two resonators. (c) The 10 µm gap at the coupling capacitors at each end of the resonators. (d) Red: The beam splitter coupling rate normalized by the lower eigenfrequency $\omega_- = \omega_m$ of the coupled resonators is plotted versus the relative coupling position. The relative coupling position is normalized to the available coupling length of 6.963 mm. Blue: The ratio of the beam splitter (BS) coupling rate g_{BS} to the two mode squeezer (TMS) coupling rate g_{TMS}. An extrapolation shows that a pure beam splitter coupling can be reached at a relative coupling position of 15.5%.

the same shape and couple over a distance of 3 mm. Their uncoupled resonant frequency is $\omega_0 = 5.44\,\text{GHz}$. For each two-resonator sample, we fabricate a respective single resonator with the same shape in order to calibrate our measurement. In our experiments, we measure the transmission spectra of both the single resonator and the two coupled resonators at 4.2 K. We have studied a large number of samples with the position of the coupling center position varying from 20% to 30% of the available resonator length of 6.963 mm.

In Fig. 1(d) we show the dependence of g_{TMS}/g_{BS} on the relative coupling position. Evidently, we can reduce the ratio g_{TMS}/g_{BS} to a value as low as ≈ 0.2 while keeping the beam splitter coupling rate $g_{BS}/\omega_m \approx 0.18$ high. Absolute values of $g_{BS}/2\pi$ above 800 MHz have been achieved at resonator frequencies $\omega_0/2\pi \simeq 5.5\,\text{GHz}$. An extrapolation of the model prediction suggests that the TMS coupling vanishes at a relative coupling position of 0.15. This configuration is then ideally suited for the construction of a pure beam splitter with large coupling rate. It can be reached with our geometry.

References

[1] I. Buluta, and F. Nori, Science **326**, 108 (2009).
[2] E. Knill, R. Laflamme, and G. J. Milburn, Nature **409**, 46 (2001).
[3] B. Peropadre, D. Zueco, F. Wulschner, F. Deppe, A. Marx, R. Gross, and J. J. García-Ripoll. Tunable coupling engineering between superconducting resonators: from sidebands to effective gauge fields. `arXiv:1207.3408` (2012).
[4] M. Haeberlein, D. Zueco, P. Assum, T. Weißl, E. Hoffmann, B. Peropadre, J. García-Ripoll, E. Solano, F. Deppe, A. Marx, and R. Gross. Fast microwave beam splitters from superconducting resonators. In preparation (2012).

Improved Gradiometric Tunable-gap Flux Qubits

M. J. Schwarz, J. Goetz, Z. Jiang, F. Deppe, A. Marx, R. Gross [1]

Superconducting quantum circuits are promising candidates for the implementation of solid state quantum information systems and the realization of fascinating quantum-optical experiments in the microwave regime. In particular, the coupling of superconducting quantum two-level systems (qubits) to microwave resonators has been successful, resulting in the rapid development of the prospering field of circuit quantum electrodynamics (QED). Depending on the degree of freedom that is used to encode quantum information, different types of superconducting qubits can be distinguished. At the WMI, we focus on flux qubits, where quantum information is encoded in the magnetic flux generated by a circulating current in a superconducting loop containing three or more Josephson junctions. One main advantage of flux qubits is their potential for ultrastrong coupling to the electromagnetic modes of high quality microwave resonators [1]. However, the standard version of the flux qubit also suffers from the disadvantage that its minimal transition frequency, where quantum coherence is optimal, is fixed by design and fabrication. Fortunately, this drawback can be overcome with an advanced flux qubit with in situ tunable minimal transition frequency [2]. In last years's report we showed the first experimental realization of such a qubit at the WMI [3]. Meanwhile, the design and fabrication process have been considerably improved and a systematic characterization of tunable-gap flux qubits has been made.

The original design of a flux qubit consists of a superconducting loop interrupted by three nm-sized Josephson junctions (JJs), one of them being smaller by a factor α [4, 5]. Its quantum coherence is optimal at the degeneracy point with minimal transition frequency. This so-called qubit gap Δ is fixed for this qubit version but exponentially dependent on the factor α. By replacing this smaller junction with a dc-SQUID, the value α can be adjusted by means of a flux applied to this SQUID loop. In the gradiometric configuration we use (cf. Fig. 1), the flux needed to change α does not affect the magnetic energy bias of the qubit loop. Last year we showed the first working tunable-gap qubit, where we could tune the qubit gap in situ with both an external magnetic field coil and an on-chip flux bias line. However, the tunability of the gap was limited to a range of $0-5\,\mathrm{GHz}$. Here, we show a considerable extension of this tuning range by optimizing the Josephson energy E_J and charging energy E_c of the qubit junctions.

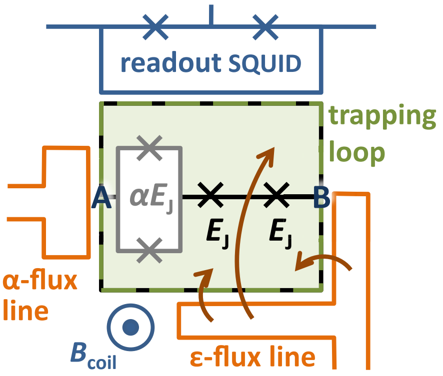

Figure 1: Circuit schematics of the tunable-gap gradiometric flux qubit. The outer loop of the flux qubit (broken olive line) forms the trapping loop, the inner (grey line) the α-loop.

Using our well-established fabrication processes [5], we improve the parameters of the gradiometric tunable-gap flux qubit and the readout SQUID. The latter is changed by enlarging the junctions and by adding shunt capacitors in order maximize readout contrast. Fig. 2(a) shows the flux dependent transition frequency $\omega_\mathrm{q}/2\pi$ for different effective values of α extracted from qubit spectroscopy via the readout SQUID at a temperature of about 30 mK. A change of the qubit hyperbolas corresponding to different values of α is clearly observable. The qubit

---

[1] We gratefully acknowledge financial support by the German Research Foundation through the Collaborative Research Center 631, the German Excellence Initiative through the Nanosystems Initiative Munich (NIM), and the EU projects CCQED and PROMISCE.

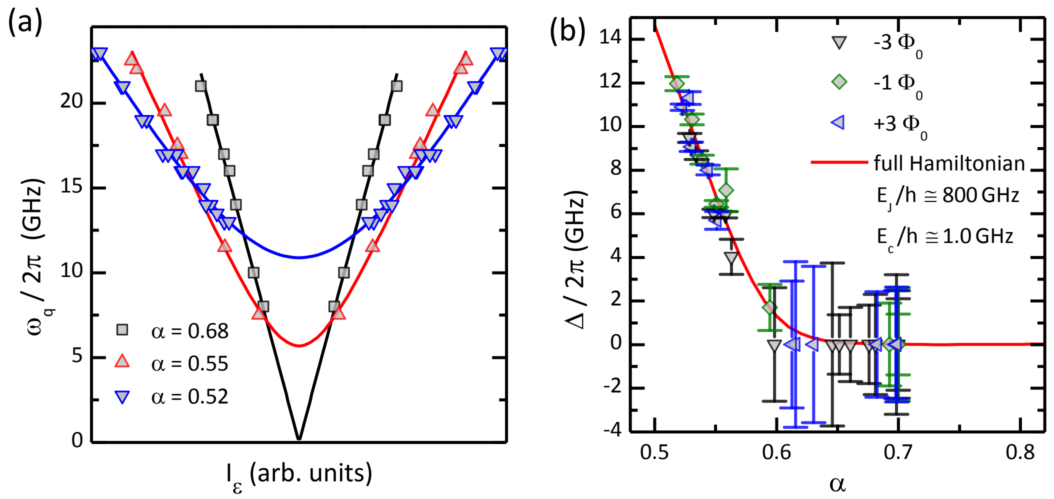

Figure 2: (a) Transition frequency $\omega_q/2\pi$ plotted versus the current through the ϵ-line changing the magnetic energy bias of a tunable-gap gradiometric flux qubit. Also shown is the result of a two-parameter fit. (b) Minimal qubit transition frequency $\Delta/2\pi$ plotted versus α for three different values of trapped flux quanta. The solid line is a fit of the data based on the full qubit Hamiltonian with the fitting parameters $E_J/h = 800\,\text{GHz}$ and $E_c/h = 1.0\,\text{GHz}$.

gap Δ obtained from these hyperbolas is plotted in Fig. 2b) as a function of the effective value of α for three different values of trapped flux quanta. These data are consistent with a fit based on the calculation of Δ from the full qubit Hamiltonian [6]. We find that the high ratio of $E_J/E_c = 800$ is the key to the increased tunability of the qubit gap. These results show that the qubit gap $\Delta/2\pi$ can be tuned in a reliable and controllable way from zero up to 12 GHz. Besides tuning the qubit gap by an external coil we have also used the on-chip flux bias line to change the effective value of α, where we have obtained a tunability of $\Delta/2\pi$ in the range of 3.5 – 11.5 GHz with a suitable constant bias set by the coil. This range of tunability is sufficient to couple and decouple the qubit from a microwave resonator with modes from 5 GHz up to 8 GHz typically used in our circuit QED experiments [1]. Besides the increased tunability, a more thorough characterization of this sample also provides insight into the import contributions of kinetic and geometric inductances of the superconducting lines forming the qubit [7].

In conclusion, we have optimized our gradiometric flux qubits with an in situ tunable tunnel coupling. We achieved a large tunability of the qubit gap both with an external coil and an on-chip bias line. Next, we plan to integrate this qubit into circuit QED experiments. The first step will be the coupling of tunable-gap flux qubits to a microwave resonator.

References

[1] T. Niemczyk, F. Deppe, H. Huebl, E. P. Menzel, F. Hocke, M. J. Schwarz, J. J. Garcia-Ripoll, D. Zueco, T. Hummer, E. Solano, A. Marx, and R. Gross, Nat. Phys. **6**, 772 (2010).

[2] F. G. Paauw, A. Fedorov, C. J. P. M. Harmans, and J. E. Mooij, Phys. Rev. Lett. **102**, 090501 (2009).

[3] M. J. Schwarz, J. Goetz, T. Niemczyk, F. Deppe, A. Marx, and R. Gross. Gradiometric Flux Quantum Bits with Tunable Tunnel Coupling. In **WMI Annual Report**, 51 (Walther-Meißner-Institut, Garching, 2011).

[4] T. P. Orlando, J. E. Mooij, L. Tian, C. H. van der Wal, L. S. Levitov, S. Lloyd, and J. J. Mazo, Phys. Rev. B **60**, 15398 (1999).

[5] T. Niemczyk, F. Deppe, M. Mariantoni, E. P. Menzel, E. Hoffmann, G. Wild, L. Eggenstein, A. Marx, and R. Gross, Supercond. Sci. Technol. **22**, 034009 (2009).

[6] J. Goetz. *Gradiometric flux quantum bits with tunable tunnel coupling*. Diplomarbeit, Technische Universität München (2011).

[7] M. J. Schwarz, J. Goetz, Z. Jiang, T. Niemczyk, F. Deppe, A. Marx, and R. Gross. Gradiometric flux qubits with tunable gap. `arXiv:1210.3982` (2012).

Building Blocks for Low Temperature Microwave Experiments

K. F. Wulschner, M. Fischer, N. Kalb, Xiaoling Lu, M. Haeberlein, F. Deppe, A. Marx, and R. Gross [1]
B. Peropadre, J. J. Garcia-Ripoll [2]

In circuit quantum electrodynamics (QED), fundamental quantum mechanical properties can be studied with macroscopic superconducting circuits [1]. More specific, microwave photons are trapped in waveguides or superconducting on chip cavities and interact with Josephson-junction based qubits [2], acting as artificial atoms. Furthermore, the large effective dipole moment of superconducting qubits allows the realization of coupling strengths [3], which are significantly higher than those in obtained in cavity QED setups in quantum optics. Here, we present building blocks for superconducting quantum circuits operated at low temperatures in the microwave regime. In the first part, we introduce a setup for tunable resonator-resonator coupling [4] and show preliminary experimental data. In the second part, we present first measurements on a 90° hybrid ring, which is analogous to a semitransparent mirror for propagating microwaves and therefore is a basic building block for experiments on propagating quantum microwaves.

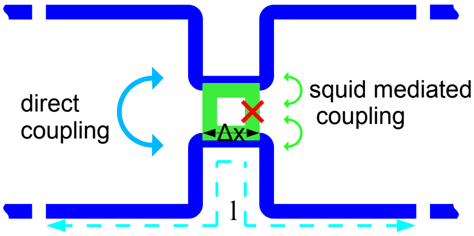

Figure 1: Setup for tunable coupling of microwave resonators (blue) connected via a rf SQUID. The latter consists of a superconducting loop (green) incorporating a Josephson junction (red cross). The arrows indicate the different coupling channels in the experiment.

In order to realize a tunable coupling between two superconducting on-chip resonators of length l, the resonators are connected via a rf SQUID with loop size Δx as depicted in Fig. 1. The standing microwave signals in a superconducting resonator are linked to macroscopic currents and voltages. Since the rf SQUID is placed in the center region of the resonators, where the resonator ground mode has a voltage node and current anti-node, the capacitive coupling between the resonators is negligible and only the inductive coupling has to be taken into account. The radio-frequency currents in the resonator induce circulating currents in the rf SQUID which in turn induce currents in the second resonator, thereby mediating resonator-resonator coupling of second order. The magnitude of the induced current in the rf SQUID loop depends on the magnetic flux Φ penetrating the loop. Therefore, the coupling can be controlled by an external magnetic field. A detailed analysis [4] leads to a coupling strength of

$$g_i = 4\pi^2 \frac{Z_0 I_c}{\Phi_0} \left(\frac{\Delta x}{l}\right)^2 \cos\left(\frac{2\pi\Phi}{\Phi_0}\right) . \tag{1}$$

Here, I_c is the critical current of the rf-SQUID junction, l and Z_0 are the total length and impedance of the resonator, respectively, and Φ_0 is the flux quantum. Note that I_c determines the maximum supercurrent circulating in the rf-SQUID loop and the cosine dependence on the magnetic flux Φ allows for an in situ control of the coupling strength.

---

[1] This work is supported by the German Research Foundation through the Collaborative Research Center 631, the German Excellence Initiative through the Nanosystems Initiative Munich (NIM), and the EU projects CCQED and PROMISCE.

[2] Instituto de Fisica Fundamental, IFF-CSIC, Madrid, Spain. Financial support by the Spanish MICINN Projects FIS2009-10061, FIS2011-25167, and CAM research consortium QUITEMAD S2009-ESP-1594 is gratefully acknowledged.

Since the resonators interact in second order, the coupling strength is proportional to the square of the relative interaction length $\Delta x/l$ shared by the resonators and the SQUID loop. A larger impedance Z_0 of the resonators implies that a larger part of the resonator energy is stored inductively, which is important for optimizing the inductive coupling mechanism.

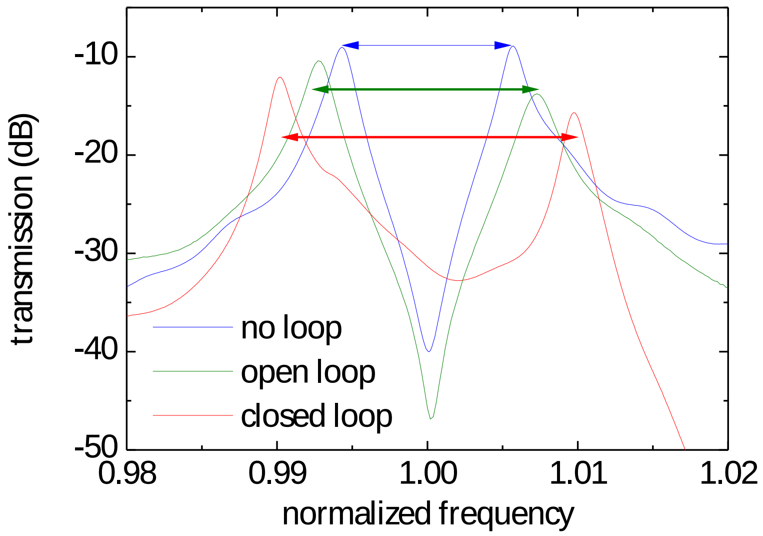

Figure 2: Transmission spectra of coupled resonators. The frequency is normalized to the frequency ω_0 of the uncoupled resonators. Split modes are observed at ω_-/ω_0 and ω_+/ω_0. The blue curve shows the result without any rf-SQUID coupling (only direct coupling is present). The green (red) curve shows the results obtained for an open (closed) superconducting loop mediating additional coupling.

The finite coupling of the two resonators leads to a splitting of the fundamental resonance frequency $\omega_0 \propto 1/l$ of the uncoupled resonators, resulting in two coupled oscillation modes at frequencies $\omega_\pm = \omega_0\sqrt{1 \pm g_i/\omega_0}$. Preliminary experimental results on the resonator-resonator coupling are shown in Fig. 2. The uncoupled resonators have a fundamental resonance frequency of 6.4 GHz. As illustrated in Fig. 1, there is a nonvanishing direct resonator-resonator coupling. This direct coupling is caused by the finite mutual inductance and capacitance between the two resonators in the coupling region with a length of 500 µm and separation of 100 µm. Outside this region the direct coupling can be neglected due to the much larger separation of the resonators. Fig. 2 shows that the normal mode splitting for the direct coupling (without loop) is $g/2\pi = 37$ MHz. Introducing an interrupted or closed superconducting loop of size $100 \times 100\,\mu\text{m}^2$, as sketched in Fig. 1, increases the coupling strength to $g/2\pi = 46$ MHz and $g/2\pi = 62$ MHz, respectively.

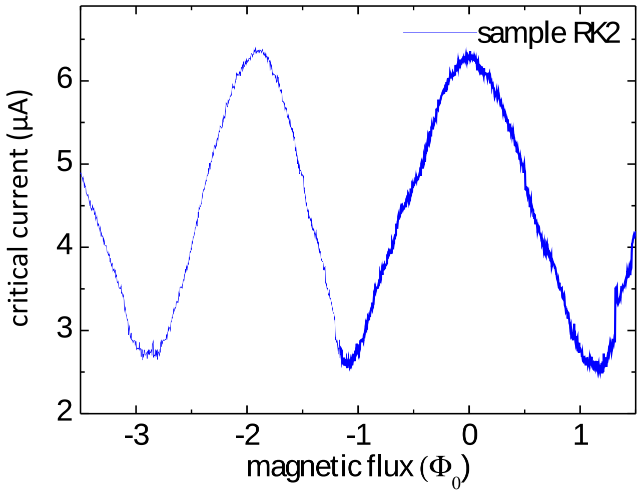

Figure 3: Critical current of a dc SQUID with a size of $100 \times 100\,\mu\text{m}^2$ plotted vs. the normalized magnetic flux.

To get information on the physical properties of the coupling structure consisting of a superconducting loop interrupted by one (or more) Josephson junctions we have fabricated individual superconducting (Nb) loops interrupted by two Josephson junctions (dc-SQUIDs). The junctions are fabricated in Nb technology using thermally oxidized AlO_x tunneling barriers. The result of preliminary studies is shown in Fig. 3. The critical current of the dc-SQUIDs shows the expected cosine dependence on the applied magnetic flux. The measured modulation period is in good agreement with that expected from the loop area of $100 \times 100\,\mu\text{m}^2$.

A rapidly growing research field in superconducting quantum circuits is the study of the potential of propagating microwave photons with respect to quantum computing and quantum communication. A key component required to manipulate propagating quantum microwave signals are beam splitters. In the microwave regime beam splitters can be realized as 90° hybrid rings, which act like a semi-transparent mirror at their center frequency. Due to the favorable port configuration of these hybrid rings, they allow the construction of on-chip interferometers, which can be used for gates in quantum computation [5]. First transmission experiments on a superconducting 90° hybrid ring are shown in Fig. 4. A coplanar waveguide design has been chosen for the hybrid ring, because it has low dielectric losses and is well suited for the coupling to flux qubits [3]. As shown in Fig. 4, a microwave signal applied at the center frequency of 9.75 GHz to port 1 is split equally to the ports 2 and 3, whereas the emission at port 4 is suppressed. Moreover, the expected 90° phase shift between the two output ports is confirmed for this sample.

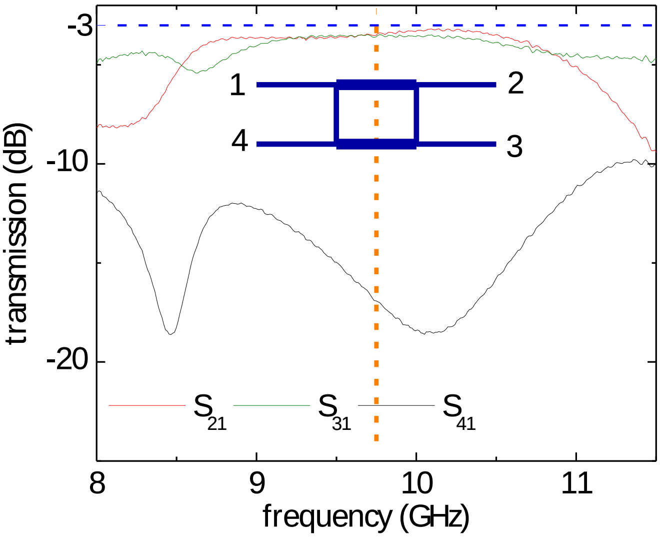

Figure 4: Transmission spectra of a 90° hybrid ring with a designed center frequency of 9.75 GHz (orange line). The notation S_{i1} means that a signal is applied at port 1 and the relative intensity is measured at port i. The blue dotted line marks the -3 dB level, expected for S_{21} and S_{31} in case of an ideal beam splitter operation. The inset shows a sketch of the hybrid ring.

References

[1] A. Wallraff, D. I. Schuster, A. Blais, L. Frunzio, R.-S. Huang, J. Majer, S. Kumar, S. M. Girvin, and R. J. Schoelkopf, Nature **431**, 162 (2004).

[2] T. Niemczyk, F. Deppe, M. Mariantoni, E. P. Menzel, E. Hoffmann, G. Wild, L. Eggenstein, A. Marx, and R. Gross, Supercond. Sci. Technology **22**, 034009 (2009).

[3] T. Niemczyk, F. Deppe, H. Huebl, E. P. Menzel, F. Hocke, M. J. Schwarz, J. J. Garcia-Ripoll, D. Zueco, T. Hümmer, E. Solano, A. Marx, and R. Gross, Nat. Phys. **6**, 772 (2010).

[4] B. Peropadre, D. Zueco, F. Wulschner, F. Deppe, A. Marx, R. Gross, and J. García-Ripoll. Tunable coupling engineering between superconducting resonators: from sidebands to effective gauge fields. `arXiv:1207.3408` (2012).

[5] J. L. O'Brien, Science **318**, 1567 (2007).

Scalable Chains of Coupled Superconducting Transmission Line Resonators

L. Zhong, L. Janker, F. Wulschner, F. Deppe, A. Marx, and R. Gross [1]

The investigation of many-body Hamiltonians is relevant to understand collective quantum behavior in solid state physics. However, solving these many-body Hamiltonians can be challenging on a classical computer. For this reason, quantum simulations are an attractive approach to investigate such complex Hamiltonians with experimentally easily accessible and well-controlled systems. In the following, we discuss our experiments towards this direction based on superconducting circuits. More precisely, we characterize chains of up to three coupled transmission line resonators in a scalable layout. After introducing nonlinearities [1–3] in the form of Josephson junctions and scaling to longer chains, our system can become a quantum simulator for Bose-Hubbard-type Hamiltonians in the future.

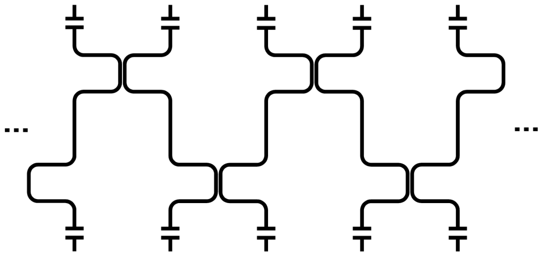

Figure 1: Coupling scheme for a one-dimensional network of transmission line resonators. Only the central conductors of the transmission lines are shown. Each resonator can be probed individually through the capacitors at both ends.

The flexibility of transmission line resonators regarding geometry and topology provides various possibilities to couple several resonators in a scalable network. In this experiment, we couple the resonators by reducing the distance between their center conductors for a certain length, as shown in Fig. 1. The advantage of this scheme is that each resonator can be probed individually. The coupling length is designed at quarter positions of the resonators, implying a coexistence of capacitive and inductive coupling for the fundamental resonance mode.

In the experiment presented here, we aim at a coupling strength between neighboring resonators larger than 50 MHz corresponding to about 10% of the resonator frequency. To optimize the design in the coupling region, we use FastCap, FastHenry, Microwave Office and Sonnet to simulate the coupling strength. The detailed information about simulation results and comparison of different programs can be found in Ref. [4]. In the end, we choose a 10 µm gap between the center conductors in the coupling region of two niobium coplanar waveguide resonators.

We characterize the transmission spectra (see Fig. 2) of a single-resonator, two coupled and three coupled resonators with a vector network analyzer at 4 K. The transmission spectrum of the single resonator exhibits a Lorentzian peak. When the second resonator is introduced, the single peak splits into two peaks because of the coupling. Next, when the third resonator is introduced, a splitting into three peaks is observed.

To understand the coupling between multiple resonators, we start with the analysis of two coupled resonators. A general model [5] based on the full Lagrangian of the two coupled transmission line resonators can be written as

$$\mathcal{H} = \sum_{j=1,2} \hbar\tilde{\omega}\, \hat{a}_j^\dagger \hat{a}_j - \hbar g_c \left(\hat{a}_1^\dagger - \hat{a}_1\right)\left(\hat{a}_2^\dagger - \hat{a}_2\right) - \hbar g_i \left(\hat{a}_1^\dagger + \hat{a}_1\right)\left(\hat{a}_2^\dagger + \hat{a}_2\right),$$

---

[1] This work is supported by the German Research Foundation through the Collaborative Research Center 631, the German Excellence Initiative through the Nanosystems Initiative Munich (NIM), and the EU projects CCQED and PROMISCE.

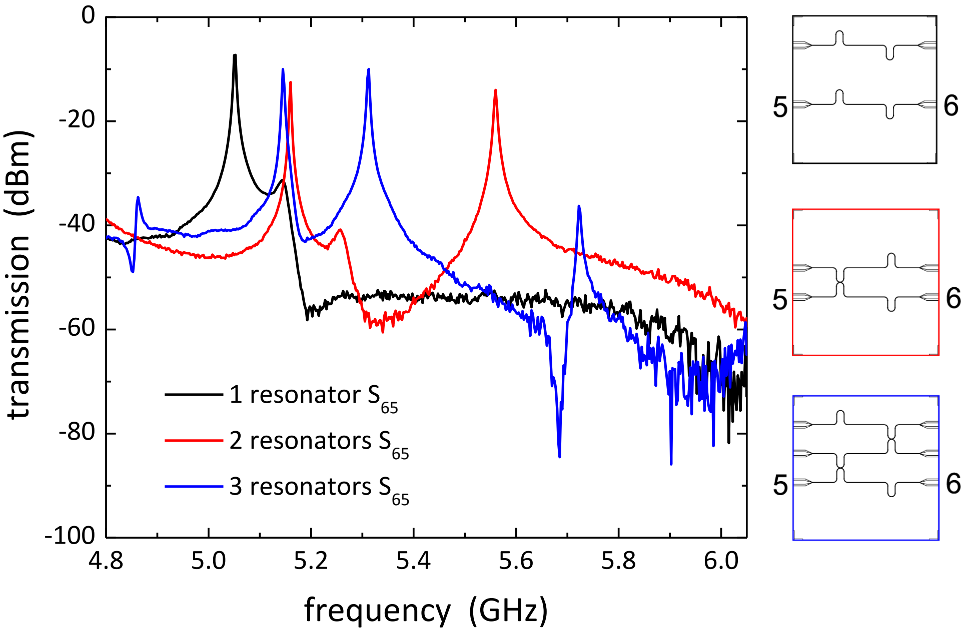

Figure 2: Transmission spectra of a single resonator, two coupled resonators and three coupled resonators measured at 4 K. The corresponding sample geometry is shown at the left.

where $\hat{a}_j^\dagger$ and $\hat{a}_j$ are the field operators which describe the fundamental mode of resonator j, and g_c and g_i are the capacitive and inductive coupling strengths, respectively. Compared to the simple beam splitter model, there are two major differences. First, the resonance frequency is normalized to $\widetilde{\omega}$. This leads to an asymmetric splitting around the resonance frequency of a single resonator. Second, the counter rotating terms, $\hat{a}_j^{\dagger 2}$ and $\hat{a}_j^2$, still need to be considered. By fitting experimental results with theory, we can estimate $g_i \approx 265\,\mathrm{MHz}$, $g_c \approx 58\,\mathrm{MHz}$, and $\widetilde{\omega} \approx 5.36\,\mathrm{GHz}$. From these parameters, we can correctly predict the spectrum of the sample with three coupled resonators.

In future, we plan to introduce Josephson junctions to obtain tunable coupling and tunable nonlinearity [1–3]. The techniques developed in this project can be used to investigate quantum correlations in linear and nonlinear networks and quantum simulations of many-body Hamiltonians.

References

[1] B. Peropadre, D. Zueco, F. Wulschner, F. Deppe, A. Marx, R. Gross, and J. García-Ripoll. Tunable coupling engineering between superconducting resonators: from sidebands to effective gauge fields. `arXiv:1207.3408v1` (2012).

[2] M. Mariantoni, F. Deppe, A. Marx, R. Gross, F. K. Wilhelm, and E. Solano, Phys. Rev. B **78**, 104508 (2008).

[3] M. Leib, F. Deppe, A. Marx, R. Gross, and M. Hartmann, New J. Phys. **14**, 075024 (2012).

[4] L. Janker. *Scalable chains of coupled superconducting transmission line resonators*. Bachelor thesis, Technische Universität München (2012).

[5] M. Haeberlein, F. Deppe, L. Augsbach, U. Ehmann, N. Kalb, A. Marx, R. Gross, D. Zueco, T. Weissl, J. Garcia-Ripoll, and E. Solano. Distributed Coupling of Superconducting Transmission Line Resonators.

Materials, Thin Film and Nanotechnology, Experimental Techniques

Dilution unit of the new refrigerator in quantum laboratory K04

Low-temperature Encapsulation of Coronene in Carbon Nanotubes

B. Botka, R. Hackl [1],
M. E. Füstös, G. Klupp, D. Kocsis, Á. Botos, K. Kamarás [2,3]
E. Székely, M. Utczás, B. Simándi [4]

Carbon nanotubes (CNT) are promising "nanocontainers" for the study of chemical reactions in a low-dimensional environment. Since single-walled carbon nanotubes (SWNT) have typical diameters in the range $0.7-2$ nm the appropriate selection of the host diameter facilitates specific reaction types. Another promising application area is protective packaging. These hybrid systems preserve the properties of the individual constituents, while the encapsulated species become more processable and mechanically stable in the cavity of the nanotubes making the systems candidates for biomedical applications. For instance, functional molecules such as fluorophores or drugs can be encapsulated while the outer surface of the nanocontainer can be functionalized with specialized targeting agents according to the needs of application [1, 2] (Fig. 1). Polycyclic aromatic hydrocarbons have evoked considerable attention lately in both areas. It was attempted to preserve their molecular fluorescence [3] inside the nanotubes or to subject them to polymerization reactions resulting in graphene nanoribbons [4].

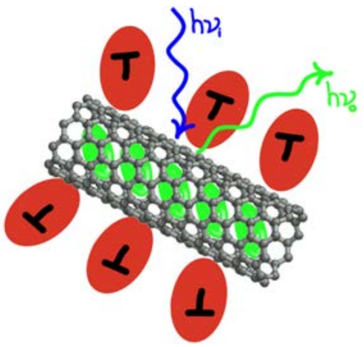

Figure 1: Principle of a possible biological application. The outer surface is functionalized with targeting agents (T), fluorescent molecules are encapsulated for optical labeling.

Coronene-filled nanotubes were first prepared by Okazaki *et al.* [3]. The stacked columns of coronene molecules inside the nanotubes were visualized by high-resolution transmission electron microscopy (HR-TEM). Talyzin *et al.* [4] likewise obtained HR-TEM images showing the coalescence of the molecules into graphene nanoribbons at elevated reaction temperatures. Besides TEM, Raman spectroscopy is a powerful tool to prove the encapsulation of molecules on a larger scale, and to provide information about side reactions between the guest molecules and about the nature of the host-guest interaction. The green luminescence found for the coronene-filled CNTs was assigned to originate from the stacked columns. However, since both the nanotubes and the coronene molecules possess extended π-electron networks, adhesion on the external surface by $\pi-\pi$ interaction is also very probable.

At moderate temperature, molecules can be encapsulated into CNTs from their molten or vapor phase and from solutions (nano-extraction, nano-condensation) [5]. The sublimation of molecules into the tubes results in filling ratios much higher than those of solution-based techniques because solvent molecules may irreversibly enter the tubes in addition to the desired species. On the other hand, at elevated temperatures the risk of undesired side reactions increases. Therefore, in contrast to the previous high temperature sublimation method at 450 °C, we used alternative techniques for coronene encapsulation with particular regard to the effect of the process temperature on the product [6]. We compared hybrids prepared by (i) vapor phase filling at high temperature (450 °C), (ii) vapor phase filling at moderate temperature (385 °C) and (iii) nano-extraction [7, 8] using supercritical CO$_2$ at 50 °C.

---

[1] Financial support was provided by the EU through the ITN Project FINELUMEN (PITN-GA-2008-215399).

[2] Wigner Research Centre for Physics, Hungarian Academy of Sciences, 1525 Budapest, Hungary.

[3] Financial support was provided by the Hungarian National Research Fund (OTKA grant 75813). M.E.F. was supported by the Sectoral Operational Programme For Human Resources Development 2007-2013, co-financed by the European Social Fund, under the project number POSDRU 107/1.5/S/76841 with the title "Modern Doctoral Studies: Internationalization and Interdisciplinarity".

[4] Budapest University of Technology and Economics, 1111 Budapest, Hungary.

For proving the encapsulation, the filled SWNT are annealed at 1250 °C to convert the enclosed molecules into inner nanotubes and thus form double-walled carbon nanotubes (DWNT) [9, 10]. This method can also differentiate between encapsulated species and those adsorbed on the outer surface. Such transformations have been studied successfully earlier for nanotubes filled with fullerenes (peapods) by the combination of various spectroscopic methods [11, 12]. For CNTs filled with coronene, new radial breathing modes (RBM) at higher energies are present for all filling techniques after annealing. They indicate the appearance of nanotubes with diameters smaller than those of the reference SWNT [13] and originate from the coalescence of the encapsulated coronene molecules (Fig. 2).

The high-temperature sublimation process produces also di-coronylene, a dimer of coronene. It is adsorbed on the outer surface of the SWNTs and can also be identified by Raman scattering experiments. The strong $\pi-\pi$ bonds between the nanotube and the dicoronylene makes it difficult to remove the dimer using standard purification techniques. This hampers the investigation of encapsulated molecules the signal of which is notoriously weak. In addition, dicoronylene adsorbed on the nanotube surface is luminescent in the green. Thus, its presence in the sample can lead to deceptive results regarding the properties of the hybrids.

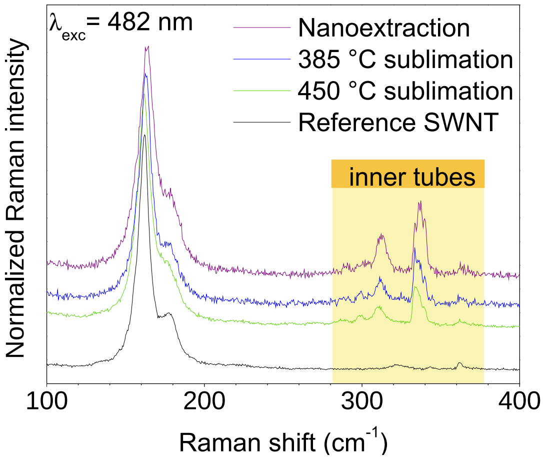

Figure 2: Raman spectra of CNTs. All samples were subject to the same annealing treatment at 1250 °C. The black line at the bottom is for the reference. The other lines represent spectra of samples after different encapsulation methods as indicated. New radial breathing modes belonging to inner tubes are shaded yellow.

With our alternative preparation methods using lower temperature, the nanotube surface remains clean making such samples particularly suitable for a detailed spectroscopic analysis and further functionalization.

References

- [1] C. A. Strassert, M. Otter, R. Q. Albuquerque, A. Höne, Y. Vida, B. Maier, and L. D. Cola, Angew. Chem. Int. Ed. **48**, 7928 (2009).
- [2] Z. Liu, S. Tabakman, K. Welsher, and H. Dai, Nano Res. **2**, 85 (2008).
- [3] T. Okazaki, Y. Iizumi, S. Okubo, H. Kataura, Z. Liu, K. Suenaga, Y. Tahara, M. Yudasaka, S. Okada, and S. Iijima, Angew. Chem. Int. Ed. **50**, 4853 (2011).
- [4] A. V. Talyzin, I. V. Anoshkin, A. V. Krasheninnikov, R. M. Nieminen, A. G. Nasibulin, H. Jiang, and E. I. Kauppinen, Nano Lett. **11**, 4352 (2011).
- [5] D. A. Britz, and A. N. Khlobystov, Chem. Soc. Rev. **35**, 637 (2006).
- [6] B. Botka, M. E. Füstös, G. Klupp, D. Kocsis, E. Székely, M. Utczás, B. Simándi, A. Botos, R. Hackl, and K. Kamarás, phys. status solidi (b) **249**, 2432 (2012).
- [7] M. Yudasaka, K. Ajima, K. Suenaga, T. Ichihashi, A. Hashimoto, and S. Iijima, Chem. Phys. Lett. **380**, 42 (2003).
- [8] A. N. Khlobystov, D. A. Britz, J. Wang, S. A. O'Neil, M. Poliakoff, and G. A. D. Briggs, J. Mater. Chem. **14**, 2852 (2004).
- [9] F. Simon, and H. Kuzmany, Chem. Phys. Lett. **425**, 85 (2006).
- [10] S. Bandow, M. Takizawa, K. Hirahara, M. Yudasaka, and S. Iijima, Chem. Phys. Lett. **337**, 48 (2001).
- [11] A. Botos, A. Khlobystov, B. Botka, R. Hackl, E. Székely, B. Simándi, and K. Kamarás, physica status solidi (b) **247**, 2743 (2010).
- [12] B. Botka, A. Pekker, A. Botos, K. Kamarás, and R. Hackl, phys. status solidi (b) **247**, 2843 (2010).
- [13] S. Reich, C. Thomsen, and J. Maultzsch. *Carbon nanotubes: Basic concepts and physical properties* (Wiley-Vch, 2008).

YIG ($Y_3Fe_5O_{12}$): Crystal Growth by the Traveling Solvent Floating Zone (TSFZ) Method

A. Erb

Yttrium iron garnet (YIG: $Y_3Fe_5O_{12}$) is a ferrimagnetic insulator with a Curie temperature of about 550 K. It shows a strong Faraday effect, high Q-factors at microwave frequencies and a very small linewidth in electron spin resonance. YIG is used in microwave, optical and in magneto-optical applications, solid-state lasers, in data storage and in nonlinear optics. Therefore this compound has been widely studied and has triggered the growth of YIG using various crystal growth techniques like growth from high temperature solutions, vapor phase growth or hydrothermal solutions. Despite these widespread applications the supply with single crystals of YIG seems to be difficult and expensive. Since the crystal growing group of the Walther-Meissner Institute and the crystal laboratory of the physics department of the TUM has excellent equipment and expertise we decided to make an attempt to grow YIG to support the group of magnetism inside the WMI, where YIG is used as a substrate for various experiments.

Yttrium Iron Garnet is a non congruently melting compound which makes it impossible to grow the crystals from a stoichiometric melt. The phase diagram has been reported by Van Hook [1] in the early sixties.

According to the phase diagram shown in Fig. 1 we selected a composition around 20 mol percent Y_2O_3 in $YFeO_3$ as a solvent for the crystals growth of YIG. The solvent pellet of about 0.5 g was placed in between feed and seed rod in our image furnace (Crystal Systems Inc., Japan). Melting was obtained at around 1500 °C and the molten zone was moved through the feed rod by moving the mirror system of the furnace. Crystal growth was performed in pure oxygen. Due to the relatively high solubility of $Y_3Fe_5O_{12}$ in its solvent the crystal growth speeds could be as high as 4 mm per hour.

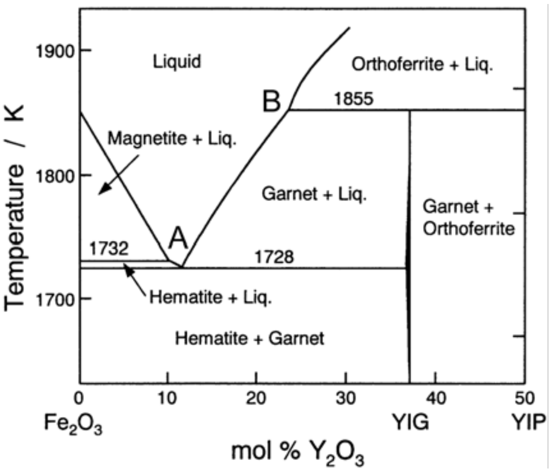

Figure 1: Phase relations in the system iron oxide - $YFeO_3$. Along the liquidus line between A and B, the $Y_3Fe_5O_{12}$ is in a thermodynamic equilibrium with a iron rich melt, which therefore can be used as a solvent for the TSFZ growth of YIG.

Fig. 2 shows some of the grown single crystals of $Y_3Fe_5O_{12}$. In lack of an oriented seed on the first growth experiments, grain selection of the predominant grain took place due to the different growth velocities in the different crystal orientations. We found that the crystals grew within a few degrees around the 111 direction. Subsequent growth experiments were then performed with 111 oriented seed crystals cut from the ingot of the first crystal growth experiments. Monocrystallinity and orientation could be easily checked using the Real Time Laue Backreflection camera (Multiwire Lab. Ltd. and Lauecamera.com) at the crystal laboratory of the faculty of physics TUM.

From the ingots we obtained from the different growth experiments many substrates were produced with different crystallographic orientation and with fine polished finish of optical

Figure 2: $Y_3Fe_5O_{12}$ single crystals grown by the TSFZ method. With growth speeds up to 4 mm/h this method is quite effective to produce large single crystals of this compound.

quality at the crystal laboratory of the faculty of physics, thus supporting the magnetism group of the Walther-Meißner-Institute.

References

[1] H. V. Hook, J. Am. Ceram. Soc. **45**, 162 (1962).

Building of a New Dilution Refrigerator in a WMI Quantum Science Laboratory

J. Goetz, M. J. Schwarz, K. F. Wulschner, J. Höß, K. Neumaier, C. Probst, F. Deppe, A. Marx, and R. Gross [1]

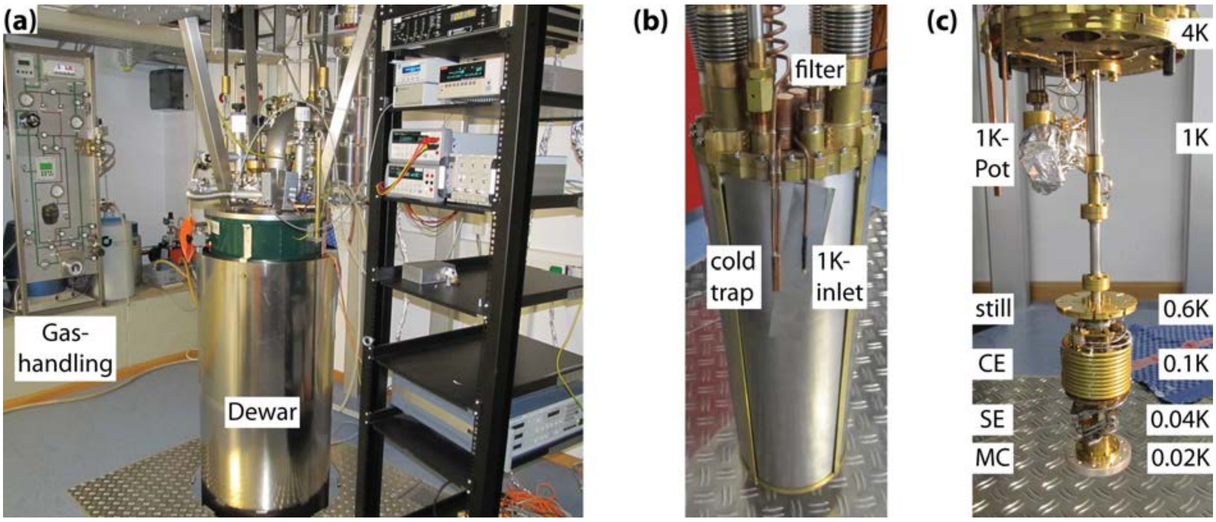

Figure 1: Photographs of the new refrigerator in the K04 lab. **(a)** Lab overview: The Dewar is shown in the center and the gas handling on the left hand side. **(b)** Mounted vacuum pot with cryoperm shield (silver shining). The incoming mixture goes through a 4 K cold trap and filters, which are also used for the 1 K-inlet. **(c)** Dilution unit installed to the 4 K stage: The temperature decreases from 4 K via the 1 K-Pot, the still, the coil exchanger (CE), the step exchanger (SE) to 20 mK at the mixing chamber (MC).

Last year, we presented first steps to set up a new liquid helium precooled dilution refrigerator for experiments with superconducting quantum circuits in the quantum laboratory K04 [1]. Here, we report on first successful cooldowns of this cryostat to base temperature. The dilution refrigerator is precooled with liquid nitrogen as well as liquid helium and uses a 1K-Pot to condense the ^{3}He/^{4}He mixture, cf. Fig. 1a - c. We designed the 1 K pot to have a large impedance $Z_{1K} = 6.6 \times 10^{11}$ to reduce helium consumption. Therefore, the time between two refills exceeds five days for a Dewar volume of 35 l. From measurements, we find a 1 K cooling power $\dot{Q}_{1K} \approx 20\,$mW (cf. Fig. 2a). The condensed mixture enters a capillary inside the still via the main impedance $Z_{\text{still}} = 3.5 \times 10^{11}$ for further precooling. The still itself has a maximum cooling power $\dot{Q}_{\text{still}} \approx 7\,$mW at 675 mK (cf. Fig. 2b). The latter is measured at a maximum throughput $\dot{n} = 175\,\mu$mol/s, which is mainly limited by the mechanical pre-pump behind the turbo molecular pump.

In a next step, the mixture enters a coil heat exchanger, which we designed with a large-sized cross-section on the diluted, ^{4}He-rich side. This allows for a maximum throughput of more than 175 µmol/s. On the other hand, we dimensioned the step exchanger sitting behind in a compact way to minimize the amount of ^{3}He for economic reasons. With this design the cryostat operates with a ^{3}He/^{4}He ratio of only 18% and a total amount of 4 l of ^{3}He gas. For our dilution unit it is possible to anchor measurement lines at the fourth winding of the coil exchanger and at the step exchanger, which reach a temperature of approximately 120 mK and 40 mK, respectively. The heart of the cryostat is the mixing chamber, which we have systematically analyzed concerning cooling power. We have determined the temperature-

---

[1] This work is supported by the German Research Foundation through the Collaborative Research Center 631, the German Excellence Initiative through the Nanosystems Initiative Munich (NIM), and the EU projects CCQED and PROMISCE.

dependent cooling power $\dot{Q}_{\mathrm{mc}}$ for different throughput (cf. Fig. 2c & d). For the maximum flow $\dot{n} = 175\,\mu\mathrm{mol/s}$ the cooling power at 100 mK reaches 80 µW and the base temperature is 18 mK. For a ^{3}He flow of 40 µmol/s the base temperature approaches a minimum below 14 mK. The ^{4}He flow of this cryostat is approximately 15%, which is an expected value.

The fridge will be used for circuit QED experiments with gradiometric tunable flux qubits coupled to superconducting transmission line resonators. We plan to implement pulsed SQUID readout schemes as well as resonator based readout [2]. Both methods provide a more detailed insight into tunable gradiometric flux qubits studied at the WMI [3, 4]. These qubits are promising candidates for the realization of various coupling schemes between qubits and coplanar waveguide resonators. They can also be utilized in establishing strong σ_x coupling between a resonator mode and the qubit enabling the simulation of relativistic quantum systems [5, 6]. These experiments require several cold amplifiers, circulators and switches at the 4 K stage of the cryostat. Considering this and planning with a larger Dewar, the space above the still was extended by 60 mm (cf. Fig. 1c). This still leaves enough space to perform first experiments with this Dewar, which are expected for next year when rf measurement lines and amplifiers have been installed. The fridge is designed for a total of 24 rf lines, which provides high flexibility for future experiments.

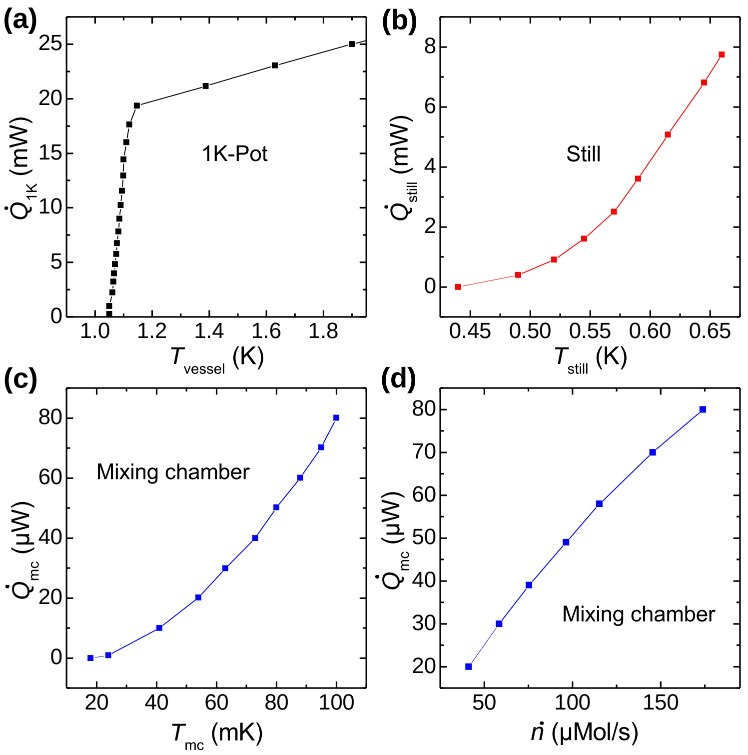

Figure 2: Cooling power for different parts of the cryostat. **(a)** Cooling power $\dot{Q}_{1\mathrm{K}}$ of the 1 K pot as a function of vessel temperature T_{vessel}. The maximum cooling power at 1.2 K is 20 mW. **(b)** Cooling power $\dot{Q}_{\mathrm{still}}$ of the distillation as a function of its temperature T_{still}. The maximum cooling power at $\dot{n} = 175\,\mu\mathrm{mol/s}$ and 675 mK is $\dot{Q}_{\mathrm{still}} \approx 7\,\mathrm{mW}$. **(c)** Cooling power $\dot{Q}_{\mathrm{mc}}$ of the mixing chamber as a function of its temperature T_{mc} for a constant flow of $\dot{n} = 175\,\mu\mathrm{mol/s}$. **(d)** Cooling power $\dot{Q}_{\mathrm{mc}}$ of the mixing chamber as a function of the flow $\dot{n}$. For $\dot{n} = 175\,\mu\mathrm{mol/s}$ the dilution unit reaches its maximum cooling power of 80 µW.

References

[1] F. Deppe, A. Marx, J. Höß, K. Neumaier, C. Probst, K. Uhlig, and R. Gross. New WMI Millikelvin Facilities for Experiments with Superconducting Quantum Circuits. In **WMI Annual Report**, 85 (Walther-Meißner-Institut, Garching, 2011).

[2] F. Deppe, T. Niemczyk, E. P. Menzel, A. Marx, and R. Gross. From Strong to Ultrastrong Coupling in Circuit Quantum Electrodynamics. In **WMI Annual Report**, 29 (Walther-Meißner-Institut, Garching, 2010).

[3] M. J. Schwarz, J. Goetz, Z. Jiang, T. Niemczyk, F. Deppe, A. Marx, and R. Gross. Gradiometric flux qubits with tunable gap. `arXiv:1210.3982` (2012).

[4] M. Schwarz, J. Goetz, T. Niemczyk, F. Deppe, A. Marx, and R. Gross. Gradiometric Flux Quantum Bits with Tunable Tunnel Coupling. In **WMI Annual Report**, 51 (Walther-Meißner-Institut, Garching, 2011).

[5] D. Porras, and J. J. Garcia-Ripoll, Phys. Rev. Lett. **108**, 043602 (2012).

[6] M. del Rey, D. Porras, and E. Martin-Martinez, Phys. Rev. A **85**, 022511 (2012).

Cryogen-free Dilution Refrigerator with Large Sample Stage

A. Marx, J. Höß, and K. Uhlig [1]

In last year's report we discussed the necessary measures to be taken to further develop our activities on quantum effects in the microwave regime. In particular, we have reported on the first steps in setting up a new cryogen-free refrigerator with a large diameter of all temperature stages in the Quantum Lab K21 providing extensive space for advanced quantum experiments based on a large number of bulky microwave components. Here, we report on the progress in the construction of this refrigerator. Both the vacuum can and three thermal shields have been externally manufactured and delivered in 2012. The gas handling systems for both the ^{3}He/^{4}He mash and for the ^{4}He (for precooling and 1 K stage) have been tested and mounted. The thermal connections between the two stages of the Pulse Tube Refrigerator (PTR) and the respective Cu plates [see Figs. 1(c) and (d)] are crucial components to provide efficient cooling of all components attached to these temperature stages. Especially, cooling the outer aluminum radiation shield as well as thorough radiation shielding turned out ot be essential to reach the base temperature at the second PTR stage. The thermal anchors made of flexible Cu mesh wire welded into Cu-parts have been successfully fabricated in the WMI workshop. The wiring for thermometry down to the second PTR stage has been installed.

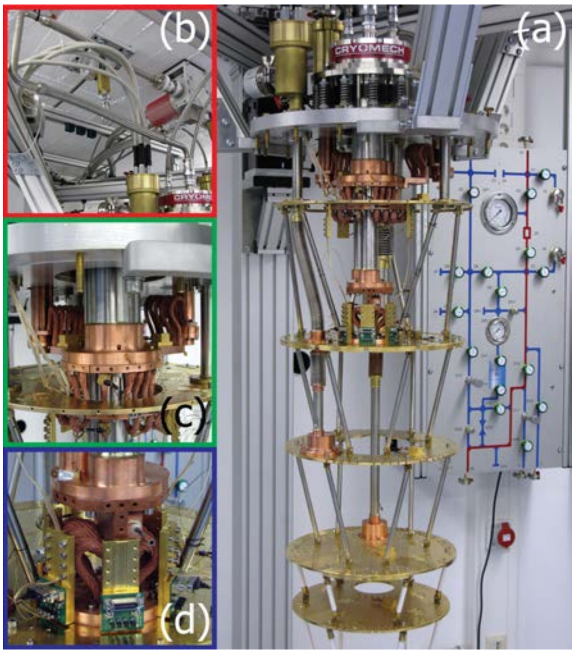

Figure 1: Photographs of the new cryogen-free dilution refrigerator. In **(b)** the U-shaped line connecting the PTR cold head to the remote motor. **(c)** Thermal anchoring of the large Cu plate and the charcoal traps to the first PTR stage via flexible Cu wires. **(d)** Thermal anchor of Cu plate and thermometry wiring to second PTR stage

To provide sufficiently high cooling power near 1 K to cool microwave components and cables, this refrigerator will be equipped with a 1 K stage (c.f. report by K. Uhlig on page 92). A majority of the components for the 1 K stage and for the dilution circuit have recently been finished in the WMI workshop. Fig. 2 shows a cool-down of the cryostat where only the first two Cu plates and the corresponding aluminum shields are mounted and thermally anchored to the PTR. In this configuration it took about 1.5 days to reach the minimum temperature of 2.5 K at the second PTR stage which is close to the unloaded design value of the PTR and 40 K at the first PTR stage.

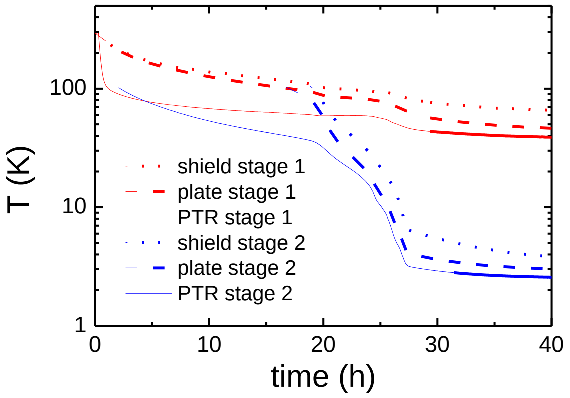

Figure 2: Cool-down of the first two temperature stages using PTR.

---

[1] We acknowledge financial support by the German Research Foundation through SFB 631, the German Excellence Initiative through the Nanosystems Initiative Munich (NIM), and the EU projects CCQED and PROMISCE.

Cryogen-free Dilution Refrigerator with ^{4}He-1 K-Stage

K. Uhlig

Introduction

Helium is a very rare and increasingly expensive commodity on our planet. Therefore, modern laboratory cryostats should be precooled by closed-cycle-refrigerators whenever possible, and not by helium dewars where the helium is lost to the atmosphere in the course of time. Besides, cryogen-free cryostats are much easier to operate than cryostats with liquid helium dewars. Modern laboratory cryostats are best precooled by pulse tube refrigerators (PTR) [1].

In last year's report we described how a ^{4}He cooling circuit was added to our cryogen-free dilution refrigerator (CF-DR) in order to make high refrigeration powers available at $T \sim 1\,\mathrm{K}$. Those are needed when the refrigeration power of the still of the DR ($T \sim 0.7\,\mathrm{K}$) is not sufficient, e.g. to cool cold amplifiers and to heat sink heavy electrical leads. The refrigeration power of the 1K-stage was as high as 100 mW, about a factor of ten higher than that of the still of the DR. In our cryostat, the two flow circuits of the DR and the 1K-stage could be run either separately or in parallel [2]. In our new design, the two circuits have been combined by running the condensation line of the DR through a heat exchanger (hx) in the pot of the 1 K-stage (see Fig. 1) [3]. The ramifications of this design are described below. Besides, an additional step heat exchanger was added to the dilution circuit to reach a lower base temperature (cf. Fig. 1), and a CMN (Cerous Magnesium Nitrate) [4] thermometer and a superconducting fixed point device (FPD) [5] were attached to the mixing chamber to measure these lower temperatures.

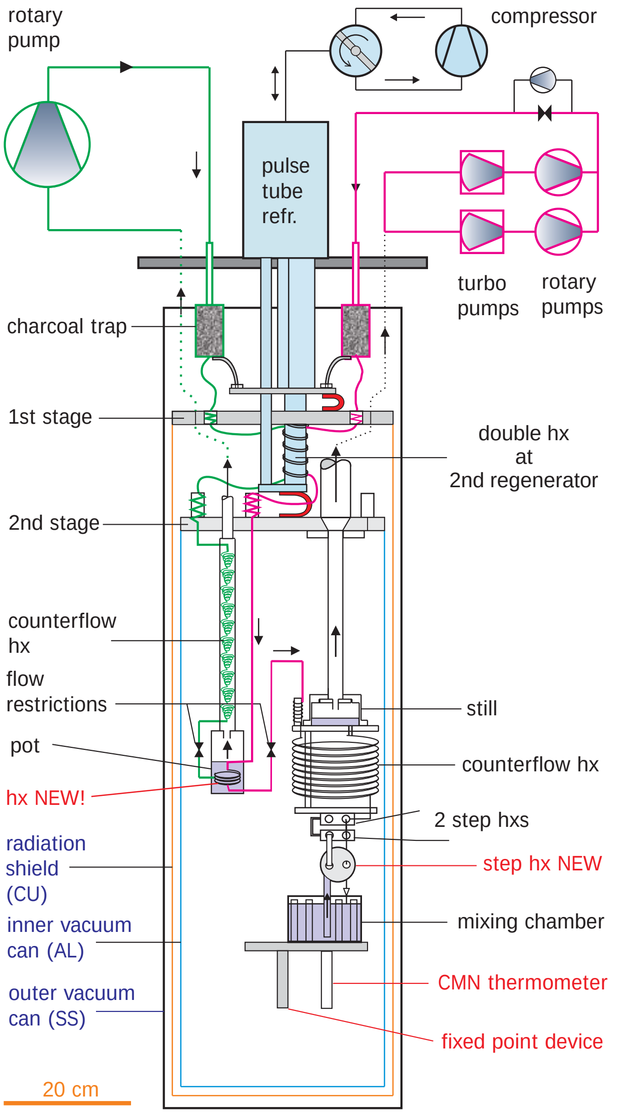

Figure 1: Cross-section of the CF-DR with 1 K-stage. The condensation line of the dilution unit is run through a hx in the pot of the 1 K-stage.

Experimental

If a ^{4}He-1 K-cooling circuit is available in a dry DR as ours, one can think of combining the dilution circuit with the 1 K-stage by running the condensation line of the DR through a hx

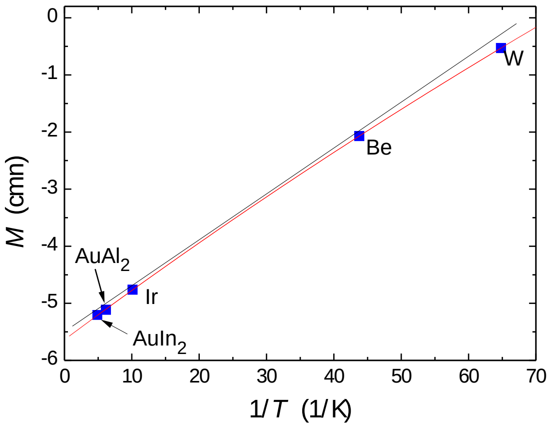

Figure 2: Calibration of our CMN thermometer with the FPD, see text. The red line is a fit to the experimental magnetization data and used for thermometry. The black straight line is a guide to the eye to show the deviation of the Curie-Weiss law from a Curie behavior.

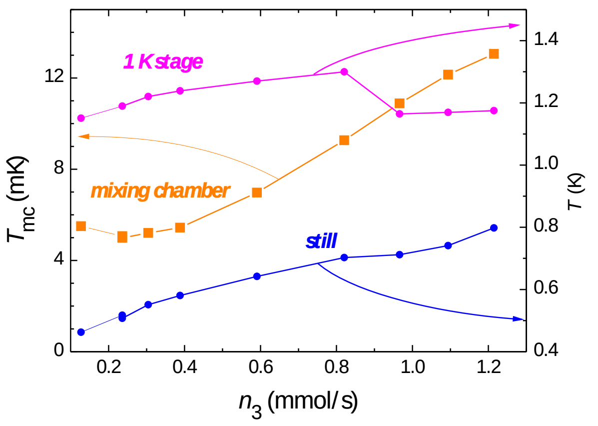

Figure 3: Temperature T_{mc} of the mixing chamber (orange curve, left scale) as a function of the ^{3}He flow n_3 (lowest temperature 5.0 mK). Also shown are the temperatures of the 1 K-stage and of the still (right scale).

which is placed in the pot of the 1 K-stage. Then, during the initial condensation of the ^{3}He/^{4}He gas mixture a better condensation rate is achieved. Experimentally we found the condensation rate was doubled (120 stdl/h). And, in addition, the condensation pressure of the ^{3}He/^{4}He mash could be kept below atmospheric pressure at all times so a compressor in the dilution circuit became superfluous. ^{3}He prices are sky-high; therefore it is of considerable advantage to keep pressures below 1 bar as the risk of losing ^{3}He is greatly reduced. For comparison, without the 1 K-stage the pressure of the ^{3}He/^{4}He mash during condensation is typically 5 bar.

Another change was the addition of a third step hx to the dilution circuit. So far, there was no concrete evidence for a sizable vibrational heat leak caused by the PTR, and thus another hx should lead to a lower base temperature of the mixing chamber. The hx has large-surface silver sponges in the concentrated and dilute side ($\sim 120\,\mathrm{m}^2$). The volume of the hx is 12.5 cm^3 for each side.

A commercial CMN thermometer was installed for thermometry; the susceptibility of Cerium-Magnesium-Nitrate follows a Curie-Weiss-law at low temperatures. For calibration, a superconducting fixed point device was available where the superconducting transition points of 5 different metal samples provide temperate fixed points which can be used for calibration purposes. To provide the best thermal contact possible between CMN and FPD, both thermometers were screwed directly into the silver bottom plate of the mixing chamber. The FPD has to be shielded from magnetic fields; this is accomplished with a cryoperm shield and a lead shield. In Fig. 2, the magnetization of our CMN thermometer is plotted for the 5 transition points of the FPD ($1/T$-plot).

In Fig. 3, the base temperatures of the DR are depicted as a function of the ^{3}He flow rate (orange curve). The lowest temperature of the mixing chamber varies between 5.0 mK for a small flow to 13 mK for the highest flow rate which is given by the pumping capacity of the turbo pumps.

Outlook

In a next step we plan to determine the influence of the acoustic vibrations of the PTR on the low temperature performance of the DR. Now, with a 1K-stage available, it is possible to turn off the PTR for a longer time span and monitor the reaction of the mixing chamber. The idea is to condense enough ^{4}He into the vessel of the 1K-stage so it can precool the DR for several minutes without the PTR in operation. Although the 2nd stage of the PTR will warm up by 5 to 10 K, the DR will be precooled by the 1K-stage and continue to operate undisturbed. This method could be used to optimize the mechanical connection between PTR and cryostat and to eliminate vibrational heat leaks into the DR.

References

[1] R. Radebaugh. Development of the PTR as a efficient and reliable cryocooler. Tech. Rep., NIST, Boulder (2000).
[2] K. Uhlig, Adv. Cryo. Eng. **57B**, 1823 (2011).
[3] .
[4] Website: www.smallcoil.com.
[5] FPD from NIST (formerly NSF).

Experimental Facilities

Overview of Key Experimental Facilities and Infrastructure

In the following basic information on the key experimental facilities and components of the technical infrastructure installed at the Walther-Meißner-Institute (WMI) is given.

UHV-Laser-MBE

The WMI operates a UHV-Laser-Molecular Beam Epitaxy (L-MBE) system for the growth of complex oxide heterostructures. The system has been designed to meet the special requirements of oxide epitaxy. The UHV cluster tool consists of the following main components:

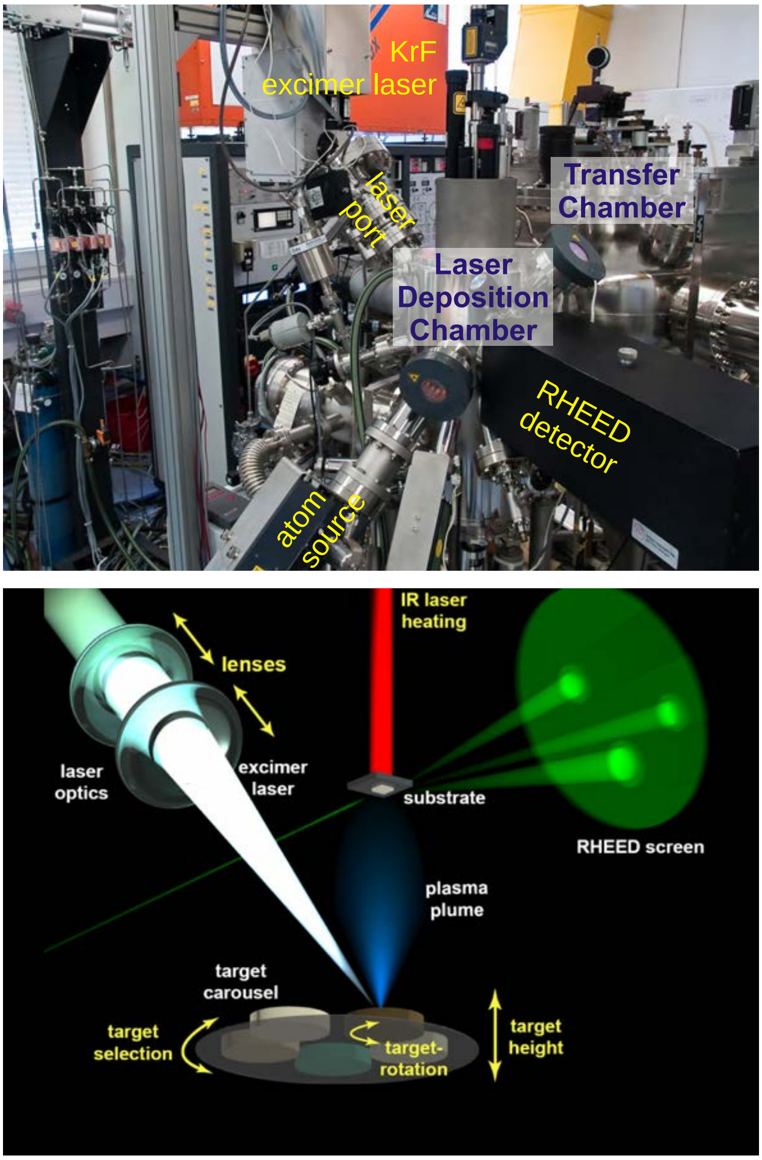

Figure 1: Top: UHV-Laser-Molecular Beam Epitaxy System. Bottom: Principle of the deposition process.

- central transfer chamber;
- load-lock chamber with heater system for substrate annealing;
- laser deposition chamber with in-situ reflection high energy electron diffraction (RHEED) system, laser substrate heating system, and atomic oxygen/nitrogen source, the RHEED system has been modified to allow for the operation at high oxygen partial pressure up to 0.5 mbar;
- surface characterization chamber with UHV scanning force microscope (Omicron);
- metallization chamber with a four heart electron gun system and a liquid nitrogen cooled sample stage. The sample holder can be tilt for shadow evaporation;
- KrF excimer laser.

The system is used for the growth of complex oxide heterostructures consisting of superconducting, magnetic, dielectric, and semiconducting materials such as the high-temperature superconductors, the doped manganites, the double perovskites, magnetite, zinc oxide, etc..

The original laser molecular beam epitaxy system (laser-MBE) designed already in 1995/96 until now has been permanently upgraded and modified. In particular, the substrate heating system and the temperature control unit was changed from a resistive radiation heater to an infrared laser heating system (see Fig. 3, left) including a pyrometer for determining the sample temperature. In addition, a source for atomic oxygen and nitrogen has been added. The main advantage of the new heating system is that only the substrate is heated while the surrounding parts are hardly affected (Fig. 3, right). In this way one can achieve an essentially better vacuum at temperatures well above 1000 °C. The achievable substrate temperature is limited by the melting point and the size of the substrate material (approx. 1410 °C for a $5 \times 5\,\mathrm{mm}^2$5 silicon substrate). The laser heating system has already been successfully used for removing the amorphous silicon oxide layer from the surface of silicon substrates at 1150 °C. This is required for the epitaxial growth of oxide thin films on this substrate.

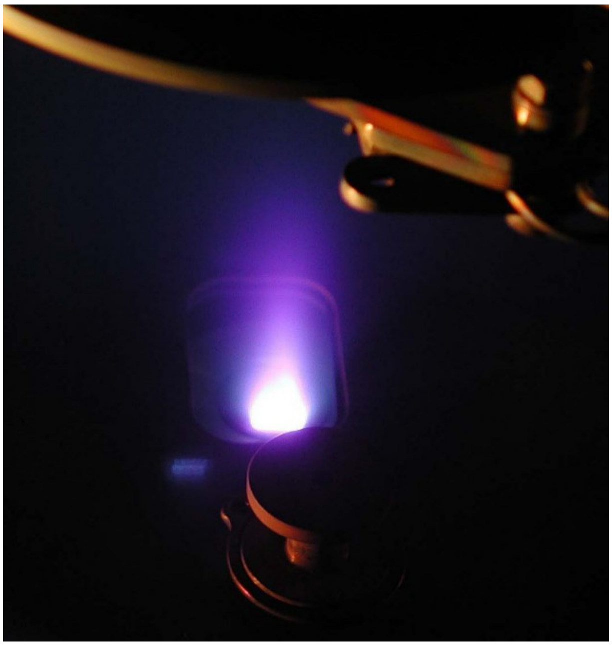

Figure 2: Pulsed Laser Deposition (PLD): When the pulse of the UV laser (KrF excimer laser, 248 nm) hits the target, the target material is ablated and the so-called laser "plume" containing highly excited atoms and molecules is formed.

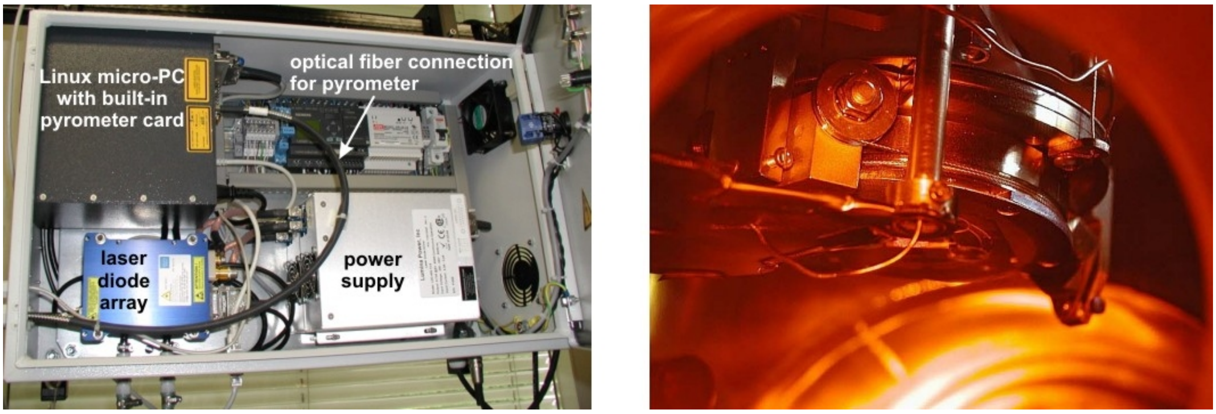

Figure 3: Components of the laser heating system: The substrate is heated using an IR diode laser head that is located in a separate box far away from the deposition chamber (left). The laser light is brought to the substrate (right) via an optical fiber.

Single Crystal Growth and Synthesis of Bulk Materials

Transition metal oxides are of great interest due to their various interesting physical properties (e.g. high temperature superconductivity, colossal magnetoresistance, ferroelectricity, nonlinear optical properties etc.) and their high potential for applications. Therefore, the WMI operates a laboratory for the synthesis of bulk materials and single crystals of transition metal oxides. Besides various chamber- and tube furnaces a four-mirror image furnace is used in the crystal growth of various oxide systems. With this furnace crystals of many different compounds of the high temperature superconductors and various other transition metal oxides have been grown as single crystals using the traveling solvent floating zone technique. The furnace consists basically of 4 elliptical mirrors with a common focus on the sample rod and with halogen lamps in their other focus. By irradiation of the focused light the sample rod is locally heated and eventually molten. The molten zone can be moved up and down along the entire sample rod under simultaneous rotation. Due to the anisotropic growth velocity a preferential growth of those grains with the fastest growth velocity along the pulling direction is obtained and the formerly polycrystalline rod is transformed into a single crystal. Single crystal growth can be performed with this furnace at maximum temperatures up to 2200 °C in the pressure range from 10^{-5} mbar up to 10 bar and in oxidizing, reducing as well as inert atmosphere.

Figure 4: The four-mirror image furnace installed at the crystal laboratory of the WMI. Crystals can be grown by the floating zone and traveling solvent floating zone technique at temperatures up to 2200 °C and pressures up to 10 bar.

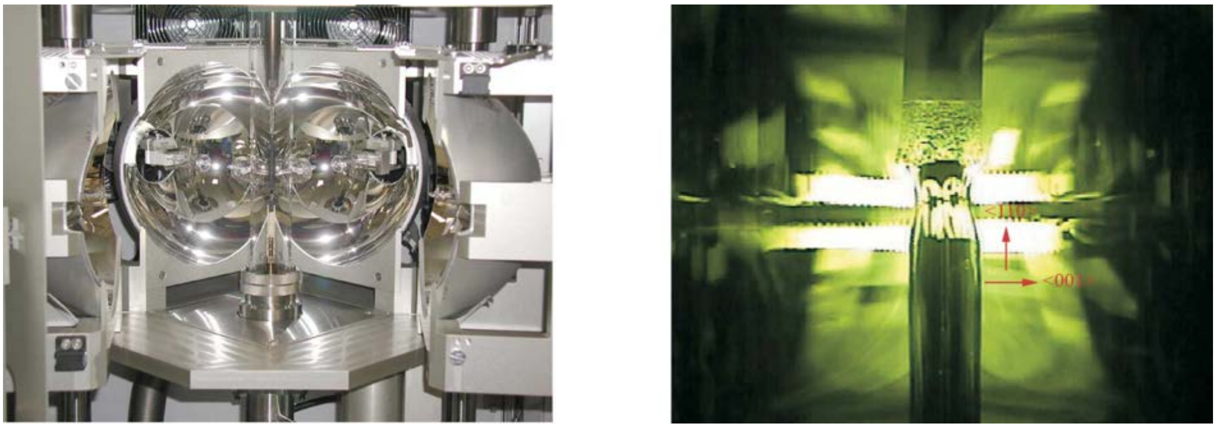

Figure 5: Left: Central part of the image furnace with the four elliptical mirrors. In the center one can see the quartz tube with the poly-crystalline rod. Right: View on the molten zone of $Pr_{2-x}Ce_xCuO_4$ (melting point: 1280 °C) obtained by a CCD camera.

The X-ray diffraction systems

For x-ray analysis the Walther-Meissner-Institute operates two X-ray diffractometers (Bruker D8 Advance and D8 Discover). The two-circle system is used for powder diffraction. In this system the samples can be heated in oxygen atmosphere up to 1600 °C. It is equipped with a Göbel mirror and an area detector to save measuring time. The second system is a high resolution four-circle diffractometer that can be used for reciprocal space mappings. It is equipped with a Göbel mirror and an asymmetric two-fold monochromator and allows for the texture analysis of thin film superlattices and single crystalline materials. In both systems measurements can be carried out fully computer controlled.

Beyond these two Bruker x-ray systems a Laue camera for single crystal analysis and a Debye-Scherrer camera are available.

Figure 6: The two-circle X-ray diffractometer Bruker D8 Advance.

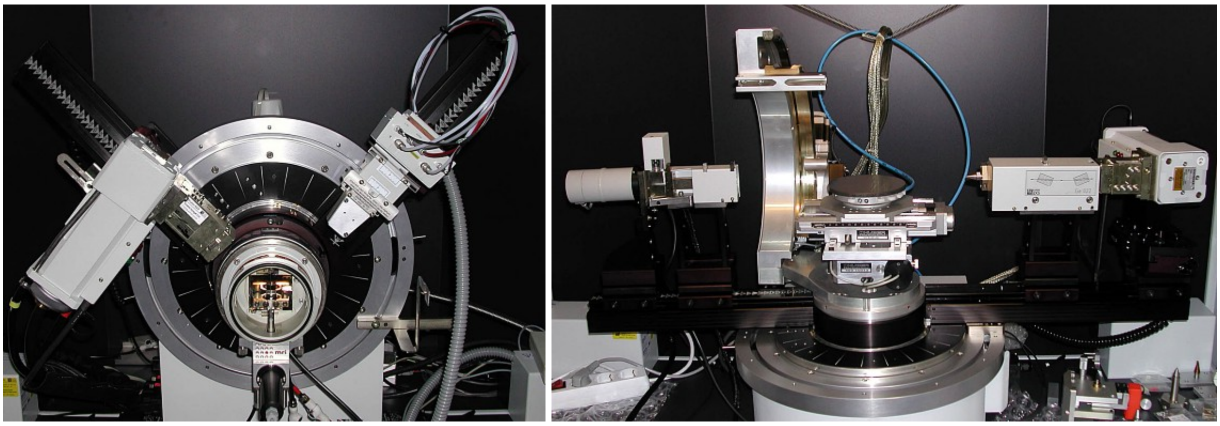

Figure 7: Left: High temperature sample holder of the D8 Advance system. Right: Four-circle high resolution X-ray diffractometer Bruker D8 Discover.

Figure 8: Quantum Design SQUID magnetometer.

The SQUID-magnetometer

For the analysis of the magnetic properties of materials, a Quantum Design SQUID magnetometer system as shown in Fig. 8 is used at the WMI. The SQUID magnetometer allows for measurements in the temperature regime from 1.5 to 400 K and provides excellent sensitivity particularly in the low field regime. Due to the excellent sensitivity of the system, thin film samples with a very small sample volume can be analyzed. In a special inset, samples can be measured up to temperatures well above room temperature (up to 500 °C). For this option the sample volume has to be reduced. The SQUID magnetometer is equipped with a superconducting solenoid allowing for a maximum field of 7 T. At present, the magnetometer is used for the characterization of magnetic materials (both in bulk and thin film form). Examples are the doped manganites, magnetite, the double perovskites, magnetic semiconductors, or multiferroics.

The High Field Laboratory

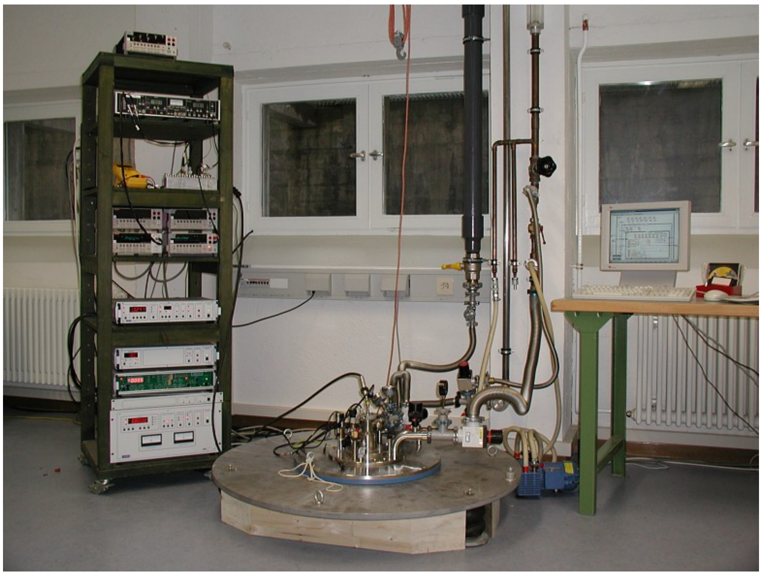

Figure 9: High field laboratory with Oxford 17 T magnet system.

Transport and thermodynamic properties of samples are often studied as a function of applied magnetic field. For such measurements several superconducting magnets are available at the WMI. Two of them (8/10 and 15/17 Tesla magnet system) are located in the high magnetic field laboratory in the basement of the WMI. The magnet systems are lowered below the ground level to facilitate the access to the top flange and the change of the sample sticks. The magnet systems are decoupled from the building to avoid noise due to mechanical vibrations. A variety of sample holders can be mounted allowing for e.g. sample rotation during the measurement. For standard sample holders the accessible temperature regime is $1.5\,\mathrm{K} < T < 300\,\mathrm{K}$. However, also ^{3}He/^{4}He dilution refrigerator inserts ($T > 20\,\mathrm{mK}$) or high temperature units ($T < 700\,\mathrm{K}$) can be mounted. All measurements are fully computer controlled (by the use of the LabView software tool) allowing for remote control and almost continuous measurements.

Since 2012, a 3D vector magnet with variable temperature insert, allowing for 2 T in-plane and 6 T out-of-plane magnetic fields is available for thermal and electrical transport experiments.

A further 3D vector magnet allowing for 1 T in-plane and 6 T out-of-plane magnetic fields is installed in the WMI Quantum Laboratories as part of a cryogen-free dilution system (see page 107).

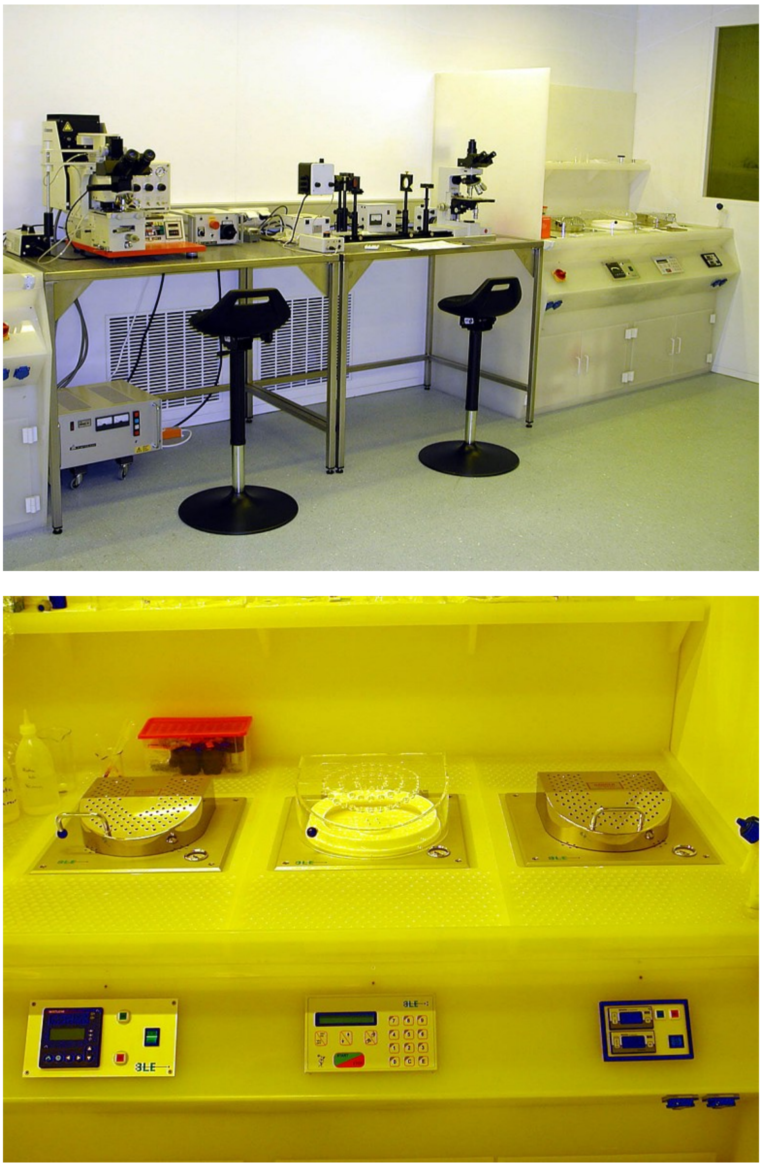

Figure 10: Top: Part of the clean room facility with optical lithography equipment and clean room benches. Bottom: Resist coater and hot plates.

The Clean Room Facility

For the fabrication of nanostructures and superconducting as well as spintronic devices the WMI operates a class 1000 clean room facility with an area of about $50\,\mathrm{m}^2$. This clean room facility has been put into operation at the WMI within the year 2001. The clean room is subdivided into two parts for optical lithography and electron beam lithography, respectively. The clean room facility is equipped with the standard tools for optical lithography such as resist coaters, hot plates, wet benches, a Karl Süss MJB3 mask aligner and an optical projection lithography system. The technical infrastructure for the clean room is located in the basement of the WMI directly below the clean room area.

Since 2005 the clean room also is equipped with a reactive ion etching system, Plasmalab 80 Plus with ICP plasma source (Oxford Instruments Plasma Technology).

Electron Beam Lithography

The Electron Beam Lithography System is installed in one part of the clean room facility. It consists of a Philips XL 30 SFEG scanning electron microscope (SEM) with a Raith Elphy Plus electron beam lithography system and a laser interferometer table for precise stitching of writing fields.

The SEM is equipped with a hot field emitter and typically provides a beam diameter of less than 1.5 nm at $\geq$ 10 keV or about 2.5 nm at 1 keV. The lithography unit allows the fabrication of nanostructures down to about 10 nm. We have realized the controlled fabrication of metallic strip patterns with a strip width of about 20 nm. The electron beam lithography is used for the fabrication of nanostructures in metallic and oxide systems required for the study of quantum effects in mesoscopic samples.

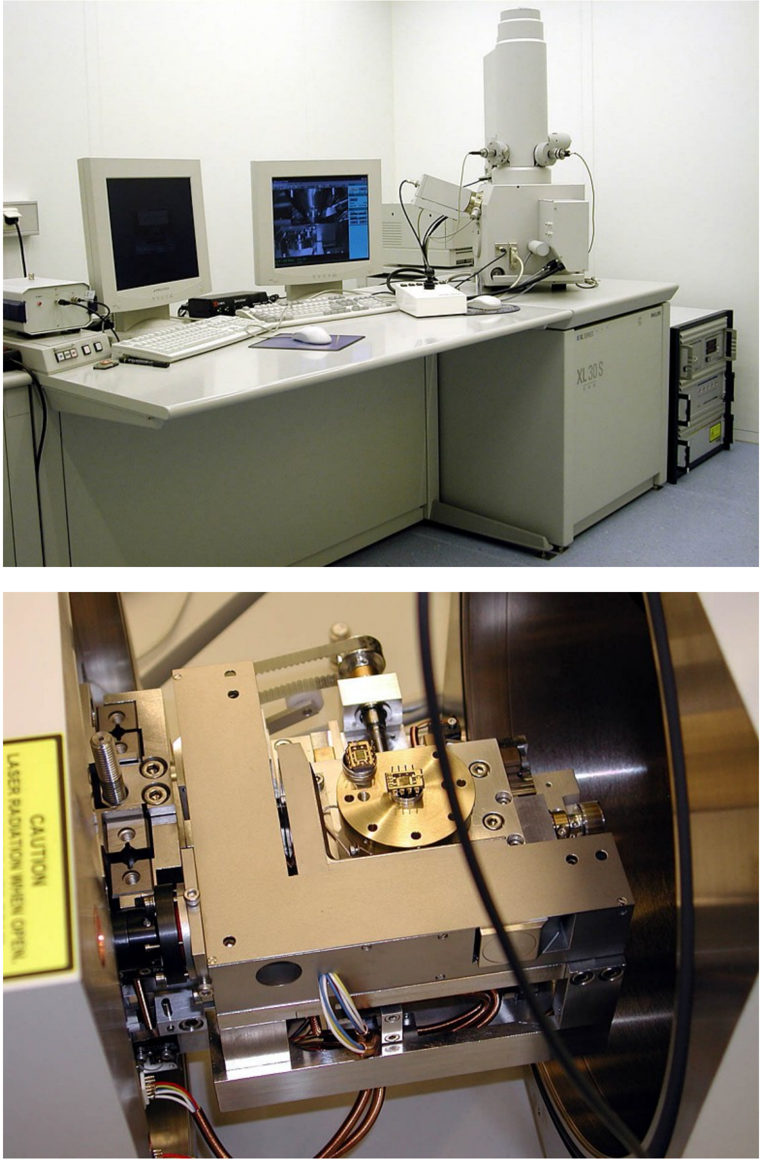

Figure 11: Top: Philips XL 30 SFEG Scanning Electron Microscope with Raith Elphy Plus Lithography System. Bottom: Raith Laser Stage.

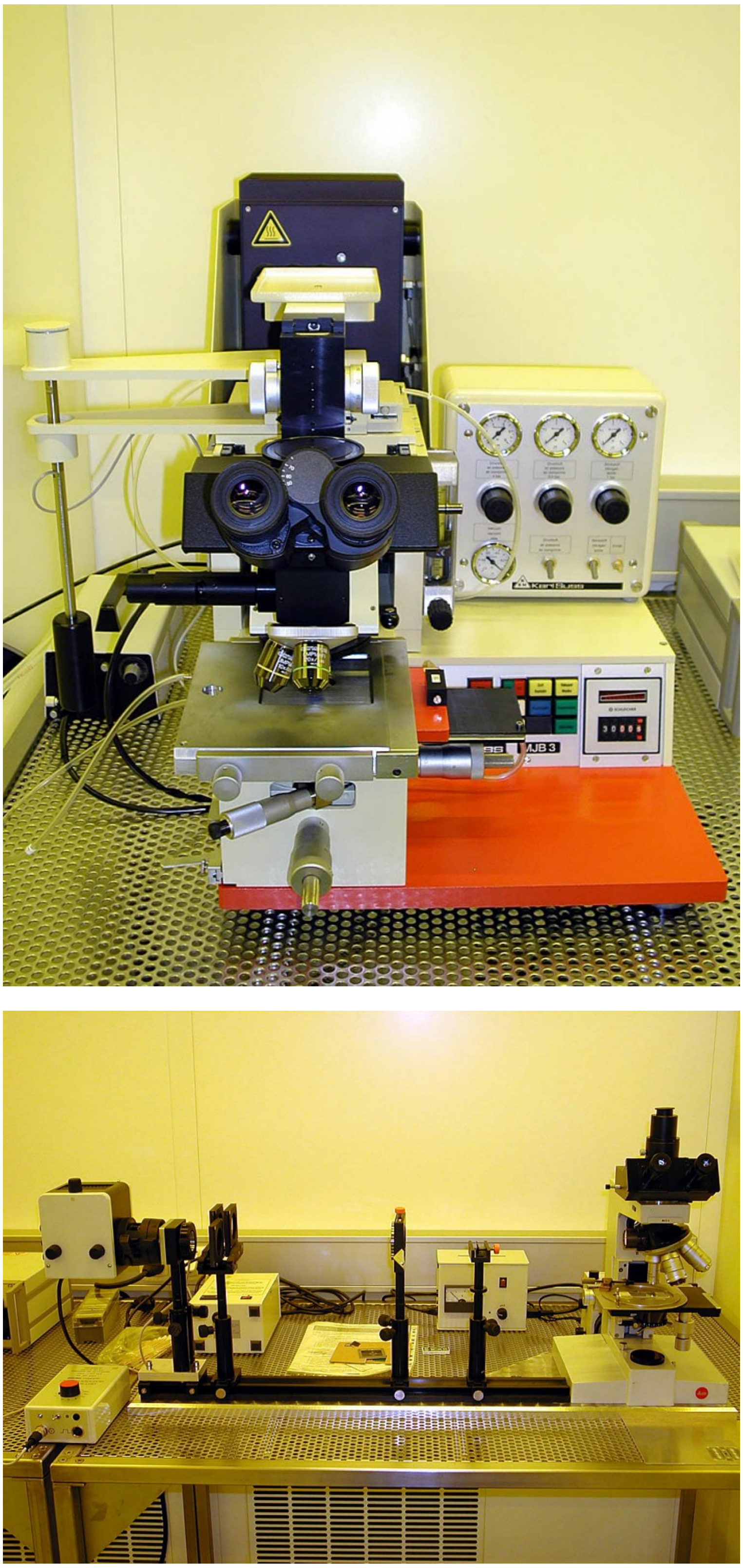

Figure 12: Top: Süss MJB 3 maskaligner for optical lithography. Bottom: Optical projection lithography based on an optical microscope.

Optical Lithography

For optical lithography a Karl Süss MJB 3 maskaligner or an optical microscope based projection system are used. The maskaligner is operating in the 1 : 1 soft or hard contact mode and is using chromium metal masks. In the projection system the mask pattern is demagnified by a factor of 5 to 100. Therefore, cheap foil masks can be used. With both systems microstructures with a lateral dimension down to 1 µm can be fabricated.

Low and Ultra-low Temperature Facilities

The WMI operates several low and ultra-low temperature facilities that have been developed and fabricated in-house.

The lowest temperature is achieved by the nuclear demagnetization cryostat "Bayerische Millimühle 2". This ultra-low temperature facility consists of an in-house built dilution refrigerator and originally of two nuclear demagnetization stages. The first of those is based on a hyperfine enhanced van Vleck paramagnet $PrNi_5$ (0.9 mol), the second, which has been removed a few years ago, was based on purified copper (0.2 mol). The lowest temperature reached with this system was slightly below 30 µK in the copper nuclear spin system. At the moment, the first stage can be cooled to below 400 µK and, due to the large heat capacity of $PrNi_5$, it stays below the mixing chamber temperature (5 mK) for nearly 3 weeks. In this cryostat three measuring sites are provided, two in a magnetic field compensated region and one in the center of an 8 T magnet. They are suitable for specific heat measurements, for capacitive torque- and SQUID magnetometry, as well as for transport measurements (electrical und thermal conductivity). The cryostat is also equipped with a pressure cell for liquid and solid ^3He, which at the moment is used for nuclear spin resonance measurements below 1 mK.

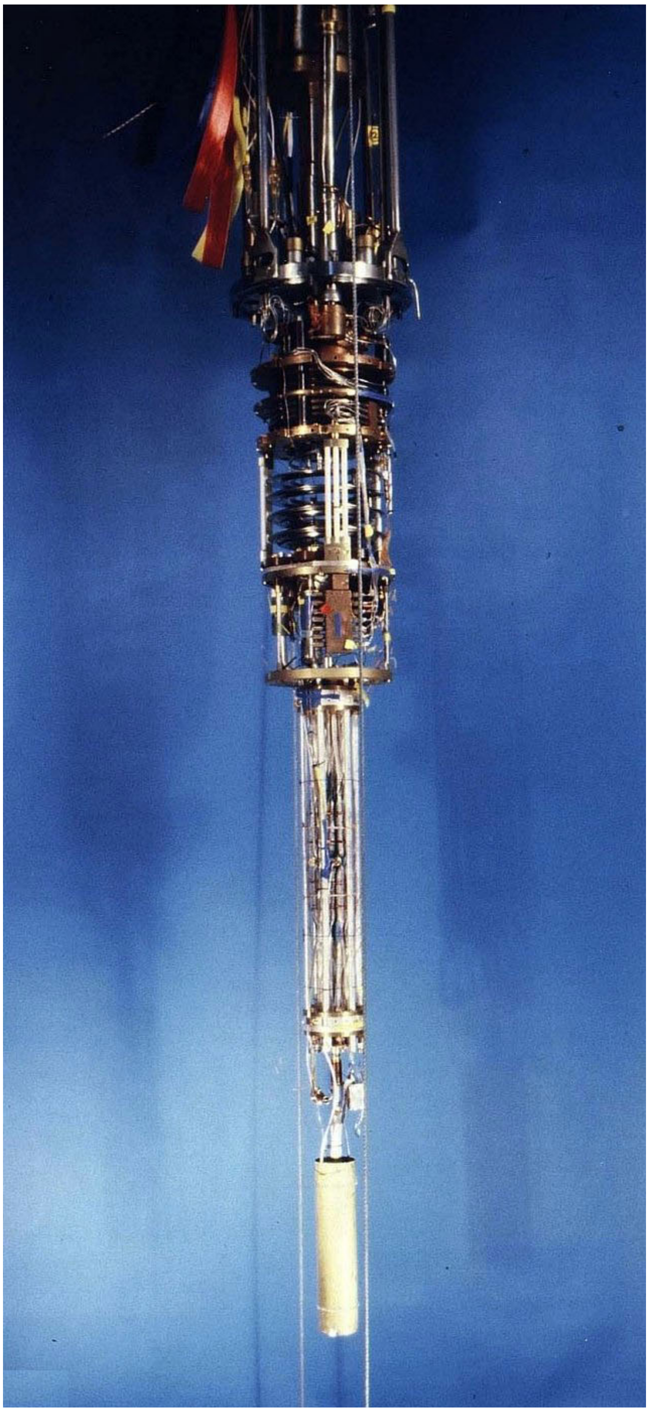

Figure 13: The dilution refrigerator and the nuclear demagnetization stage of the nuclear demagnetization cryostat "Bayerische Millimühle 2".

Figure 14: The "dry" dilution refrigerator of the WMI.

Figure 15: Low-temperature unit of a WMI dilution refrigerator ready to go into a cryostat.

Some years ago, at the WMI, we have constructed the first dilution refrigerator with pulse tube precooling for ultra-low temperature experiments. This type of refrigerator works without cryo-liquids, and thus is a lot more practical, more economical and more reliable than cryostats with liquid helium pre-cooling. These days, all major cryoengineering firms are offering commercial versions of this milli-Kelvin cooler, and these so-called "dry" refrigerators outsell conventional refrigerators by a wide margin. The general construction concept of most manufacturers is unchanged from our original prototype, where the refrigerator consists of three basic components. The first cooling stage is a commercial pulse tube cryocooler which reaches a base temperature of 2.5 K. The second stage is a Joule-Thomson stage, and the last stage is a dilution refrigeration stage, where the lowest temperature of the cryostat is about 0.01 K (Fig. 14).

In many low temperature applications high refrigeration capacities are required. Our design allows for a high circulation rate of ^{3}He which in the end determines the cooling power of a dilution refrigerator. Presently our "dry" fridge reaches a refrigeration capacity of 700 µW at a temperature of the mixing chamber of 0.1 K, seven times the cooling power of the WMI nuclear demagnetization cryostat. Goals of our present work are a further increase of cooling power and a lower base temperature of the dry dilution refrigerator.

Figure 16: Two mixing chamber mounting plates with silver sponges. Those are needed to overcome the thermal resistance (Kapitza resistance) between the liquid ^{3,4}He and the mounting plate of the mixing chamber. To fabricate the mounting of the sponge (square pins embedded in the sponge) a spark erosion technique has been employed.

A smaller version of our cryogen-free fridge has become commercially available at VeriCold Technologies, Ismaning. It has a refrigeration capacity of 250 µW at a mixing chamber temperature of 0.1 K (Fig. 15).

The WMI also develops and fabricates dilution refrigerator inserts for temperatures down to about 20 mK. The inserts fit into all cryogenic systems (e.g. superconducting magnets) having a two inch bore. They allow fast sample change and rapid cool down cycles of less than five hours. The dilution refrigerator inserts are engineered and fabricated in-house and are also provided to other low temperature laboratories for ultra low temperature experiments.

Millikelvin Temperatures in Combination with 3D Vector Magnetic-Fields

Figure 17: The dilution system with the 3D vector magnet located in the Quantum Laboratories and operating at base-temperature.

Part of the Quantum Laboratories at the Walther-Meißner-Institut is a cryogen-free dilution system equipped with a 3D vector magnet allowing for 1 T in-plane and 6 T out-of-plane magnetic fields. Additional microwave coaxial lines allow for the microwave spectroscopy up to 18 GHz under these experimental conditions.

Scientifically, several directions in the field of fundamental light matter interaction are envisaged:

(i) Circuit quantum electrodynamics (circuit QED), where superconducting qubits form hybrids with microwave resonators. These experiments are time consuming, because quantum effects arise in the limit of low excitation numbers. Hereby, challenging requirements are imposed on the detection systems allowing to detect microwave signals in the atto-Watt regime.

(ii) Storage of quantum states. One possibility is the transfer of the quantum information contained in photons to long-lived spin states. Additionally, exchange coupled systems or ferromagetic systems come into focus, because the effective coupling strength scales with the square-root of the number of spins contributing. In general, we study the light-matter interaction with long-lived spin systems and integrate superconducting quantum circuits.

(iii) Spin-Systems. Here, the investigations are not limited to paramagnetic spin systems, but will be extended to exchange coupled (ferro-) magnetic systems. Hereby, magnetization damping can be investigated as function of the temperature, frequency and magnetic field direction.

(iv) Circuit electro-mechanical hybrid systems consisting of a nanomechanical element coupled to a superconducting microwave resonator. In this context, sideband cooling of the mechanical system into its ground state and pulsed spectroscopy of hybrid system are performed and will be extended.

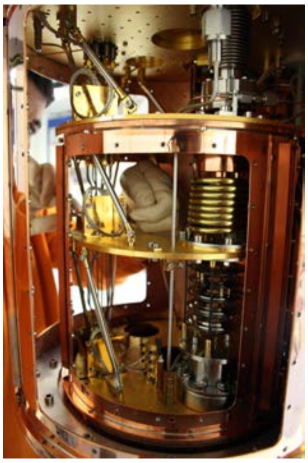

Figure 18: Inside of the dilution system. The windows of the 4 K and the still-shield are removed providing access to the low-temperature stages.

Low Temperature Scanning Tunneling Microscope with Ultra-High-Vacuum Characterization and Preparation Facilities

The low temperature scanning tunneling microscope allows investigation of low dimensional systems such as self-organized molecules, superconductors, magnetic and hetero-structure surfaces. The LT-STM is integrated into an ultra-high vacuum (UHV) chamber together with a variety of analytical as well as preparation tools. A newly added Quartz-Crystal-Microbalance allows quantitative controlling of evaporation processes. Monitoring is possible from island growth up to a film thickness of hundreds of atomic layers.

The Low Temperature Scanning Tunneling Microscope. The LT-STM (see Fig. 19a) is designed for easy handling under UHV as well as low temperature conditions. We control the Omicron STM by an electronics of the RHK company (see Fig. 19b).

Following, the technical features are listed:

- In-situ sample and tip exchange (manipulator see Figure 20 a).
- Vibration isolation ensured by a spring suspension system with eddy current damping and pneumatic damping legs.
- Variable temperatures from K (pumped 2 K) up to room temperature (≈ 300 K).
- Fast system cool-down (5 K within ≈ 6 hours).
- Sample pre-cooling to 50 K on the manipulator stage.
- Fast sample cool-down (5 K within ≈ 2 hours).
- On-line optical access and on-line four terminal transport measurements.
- Up to 6 samples can be stored at low temperature (77 K).

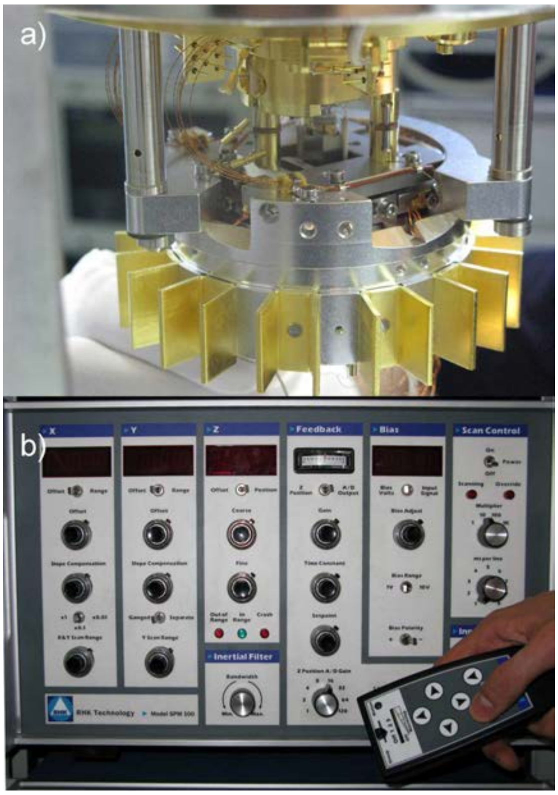

Figure 19: a) Inner view on the STM displaying part of the damping system, various cables and the scanning head (barely visible in the middle above the well). b) Photograph of our RHK scan electronic.

Preparation and Characterization Facilities. In addition to the LT-STM analysis chamber a second UHV chamber allows for sample preparation and characterization under UHV-conditions. Substrates can be prepared by an argon sputter gun and thermal annealing. A three crucible evaporator allows the deposition of molecules onto the surface; the deposition process is controlled by a quartz crystal microbalance. For sample characterization low-energy-electron-diffraction (LEED) and quadrupole mass spectrometry are available.

Argon Sputter Gun: Inside the preparation chamber clean single crystalline substrates are prepared by ion-sputtering and subsequent thermal annealing, which can be controlled by a three-grid low energy electron diffractometer (LEED) (see below) in a vacuum of 10^{-11} mbar.

Sample Heating/Cooling Stage: On the manipulator (see figure 20 a) samples can be prepared by direct current and indirect heating (see figure 20 b). Sample temperatures of up to 1073 K can be realized and the sample can be cooled to 50 K before transferring to the STM.

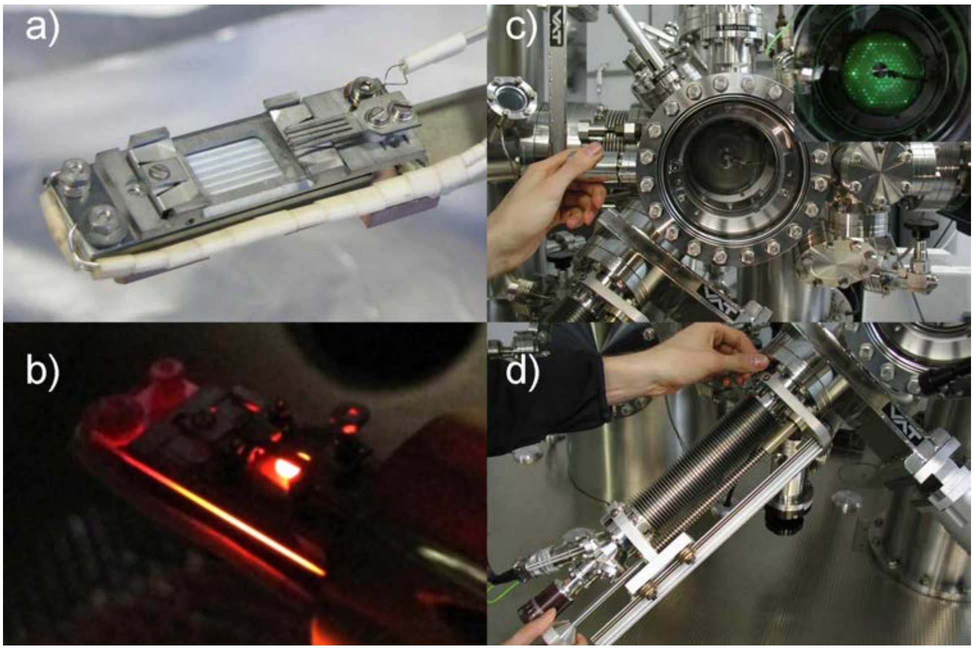

Figure 20: a) Close up on the manipulator for sample handling in the UHV chamber. b) Manipulator with Si-sample at 510 °C under UHV conditions. The body of the manipulator is cooled to prevent damage. c) LEED spectrometer; inset LEED-diffraction image of the Si [111] 7 × 7 reconstruction. d) Photograph of the evaporator.

Low Energy Electron Diffraction (LEED): The surface ordering of (reconstructed) substrate/single crystal surfaces or molecular ad-layers can be analyzed by low energy electron diffraction (see figure 20 c).

Evaporator for Organic Material: A microprocessor controlled evaporator allows deposition of up to three different organic materials at the same time (see figure 20 d). Crucibles are refilled without breaking the vacuum of the main chamber.

Quartz-Crystal-Microbalance: For controlling the evaporation process and quantitative measurements of the number of adsorbed layers on/coverage of the substrate during evaporation a quartz-crystal-microbalance was recently added. Growth rates of 0.01 nm/s corresponding to a frequency change of 0.03 Hz/s can be monitored.

Quadrupole Mass Spectrometer: Samples are additionally characterized by desorption spectroscopy with a quadrupole mass spectrometer. The desorbing molecules are ionized in a crossbeam ion source and accelerated in the quadrupole mass spectrometer, which either uses a Faraday cup or secondary electron multiplier (SEM) as detector with a mass resolution up to 2048 u.

Multiple additional vacuum ports allow further extensions of the Omicron STM in the future.

Tip etching facility (ex situ): The standard procedure for preparing STM tips - suitable for STM measurements - is cutting a PtIr-wire with scissors. Other tip materials (e.g. Tungsten, Gold, Niobium,. . .) have to be etched in order to form the necessary tip radii. A newly constructed tip etching facility allows for more tip materials than PtIr opening up the possibility of usage of e.g. superconducting tips.

Magnetic Field Low Temperature Ultra-High-Vacuum (UHV) – Scanning Tunneling Microscope (STM). The high stability of the instrument, the magnetic field as well as temperatures as low as 2.7 K allow the investigation of high temperature superconductors (HTSC) and organic superconductors. The STM is optimized for low temperature tunneling imaging and spectroscopy in high magnetic fields under UHV-conditions (see figure 21). A home-built electronics allows tunneling spectroscopy at points along lines, in grids and in a high density modus.

Figure 21: The current setup of the instrument: visible is the cryostat with microscope inside, as well as parts of the control electronics.

Technical Features of the STM.

- Imaging resolution:
  0.01 nm in $x-y$-direction and 0.005 nm in z-direction.
- Current-voltage spectroscopy $(I-V)$ (voltage resolution: 0.05 meV).
- Current-distance curves $(I-d)$.
- Maximum scan size: $1 \times 1\,\mu\text{m}^2$ at 4.2 K.
- Superconducting magnet up to 4 T with persistent switch.
- Vibration damping through spring suspension.
- Temperature range from room temperature down to liquid helium temperature at 4.2 K (pumped 2.7 K).
- Cryostat with LHe durability of one week (without thermal load).

Publications

1. **Path Entanglement of Continuous-Variable Quantum Microwaves**
E. P. Menzel, R. Di Candia, F. Deppe, P. Eder, L. Zhong, M. Ihmig, M. Haeberlein, A. Baust, E. Hoffmann, D. Ballester, K. Inomata, T. Yamamoto, Y. Nakamura, E. Solano, A. Marx, R. Gross
Phys. Rev. Lett. **109**, 250502 (2012).

2. **Local charge and spin currents in magnetothermal landscapes**
Mathias Weiler, Matthias Althammer, Franz D. Czeschka, Hans Huebl, Inga-Mareen Imort, Günter Reiss, Andy Thomas, Rudolf Gross, and Sebastian T. B. Goennenwein
Phys. Rev. Lett. **108**, 106602 (2012).

3. **Magneto-optical imaging of elastic strain-controlled magnetization reorientation**
A. Brandlmaier, M. Brasse, S. Geprägs, M. Weiler, R. Gross, S. T. B. Goennenwein
Eur. Phys. J. B **85**, 124 (2012).

4. **Networks of nonlinear superconducting transmission line resonators**
Martin Leib, Frank Deppe, Achim Marx, Rudolf Gross, Michael Hartmann
New J. Phys. **14**, 075024 (2012).

5. **Spin Pumping with Coherent Elastic Waves**
M. Weiler, H. Huebl, F. S. Goerg, F. D. Czeschka, R. Gross, and S. T. B. Goennenwein
Phys. Rev. Lett. **108**, 176601 (2012).

6. **Spin transport and Spin Dephasing in Zinc Oxide**
Matthias Althammer, Eva-Maria Karrer-Müller, Sebastian T. B. Gönnenwein, Matthias Opel, and Rudolf Gross
Appl. Phys. Lett. **101**, 082404 (2012).

7. **Surface Acoustic Wave-Driven Ferromagnetic Resonance in Nickel Thin Films: Theory and Experiment**
L. Dreher, M. Weiler, M. Pernpeintner, H. Huebl, R. Gross, M.S. Brandt, S.T.B. Goennenwein
Phys. Rev. B, **86**, 134415 (2012).

8. **Giant Magnetoelastic Effects in $BaTiO_3$-based Extrinsic Multiferroic Hybrids**
Stephan Gepraegs, Matthias Opel, Sebastian T. B. Goennenwein, and Rudolf Gross
Phys. Rev. B, **86**, 134432 (2012).

9. **Festkörperphysik**
R. Gross, A. Marx
Oldenbourg Wissenschaftsverlag München (2012), ISBN 978-3-486-71294-0.

10. **Magnetic field effects on the charge-density-wave and superconducting state in pressurized α-(BEDT-TTF)$_2$KHg(SCN)$_4$**
M.V. Kartsovnik, W. Biberacher, D. Andres, S. Jakob, M. Kunz, K. Neumaier, H. Müller, N.D. Kushch
Physica B **407**, 1919–1922 (2012).

11. **Quantum Simulation of the Ultrastrong-Coupling Dynamics in Circuit Quantum Electrodynamics**
D. Ballester, G. Romero, J. J. García-Ripoll, F. Deppe, E. Solano
Phys. Rev. X **2**, 021007 (2012).

12. **Vortex lock-in transition coinciding with the 3D to 2D crossover in $YBa_2Cu_3O_7$**
S. Bosma, S. Weyeneth, R. Puzniak, A. Erb, and H. Keller
Phys. Rev. B **86**, 174502(2012).

13. **^{139}La NMR investigation in underdoped $La_{1.93}Sr_{0.07}CuO_4$**
S.-H. Baek, A. Erb, B. Büchner, and H.-J. Grafe
Phys. Rev. B **85**, 184508 (2012).

14. **Feedback effect on high-energy magnetic fluctuations in the model high-temperature superconductor $HgBa_2CuO_{4+\delta}$ observed by electronic Raman scattering**
Yuan Li, M. Le Tacon, M. Bakr, D. Terrade, D. Manske, R. Hackl, L. Ji, M. K. Chan, N. Barisic, X. Zhao, M. Greven, B. Keimer

Phys. Rev. Lett. **108**, 227003 (2012).

15. **Spin caloritronics: Electron spins blow hot and cold**
Sebastian T. B. Goennenwein, Gerrit E. W. Bauer
Nature Nanotechnology **7**, 145–147 (2012).

16. **Structural, magnetic and electric behavior of the new Ba_2TiMoO_6 material**
C. E. Alarcon-Suesca, M. Opel, D. A. TellezLandínez Téllez, J. Roa-Rojas
Physica B **4070**, 3074–3077 (2012).

17. **Cryogen-free dilution refrigerator with separate 1 K cooling circuit**
K. Uhlig,
Adv. Cryo. Eng. **57B**, 1823–1829 (2012).

18. **Low-temperature encapsulation of coronene in carbon nanotubes**
B. Botka, M.E. Füstös, G. Klupp, D. Kocsis, E. Székely, M. Utczás, B. Simándi, Á. Botos, R. Hackl, K. Kamarás
Phys. Status Solidi B **249**, 2432 (2012).

19. **Spintronic oxides grown by laser-MBE**
M. Opel,
J. Phys. D: Appl. Phys. **45**, 033001 (2012).

20. **Kinetic Theory for Response and Transport in Non-centrosymmetric Superconductors**
Ludwig Klam, Dirk Manske, Dietrich Einzel
in "Non-Centrosymmetric Superconductors", E. Bauer, M. Sigrist (Eds), Springer eBook, ISBN 978-3-642-24624-1, Lecture Notes in Physics, Volume **847**, 211–245 (2012).

21. **Lock-in detection for pulsed electrically detected magnetic resonance**
F. Hoehne, L. Dreher, J. Behrends, M. Fehr, H. Huebl, K. Lips, A. Schnegg, M. Suckert, M. Stutzmann, M. S. Brandt
Rev. Sci. Instr. **83**, 043907 (2012).

22. **Mössbauer studies of subfossil oak**
U. van Bürck, F.E. Wagner, A. Lerf
Phys. Hyperfine Interact. **208**, 105 (2012).

23. **Influence of Annealing on the Optical and Scintillation Properties of $CaWO_4$ Single Crystals**
M. v. Sivers, C. Ciemniak, A. Erb, F. v. Feilitzsch, A. Gütlein, J.-C. Lanfranchi, J. Lepelmeier, A. Münster, W. Potzel, S. Roth, R. Strauss, U. Thalhammer, S. Wawoczny, M. Willers, A. Zöller
Optical Materials **34**, 1843 (2012).

24. **Magnetic-field-induced dimensional Crossover in the organic metal α-(BEDT-TTF)$_2$KHg(SCN)$_4$**
P.D. Grigoriev, M.V. Kartsovnik, W. Biberacher
Phys. Rev. B **86**, 166125 (2012).

25. **Staggered Spin Order of Localized π-Electrons in the Insulating State of the Organic Conductor κ-(BETS)$_2$Mn(N(CN)$_2$)$_3$**
O.M. Vyaselev, M.V. Kartsovnik, N.D. Kushch, E.B. Yagubskii
JETP Letters **95**, 565 (2012).

26. **Cryogen-free dilution refrigerator with 1 K-stage**
K. Uhlig
Cryocoolers **17**, 471 (2012).

27. **The Discovery of Fluxoid Quantization**
D. Einzel
in *100 Years of Superconductivity*, H. Rogalla, P. H. Kes (Eds), Taylor & Francis Group, Boca Raton (2012), pp. 161 – 170 (ISBN: 978-1-4398-4946-0).

28. **Electron-tunneling measurements of low-T_c single-layer $Bi_{2+x}Sr_{2y}CuO_{6+\delta}$: Evidence for a scaling disparity between superconducting and pseudogap states**
T. Jacobs, S.O. Katterwe, H. Motzkau, A. Rydh, A. Maljuk, T. Helm, C. Putzke, E. Kampert, M.V. Kartsovnik, V.M. Krasnov

Phys. Rev. B **86**, 214506 (2012).

29. **Alternative route to charge density wave formation in multiband systems**
H.-M. Eiter, M. Lavagnini, R. Hackl, E.A. Nowadnick, A.F. Kemper, T.P. Devereaux, J.-H. Chu, J.G. Analytis, I.R. Fisher, L. Degiorgi
PNAS, to appear (2012).

30. **Cryogen-free Dilution Refrigerators**
K. Uhlig,
J. Phys.: Conf. Ser. **400**, 052039 (2012).

31. **Electromechanically induced absorption in a circuit nano-electromechanical system**
Fredrik Hocke, Xiaoqing Zhou, Albert Schliesser, Tobias J. Kippenberg, Hans Huebl, Rudolf Gross
New J. Phys. **14**, 123037 (2012).

32. **Investigation of induced Pt magnetic polarization in Pt/$Y_3Fe_5O_{12}$ bilayers**
Stephan Geprägs, Sibylle Meyer, Stephan Altmannshofer, Matthias Opel, Fabrice Wilhelm, Andrei Rogalev, Rudolf Gross, and Sebastian T. B. Goennenwein
Appl. Phys. Lett. **101**, 262407 (2012).

33. **Control of Microwave Signals Using Circuit Nano-Electromechanics**
X. Zhou, F. Hocke, A. Schliesser, A. Marx, H. Huebl, R. Gross, and T. J. Kippenberg
arXiv:1206.6052, Nature Physics, accepted for publication (2012).

34. **High Cooperativity in Coupled Microwave Resonator Ferrimagnetic Insulator Hybrids**
Hans Huebl, Christoph Zollitsch, Johannes Lotze, Fredrik Hocke, Moritz Greifenstein, Achim Marx, Sebastian T. B. Goennenwein, and Rudolf Gross
arXiv:1208.0001v1, Phys. Rev. Lett., accepted for publication (2012).

35. **Gradiometric flux qubits with tunable gap**
M. J. Schwarz, J. Goetz, Z. Jiang, T. Niemczyk, F. Deppe, A. Marx, R. Gross
arXiv:1210.3982, submitted for publication (2012).

36. **Spin Hall Magnetoresistance Induced by a Non-Equilibrium Proximity Effect**
H. Nakayama, M. Althammer, Y.-T. Chen, K. Uchida, Y. Kajiwara, D. Kikuchi, T. Ohtani, S. Geprägs, M. Opel, S. Takahashi, R. Gross, G. E. W. Bauer, S. T. B. Goennenwein, E. Saitoh
arXiv:1211.0098, submitted for publication (2012).

37. **Evidence of competing s- and d-wave pairing channels in iron-based superconductors**
Florian Kretzschmar, Bernhard Muschler, Thomas Böhm, Andreas Baum, Rudi Hackl, Hai-Hu Wen, Vladimir Tsurkan, Joachim Deisenhofer, Alois Loidl
arXiv:1208.5006, submitted for publication(2012).

38. **Selection rules in a strongly coupled qubit-resonator system**
T. Niemczyk, F. Deppe, E. P. Menzel, M. J. Schwarz, H. Huebl, F. Hocke, M. Häberlein, M. Danner, E. Hoffmann, A. Baust, E. Solano, J. J. Garcia-Ripoll, A. Marx, R. Gross
arXiv:1107.0810, submitted for publication (2012).

39. **Tunable Coupling Engineering Between Superconducting Resonators: From Sidebands to Effective Gauge Fields**
Borja Peropadre, David Zueco, Friedrich Wulschner, Frank Deppe, Achim Marx, Rudolf Gross, and Juan José García-Ripoll
arXiv:1207.3408, submitted for publication (2012).

40. **Magnetic separation of $FeSi_2$-nanoparticles**
W. Aigner, S. Niesar, E. Mehmedovic, M. Opel, F. Wagner, H. Wiggers, M. Stutzmann
Nano Lett., submitted for publication (2012).

41. **Growth of High-Purity Scintillating $CaWO_4$ Single Crystals for the Low-Temperature Direct Dark Matter Search Experiments CRESST II and EURECA**
A. Erb, J.-C. Lanfrachi
Cryst. Eng. Comm. Themed Edition, submitted for publication (2012).

42. **Charge inhomogeneity in electron-doped $Pr_{1.85}Ce_{0.15}CuO_4$**
M. Jurkutat, J. Haase, A. Erb
J. Supercond. Novel Magn., submitted for publication (2012).

Theses, Appointments, Honors and Awards, Membership in Advisory Boards, etc.

Completed and ongoing Ph.D. Theses

Completed Ph.D. Theses:

1. **Josephson Junctions with Ferromagnetic Interlayer**
   Georg Wild, TU München, Februar 2012.
2. **Magnon-Phonon Interactions in Ferromagnetic Thin Films**
   Mathias Weiler, TU München, Mai 2012.
3. **Study of the Interaction Processes in Cuprate Superconductors by a Quantitative Comparison of Spectroscopic Experiments**
   Wolfgang Prestel, TU München, Juli 2012.
4. **Spin Transport Phenomena in Metals, Semiconductors, and Insulators**
   Matthias Althammer, TU München, Juli 2012.
5. **Carrier Dynamics of $Ba(Fe_{1-x}Co_x)_2As_2$ as a Function of Doping**
   Bernhard Muschler, TU München, Juli 2012.

Ongoing Ph.D. Theses:

6. **Kohärente Dynamik und Dekohärenz in supraleitenden Quantenbits**
   Edwin Menzel, TU München, seit Januar 2006.
7. **Herstellung und Charakterisierung von supraleitenden Schaltkreisen zur Realisierung von gekoppelten supraleitenden Quantenbauelementen**
   Elisabeth Hoffmann, TU München, seit April 2008.
8. **Quantenexperimente mit elektromechanischen Systemen**
   Fredrik Hocke, TU München, seit Mai 2008.
9. **Wechselwirkung zwischen Spin-, Gitter- und Ladungsfreiheitsgraden in korrelierten Metallen ohne Inversionszentrum**
   Hans-Martin Eiter, TU München, seit Oktober 2008.
10. **Properties of High-T_c Cuprates in Large Magnetic Fields**
    Toni Helm, TU München, seit März 2009.
11. **Superconducting Flux Qubits with Tunable Gap**
    Manuel Schwarz, TU München, seit Juni 2009.
12. **All Optical Quantum Computing**
    Max Häberlein, TU München, seit Dezember 2009.
13. **Raman-Untersuchungen an stark korrelierten Systemen mit hoher Ortsauflösung**
    Florian Kretschmar, TU München, seit Januar 2010.
14. **Vibrational Investigations of Luminescence Molecules**
    Nitin Chelwani, TU München, seit September 2010.
15. **Time-Domain Measurements on Ultra-strong-coupled Qubit-Resonator Systems**
    Alexander Baust, TU München, seit Oktober 2010.
16. **Spinabhängige thermogalvanische Effekte in ferromagnetischen Dünnschichten**
    Johannes Lotze, TU München, seit April 2011.
17. **Generation and Detection of Quantum Correlations in Circuit QED Systems**
    Ling Zhong, TU München, seit November 2011.
18. **Superconducting Quantum Circuits for Qunatum Electrodynamics Experiments**
    Karl Friedrich Wulschner, TU München, seit Januar 2012.

19. **Circuit Quantum Electrodynamics Experiments with Tunable Flux Qubits**
    Jan Goetz, TU München, seit Januar 2012.
20. **Single Excitation Transfer in the Quantum Regime: A Spin-Based Solid State Approach**
    Christoph Zollitsch, TU München, seit Januar 2012.
21. **Untersuchung der verschiedenen Phasen eisenbasierter Supraleiter mittels Raman-Streuung**
    Andreas Baum, TU München, seit April 2012.
22. **Superconducting Properties of Organic Metals in the Vicinity of Ordering Instabilities**
    Michael Kunz, TU München, seit August 2012.
23. **Quantum Information Processing with Propagating Quantum Microwaves**
    Peter Eder, TU München, seit November 2012.
24. **Coupled Electro-Nanomechanical Systems**
    Matthias Pernpeintner, TU München, seit November 2012.
25. **Spin transport in ferrromagnetic microsturctures**
    Michael Schreier, TU München, seit Dezember 2012.

The following Ph.D. students of the Walther-Meißner-Institute have finished their theses in 2012:

Bernhard Muschler

Matthias Althammer

Wolfgang Prestel

Mathias Weiler

Georg Wild

Completed and ongoing Diploma, Bachelor, Master Theses

Completed Master and Diploma Theses:

1. **Grundlagenuntersuchungen zur plasmainduzierten Entflammung bei hochaufgeladenen Ottomotoren**
   Thorsten Wolf, Diploma Thesis, TU München, Januar 2012.
2. **Dual-path Receiver for State Reconstruction of Propagating Quantum Microwaves**
   Peter Eder, Diploma Thesis, TU München, Januar 2012.
3. **Raman-Streuung an unkonventionellen Supraleitern**
   Thomas Böhm, Diploma Thesis, TU München, Januar 2012.
4. **Magneto-thermogalvanische Experimente an (Ga,Mn)As Dünnfilmen**
   Sibylle Meyer, Diploma Thesis, LMU München, Februar 2012.
5. **Untersuchung des Spindichtewellen-Übergangs in $BaFe_2As_2$**
   Andreas Baum, Diploma Thesis, TU München, Februar 2012.
6. **Analyse und Optimierung der Lebensdauerabsicherung von Lithium-Ionen Hochvoltspeichern**
   Lisa Plesch, Diploma Thesis, TU München, April 2012.
7. **Modellierung und Simulation eines thermoelektrischen Generators unter Berücksichtigung von lokalen Effekten**
   Torsten Steinert, Diploma Thesis, TU München, August 2012.
8. **Elektronenspinresonanz mit supraleitenden Mikrowellenresonatoren bei Millikelvin-Temperaturen**
   Moritz Greifenstein, Diploma Thesis, TU München, Juli 2012.
9. **Characterization of the Ultra Non-linear Switching Kinetics in Oxide Based Memory Cells**
   Thomas Jörn Selle, Diploma Thesis, TU München, Juli 2012.
10. **Einfluss der thermischen Leitfähigkeit von DLC-Schichten auf das Reibungsverhalten in der Flüssigkeitsreibung**
    Markus Felgenbauer, Diploma Thesis, TU München, August 2012.
11. **Towards Tunable Coupling Between Two Superconducting Transmission Line Resonators**
    Xiaoling Lu, Master Thesis, Université de Lyon, August 2012.
12. **Epitaxie und Charakterisierung von dünnen Schichten des ferromagnetischen Isolators $Y_3Fe_5O_{12}$**
    Stephan Altmannshofer, Master Thesis, Hochschule für Angewandte Wissenschaften München, Oktober 2012.
13. **Untersuchung der Gitter- und Ladungsträgerdynamik von MnSi in der Umgebung der magnetisch geordneten Phase**
    Peter Jaschke, Diploma Thesis, TU München, Oktober 2012.
14. **Spatially Resolved Spin Seebeck Experiments**
    Michael Schreier, Diploma Thesis, Oktober 2012.
15. **Magnon-Phonon Coupling in Ferromagnetic Thin Films**
    Matthias Pernpeinter, Diploma Thesis, TU München, Oktober 2012.
16. **Time-domain Control of Light-Matter Interaction with Superconducting Circuits**
    Thomas Losinger, Diploma Thesis, TU München, November 2011.
17. **Response und kollektive Anregungen in Zweiband-Supraleitern**
    Nikolaj Bittner, Diploma Thesis, TU München, November 2012.
18. **Improved Gradiometric Flux Quantum Qubits with Tunable Gap**
    Zhaohai Jiang, Diploma Thesis, TU München, Dezember 2012.

Completed Bachelor Theses:

19. **Tempern und Charakterisierung von oxidischen Proben**
Michael Rehm, Bachelor Thesis, TU München, 2012.
20. **Spitzenverstärkte Raman-Streuung (TERS)**
David Hoch, Bachelor Thesis, TU München, 2012.
21. **Study of Superconductors in a Diamond Anvil Cell**
Georg Haunschild, Bachelor Thesis, TU München, 2012.
22. **Fast microwave beam splitters based on superconducting resonators**
Philipp Assum, Bachelor Thesis, TU München, 2012.
23. **Scalable chains of coupled superconducting transmission line resonators**
Lisa Janker, Bachelor Thesis, TU München, 2012.
24. **Supraleitende Mikrowellenstrahlteiler**
Michael Fischer, Bachelor Thesis, TU München, 2012.
25. **Abstimmbare Resonatoren für akustische Oberflächenwellen**
Alexander Späh, Bachelor Thesis, TU München, 2012.
26. **Herstellung und Charakterisierung supraleitender Mikrowellen-Resonatoren für Messungen im magnetischen Feld**
Alexander Backs, Bachelor Thesis, TU München, 2012.
27. **Analytische Ginzburg-Landau-Beschreibung von supraleitenden Platten und Zylindern**
Jonas Woste, Bachelor Thesis, TU München, 2012.
28. **Spatially and Temporally Resolved Spin Seebeck Experiments**
Kathrin Ganzhorn, Bachelor Thesis, TU München, 2012.

Ongoing Master and Diploma Theses:

29. **DC-Readout of a Qubit-Resonator System**
Franz Sterr, Diploma Thesis, TU München, since März 2012.
30. **Magnetische Resonanz und Spin-Pumpen in Ferromagneten und Antiferromagneten**
Marc Philipp Ross, Diploma Thesis, TU München, since März 2012.
31. **Charakterisierung von Szintillatoren für Röntgenverfahren in der Medizintechnik**
Tobias Lamm, Master-Thesis, TU München, since Juli 2012.
32. **Schrotrauschen von Spin-Strömen**
Friedrich Paul Witek, Master Thesis, TU München, since September 2012.
33. **Spinkaloritronik**
Mathias Frank, Master Thesis, TU München, since November 2012.
34. **Superconducting Quantum Circuits: Flux Qubit Fabrication**
Edwar Xie, Master Thesis, TU München, since November 2012.
35. **Supraleitende Strahlteiler und Interferometer**
Ferdinand Loacker, Diploma Thesis, TU München, seit November 2012.

Honors and Awards

Prize of the Karl Thiemig Foundation 2012

Dr. Hans Huebl of WMI received the ***Prize of the Karl Thiemig-Stiftung 2012*** of the Bavarian Academy of Sciences and Humanities in recognition of his pioneering research on solid state quantum systems as the basis for future quantum information systems.

Hans Huebl is head of a junior group at Walther-Meißner-Institut since 2009. He also is member and principal investigator of the Collaborative Research Center 631 on "Solid State Quantum Information Processing" and one of the promising junior scientists of the Excellence Cluster "Nanosystems Initiative Munich". His research work resulted in important new scientific findings on spin based quantum information systems and nanoelectromechanical systems close to the quantum limit. His work received broad international attention and is of particular relevance for the development of novel information and communication systems based on quantum mechanical principles.

Hans Huebl (right) with the President of the Bavarian Academy (left). Bild: BAdW/F. Schmidt

The Bavarian Academy annually gives the Prize of the Karl Thiemig Foundation for the promotion of young scientists in all disciplines. The prize has been presented to Hans Huebl on December 8, 2012 by the president of the Academy within an Annual Meeting of the Bavarian Academy of Sciences and Humanities in the Munich Residence.

Prize of the Dimitris N. Chorafas Foundation 2012

Dr. Mathias Weiler of WMI received the ***Prize of the Dimitris N. Chorafas Foundation*** in recognition of his excellent Ph.D. thesis on "Magnon-Phonon Interactions in Ferromagnetic Thin Films". Since 1996, the awards of the Chorafas Foundation are granted directly to prize winners selected by partner Universities in Europe, North America, the Middle East and Asia. These awards target the best doctorate students chosen by each partner University and confirmed by the Board of the Foundation. Each award is of USD 4'000. Selection is made among a statistically valid sample of candidates. There have been 20 to 30 prizes per year, the exact number depending on the candidates retained for the prizes by the partner Universities. As of today, there are 26 partner Universities in 15 countries. In Germany, the partner universities are the Technical University of Munich and the Technical University of Berlin.

Mathias Weiler joined WMI in December 2006 when he started his diploma thesis on the "Magnetization Control in Multiferroic Heterostructures". After completing his diploma thesis in December 2008, he started a Ph.D. project on "Magnon-Phonon Interactions in Ferromagnetic Thin Films", which he completed in May 2012 with distinction. In his doctoral thesis, Mathias Weiler made outstanding contributions to the new fields of spin electronics and spin caloritronics by several pioneering experiments, important technological developments as well as numerical simulations. His pioneering work on radio frequency spin mechanics, spin pumping and spatially resolved spin caloritronics is of fundamental importance for future spintronic devices which may find broad application in data storage, logic circuits and sensors. His work resulted in several high level articles, including 3 publications in the high profile journal Physical Review Letters with him as the first author. His work attracted tremendous international interest and resulted in two invited talks in 2012 at international conferences.

DAAD Postdoctoral Scholarship

Dr. Mathias Weiler of WMI received a DAAD Postdoctoral Scholarship allowing him to spend a two-year postdoctoral stay in the group of Tom Silva and Ron Goldfarb at the National Institute of Standards and Technology (NIST) in Boulder, Colorado.

Appointments, Membership in Advisory Boards, etc.

1. **Werner Biberacher** is member of the Selection Panel EuroMagNet II of the Joint European High Magnetic Field Laboratories.
2. **Werner Biberacher** is member of the Scientific Council of the High Magnetic Field Laboratory (LNCMI) Grenoble/Toulouse, France.
3. **Dietrich Einzel** is one of the four spokesmen of the scientific staff of the Bavarian Academy of Sciences and Humanities.
4. **Andreas Erb** has been appointed “Honorarprofessor" for Experimental Physics at the University of Leipzig.
5. **Sebastian Gönnenwein** is associate member of the Cluster of Excellence *Nanosystems Initiative Munich (NIM)*.
6. **Rudolf Gross** was acting as member of the International Advisory Board of the Materials Science Summit, 27-30 November, 2012, Sendai, Japan.
7. **Rudolf Gross** is member of the Scientific Advisory Board of the Leibniz Institute for Solid-State and Materials Research, Dresden.
8. **Rudolf Gross** is member of the Kuratorium of the Physik Journal of the German Physical Society.
9. **Rudolf Gross** is member of the selection committee of the Stern-Gerlach-Medal of the German Physical Society.
10. **Rudolf Gross** is deputy spokesman of the division of *Low Temperature Physics* of the Condensed Matter Section of the German Physical Society.
11. **Rudolf Gross** is spokesman of the Collaborative Research Center 631 on *Solid State Quantum Information Processing* of the German Research Foundation.
12. **Rudolf Gross** is member of the Executive Board of the Cluster of Excellence *Nanosystems Initiative Munich (NIM)* and coordinator of the Research Area 1 on *Quantum Nanosystems*.
13. **Rudolf Gross** is member of the Board of Editors of the European Physical Journal B.
14. **Rudolf Hackl** is deputy coordinator of the DFG Priority Program SPP 1458 on “High Temperature Superconductivity in the Iron Pnictides”.
15. **Rudolf Hackl** was acting as member of the International Advisory Board of the Conference “Low Energy Electron Dynamics LEES 2012”.
16. **Rudolf Hackl** is member of the evaluation board of the neutron source Heinz Maier-Leibnitz (FRM II).

Research Projects and Cooperations

A large number of our research projects are benefiting from the collaboration with external groups in joint research projects, as well as from individual collaborations, exchange programs and visitors. Most collaborations are based on joint projects, which are funded by different research organizations (see list below). A considerable number of collaborations also exists with universities, other research institutions and industry without direct financial support.

Funded Projects

A. German Research Foundation: Excellence Initiative

Cluster of Excellence "Nanosystems Initiative Munich"

1. Project Area I: *Quantum Nanophysics*
   F. Deppe, S.T.B. Gönnenwein, R. Gross, H. Huebl, A. Marx
2. Project Area II: *Hybrid Nanosystems*
   S.T.B. Gönnenwein, R. Gross, H. Huebl

B. German Research Foundation: Collaborative Research Centers

Collaborative Research Center 631: "Solid-State Quantum Information Processing: Physical Concepts and Materials Aspects"

1. Project A3: *Superconducting Quantum Circuits as Basic Elements for Quantum Information Processing*
   R. Gross, A. Marx
2. Project A8: *Cavity Quantum Electrodynamics with Superconducting Devices*
   A. Marx, R. Gross
3. Project C3: *Fundamentals of Quantum Logic Gates in Silicon*
   M. Brandt, H. Huebl, M. Stutzmann
4. Project S: *Coordination of the Collaborative Research Center*
   R. Gross

Transregional Collaborative Research Center TRR 80: "From Electronic Correlations to Functionality"

1. Project A2: *Spatially und Momentum Resolved Raman Studies of Correlated Systems*
   R. Hackl

C. German Research Foundation: Priority Programs

1. Spin-dependent thermo-galvanic effects: experiment
   within the DFG Priority Program 1538 *Spin-Caloric Transport – SpinCAT*
   S.T.B. Gönnenwein, R. Gross (Az. GO 944/4-1)
2. Project: *Spin injection, spin transport and controllable ferromagnetism in transition metal doped ZnO*
   within the DFG Priority Program 1285 *"Halbleiter-Spinelektronik"*
   R. Gross, S.T.B. Gönnenwein, M. Opel (Az. GR 1132/14-1, GR 1132/14-2, GR 1132/14-3)

3. Project: *Raman study of electron dynamics and phase transitions in iron-pnictide compounds* within the DFG Priority Program 1458 *"High-Temperature Superconductivity in Iron-Pnictides"*
   R. Hackl, R. Gross, B. Büchner, D. Johrendt, C. Honerkamp (Az. HA 2071/7-1)

D. German Research Foundation: Research Projects

1. Project: *Doping dependent evolution of the Fermi surface and competing ordering phenomena in superconducting cuprates*
   R. Gross, M. Kartsovnik, A. Erb (Az. GR 1132/15-1)
2. Project: *Interaction between spin, lattice, and charge in non-centrosymmetric correlated metals*
   R. Hackl, R. Gross (Az. HA 2071/5-1)
3. Project: *Study of π-d interaction in crystalline organic (super)conductors with 3d metal-complex ions*
   W. Biberacher (Az.: BI 340/3-1), bilateral cooperation with institutes of the Russian Academy of Science.
4. Project: *Local Magnetotransport Properties of Thin Ferromagnetic Layers and Heterostructures*
   S.T.B. Gönnenwein (Az. GO 944/3-1)

E. European Union

1. EU Collaborative Project (call identifier FP7-ICT-2011-C), project title *Quantum Propagating Microwaves in Strongly Coupled Environments – PROMISCE*
   F. Deppe, A. Marx, R. Gross, Grant Agreement no. 284566
   partners: several European Universities and research facilities.
2. Marie Curie Network for Initial Training (call identifier FP7-PEOPLE-2010-ITN), project title *Circuit and Cavity Quantum Electrodynamics (CCQED)*
   R. Gross, A. Marx, F. Deppe, Grant Agreement No. PITN-GA-2010-264666
   partners: several European Universities and research facilities.
3. Marie Curie Network for Initial Training (call identifier FP7-PEOPLE-2009-ITN), project title *Cavity-confined Luminophores for Advanced Photonic Materials: A Training Action for Young Researchers (FINELUMEN)*
   R. Hackl, Grant Agreement Number PITN-GA-2008-215399
   partners: several European Universities and research facilities.

F. German Academic Exchange Service

1. German-Indian STAR Scholarship for Technology and Research, collaboration with IIT Madras (Prof. M.S.R. Rao)
   R. Gross

G. Ministerio de Educacion y Ciencia, Spanien

1. Intercalación de minerales de la arcilla por medio de tratamiento con ultrasonidos y reacciones de transferencia de electrones. Producciòn de arcillas funcionalizadas con estructuras complejas jerarquizadas en el espacio interlaminar.
   J.L. Perez-Rodriguez, A. Lerf, reference No.: MAT2005-04838

H. Bavaria California Technology Center (BaCaTeC)

1. Project "Nematic order and new phases in quantum materials"
   R. Hackl,
   partners: Profs. Thomas Devereaux, Steve Kivelson, and Sri Raghu (Stanford University)

I. Others

1. Grant of the Federal Agency for Science and Innovations of the Russian Federation
   M. Kartsovnik, project No. 14.740.11.0911

Conferences and Workshops

The Walther-Meißner-Institute has organized/co-organized the following conferences and workshops in 2012:

1. **Winter School of the Marie Curie Network for Initial Training on "Circuit and Cavity Quantum Electrodynamics (CCQED)"**
   February 26 – March 02, 2012, Les Houches, France.

Participants of the Winter School of the CCQED ITN network
26 February – 2 March 2012, Les Houches, France

The school was organized by the *EU Marie Curie Network CCQED*. It aimed at Ph.D. students and Postdocs working in the field of circuit and cavity QED. Besides a general introductory course on the principles of the field, there were lectures on the experimental realizations in different physical systems such as atoms in optical cavities, superconducting circuits, quantum dots in photonic crystal cavities and many more. The participants learnt about the possibilities and the difficulties that each of the systems is offering. Theory sessions complemented the experimental lectures to give a deeper insight in current theoretical approaches.

The network Circuit and Cavity Quantum Electrodynamics (CCQED) has been granted 3.5 Million Euros by the European Union through a Marie Curie Action within the Seventh Framework Program Initial Training Network ITN-People-2010. The aim of CCQED is to bridge two communities in physics, in the academic and private sectors, to share, pursue and diffuse within Europe the benefits of collaborations in the science of elementary quanta. Jobs are available for 12 Early Stage Researchers (ESR) for a 3 years Ph.D. program, and for 2 Experienced Researchers (ER) for postdoctoral research during 2 years.

2. **Workshop on "Superconductivity in Iron-based Compounds"**,
   March 21 – March 23, 2012, Munich Residenz, Munich, Germany.

The International Workshop on "Superconductivity in iron-based compounds" was providing a forum for the dissemination of the most recent results and for intense discussions on the new iron-based superconductors. The discovery of high temperature superconductivity in iron-based compounds triggered enormous research efforts. The materials are not only interesting for their high critical temperatures of up to 55 K, but also for their model character in the family of superconductors without electron-phonon coupling and for their application potential. The workshop program comprised oral presentations by invited international speakers and contributed poster presentations.

The workshop was organized by Rudi Hackl (WMI) and funded by the DFG via the program SPP 1458. The *DFG Priority Program SPP 1458* is a focused effort to get deeper insight into the materials and mechanisms of this new class of superconductors.

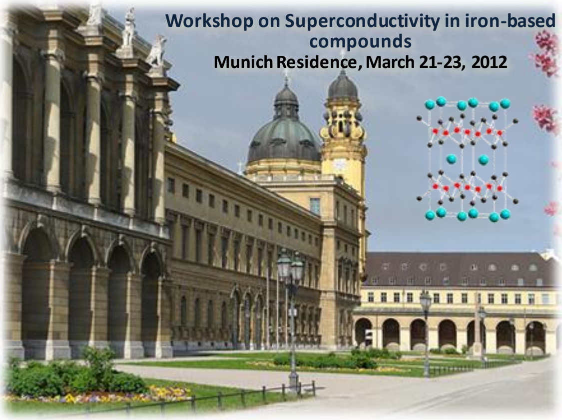

3. **Course 3 on "Physics and Electronics in Everyday Life" of the Ferienakademie 2012** September 23 – October 05, 2012, Sarntal, Italy.

The course was hold by Rudolf Gross of WMI together with Prof. Dr. Roland Roth, University of Erlangen-Nuremberg, and Prof. Dr. Gert Denninger, University of Stuttgart, within the *Ferienakademie*. The Ferienakademie is jointly organized by the Technische Universität München, the University of Erlangen/Nuremberg, and the University of Stuttgart to motivate and foster highly talented students. It takes place in the Italian Alps.

4. **"5th Doktoranden-Workshop" of the Collaborative Research Center 631 on Solid State Quantum Information Processing**
   05. – 08. 10. 2012, Auffach, Austria

   Due to the interdisciplinary character of the research field and the involvement of four universities, the stimulation of the direct exchange and interaction between the the Ph.D. students working in the different research projects of the ***Collaborative Research Center 631 (SFB 631)*** has been recognized as an important task from the beginning. Therefore, SFB 631 regularly organizes two- to three-day workshops for the Ph.D. students without their supervisors. The "5th Doktoranden-Workshop on Solid State Quantum Information Processing" was taking place at Auffach, Austria from October 05 – 08, 2012. It was organized by Hans Huebl of WMI.

   During the workshop the Ph.D. students reported on the progress of the research work to their fellow students and discussed future directions of their work. The workshop turned out to be very fruitful for the interaction among the Ph.D. students and the mutual information both on their research work and practical problems. Moreover, due to the tutorial style of the presentations during the workshops, those Ph.D. students that had joined SFB 631 only recently were able to get a broad overview on the research activities going on within SFB 631.

Collaborations

Other collaborations without direct project funding involve:

- Stanford University, Stanford, USA (Profs. T.P. Devereaux, M. Greven, Z.-X. Shen, I. Fisher)
- Universidad del País Vasco and Ikerbasque Foundation, Bilbao, Spain (Prof. Dr. E. Solano)
- Instituto de Fisica Fundamental, Madrid, Spain (Prof. Dr. J.J. Garcia-Ripoll)
- Instituto de Ciencia de Materiales de Sevilla, Spain (Prof. J. Poyato, Prof. J.L. Perez-Rodriguez)
- Research Institute for Solid State Physics and Optics, Hungarian Academy of Sciences, Budapest, Hungary (Prof. K. Kamaras and Prof. I. Tüttö, Dr. J. Balogh)
- University of Rome "La Sapienza", Rome, Italy (Profs. S. Caprara, C. Di Castro, M. Grilli)
- Hungarian Academy of Sciences, Budapest University of Technology and Economics, Budapest, Hungary (Dr. A. Virosztek, Profs. A. Zawadowski, G. Mihály)
- Central Research Institute of the Electric Power Industry, Tokyo, Japan (Dr. S. Ono, Dr. Y. Ando)
- Green Innovation Research Laboratories, NEC Corporation, Japan (Dr. Y. Nakamura, Dr. J.S. Tsai, Dr. K. Inomata, Dr. T. Yamamoto)
- University of Tohoku, Sendai, Japan (Profs. Gerrit E.W. Bauer, Eiji Saitoh)
- European Synchrotron Radiation Facility (ESRF), Grenoble (Dr. H. Müller, Dr. J. Criginski Cezar, Dr. D. Mannix, Dr. F. Wilhelm)
- Materials Science Research Centre, IIT Madras, India (Prof. Dr. M.S. Ramachandra Rao)
- Raja Ramanna Centre for Advanced Technology, Indore, India (Prof. Dr. Lalit M. Kukreja)
- Clarendon Laboratory, University of Oxford, England (Dr. A. Karenowska)
- High Magnetic Field Laboratory, Toulouse (C. Proust, D. Vignolles)
- ETH-Zurich, Switzerland (Profs. L. Degiorgi, R. Monnier, Dr. M. Lavagnini)
- Chalmers University of Technology Gothenburg, Sweden (Prof. Dr. P. Delsing)
- MINT Center, University of Alabama (Prof. Dr. A. Gupta)
- Materials Physics Laboratory, Helsinki University of Technology, Finland (Dr. Tero Heikkilä)
- Kavli Institute of NanoScience, Delft University of Technology, Delft, The Netherlands (Prof. Dr. T.M. Klapwijk, Prof. G.E.W. Bauer)
- High-Magnetic-Field Laboratory, Grenoble, France (Dr. I. Sheikin)
- B. Verkin Institute for Low Temperature Research and Engineering, Kharkov, Ukraine (Prof. Dr. V.G. Peschansky)
- Landau Institute for Theoretical Physics, Chernogolovka, Russia (Dr. P. Grigoriev)
- Russian Academy of Sciences, Chernogolovka, Russia (Dr. N. Kushch, Dr. A. Palnichenko)
- High Magnetic Field Laboratory, Dresden (Dr. E. Kampert, Prof. Dr. J. Wosnitza)
- National High Magnetic Field Laboratory, Tallahassee, USA (Prof. Dr. J. Brooks)
- University of Bonn, Germany (Prof. Dr. W. Mader)
- IFW Dresden, Germany (Prof. Dr. B. Büchner, Prof. Dr. J. Fink, Dr. S.V. Borisenko, Dr. M. Knupfer)
- Max-Planck-Institut für Festkörperforschung, Stuttgart (Prof. Dr. B. Keimer, Dr. L.

Boeri)
- University of Tübingen, Germany (Prof. Dr. R. Kleiner, Prof. Dr. D. Kölle)
- University of Würzburg, Germany (Prof. Dr. W. Hanke, Prof. Dr. F. Assaad, Prof. Dr. C. Honerkamp, Dr. M. Potthoff)
- University of Augsburg, Germany (Prof. Dr. P. Hänggi, Prof. A. Wixforth, Prof. J. Mannhart, Prof. A. Kampf, Prof. A. Loidl, Dr. J. Deisenhofer, Dr. V. Tsurkan)
- University of Hamburg, Germany (Dr. G. Meier, Prof. Dr. W. Wurth)
- University of Leipzig, Germany (Prof. Dr. J. Haase)
- Abt. Halbleiterphysik, University of Ulm, Germany (Dr. W. Limmer)
- RWTH Aachen, Germany (Prof. Dr. G. Güntherodt, Dr. B. Beschoten)
- Georg-August-Universität, Göttingen, Germany (Prof. Dr. M. Münzenberg)
- Institut für Experimentelle und Angewandte Physik, Universität Regensburg, Germany (Prof. Dr. Christian Back, Dr. Georg Woltersdorf)
- Universität Bielefeld, Germany (Dr. A. Thomas)
- University of British Columbia, Vancouver, Canada (Prof. Dr. D. Bonn, Prof. Dr. A. Damascelli)
- Max-Planck-Institut für Chemische Physik fester Stoffe, Dresden, Germany (Prof. Dr. F. Steglich)
- Technische Universität München, Physics Department, Germany (Profs. P. Böni, F. von Feilitzsch, D. Grundler, Ch. Pfleiderer, F.C. Simmel, Dr. Jean Come Lanfranchi)
- Walter Schottky Institut, TU München, Germany (Profs. G. Abstreiter, M. Stutzmann, J. Finley, M. Brandt, A. Holleitner, Dr. Dominique Bougeard)
- Ludwig-Maximilians-Universität München, Physics Department, Germany (Profs. J.P. Kotthaus, J. von Delft, E. Frey, J. Rädler, Dr. E. Weig, Dr. S. Ludwig)
- Ludwig-Maximilians-Universität München, Chemistry Department, Germany (Prof. Dr. Hubert Ebert, Dr. Diemo Ködderitzsch)
- University of Birmingham, UK (Prof. Dr. E.M. Forgan)
- Paul Scherrer Institute, ETH Zürich (Prof. Dr. Joel Mesot)
- University of Geneva, Switzerland (Prof. Dr. O. Fischer)
- HMI Berlin, Germany (Dr. A. Buchsteiner, Dr. J. Pieper, Dr. K. Siemensmeyer)
- Royal Holloway University, London UK (Prof. Dr. J. Saunders)
- University of Liverpool, UK (Dr. J. Goff)
- CNRS Grenoble, France (Prof. Dr. H. Godfrin)
- University of Florida, USA (Prof. Dr. D. Adams, Prof. Dr. Y. Takano)
- Departamento de Fisica de la Materia Condensada, Universidad de Zaragoza, Spain (Prof. Dr. L. Morellon, Prof. Dr. J.M. de Teresa, D. Zueco)
- EPFL Lausanne, Switzerland (Prof. Dr. H. Ronnov)
- University of New South Wales, Sydney, Australia (Dr. M. Simmons, Dr. A. Morello)
- McMaster University, Hamilton, Canada (Prof. Dr. J.P. Carbotte)
- Technische Universität Graz, Austria (Dr. E. Schachinger)
- Universität Konstanz (Prof. A. Leitenstorfer, Dr. J. Demsar, Dr. A. Pashkin)
- BMW Group, Munich, Germany (Dr. J. Schnagl)
- Siemens AG, CT MM 2, Munich, Germany (Dr. R. Matz, Dr. W. Metzger)
- Attocube, Munich, Germany (Prof. Dr. K. Karrai, Dr. D. Andres)
- THEVA Dünnschichttechnik, Ismaning, Germany (Dr. W. Prusseit)
- Institut für Halbleiter- und Festkörperphysik, Johannes-Kepler-Universität Linz, Austria

(Prof. A. Ney)

- Forschungs-Neutronenquelle “Heinz Maier-Leibnitz” (FRM II), Garching, Germany (Dr. G. Simeoni)
- Lehrstuhl für Technische Elektronik, Technische Universität München (Dr. M. Becherer)
- Institut für Angewandte Photophysik, Technische Universität Dresden (Prof. L. Eng, Dr. D. Köhler, J. Becherer)
- Jülich Centre for Neutron Science JCNS (Dr. S. Pütter)

Stays abroad

Extended visits of members of the Walther-Meißner-Institute at foreign research laboratories:

1. **Toni Helm**
   High Magnetic Field Laboratory, Dresden, Germany
   11. 03. – 27. 03. 2012
2. **Mark Kartsovnik**
   High Magnetic Field Laboratory, Dresden, Germany
   25. 03. – 30. 03. 2012
3. **Mark Kartsovnik, Toni Helm**
   High Magnetic Field Laboratory, Toulouse, France
   22. 04. – 04. 05. 2012
4. **Toni Helm, Mark Kartsovnik**
   High Magnetic Field Laboratory, Grenoble, France
   30. 09. – 08. 10. 2012
5. **Mark Kartsovnik**
   Institute of Solid State Physics, Chernogolovka, Russia
   14. 06. – 15. 07. 2012, 28. 10. âĂŞ 20. 11. 2012
6. **Matthias Opel**
   European Synchrotron Radiation Facility (ESRF), Grenoble, France
   24. 05. – 29. 05. 2012
7. **Ling Zhong**
   Departamento de Quimica Fisica, Universidad del Pais Vasco, Bilbao, Spain
   29. 05. – 12. 06. 2012
8. **Alexander Baust**
   Departamento de Quimica Fisica, Universidad del Pais Vasco, Bilbao, Spain
   08. 07. – 24. 07. 2012
9. **Alexander Baust**
   Instituto de Fisica Fundamental Madrid, Spain
   17. 07. – 24. 07. 2012
10. **Friedrich Wulschner**
    Instituto de Fisica Fundamental Madrid, Spain
    21. 05. – 25. 05. 2012
11. **Stephan Geprägs**
    European Synchrotron Radiation Facility (ESRF), Grenoble, France
    25. 03. – 29. 03. 2012

Conference Talks and Seminar Lectures

Andreas Baum

1. **Untersuchung des Spindichtewellen-Übergangs in $BaFe_2As_2$**
   Seminar Talk, IFW Dresden, Dresden, Germany.
   27. 11. 2012

Alexander Baust

1. **Circuit QED with Superconducting Flux Qubits**
   5. Doktoranden-Workshop des SFB 631 über Festkörperbasierte Quanteninformationsverarbeitung, Wildschönau, Austria.
   08. – 10. 10. 2012

Thomas Böhm

1. **Light scattering from superconducting $Rb_2Fe_4Se_5$**
   Seminar Talk, Stanford University, Stanford, USA.
   30. 07. 2012

Bea Botka

1. **Coronene filled nanotubes**
   Biannual Meeting of the EU Marie Curie Project (FINELUMEN), Brussels, Belgium.
   29. – 30. 03. 2012

Nitin Chelwani

1. **Ligand effect of vibrational properties of luminescent molecules and progress report on TERS**
   Biannual Meeting of the EU Marie Curie Project (FINELUMEN), Brussels, Belgium.
   29. – 30. 03. 2012

Frank Deppe

1. **Path entanglement of continuous variable quantum microwaves**
   Seminar Talk, Karlsruher Institut für Technologie (KIT), Karlsruhe, Germany.
   09. 07. 2012
2. **Path entanglement of continuous-variable propagating quantum microwaves**
   Physikalisches Kolloquium, Universität des Saarlandes, Saarbrücken, Germany.
   19. 07. 2012
3. **Superconducting flux quantum circuits**
   Tutorial Talk, Tagung "Kryogene Bauelemente (Kryo 2012)", Freudenstadt, Germany.
   30. 09. 2012
4. **Path entanglement of continuous-variable propagating quantum micorwaves**
   Invited Talk, Tagung "Kryogene Bauelemente (Kryo 2012)", Freudenstadt, Germany.
   02. 10. 2012

Hans-Martin Eiter

1. **The Chiral Magnet MnSi**
   Seminar Talk, Stanford University, Stanford, USA.
   30. 07. 2012

Andreas Erb

1. **Züchtung von $CaWO_4$ Massivkristallen für die Suche nach dunkler Materie**
   Deutsche Kristallzüchtertagung, Freiburg, Germany.
   07. – 09. 03. 2012
2. **Growth of High-Purity $CaWO_4$ Single Crystals for the Low-Temperature Dark Matter Research**
   European Conference of Crystal Growth, Glasgow, UK.
   17. – 20. 06. 2012

3. **Kristallzüchtung verschiedener Oxide nach dem TSFZ Verfahren**
   DGKK-Arbeitskreis-Treffen, Frankfurt/Main, Germany.
   10. – 11. 10. 2012

Stephan Geprägs

1. **Electric field controlled manipulation of the magnetization in $BaTiO_3$ based ferroelectric/ferromagnetic hybrid structures**
   Spring Meeting of the German Physical Society, Berlin, Germany.
   26. 03. 2012
2. **Detailed study of magnetoelastic and magnetoelectric effects in composite multiferroic hybrid structures**
   Nature Conference 2012, Aachen, Germany.
   18. 06. 2012
3. **Magnetoelastic and magnetoelectronic effects in composite multiferroic hybrid structures**
   Joint European Magnetic Symposia JEMS 2012, Parma, Italy.
   12. 09. 2012
4. **Converse Magnetoelectric Interactions in Extrinsic Multiferroic Composites**
   Magnetoelectrics at the Mesoscale (2012), Kavli Royal Society International Centre, Chicheley, England.
   26. 09. 2012

Sebastian Gönnenwein

1. **Elastically Driven Ferromagnetic Resonance in Nickel Thin Films**
   Vortrag im Seminar des I. Physikalischen Instituts, Universität Göttingen, Germany.
   23. 01. 2012
2. **Spin and Charge Currents in Magneto-Thermal Landscapes**
   23. Edgar-Lüscher-Seminar, Klosters, Switzerland.
   04. 02. 2012
3. **Spin Currents in Ferromagnetic Insulator/Normal Metal Hybrid Devices**
   Spring Meeting of the German Physical Society, Berlin, Germany.
   29. 03. 2012
4. **Spin Currents in Ferromagnetic Insulator/Normal Metal Hybrid Devices**
   Physikalisches Kolloquium der Universität Bielefeld, Germany.
   21. 05. 2012
5. **Spin pumping with photons and phonons**
   International Workshop "Spin Caloritronics IV", Sendai Japan.
   03. 06. 2012
6. **Spin Current-Based Experiments in Ferromagnet/Normal Metal Hybrid Structures**
   520. Wilhelm and Else Heraeus Seminar, Bad Honnef, Germany.
   05. 12. 2012

Rudolf Gross

1. **Quantenoptik mit supraleitenden Schaltkreisen**
   R. Gross
   Berliner Physikalisches Kolloquium im Magnus-Haus, Berlin, Germany.
   12. 04. 2012
2. **Quantum Optics with Superconducting Circuits**
   R. Gross
   Physikalisches Kolloquium, Technische Universität Dortmund, Germany.
   15. 05. 2012
3. **Quantum Optics with Superconducting Circuits**
   R. Gross
   Invited Talk, 19th Central European Workshop on "Quantum Optics"
   01 – 06 July, 2012, Sinaia, Romania.
4. **Fermi Surfaces in Electron-Doped Cuprate Superconductors**
   R. Gross

12th Japanese-German Symposium on "Emergent Phenomena in Novel Quantum Phases of Condensed Matter"
14 – 17 July, 2012, Shuzenji, Isu, Japan.

5. **Quantum Electronics**
R. Gross
Tutorial Talk, Ferienakademie, jointly organized by TU Munich, University of Erlangen-Nuremberg, and University of Stuttgart
23 September – 05 October, 2012, Sarntal, Italy.
6. **Quantum Optics with Superconducting Circuits**
R. Gross
Colloquium, Raja Ramanna Centre for Advanced Technology, Indore, India.
15. 10. 2012
7. **Quantum Optics with Superconducting Circuits**
R. Gross
Colloquium, Nano Functional Materials Technology Center, IIT Madras, India.
16. 10. 2012
8. **Quantum Spin Physics with Magnetic Nanostructures**
R. Gross
Plenary Talk, 4th International Conference on "Advanced Nanomaterials"
17 – 19 October, 2012, Chennai, India.
9. **Superconducting Quantum Circuits & Hybrids**
R. Gross
Colloquium, Max-Planck-Institut für Quantenoptik, Garching, Germany.
20. 11. 2012
10. **Towards Quantum Teleportation and Communication in the Microwave Regime**
R. Gross
Invited Talk, Symposium on "Physics and Metrology at Very Low Temperatures"
13 – 14 December, 2012, Berlin, Germany.

Rudolf Hackl

1. **s- and d-wave pairing channels in Fe-based superconductors**
FeSe Superconductors Workshop, Augsburg, Germany.
26. 05. 2012
2. **An introduction to inelastic light scattering**
SPP 1458 Summer School, Achatswies, Germany.
30. 07. – 04. 08. 2012
3. **Raman scattering in Fe-based superconductors**
SPP 1458 Summer School, Achatswies, Germany.
30. 07. – 04. 08. 2012

Hans Hübl

1. **Magnetoelastic Magnetization Control and Magnetization Dynamics at Low Temperatures**
Spring Meeting of the German Physical Society, Berlin, Germany.
14. – 17. 03. 2012
2. **Coupling phosphorus donors to superconducting microwave resonators**
SiQIP Workshop, Warwick, UK.
13. – 15. 09. 2012
3. **High cooperativity in coupled microwave resonator ferromagnetic insulator hybrids**
Wilhelm und Else Heraeus Workshop, Bad Honnef, Germany.
25. – 28. 11. 2012
4. **Coupled harmonic Oscillators in the Solid State**
Cambridge University, Cambridge, UK.
10. – 12. 12. 2012

Mark Kartsovnik

1. **High-field magnetotransport in the electron-doped cuprate superconductor $Nd_{2-x}Ce_xCuO_4$: in search of a quantum phase transition**

EuroMagNET II Workshop, Les Houches, France.
21. – 25. 05. 2012

2. **High-field magnetotransport properties and the Fermi surface of the electron-doped cuprate superconductor $Nd_{2-x}Ce_xCuO_4$**
   Institute of Solid State Physics, Russian Academy of Science, Chernogolovka, Russia.
   04. 07. 2012
3. **Magnetic quantum oscillations in electron-doped cuprate superconductors**
   Materials and Mechanisms of Superconductivity, M^2S-2012, Washington, USA.
   29. 07. – 03. 08. 2012
4. **Molecular organic metals and superconductors: Model objects in condensed matter physics**
   Chernogolovka Interinstitute Seminar, Chernogolovka, Russia.
   31. 10. 2012

Anton Lerf

1. **Chemistry of iron gall inks: a Mössbauer spectroscopic investigation**
   Universidad de Granada, Facultad de Bellas Artes, Granada, Spain.
   16. 03. 2012
2. **Intercalation of Hydrated Fe^{2+} and Fe^{3+} in the Vermiculites from Santa Olalla and Ojén. A Mössbauer spectroscopic investigation**
   Instituto de Ciencia de Materiales de Sevilla, Spain.
   19. 03. 2012

Achim Marx

1. **Path entanglement of continuous-variable propagating quantum microwaves**
   Workshop on Quantum Simulations, Bilbao, Spain.
   22. – 25. 10. 2012

Matthias Opel

1. **Spin-Elektronik: Von der Entdeckung des Riesenmagnetwiderstandes bis zur modernen Computerfestplatte**
   Naturforschende Gesellschaft Schaffhausen, Switzerland.
   29. 10. 2012
2. **Functional Oxides for Spintronics: Dilute Magnetic Doping and Electrical Spin Transport**
   Physik-Kolloquium, Fachbereich Physik, Johannes-Kepler-Universität Linz, Austria.
   22. 11. 2012
3. **Electrical Spin Injection and Spin Transport in Zinc Oxide**
   Frontiers in Electronic Materials, Aachen, Germany.
   19. 06. 2012
4. **Spin Valves for Spin Transport in Zinc Oxide**
   Joint European Magnetic Symposia (JEMS), Parma, Italy.
   13. 09. 2012
5. **Spin Transport and Spin Dephasing in Zinc Oxide**
   Annual Meeting of the DFG Priority Program SPP 1285 "Halbleiter-Spintronik", Leibniz-Universität Hannover, Germany.
   09. 10. 2012

Manuel Schwarz

1. **Gradiometric persistent current flux qubit with tunable tunnel coupling**
   Spring Meeting of the German Physical Society, Berlin, Germany.
   25. – 30. 03. 2012
2. **Gradiometric flux qubits with tunable gap**
   5. Doktoranden-Workshop des SFB 631 über Festkörperbasierte Quanteninformationsverarbeitung, Wildschönau, Austria.
   08. – 10. 10. 2012

Kurt Uhlig

1. **Cryogen-free dilution refrigerator with 1 K-stage**
   17th International Cryocooler Conference, Los Angeles, USA.
   09. – 12. 07. 2012
2. **Trockener ^{3}He/^{4}He-Mischkühler mit separater 1 K-Stufe**
   Deutsche Kälte-Klima-Tagung 2012, Würzburg, Germany.
   22. 11. 2012

Lectures, Seminars, Courses and other Scientific Activities

Several members of Walther-Meißner-Institute give lectures and seminars at the Technische Universität München.

Lectures

Dietrich Einzel

WS 2011/2012
- Mathematische Methoden der Physik I (Mathematical Methods of Physics I)
- Übungen zu Mathematische Methoden der Physik I (Mathematical Methods of Physics I, Problem Sessions)
- WMI-Seminar über aktuelle Fragen der Tieftemperatur-Festkörperphysik (WMI Seminar on Current Topics of Low Temperature Solid State Physics, with R. Gross, S.B.T. Gönnenwein, A. Marx, M. Opel, R. Hackl)
- Seminar: Advances in Solid-State Physics (with R. Gross, M. Opel, A. Marx, S.T.B. Gönnenwein)

SS 2012
- Mathematische Methoden der Physik II (Mathematical Methods of Physics II)
- Übungen zu Mathematische Methoden der Physik II (Mathematical Methods of Physics II, Problem Sessions)
- WMI-Seminar über aktuelle Fragen der Tieftemperatur-Festkörperphysik (WMI Seminar on Current Topics of Low Temperature Solid-State Physics, with R. Gross, S.B.T. Gönnenwein, A. Marx, M. Opel, R. Hackl)
- Seminar: Advances in Solid-State Physics (with R. Gross, M. Opel, A. Marx, S.T.B. Gönnenwein)

WS 2012/2013
- Mathematische Methoden der Physik I (Mathematical Methods of Physics I)
- Übungen zu Mathematische Methoden der Physik I (Mathematical Methods of Physics I, Problem Sessions)
- WMI-Seminar über aktuelle Fragen der Tieftemperatur-Festkörperphysik (WMI Seminar on Current Topics of Low Temperature Solid-State Physics, with R. Gross, S.B.T. Gönnenwein, H. Hübl, A. Marx, M. Opel, R. Hackl)
- Seminar: Advances in Solid-State Physics (with R. Gross, M. Opel, A. Marx, S.T.B. Gönnenwein)

Frank Deppe

WS 2011/2012
- Angewandte Supraleitung: Josephson-Effekte und Supraleitungselektronik (Applied Superconductivity: Josephson-Effects and Superconducting Electronics)
- Übung zu Angewandte Supraleitung: Josephson-Effekte und Supraleitungselektronik (Applied Superconductivity: Josephson-Effects and Superconducting Electronics, Problem Sessions)

- Seminar: Supraleitende Quantenschaltkreise (mit R. Gross, A. Marx) (Seminar on Superconducting Quantum Circuits)

SS 2012
- Seminar: Advances in Solid-State Physics (with R. Gross, M. Opel, A. Marx, S.T.B. Gönnenwein, D. Einzel)
- Seminar: Supraleitende Quantenschaltkreise (mit R. Gross, A. Marx) (Seminar on Superconducting Quantum Circuits)

WS 2012/2013
- Seminar: Advances in Solid-State Physics (with R. Gross, M. Opel, A. Marx, S.T.B. Gönnenwein, D. Einzel)
- Seminar: Supraleitende Quantenschaltkreise (mit R. Gross, A. Marx) (Seminar on Superconducting Quantum Circuits)

Rudolf Gross

WS 2011/2012
- Supraleitung und Tieftemperaturphysik I (Superconductivity and Low Temperature Physics I)
- Übungen zu Supraleitung und Tieftemperaturphysik I (Superconductivity and Low Temperature Physics I, Problem Sessions)
- WMI-Seminar über aktuelle Fragen der Tieftemperatur-Festkörperphysik (WMI Seminar on Current Topics of Low Temperature Solid-State Physics, with D. Einzel, S.T.B. Gönnenwein, R. Hackl, H. Hübl, A. Marx, M. Opel)
- Seminar: Advances in Solid-State Physics (with D. Einzel, S.T.B. Gönnenwein, R. Hackl, H. Hübl, A. Marx, M. Opel)
- Seminar: Superconducting Quantum Circuits (with F. Deppe, A. Marx)
- Festkörperkolloquium (Colloquium on Solid-State Physics, with D. Einzel)

SS 2012
- Supraleitung und Tieftemperaturphysik II (Superconductivity and Low Temperature Physics II)
- Übungen zu Supraleitung und Tieftemperaturphysik II (Superconductivity and Low Temperature Physics II, Problem Sessions)
- Seminar: Advances in Solid-State Physics (with D. Einzel, S.T.B. Gönnenwein, R. Hackl, H. Hübl, A. Marx, M. Opel)
- WMI-Seminar über aktuelle Fragen der Tieftemperatur-Festkörperphysik (WMI Seminar on Current Topics of Low Temperature Solid-State Physics, with D. Einzel, S.T.B. Gönnenwein, R. Hackl, H. Hübl, A. Marx, M. Opel)
- Seminar: Superconducting Quantum Circuits (with F. Deppe, A. Marx)
- Festkörperkolloquium (Colloquium on Solid-State Physics, with D. Einzel)
- Ferienakademie: Kurs 3 "Physik und Elektronik im Alltag" (Ferienakademie: Course 3 "Physics and Electronics in Everyday Life")

WS 2012/2013
- Supraleitung und Tieftemperaturphysik I (Superconductivity and Low Temperature Physics I)
- Übungen zu Supraleitung und Tieftemperaturphysik I (Superconductivity and Low Temperature Physics I, Problem Sessions)
- WMI-Seminar über aktuelle Fragen der Tieftemperatur-Festkörperphysik (WMI Seminar on Current Topics of Low Temperature Solid-State Physics, with D. Einzel, S.T.B. Gönnenwein, R. Hackl, H. Hübl, A. Marx, M. Opel)

- Seminar: Advances in Solid-State Physics (with D. Einzel, S.T.B. Gönnenwein, R. Hackl, H. Hübl, A. Marx, M. Opel)
- Seminar: Superconducting Quantum Circuits (with F. Deppe, A. Marx)
- Festkörperkolloquium (Colloquium on Solid-State Physics, with D. Einzel)

Sebastian T.B. Gönnenwein

WS 2011/2012

- Seminar: Advances in Solid-State Physics (with R. Gross, A. Marx, M. Opel, D. Einzel, R. Hackl, H. Hübl)
- Seminar: Spin Caloritronics and Spin Pumping
- WMI-Seminar über aktuelle Fragen der Tieftemperatur-Festkörperphysik (WMI Seminar on Current Topics of Low Temperature Solid State Physics, with R. Gross, D. Einzel, H. Hübl, A. Marx, M. Opel, R. Hackl)
- Seminar zu aktuellen Fragen der Magneto- und Spinelektronik (Seminar on Current Topics in Magneto and Spin Electronics, with M. Brandt, M. Opel)

SS 2012

- Seminar: Spinmechanik und Spindynamik (Seminar on Spin Mechanics and Spin Dynamics)
- Seminar: Advances in Solid-State Physics (with R. Gross, A. Marx, M. Opel, D. Einzel, R. Hackl, H. Hübl)
- WMI-Seminar über aktuelle Fragen der Tieftemperatur-Festkörperphysik (WMI Seminar on Current Topics of Low Temperature Solid-State Physics, with R. Gross, D. Einzel, A. Marx, M. Opel, R. Hackl)
- Seminar zu aktuellen Fragen der Magneto- und Spinelektronik (Seminar on Current Topics in Magneto and Spin Electronics, with M. Brandt, M. Opel)

WS 2012/2013

- Seminar: Advances in Solid-State Physics (with R. Gross, A. Marx, M. Opel)
- Magnetismus (Magnetism)
- Übungen zu Magnetismus (Magnetism, Problem Sessions)
- WMI-Seminar über aktuelle Fragen der Tieftemperatur-Festkörperphysik (WMI Seminar on Current Topics of Low Temperature Solid State Physics, with R. Gross, D. Einzel, H. Hübl, A. Marx, M. Opel, R. Hackl)
- Seminar zu aktuellen Fragen der Magneto- und Spinelektronik (Seminar on Current Topics in Magneto and Spin Electronics, with M. Brandt, H. Hübl)

Rudi Hackl

WS 2011/2012

- Seminar: Advanced in Solid-State Physics (with R. Gross, S.T.B. Gönnenwein, H. Hübl, A. Marx, M. Opel)
- WMI-Seminar über aktuelle Fragen der Tieftemperatur-Festkörperphysik (WMI Seminar on Current Topics of Low Temperature Solid-State Physics, with R. Gross, S.B.T. Gönnenwein, H. Hübl, A. Marx, M. Opel, D. Einzel)

SS 2012
- Seminar: Advanced in Solid-State Physics (with R. Gross, S.T.B. Gönnenwein, H. Hübl, A. Marx, M. Opel)
- WMI-Seminar über aktuelle Fragen der Tieftemperatur-Festkörperphysik (WMI Seminar on Current Topics of Low Temperature Solid-State Physics, with R. Gross, S.B.T. Gönnenwein, H. Hübl A. Marx, M. Opel, D. Einzel)
- Seminar: Many-body effects and scattering methods (with C. Pfleiderer and W. Zwerger)

WS 2012/2013
- Seminar: Advances in Solid-State Physics (with R. Gross, S.T.B. Gönnenwein, H. Hübl, A. Marx, M. Opel)
- WMI-Seminar über aktuelle Fragen der Tieftemperatur-Festkörperphysik (WMI Seminar on Current Topics of Low Temperature Solid-State Physics, with R. Gross, S.B.T. Gönnenwein, H. Hübl, A. Marx, M. Opel, D. Einzel)

Hans Hübl

WS 2011/2012
- Magnetismus (Magnetism)
- Übungen zu Magnetismus (Magnetism, Problem Sessions)
- Seminar: Advances in Solid-State Physics (with R. Gross, D. Einzel, S.T.B. Gönnenwein, A. Marx, M. Opel)
- WMI-Seminar über aktuelle Fragen der Tieftemperatur-Festkörperphysik (WMI Seminar on Current Topics of Low Temperature Solid State Physics, with R. Gross, D. Einzel, S.T.B. Gönnenwein, A. Marx, M. Opel, R. Hackl)
- Seminar zu aktuellen Fragen der Magneto- und Spinelektronik (Seminar on Current Topics in Magneto and Spin Electronics, with S.T.B. Gönnenwein, M. S. Brandt)

SS 2012
- Spinelektronik (Spin Electronics)
- Übungen zu Spinelektronik (Spin Electronics, Problem Sessions)
- Seminar: Advances in Solid-State Physics (with R. Gross, A. Marx, M. Opel, S.T.B. Gönnenwein, D. Einzel)
- WMI-Seminar über aktuelle Fragen der Tieftemperatur-Festkörperphysik (WMI Seminar on Current Topics of Low Temperature Solid-State Physics, with R. Gross, D. Einzel, A. Marx, M. Opel, R. Hackl)
- Seminar zu aktuellen Fragen der Magneto- und Spinelektronik (Seminar on Current Topics in Magneto and Spin Electronics, with S.T.B. Gönnenwein, M. S. Brandt)

WS 2012/2013
- Seminar: Spin Caloritronics and Spin Pumping
- Seminar: Advances in Solid-State Physics (with R. Gross, D. Einzel, S.T.B. Gönnenwein, A. Marx, M. Opel)
- WMI-Seminar über aktuelle Fragen der Tieftemperatur-Festkörperphysik (WMI Seminar on Current Topics of Low Temperature Solid State Physics, with R. Gross, D. Einzel, S.T.B. Gönnenwein, A. Marx, M. Opel, R. Hackl)

- Seminar zu aktuellen Fragen der Magneto- und Spinelektronik (Seminar on Current Topics in Magneto and Spin Electronics, with S.T.B. Gönnenwein, M. S. Brandt)

Anton Lerf

WS 2011/2012	• Moderne Aspekte der Chemie für Physiker I (Modern Aspects of Chemistry for Physicists I)
SS 2012	• Moderne Aspekte der Chemie für Physiker II (Modern Aspects of Chemistry for Physicists II) • Nanostrukturierte Materie (Nanostructured Matter, with Prof. J. Plank) • Stoffströme in Natur und Technik (Material fluxes in nature and technology, with Prof. T. Brück)
WS 2012/2013	• Moderne Aspekte der Chemie für Physiker I (Modern Aspects of Chemistry for Physicists I)

The WMI Seminars

The Friday Seminar – Walther-Meißner-Seminar on Current Topics in Low Temperature Physics

SS 2012:

1. **Quantum simulation of the quantum Rabi model in circuit QED**
   Dr. Daniel Ballester, Universidad del Pais Vasco, Bilbao, Spain
   03. 04. 2012
2. **1/f Flux Noise**
   Prof. Dr. John Clarke, Physics Department, University of California, Berkeley, USA
   17. 04. 2012
3. **Quantum limited SQUID amplifiers and their impact on the Axion Dark Matter experiment (ADMX)**
   Prof. Dr. John Clarke, Physics Department, University of California, Berkeley, USA
   17. 04. 2012
4. **A Surprising Discovery in the Group 5 Transition Metals**
   Prof. Dr. John J. Neumeier, Department of Physics, Montana State University, Bozeman, USA
   14. 05. 2012
5. **Jahn-Teller Effect in expanded Fullerenes**
   Prof. Dr. Katalin Kamarás, Institute for Solid State Physics and Optics, Wigner Research Centre for Physics, Hungarian Academy of Sciences, Budapest, Hungary
   23. 05. 2012
6. **Quantum magnetomechanics-magnetically levitated quantum mechanical systems**
   Prof. Dr. Jason Twamley, ARC Centre of Excellence in Quantum Computer Technology and MQ Research Centre for Quantum Science and Technology, Macquarie University, Australia
   01. 06. 2012
7. **Coherence in High Quality TiN Resonators and Epitaxial Re/Al2Al3 Transmon Qubits**
   Dr. Martin Weides, Karlsruher Institut für Technologie, Karlsruhe
   15. 06. 2012
8. **Measuring the Spin Polarization of the 5/2 Fractional Quantum Hall State**
   Dipl.-Phys. Benedikt Frieß, Max-Planck-Institute for Solid State Research, Stuttgart
   25. 06. 2012
9. **Observation of entanglement between a superconducting qubit and an itinerant microwave photon field**
   Christoph Eichler, Quantum Device Laboratory, ETH Zurich, Switzerland
   29. 06. 2012
10. **Unconventional Superconductivity in LiFeAs: Insights from Transport and Tunneling**
    Dr. Christian Hess, Institut für Festkörperforschung, IFW Dresden
    13. 07. 2012
11. **Studies on metal to semiconductor transition in ZnO thin films sparsely doped with Al**
    Prof. Dr. Lalit M. Kukreja, Laser Materials Processing Division, Raja Ramanna Centre for Advanced Technology, Indore, India
    27. 07. 2012
12. **Electrical and Thermal Spintronics in Silicon**
    Prof. Dr. Ron Jansen, National Institute of Advanced Industrial Science and Technology (AIST), Spintronics Research Center, Tsukuba, Ibaraki, Japan
    17. 09. 2012
13. **Odd-frequency Pairing in Superconducting Hybrids and Unconventional Superconductors**
    Prof. Dr. A.A. Golubov, Faculty of Science and Technology and MESA Institute of Nanotechnology, University of Twente, The Netherlands
    21. 09. 2012

WS 2012/2013:

14. **Dynamics in Quantum Antiferromagnets**
    Prof. Dr. Goetz Uhrig, Lehrstuhl für Theoretische Physik I, Technische Universität Dortmund,

Germany
03. 12. 2012

15. **Exotic phases of matter: from critical metals to chiral magnets**
Prof. Dr. Markus Garst, Institut für Theoretische Physik, Universität zu Köln, Germany
04. 12. 2012
16. **Quantum Transport in Hybrid Nanosystems**
Prof. Dr. Jürgen König, Fakultät für Physik, Universität Duisburg-Essen, Germany
10. 12. 2012
17. **A Quantum Impurity Perspective on Strongly Correlated Systems**
Prof. Dr. Walter Hofstetter, Institut für Theoretische Physik, Johann Wolfgang Goethe-Universität Frankfurt, Germany
20. 12. 2012
18. **to be announced**
Prof. Dr. Matthias Vojta, Institut für Theoretische Physik, Technische Universität Dresden, Germany

Topical Seminar on Advances in Solid State Physics – WS 2011/2012, SS 2012 and WS 2012/2013

WS 2011/2012:

1. **Preliminary discussion and assignment of topics**
R. Gross, Walther-Meißner-Institut
18. 10. 2011
2. **Ferromagnetic resonance at low temperatures**
Christoph Zollitsch, Walther-Meißner-Institut
13. 12. 2011
3. **Gradiometric flux quantum bits with tunable tunnel coupling**
Jan Götz, Walther-Meißner-Institut
20. 12. 2011
4. **Nb/AlO$_x$/Nb Josephson junctions for superconducting quantum circuits**
Friedrich Wulschner, Walther-Meißner-Institut
17. 01. 2012
5. **Interlayer Magnetoresistance of the Quasi-twodimensional Charge Density Wave Superconductor α-(BEDT-TTF)$_2$KHg(SCN)$_4$ at Low Temperatures**
Michael Kunz, Walther-Meißner-Institut
31. 01. 2012
6. **Magnetoresistive and magnetogalvanic effects in (Ga,Mn)As**
Sibylle Meyer, Walther-Meißner-Institut
07. 02. 2012

SS 2012:

7. **Preliminary discussion and assignment of topics**
R. Gross, Walther-Meißner-Institut
17. 04. 2012, 24. 04. 2012
8. **Superconducting qubit in wavequide cavity with coherence time approaching 0.1ms**
Michael Fischer, Technische Universität München
15. 05. 2012
9. **Quantum simulations with trapped ions**
Michael Gerl, Technische Universität München
22. 05. 2012
10. **Quantum simulations with ultracold quantum gases**
Djuro Bikaljevic, Technische Universität München
05. 06. 2012
11. **Untersuchung des Spindichtewellenübergangs in BaFe2As2**
Andreas Baum, Walther-Meißner-Institut

19. 06. 2012

12. **Scalable chains of superconducting microwave resonators**
    Lisa Janker, Technische Universität München
    03. 07. 2012
13. **Towards fast beam splitters from superconducting resonators**
    Philipp Assum, Technische Universität München
    03. 07. 2012
14. **Untersuchung von Supraleitern in einer Diamantdruckzelle**
    Georg Haunschild, Technische Unversität München
    10. 07. 2012
15. **Ginzburg-Landau description of superconducting cylinders**
    Jonas Woste, Technische Universität München
    17. 07. 2012
16. **Tempern und Charakterisierung von oxydischen Proben**
    Michael Rehm, Technische Universität München
    17. 07. 2012
17. **Spitzenverstärkte Raman-Steuerung (TERS)**
    David Hoch, Technische Universität München
    24. 07. 2012

WS 2012/2013:

18. **Preliminary discussion and assignment of topics**
    R. Gross, Walther-Meißner-Institut
    16. 10. 2012, 23. 10. 2012
19. **Spin Seebeck Insulator**
    Niklas Roschewsky, Technische Universität München
    20. 11. 2012
20. **Response and collective modes in non-cetrosymmetric superconductors**
    Nikolaj Bittner, Walther-Meißner-Institut
    27. 11. 2012
21. **Determination of the energy gap in superconductors via scanning tunneling spectroscopy**
    Andreas Walter, Technische Universität München
    04. 12. 2012
22. **Quantum-coherent coupling of a mechanical oscillator to an optical cavity mode**
    Marco Bobinger, Technische Universität München
    11. 12. 2012
23. **Storing Quantum Information in Spin Systems âĂŞ Concepts and Perspectives**
    Jochen Bissinger, Technische Universität München
    18. 12. 2012
24. **Inverse Spin Hall Effect**
    Johannes Mendil, Technische Universität München
    15. 01. 2013
25. **Electrical control of the ferromagnetic phase transition in cobalt at room temperature**
    Philipp Metzner, Technische Universität München
    22. 01. 2013

Topical Seminar: Spin Mechanics and Spin Dynamics – SS 2012

1. **Preliminary discussion and assignment of topics**
   Sebastian Gönnenwein, Walther-Meißner-Institut
   18. 04. 2012
2. **Thermoelectric effects without a spin**
   Sebastian Gönnenwein, Walther-Meißner-Institut
   16. 05. 2012

3. **Transverse magneto-thermo-electric effects**
   Eri Sato, Technische Universität München
   23. 05. 2012
4. **Superconducting coplanar waveguide microwave resonators**
   Alexander Backs, Technische Universität München
   06. 06. 2012
5. **Spin-dependent Seebeck effect**
   Susanne Goerke, Technische Universität München
   13. 06. 2012
6. **Spin pumping**
   Schorsch Sauther, Technische Universität München
   27. 06. 2012
7. **Antiferromagnetic resonance**
   Johannes Lotze, Walther-Meißner-Institut
   04. 07. 2012
8. **Seebeck spin tunneling**
   Mathias Frank, Technische Universität München
   11. 07. 2012
9. **Intrinsic spin-dependent transport**
   Sibylle Meyer, Walther-Meißner-Institut
   18. 07. 2012

Topical Seminar: Spin Caloritronics and Spin Pumping – WS 2012/2013

1. **Preliminary discussion and assignment of topics**
   Hans Hübl, Walther-Meißner-Institut
   17. 10. 2012, 24. 10. 2012
2. **Thermoelectric effects without a spin**
   Julia Winnerl, Technische Universität München
   05. 12. 2012
3. **Ferromagnetic Resonance**
   Andreas Rauscher, Technische Universität München
   19. 12. 2012
4. **Spin hall effect**
   Friedrich Witek, Technische Universität München
   09. 01. 2013
5. **Spin Seebeck effect**
   Hans Hübl, Walther-Meißner-Institut
   16. 01. 2013
6. **Spin Peltier effect**
   Andreas Duensing, Technische Universität München
   23. 01. 2013

Topical Seminar on Superconducting Quantum Circuits – WS 2011/2012, SS 2012 and WS 2012/2013

WS 2011/2012:

1. **Preliminary discussion and assignment of topics**
   F. Deppe, A. Marx, R. Gross, Walther-Meißner-Institut
   18. 10. 2011
2. **Superconducting qubit as a quantum transformer routing entanglement between a microscopic quantum memory and a macroscopic resonator**
   Elisabeth Hoffmann, Walther-Meißner-Institut
   15. 11. 2011

3. **Quantum walks of correlated particles**
   Jan Goetz, Walther-Meißner-Institut
   22. 11. 2011
4. **Noise spectroscopy through dynamical decoupling with a superconducting flux qubit**
   Ling Zhong, Walther-Meißner-Institut
   06. 12. 2011
5. **Quantum State Tomography of an Itinerant Squeezed Microwave Field**
   Alexander Baust, Walther-Meißner-Institut
   20. 12. 2011
6. **Full-field implementation of a perfect eavesdropper on a quantum cryptograph system**
   Max Häberlein, Walther-Meißner-Institut
   10. 01. 2012

SS 2012:

7. **Preliminary discussion and assignment of topics**
   F. Deppe, A. Marx, R. Gross, Walther-Meißner-Institut
   17. 04. 2012, 24. 04. 2012
8. **On-chip quantum simulation with superconducting circuits**
   Jan Goetz, Walther-Meißner-Institut
   08. 05. 2012
9. **Observation of the dynamical Casimir effect in a superconducting circuit**
   Ling Zhong, Max Häberlein, Alex Baust, Walther-Meißner-Institut
   15. 05. 2012
10. **Coupling a flux qubit to a superconducting transmission line resonator**
    Thomas Losinger, Walther-Meißner-Institut
    05. 06. 2012
11. **Demonstrating quantum speedup in a superconducting two-qubit processor**
    Manuel Schwarz, Max Häberlein, Walther-Meißner-Institut
    12. 06. 2012
12. **Widely tunable, nondegenerate three-wave mixing device operating at the quantum limit**
    Friedrich Wulschner, Walther-Meißner-Institut
    19. 06. 2012
13. **Progress report**
    Fredrik Hocke, Walther-Meißner-Institut
    26. 06. 2012
14. **Producing and measuring entanglement between two beams of microwave light**
    Edwar Xie, Walther-Meißner-Institut
    03. 07. 2012
15. **Towards tunable coupling of superconducting transmission line resonators**
    Xiaoling Lu, Walther-Meißner-Institut
    10. 07. 2012
16. **Superconducting flux qubits with tunable tunnel coupling**
    Zhaohai Jiang, Walther-Meißner-Institut
    17. 07. 2012

WS 2012/2013:

17. **Preliminary discussion and assignment of topics**
    F. Deppe, A. Marx, R. Gross, Walther-Meißner-Institut
    16. 10. 2012, 23. 10. 2012
18. **Hybrid circuit cavity quantum electrodynamics with a micromechanical resonator**
    Fredrik Hocke, Walther-Meißner-Institut
    13. 11 .2012
19. **Progress Report**
    Franz Sterr, Walther-Meißner-Institut
    20. 11. 2012

20. **Computing prime factors with a Josephson phase qubit quantum precessor**
    Stefan Zenger, Technische Universität München
    27. 11. 2012
21. **Observation of Entanglement between Itinerant Microwave Photons and a Superconducting Qubit**
    Miriam Müting, Technische Universität München
    11. 12. 2012
22. **Stabilizing Rabi oscillations in a superconducting qubit using quantum feedback**
    Michael Fischer, Technische Universität München
    08. 01. 2013
23. **Quantum Simulation of Tunneling in Small Systems**
    Jan Goetz, Walther-Meißner-Institut
    22. 01. 2013
24. **Josephson junction-embedded transmission-line resonators: from Kerr medium to in-line transmon**
    Friedrich Wulschner, Walther-Meißner-Institut
    05. 02. 2013
25. **A Josephson quantum electron pump**
    Ling Zhong, Walther-Meißner-Institut
    19. 02. 2013

C: Solid State Colloquium

The WMI has organized the Solid-State Colloquium of the Faculty of Physics in WS 2011/2012, SS 2012, and WS 2012/2013. The detailed program can be found on the WMI webpage: http://www.wmi.badw-muenchen.de/teaching/Seminars/fkkoll.html.

Staff of the Walther-Meißner-Institute

Director
Prof. Dr. Rudolf Gross

Deputy Director
Dr. Werner Biberacher

Technical Director
Dr. Achim Marx

Administration/Secretary's Office
Ludwig Ossiander
Emel Dönertas

Scientific Staff
Dr. Werner Biberacher
Dr. Frank Deppe
Priv.-Doz. Dr. habil. Dietrich Einzel
Prof. Dr. Andreas Erb
Dr. Stephan Geprägs
Priv.-Doz. Dr. habil. Sebastian Gönnenwein
Priv.-Doz. Dr. habil. Rudolf Hackl
Dr. Hans Hübl
Dr. Mark Kartsovnik
Prof. Dr. Anton Lerf
Dr. Achim Marx
Dr. Matthias Opel
Dr. Kurt Uhlig

Dipl.-Phys. Matthias Althammer
Dipl.-Phys. Andreas Baum
Dipl.-Phys. Alexander Baust
Dipl.-Phys. Nitin Chelwani
Dipl.-Phys. Hans-Martin Eiter
Dipl.-Phys. Max Häberlein
Dipl.-Phys. Toni Helm
Dipl.-Phys. Fredrik Hocke
Dipl.-Phys. Elisabeth Hoffmann
Dipl.-Phys. Florian Kretzschmar
Dipl.-Phys. Michael Kunz
Dipl.-Phys. Johannes Lotze
Dipl.-Phys. Edwin Menzel
Dipl.-Phys. Sibylle Meyer
Dipl.-Phys. Matthias Pernpeintner
Dipl.-Phys. Michael Schreier
Dipl.-Phys. Manuel Schwarz
Dipl.-Phys. Mathias Weiler
Dipl.-Phys. Ling Zhong
Dipl.-Phys. Christoph Zollitsch

Technical Staff
Peter Binkert
Dipl.-Ing. (FH) Thomas Brenninger
Dipl.-Ing. (FH) Ulrich Guggenberger
Dieter Guratzsch
Astrid Habel
Karen Helm-Knapp
Dipl.-Ing. (FH) Josef Höss
Namvar Jahanmehr

Julius Klaus
Robert Müller
Jan Naundorf
Georg Nitschke
Christian Reichlmeier
Harald Schwaiger
Helmut Thies
Siegfried Wanninger

Assistants

Sybilla Plöderl
Brigitte Steinberg

Permanent Guests

Prof. Dr. B. S. Chandrasekhar
Dr. Robert Doll
Dr. Karl Neumaier
Dr. Christian Probst
Prof. Dr. Erwin Schuberth

Guest Researchers

1. Prof. Dr. B.S. Chandrasekhar
   permanent guest
2. Dr. Robert Doll
   permanent guest
3. Dr. Karl Neumaier
   permanent guest
4. Dr. Christian Probst
   permanent guest
5. Prof. Dr. Erwin Schuberth
   permanent guest
6. Dr. Guillermo Romero, Universidad del Pais Vasco, Bilbao, Spain
   05. 03. – 11. 03. 2012
7. Prof. Vladimir Zverev, Institute of Solid Physics, Chernogolovka, Russia
   11. 03. – 30. 04. 2012
8. Roberto Di Candia, Universidad del Pais Vasco, Bilbao, Spain
   14. 03. – 31. 03., 13. 08. âĂŞ 17. 08. 2012
9. Prof. Enrique Solano, Universidad del Pais Vasco, Bilbao, Spain
   16. 03. – 20. 03. 2012
10. Dr. Pavel Grigoriev, Landau Institute, Chernogolovka, Russia
    01. 04. – 30. 04. 2012
11. Dr. Daniel Ballester, Universidad del Pais Vasco, Bilbao, Spain
    02. 04. – 05. 04. 2012
12. Prof. John Clarke, University of California, Berkeley, USA
    16. 04. – 18. 04. 2012
13. Prof. Peter Knoll, Institut für Experimentalphysik, Karl-Franzens-Universität, Graz, Austria
    02. 05. – 06. 05. 2012
14. Prof. John J. Neumeier, Montana State University, Bozeman, USA
    14. 05. – 17. 05. 2012
15. Prof. Katalin Kamarás, Institute for Solid State Physics and Optics, Wigner Research Centre for Physics, Hungarian Academy of Sciences, Budapest, Hungary
    21. 05. – 25. 05. 2012 and 08. 07. – 11. 07. 2012
16. Akashdeep Kamra, Kavli Institute of Nanoscience, Delft University of Technology, Delft, The Netherlands
    15. 06. – 30. 06. 2012 and 28. 09. – 13. 10. 2012
17. Prof. Dr. Juan Poyato Ferrera, Instituto de Ciencia de Materiales, Sevilla, Spain
    01. 07. – 26. 07. 2012
18. Dr. Milos Negyedi, Technische Universität Budapest, Hungary
    02. 07. – 14. 07. 2012
19. Prof. Ferenc Simon, Budapest University of Technology and Economics, Budapest, Hungary
    05. 07. – 07. 07. 2012
20. Prof. Lalit M. Kukreja, Raja Ramanna Centre for Advanced Technology, Indore, India
    26. 07. – 30. 07. 2012
21. Hiroyasu Nakayama, Institute for Materials Research Tohoku University, Sendai, Japan
    28. 07. – 31. 07. 2012

22. Dr. Nadezda Panarina, Leibniz Institute for Solid State and Materials Research, Dresden, Germany
    02. 08. – 04. 08. 2012
23. Ivan Soldatov, Leibniz Institute for Solid State and Materials Research, Dresden, Germany
    02. 08. – 04. 08. 2012
24. Jorge Casanova, Universidad del Pais Vasco, Bilbao, Spain
    05. 08. – 18. 08. 2012
25. Lucas Lamata, Universidad del Pais Vasco, Bilbao, Spain
    05. 08. – 11. 08. 2012
26. Dr. Jeroen Clusters, Vienna University of Technology, Vienna, Austria
    13. 08. – 19. 08. 2012
27. Simone Felicetti, Universidad del Pais Vasco, Bilbao, Spain
    14. 09. – 19. 09. 2012
28. Prof. A.A. Golubov, Faculty of Science and Technology and MESA, University of Twente, The Netherlands
    20. 09. – 23. 09. 2012
29. Evgeny Zamburg, Southern Federal University, Rostov, Russia
    01. 10. 2012 – 28. 02. 2013
30. Dr. Oleg Vyaselev, Institute of Solid Physics, Chernogolovka, Russia
    01. 12. – 24. 12. 2012
31. Prof. A. Zawadowski, Budapest University of Technology and Economics, Budapest, Hungary
    06. 12. – 16. 12. 2012
32. Isaac Fernando Quijandria Diaz, CSIC Universidad de Zaragoza, Zaragoza, Spain
    12. 12. – 19. 12. 2012

Commission for Low Temperature Physics

Members of the Commission for Low Temperature Research of the Bavarian Academy of Sciences and Humanities:

Vollhardt, Dieter, chairman (Universität Augsburg)
Abstreiter, Gerhard, deputy chairman (Technische Universität München)
Gross, Rudolf (Walther-Meißner-Institut)
Kaiser, Wolfgang (Technische Universität München)
Landwehr, Gottfried (Universität Würzburg)
Hänsch, Theodor (Max-Planck-Institut für Quantenoptik, Garching)
Schwoerer, Markus (Universität Bayreuth)
Weiss, Dieter (Universität Regensburg)